Wegener Center for Climate and Global Change
University of Graz

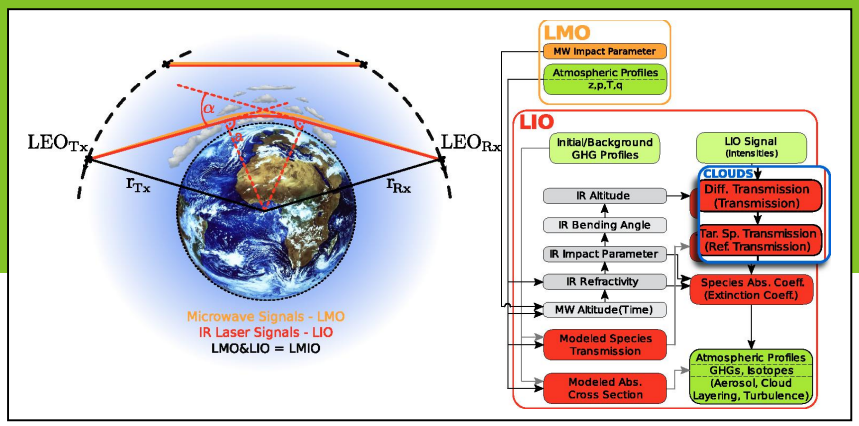

Scientific Report No. 63-2014

Greenhouse gas profiling by infrared-laser and microwave occultation: Atmospheric influences and retrieval algorithm in clear and cloudy air

Veronika Proschek

December 2014

Financially supported by

The **Wegener Center for Climate and Global Change** combines as an interdisciplinary, internationally oriented research institute the competences of the University of Graz in the research area “Climate, Environmental and Global Change”. It brings together, in a dedicated building close to the University central campus, research teams and scientists from fields such as geo- and climate physics, meteorology, economics, geography, and regional sciences. At the same time close links exist and are further developed with many cooperation partners, both nationally and internationally. The research interests extend from monitoring, analysis, modeling and prediction of climate and environmental change via climate impact research to the analysis of the human dimensions of these changes, i.e., the role of humans in causing and being effected by climate and environmental change as well as in adaptation and mitigation. (more information at www.wegcenter.at)

The present report is the result of a dissertation work completed in April 2014. The work was funded by the European Space Agency (ESA) under ESA-ESTEC Contract No. 21507/08/NL/HE (ACTLIMB project) and the Austrian Space Applications Programme (ASAP) / Austrian Research Promotion Agency (FFG) under FFG-ALR Contract No. 819706 (ACCU-Clouds project).

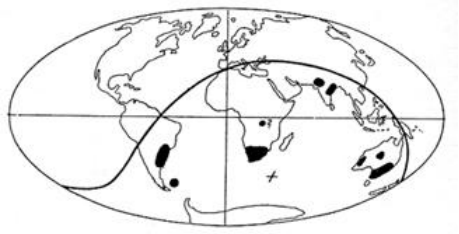

Alfred Wegener (1880-1930), after whom the Wegener Center is named, was founding holder of the University of Graz Geophysics Chair (1924-1930). In his work in the fields of geophysics, meteorology, and climatology he was a brilliant scientist and scholar, thinking and acting in an interdisciplinary way, far ahead of his time with this style. The way of his ground-breaking research on continental drift is a shining role model—his sketch on the relations of continents based on traces of an ice age about 300 million years ago (left) as basis for the Wegener Center Logo is thus a continuous encouragement to explore equally innovative ways:
paths emerge in that we walk them (Motto of the Wegener Center).

Wegener Center Verlag • Graz, Austria

ISBN 978-3-9503918-0-0

December 2014

Contact: DI Dr. Veronika Proschek
veronika.proschek@uni-graz.at

Wegener Center for Climate and Global Change
University of Graz
Brandhofgasse 5
A-8010 Graz, Austria
www.wegcenter.at

Wegener Center for Climate and Global Change
Institute for Geophysics, Astrophysics, and Meteorology
University of Graz

Dissertation
zur Erlangung des akademischen Grades einer Doktorin der Naturwissenschaften

Greenhouse gas profiling by infrared-laser and microwave occultation: Atmospheric influences and retrieval algorithm in clear and cloudy air

Veronika Proschek

April 2014
Editiert: Dezember 2014

Betreuer:
Univ.-Prof. Mag. Dr. Gottfried Kirchengast

Wegener Center for Climate and Global Change,
University of Graz, Brandhofgasse 5, A-8010 Graz, Austria
Inst. for Geophysics, Astrophysics, and Meteorology/Inst. of Physics,
University of Graz, Universitätsplatz 5, A-8010 Graz, Austria

This thesis was submitted in April 2014 and modified in December 2014. Chapter four was edited to the final, published paper version.

Abstract

The ACCURATE—Climate Benchmark Profiling of Greenhouse Gases and Thermodynamic Variables and Wind from Space satellite mission concept is a synergistic combination of the Low Earth Orbit microwave occultation (LMO) and Low Earth Orbit infrared-laser occultation (LIO) technique together termed Low Earth Orbit microwave and infrared-laser occultation (LMIO). It enables the measurement of physical and chemical profiles in the upper troposphere–lower stratosphere (UTLS) with high vertical resolution and in a long-term stable, global, consistent and self-calibrating way.

This thesis contributes to the feasibility study of the LMIO mission concept.

Firstly, an assessment of atmospheric influences on Infrared Laser (IRL) signals performing a limb-scan of the UTLS region was done. Thoroughly defined IRL on-absorption and off-channels are found to be ideal candidates for the LIO technique. Atmospheric broadband effects are highly correlated for channel pairs so that the differential transmission principle accurately corrects them.

Secondly, an LMIO retrieval algorithm was developed to retrieve a set of greenhouse gases (GHGs) in clear-air conditions, including defocusing loss, aerosol extinction and Rayleigh scattering. A consecutive retrieval order of the forward-simulated IRL signals enables to retrieve unbiased volume mixing ratio profiles of GHGs with r.m.s. errors smaller than 1 % to 3 %.

Thirdly, a LMIO retrieval was developed to cover cloudy-air conditions. IRL signals are strongly affected by cloud extinction, reducing the tropospheric penetration depth of occultation events. Intermittent cloud layers or thin cirrus, perturbing the IRL transmission profile, can be bridged and increase the penetration depth and thus the number of occultation events for climate benchmark observations.

The results show promising prospects for climate benchmark contributions with unprecedented accuracy for monitoring the physical and chemical state of the UTLS.

Zusammenfassung

Das Satellitenmissions-Konzept ACCURATE—Climate Benchmark Profiling of Greenhouse Gases and Thermodynamic Variables and Wind from Space ist eine Synergie der Mikrowellen-Okkultation (LMO) und der Infrarotlaser-Okkultation (LIO), vereinigt zu der Mikrowellen- und Infrarotlaser-Okkultation für Satelliten (LMIO). Es ermöglicht die Messung physikalischer und chemischer Profile in der oberen Tropo- und unteren Stratosphäre (UTLS) mit hoher vertikaler Auflösung, Langzeit-Stabilität, globaler Abdeckung und funktioniert selbst-kalibrierend.

Diese Arbeit trägt zu Machbarkeitsstudien zum LMIO Konzept bei.

Erstens: zur Erfassung der atmosphärischen Einflüsse auf das Infrarotlaser (IRL) Signal während des Limb-Scan in der UTLS. Sorgfältig gewählte IRL-absorbierende und nicht-absorbierende Kanäle sind ideale Kandidaten für die LIO Technik. Signalpaare weisen hohe Korrelation bei atmosphärischen Breitbandeffekten auf, die durch Signal-Subtraktion korrigiert werden.

Zweitens: ein LMIO Retrieval Algorithmus zur Gewinnung von Treibhausgaskonzentrationen GHGs, welcher Defokusierungs-Verluste, Aerosol-Extinktion und Rayleigh-Streuung beinhaltet, wurde entwickelt. Eine Abfolge von vorwärts simulierten IRL Signalen ermöglicht eine Retrievalgenauigkeit für GHGs frei von systematischen Fehlern und Restfehlern kleiner als 1 % bis 3 %.

Drittens: ein LMIO Retrieval wurde entwickelt, um auch Wolkeneffekte mit abzudecken. IRL Signale sind stark beeinflusst von Wolken und reduzieren somit die troposphärische Eindringtiefe für Okkultationen. Wolkenschichten oder dünne Zirren, welche das IRL-Transmissionsprofil stören, werden überbrückt und erhöhen somit die Eindringtiefe und daher die Anzahl der Okkultationen für Klima-Benchmark-Beobachtungen.

Die Ergebnisse zeigen vielversprechende Aussichten für Klimamessungen mit noch nie dagewesener Genauigkeit zum Beobachten des physikalischen und chemischen Zustandes der Erdatmosphäre.

Acknowledgments

> "Everyone thinks of changing the world, but no one thinks of changing himself."
>
> *(Leo Tolstoy)*

In the working of a thesis one gets a deep inside of the specific work the topic of the thesis is dealing with. Although, during this time I got the chance to work not only in a computational way—although the thesis is solely based on the simulative part—but also as part of a team that performed the first experimental proof of an infrared-laser link for greenhouse gas measurements, applying the differential transmission principle, widening the view of scientific objectives.

Therefore, I want to thank my supervisor Univ.-Prof. Dr. Gottfried Kirchengast for these opportunities. Under his guidance I got the chance to participate in a broadened sense in an innovative mission development. Thank you for the time and patience answering any scientific questions to me, and supporting all the paper and report preparations along the road.

I also want to thank Susanne Schweitzer, co-member of the Wegener Center's ACCURATE team, for particularly being very accurate when co-editing work and helping introduce me into the LEO–LEO microwave and infrared-laser occultation (LMIO) mission with its issues and tasks. A Thank you goes as well to Claudia Emde from the Ludwig Maximilian University, Munich. She co-guided me particularly during the research stay at her institute regarding cloud simulation issues.

For financial support I want to thank the European Space Agency (ESA), and technical officer Armin Löscher, and the Austrian Space Applications Programme (ASAP) for enabling the feasibility studies of ACCURATE which also funded my work.

It would have been very difficult to work on the thesis without the help of Johannes Fritzer, to whome I am grateful for the extended support concerning EGOPS or xEGOPS software issues and module development. I am also very thankful to Michael Pock, who gave me an extraordinary insight into programming with the patience and time to explain and answer every question mark. I am also thankful for his meticulously developed LaTeX framework I used for my thesis and every-day work. Thank you to Florian Ladstädter for his patience forcing me into the powerful open-source tools and getting to know John Richard Pilger. Gratitude goes to Armin Leuprecht for many very helpful Linux tricks and lots of fun. I also really appreciate proofreading of my thesis by Andreas Plach.

Many thanks go to the Wegener Center members for the very warm working atmosphere, contributing to an open minded and interesting working place; Bettina Schlager and Sabine Tschürtz and the admin team for support in any sort of (non) administrative concerns; my office fellows, Thomas Kabas and Florian Ladstädter, Therese Rieckh, Thomas Schinko and Brigitte Wolkinger for lots of fruitful discussions concerning (non) climate change topics. They made the office a pleasant *jungle* to work in.

I have to say in many ways Thank you to my closest friends Stefanie Halbwirth, Christine Leitner, Karin and Martin Viertler for their friendship, support, honesty and simplicity during my Ph.D. time and far beyond. Thank you to Manuela Sornig for lots of encouragement, my entire family—my backbone—who I have to thank a lot for and finally, Christian Deinhammer for love, trust, friendship, fun and just being there for me.

Preface

This Ph.D. thesis is mainly based on the following publications:

S. Schweitzer, G. Kirchengast and V. Proschek (2011). 'Atmospheric influences on infrared-laser signals used for occultation measurements between Low Earth Orbit satellites'. In: *Atmos. Meas. Tech.* 4, pp. 2273–2292. DOI: 10.5194/amt-4-2273-2011. URL: http://www.atmos-meas-tech.net/4/2273/2011/

V. Proschek, G. Kirchengast and S. Schweitzer (2011). 'Greenhouse gas profiling by infrared-laser and microwave occultation: retrieval algorithm and demonstration results from end-to-end simulations'. In: *Atmos. Meas. Tech.* 4, pp. 2035–2058. DOI: 10.5194/amt-4-2035-2011. URL: http://www.atmos-meas-tech.net/4/2035/2011/

V. Proschek et al. (2014a). 'Greenhouse gas profiling by infrared-laser and microwave occultation in cloudy air: results from end-to-end simulations'. In: *J. Geophys. Res. Atmos.* 119, pp. 12,372–12,390. DOI: 10.1002/2014JD021938

During the time of the Ph.D. theses work further complementary publications were worked out, where I participated as (co-)author but which are not part of the Ph.D. thesis. For complementary information these publications are listed below:

J. S. A. Brooke et al. (2012). 'Greenhouse gas measurements over a 144 km open path in the Canary Islands'. In: *Atmos. Meas. Tech.* 5, pp. 2309–2319. DOI: 10.5194/amt-5-2309-2012. URL: http://www.atmos-meas-tech.net/5/2309/2012/

A. S. Gurvich et al. (2012). 'Spatiotemporal structure of a laser beam over 144 km in a Canary Islands experiment'. In: *Appl. Opt.* 51, pp. 7374–7383. DOI: 10.1364/AO.51.007374. URL: http://ao.osa.org/abstract.cfm?URI=ao-51-30-7374

A. S. Gurvich et al. (2014). 'Spatiotemporal structure of a laser beam at a path length of 144 km: comparative analysis of spatial and temporal spectra'. In: *Appl. Opt.* 53.12, pp. 2625–2631. DOI: 10.1364/AO.53.002625. URL: http://ao.osa.org/abstract.cfm?URI=ao-53-12-2625

V. Proschek et al. (2014b). 'Retrieval and validation of carbon dioxide, methane and water vapor for the Canary Islands infrared-laser occultation experiment'. In: *Atmos. Meas. Tech. Discuss.* 7, pp. 11593–11652. DOI: 10.5194/amtd-7-11593-2014. URL: http://www.atmos-meas-tech-discuss.net/7/11593/2014/amtd-7-11593-2014.html

A. Plach, V. Proschek and G. Kirchengast (2014). 'Profiling wind and greenhouse gases by infrared-laser occultation: algorithm and end-to-end simulation results in windy air'. In: *Atmos. Meas. Tech.* submitted

Contents

Introduction

Climate change, a phrase everybody heard at least once in live, and whether it is influenced by human activities is often a topic of discussion in modern mass media. As result the general public is still somewhat doubtful about the humans role in climate change. In the scientific climate community there is little doubt about the human impact on Earth's climate, however.

Svante Arrhenius, a Swedish physicist, already claimed in 1896 that an increase of carbon dioxide (CO_2) in the atmosphere results in an increase of the Earth's surface temperature caused by the greenhouse effect (Arrhenius 1896). Since then scientists try to better understand the Earth's climate, the single contributing effects and determine the quantitative impact of these effects in a more accurate manner. Therefore, scientist develop climate models based on analytic physical laws, like the thermodynamic equations, and empirically found relations. The latter are based on observations.

One of the most important observations proofing the CO_2 increase in the atmosphere over the last decades is the *Keeling Curve* (Keeling 1970; From and Keeling 1986). Charles David Keeling, an American scientist, recorded the atmospheric CO_2 content at the Mauna Loa Observatory on the Hawaiian island starting in 1958. It turned out to become the longest continuous recording of CO_2 data in the atmosphere, showing seasonal variations within a steadily increasing long-term trend. Land-surface temperature observations, dated back to the year 1880 (Williams, Menne and Lawrimore 2012), showed similar increasing trends correlating to the CO_2 concentration increase. With the years more and more accurate observations or reconstructions of temperature and CO_2 profiles, based for example on conventional temperature measurement methods, satellite measurements or ice-cores, also showed similar increasing trend (Moberg et al. 2005; Morice et al. 2012).

Still, the science community requires atmospheric data with higher resolution and accuracy, continuously recorded, long-term stable and with even coverage of the entire globe. These are needed to determine the anthropogenic impact and understand the climate system in such a way that also future climate model projections become more and more reliable. This leads us to the motivation of this Ph.D. thesis.

The new satellite mission concept ACCURATE—Climate Benchmark Profiling of Greenhouse Gases and Thermodynamic Variables and Wind from Space is based on the Low Earth Orbit (LEO–LEO) microwave and infrared-laser occultation (LMIO)

principle, which is a synergistic combination of the LEO–LEO microwave occultation (LMO) and LEO–LEO infrared-laser occultation (LIO) measurement technique. LMIO is an intriguing new climate benchmark measurement method to record atmospheric parameters and greenhouse gas content within the upper troposphere–lower stratosphere (UTLS). It covers the globe with sufficient repetition frequency for large-scale climate monitoring, is accurate and long-term stable, independent, self-calibrating and provides a very good vertical resolution.

In this thesis i) an assessment of the atmospheric influences on ACCURATE selected Infrared Laser (IRL) signals, ii) an LIO retrieval algorithm for multi-species of greenhouse gas (GHG) retrieval in clear-air, and iii) GHG retrieval under cloudy-air conditions, accounting also for atmospheric turbulence, are introduced. These studies substantially contribute to assessing and establishing the feasibility and high scientific utility of an ACCURATE mission.

The thesis is structured into:

Chapter 1 This chapter provides a synoptic introduction to the thesis, including key methods and tools used. It gives a short summary of climate change, its history and the relation with greenhouse gases regarding the man-made contributions and an overview of the current state of remote GHG measurements within the atmosphere. Further an overview of the LMIO mission concept is provided. It also gives a brief insight into the assessment work and retrieval development work, which was done to help demonstrate the feasibility of the LMIO method. And at last an overview is provided on the software tool eXtended End-to-End Generic Occultation Performance Simulation and Processing System (xEGOPS) developed at the Wegener Center. It is an extension of the kernel software tool EGOPS and the main tool for the LMIO simulations for the studies reported in the next chapter.

Chapter 2 This chapter presents the published work about atmospheric influences on IRL signals in the atmosphere. It discusses the various atmospheric influences, such as refraction, defocusing loss, molecular absorption, aerosol extinction and Rayleigh scattering, contributing to attenuation of IRL signals in an occultation measurement setup, and thus determines the scientific requirements for GHG measurements by the LMIO technique.

Chapter 3 This chapter presents the published work about development and performance assessment of an algorithm for retrieval of GHG profiles in clear-air conditions. It provides a detailed description of the algorithm design and the specific steps to calculate from LMO-derived variables and IRL signals the volume mixing ratio (VMR) for the targeted greenhouse gases (GHGs). The accuracy of the retrievals is then assessed for main GHGs including carbon dioxide, methane, water vapor, and ozone.

Chapter 4 This chapter presents the work submitted for publication about GHG retrieval in cloudy-air conditions. It builds on the clear-air algorithm from the previous chapter and expands that basis algorithm with specific cloud algorithm steps. These advancements enable to recover cloud-perturbed IRL signal profiles, bridging cloud-induced gaps in profiles, and allow to obtain GHG profiles through broken cloudiness deeper into the troposphere.

Summary and Conclusions This closing section provides a concise summary and conclusions.

CHAPTER 1

ACCURATE in the context of climate change

1.1 Climate change and greenhouse gases

SINCE the existence of the Earth, our planet undergoes a *Natural Climate Change*. This natural climate variability is driven by the Earth's movement relative to the Sun and it's radiation influences and the very slow movement of the lithosphere. The latter releases greenhouse gases (GHGs) when continents collide or drift at each other or due to natural impacts, like volcanic eruptions or meteor impacts (Rahmsdorf and Schellnhuber 2007). An overview about the evolution of the GHGs and of temperature, their interdependence and why an accurate knowledge of these parameters is so important to determine the human impact on climate change is given in this chapter.

1.1.1 Greenhouse gases evolution

Hundreds million years ago the GHG content in the *free atmosphere*, denoting the atmosphere above ∼2 km from ground, varied strongly. For one of the main GHGs, carbon dioxide (CO_2), the concentration showed levels of < 500 ppm during periods of long-lived and wide-spread glaciation, and up to > 1000 ppm for warmer periods (Royer et al. 2004). This content varied due to natural variability or natural impacts (e.g. volcanic eruptions or meteor impacts). The last 25 to 9 million years ago the amount of CO_2 in the free-atmosphere decreased down between the 190 ppmv and 260 ppmv level (Pagani, Arthur and Freeman 1999) and was oscillating with the glacial periodicity of ∼100,000 years (Milanković cycle) during the last 420,000 years below the ∼280 ppmv level (Fischer et al. 1999; Petit et al. 1999).

During the last ∼11,000 years, the Earth is in a warm (inter-glacial) state within an ice-age, the so called Holocene. Figure 1.1 a (gray shaded area) shows various ice core and firn air investigations from Antarctica for CO_2, methane (CH_4), and nitrous

oxide (N_2O) concentrations, representing conditions during the Holocene in a rather static concentration (Blunier et al. 1994; Flückiger et al. 2002; Monnin et al. 2004; MacFarling-Meure et al. 2006; Schilt et al. 2010; Ciais et al. 2013).

Looking into detail in the white shaded area of Fig. 1.1 a, the last 2,000 years show rather constant levels of CO_2 (<∼284 ppm), CH_4 (<∼720 ppb) and N_2O (<∼280 ppb) until ∼1800 AD. This 2,000 year period is expanded in Figure 1.1 b, showingthe near-constant pre-industrial level and the greenhouse gas (GHG) development from the beginning of the industrial revolution in the second half of the 18^{th} century with a steady increase of CO_2 (green dots), CH_4 (orange dots), and N_2O (red dots) up to levels of ∼360 ppm for CO_2, ∼1700 ppb for CH_4 and ∼315 ppb for N_2O after MacFarling-Meure et al. (2006) (taken from IPCC Fifth Assessment Report (AR5), Ciais et al. (2013), and references therein).

The solid blue lines are direct atmospheric measurements from the Cape Grim observatory (Francey et al. 1999), extrapolating the ice core and firn air measurements up to the year 2013 to a CO_2 level of ∼390 ppm, a CH_4 level of ∼1760 ppb and N_2O up to ∼325 ppb. This graph shows a significantly stronger GHG change and increase to higher levels within a short time-period than all fluctuations in the last 420,000 years as mentioned above.

In the year 2013, we peaked at a CO_2 amount of ∼400 ppm, measured at Mauna Loa (Tans and Keeling 2013). This represents a value never reached since the existence of mankind. This value is nearly 1.5 times higher than before the beginning of the industrial revolution (Joos and Spahni 2008), the latter representing a warm period inter-glacial CO_2 value.

1.1.2 Temperature evolution

The concentrations of all GHGs in the free-atmosphere play a crucial role for Earth's climate. These gases increase the global temperature by absorbing long-wave back radiation in the atmosphere, transmitted from the Earth, which is in a thermodynamic equilibrium due to absorbed short-wave sun radiation, termed the *Natural Greenhouse Effect*. Without this effect the Earth would be at a thermodynamic state of about −19° C. Instead, the global mean near-surface temperature is at ∼ 14° C for a stable pre-industrial GHG concentration level (Solomon et al. 2007a). An additional forcing due to higher GHG concentrations results in an increase of the global mean near-surface temperature (Barnett et al. 2000; Brohan et al. 2006).

The era we live in today is named *Anthropocene*, reflecting the influence of mankind, since the additional forcing to climate change is man-made. The correlation of global GHG increase with global surface temperature increase was already shown by Arrhenius (1896). The evolution of the temperature on Earth can be reconstructed with proxy data from ice cores for a very long time span, as well as from tree-ring data (Mann et al. 2008) and lake or ocean sediment investigation (Moberg et al. 2005). For investigations of

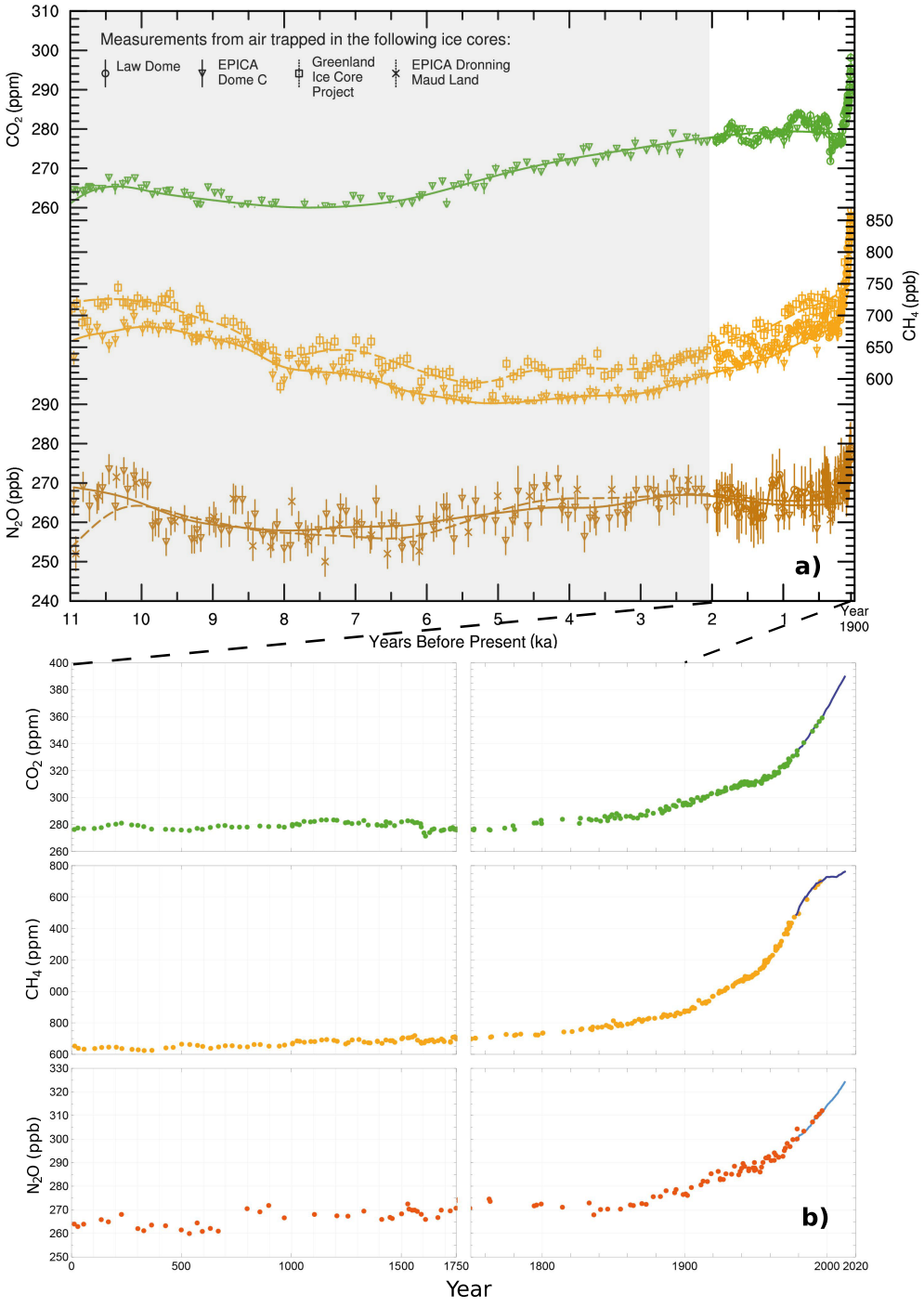

Figure 1.1: a) shows the concentrations of CO_2, CH_4, and N_2O from the year 11,000 ka before present until 1900; b) shows the GHG time series for the period from 0 AD to 2020 AD; (Figures are taken from Ciais et al. (2013) and modified).

temperature trends since the industrial revolution, measured data from ground stations all over the world are taken, cleared and homogenized and example results are published by Morice et al. (2012).

In the AR5 report (Masson-Delmotte et al. 2013) a compiled version of several proxy temperature data sets from tree-rings, ice cores and sediments is derived for the last 2000 years. This is shown in Fig. 1.2 (a) for the Northern Hemisphere (NH), (b) for the Southern Hemisphere (SH) and (c) for the entire Globe. These compiled data (red: land-only all latitudes; orange: land-only extra tropical latitudes, light blue: land and sea extra-tropical latitudes; dark blue: land an sea all latitudes) include besides the proxy data measured temperature data, shown by black lines for the last ∼150 years (for data set details see Sec. 5.3.5 in Masson-Delmotte et al. (2013) and Appendix 5.A.1 therein). The time series shows a clear increase of the temperature anomaly within the last two centuries with a positive trend relative to the mean reference temperature (horizontal dotted black line) derived from the years 1881 to 1980. This is significantly different from the temperature evolution before the start of the industrial revolution. The time series also includes a warm period in the medieval (PAGES 2k Consortium 2013) and colder period during the Maunder Minimum in the 17^{th} century (Lockwood et al. 2010), with a weaker change in temperature within a century.

1.1.3 Greenhouse gases and temperature change

A comparison study to understand the magnitude of temperature anomaly impact due to increasing human impact (GHG and aerosols) is shown in Fig. 1.3. Here, a time series of global and annual-averaged surface temperature anomalies calculated from Atmosphere-Ocean Global Circulation Model (AOGCM) simulations is compared with measured temperature anomaly data and a comparison of spatial patterns of local surface temperature trends published in Bindoff et al. (2013) is shown.

The left panel of Fig. 1.3 shows a set of simulation runs, performed with in the Coupled Model Intercomparison Project (CMIP-3) and Coupled Model Intercomparison Project (CMIP-5) model (Hegerl et al. 2007; Forster et al. 2013; Jones, Stott and Christidis 2013), include anthropogenic GHG and aerosols, resulting in an increasing temperature anomaly (left top panel, blue and red lines are mean of multi-model runs of CMIP-3 and CMIP-5, respectively). The second set of simulation runs include only natural forcing (left bottom panel, multi-model mean blue and red line). Therein, the solid black line shows the measured data-set from Hadley Centre/Climatic Research Unit gridded surface temperature data set 4 (HadCRUT4) (Morice et al. 2012), which overlap very well with the simulated data including anthropogenic influence.

In the plots one can clearly see the influence due to natural impact of volcanic eruptions, releasing a sudden high amount of aerosols. Such events induce a decrease of the temperature anomaly due to blocking of incident short-wave solar radiation by the aerosols as the Pinatubo example event in the year 1991 (Ammann et al. 2003). But the

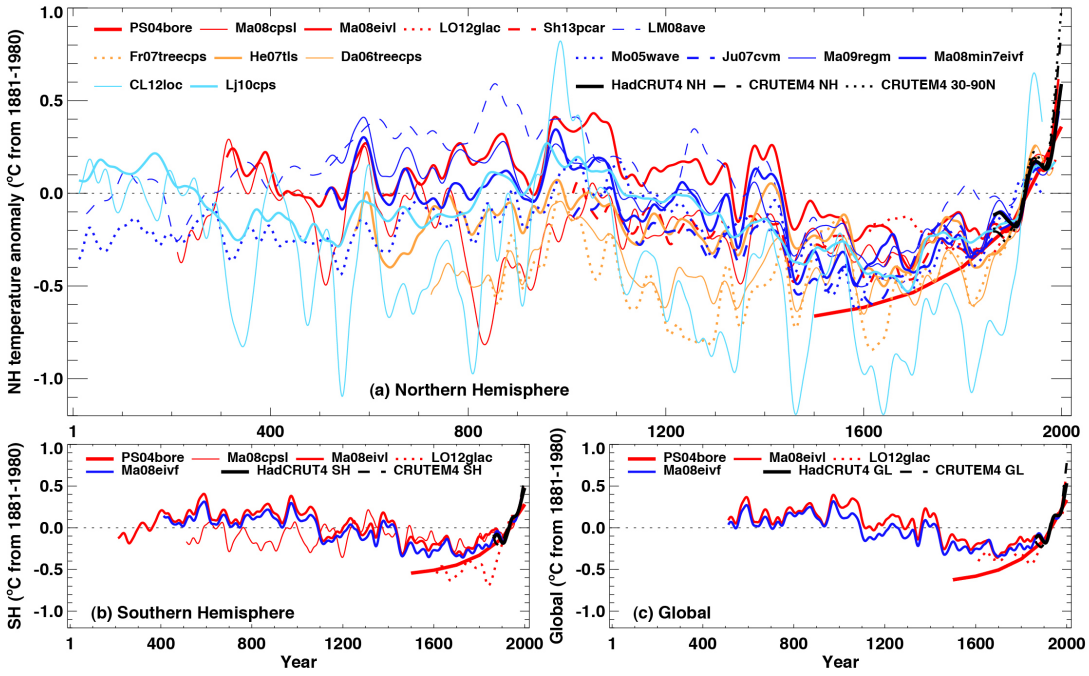

Figure 1.2: Compilation of individual reconstructions and measured data of temperature anomalies for the last 2000 years with the reference temperature from 1881 – 1980 (red: land-only all latitudes; orange: land-only extra tropical latitudes, light blue: land and sea extra-tropical latitudes; dark blue: land an sea all latitudes); a) shows the NH, b) the SH and c) the global temperature anomaly. Further details see Appendix 5.A.1 from Masson-Delmotte et al. (2013). Figure taken from Masson-Delmotte et al. (2013).

released GHGs can later contribute to a positive feedback in the radiative forcing since they stay longer in the free-atmosphere than aerosols. The latter are washed out at the lower troposphere after weeks or settle out from the stratosphere after months of global re-distribution due to the Brewer-Dobson circulation.

The right panel of Fig. 1.3 shows the spatial pattern of the temperature trends from 1951 to 2010. The top right panel shows CMIP-5 simulations with natural forcing only. The middle panel shows the observed trends between 1951 and 2010 from the HadCRUT4 data set and the bottom right panel shows the CMIP-5 simulations with natural and human forcing. These results show that the simulations including the human forcing are similar to the observational results, while the natural forcing only is not capable to represent the observed pattern.

1.1.4 Why measurement development?

The vast majority of climate scientists is convinced of the anthropogenic climate change, though it is still important to improve climate benchmark data sets to determine the impact of man-made climate change in a more precise way, to understand the physical processes in more detail and to provide better projections for possible future scenarios.

A very important information source to improve the General Circulation Models (GCMs) (the fist model was invented by Manabe and Wetherald (1967)) and climate change results are vertical measured profiles of the thermodynamic state variables, aerosol/particle content and GHGs. This era started with the invention of radiosonde data in 1930, remote sensing instruments from ground stations or airplanes or in-situ measurements from airplanes and finally satellite measurements starting form the 1970ties onward. The latter provide global coverage of the needed information.

Vertical profiling is very important since climate change for example respond differently in the stratosphere and in the troposphere, as published for example by latest results by Santer et al. (2013) and shown in Fig. 1.4. In this plot one can see the time series of monthly means near-global temperature anomalies from CMIP-5 simulations. Simulations including anthropogenic forcing (orange/red) show a decrease of the temperature anomaly for the lower stratosphere (top panel) and an increase for the mid- to upper troposphere (middle panel) and the lower troposphere (bottom panel). The anomalies stay rather stable for all altitude regions including natural forcing only (cyan/blue). Significant peaks appear after volcanic eruption events. Such model simulations profit from comparisons and evaluations with observed data.

Therefore, vertical profile measurements of the thermodynamic and chemical state are necessary to quantify and qualify physical processes.

Nowadays, there are initiatives providing Essential Climate Variable (ECV) for the Global Climate Observing System (GCOS) in an elaborate way aiming to and satisfy the World Meteorological Organization (WMO) conditions for long-term climate change observables. The object of GCOS (Karl et al. 1996) is to provide surface, upper-air,

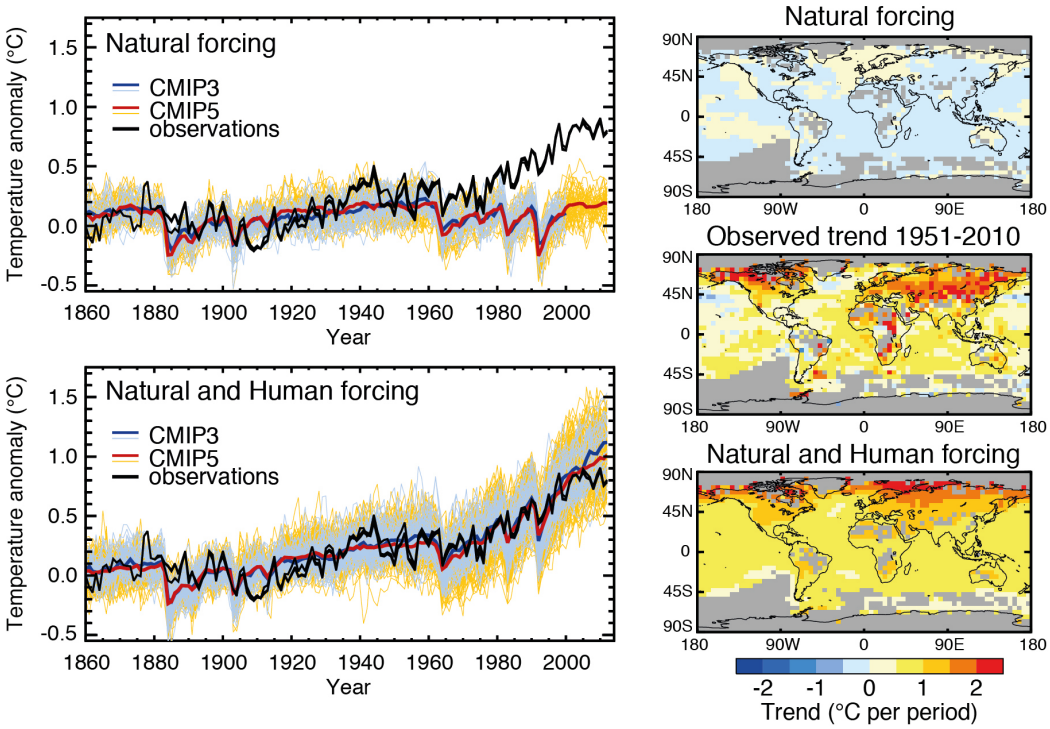

Figure 1.3: Left panel: comparison of simulated time series of global and annual-averaged surface temperature anomalies driven by anthropogenic GHG and aerosols (top panel blue (CMIP-3) and red (CMIP-5) line) and by natural forcing (bottom panel blue and red line, respectively). The black line shows the measured global mean temperature anomaly based on the HadCRUT4 data-set. Right panel: spatial patterns of local surface temperature trends from 1951 to 2010; top panel: CMIP-5 simulations with natural forcing; middle panel: observations from HadCRUT4 and bottom panel: CMIP-5 simulations including natural and human forcing; Figure taken from Bindoff et al. (2013).

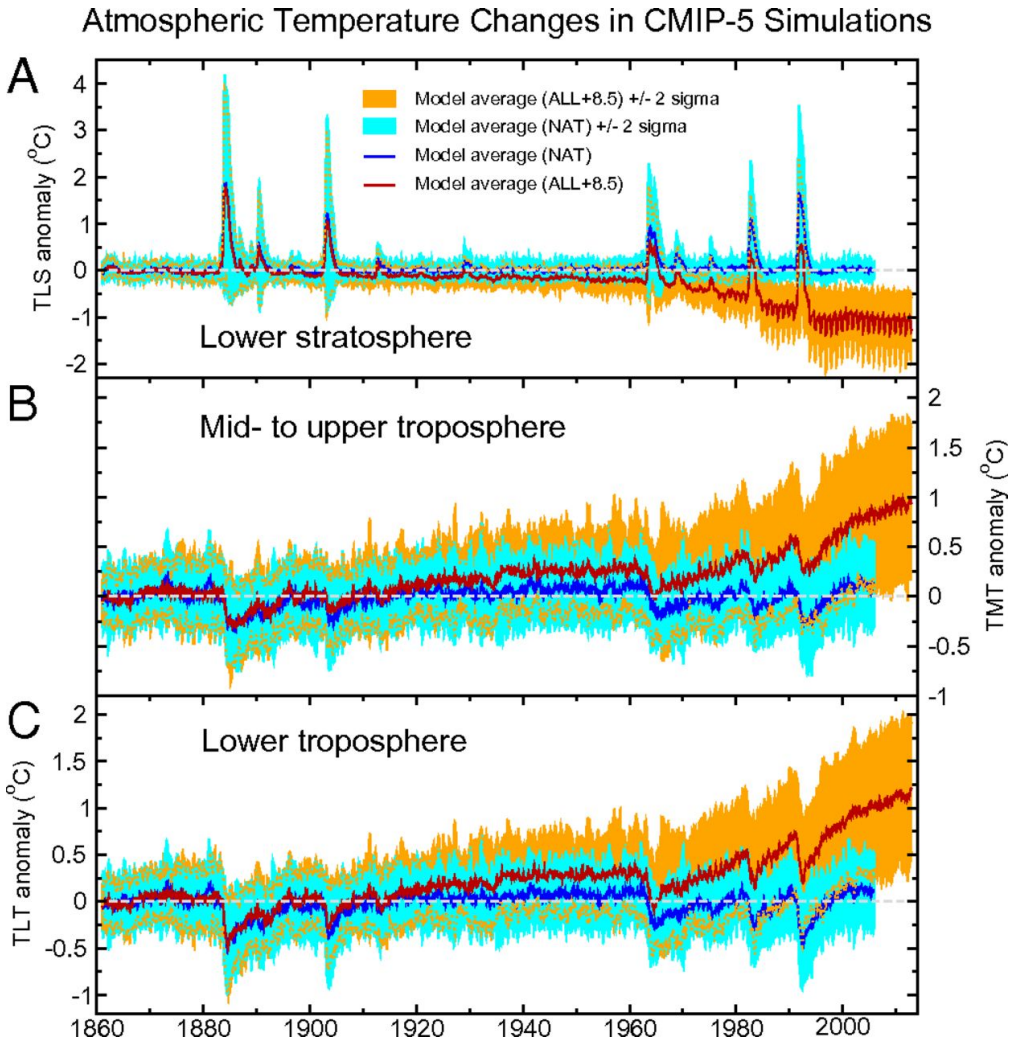

Figure 1.4: Time series of temperature anomalies in the lower stratosphere (A), mid- to upper troposphere (B), and lower troposphere (C) from 1860–2010. Figure taken from Santer et al. (2013).

marine, aircraft-based, satellite-based and other observation platform data for climate change investigations/observations. It embeds for example the Total Carbon Column Observing Network (TCCON) including in-situ and remote sensing products of ECVs as temperature and humidity measurements. GCOS Reference Upper-Air Network (GRUAN), a sub-project of GCOS provides upper-air long-term high-quality climate records from radiosondes. It will serve as international reference/validation/calibration database (Immler et al. 2010) and will help to better understand processes in the free-atmosphere. The European Earth Observation Programme—Copernicus (Aschbacher and Milagro-Pérez 2012), with a sub-project Monitoring Atmospheric Composition and Climate - Interim Implementation (MACC-II 2014), delivers data for monitoring emission-related ECVs, GHGs, aerosols, on global basis as European supporting part to the GCOS based on modeling and observation data. And the Global Carbon Project plans to monitor the live cycle of carbon. It keeps track of annual carbon budgets from past over present to future development to build a complete picture of the carbon cycle (Le Quéré et al. 2013).

Remote sensing of GHGs from satellites for sources and sinks of GHGs and the distribution in the free-atmosphere over the globe becomes thus more and more important.

There exist limb sounding spectrometers. Examples are the Michelson Interferometer for Passive Atmospheric Sounding (MIPAS) and Scanning Imaging Absorption Spectrometer for Atmospheric Cartography (SCIAMACHY)-limb on Environmental Satellite (ENVISAT 2014) and Atmospheric Chemistry Experiment (ACE)-Fourier Transform Spectrometer (FTS) on Scientific Satellite–1 (SciSat-1 2014). They operate in the ultraviolet (UV) to short wave infrared (SWIR) range using passive limb sounding radiometry or the occultation technique from sun, stars and the moon.

Further more there are passive/active nadir sounders. Example instruments are SCIAMACHY-nadir on Environmental Satellite (ENVISAT), Atmospheric Infrared Sounder (AIRS) on NASA Science Satellite-Earth Observation System (AQUA 2014), Infrared Atmospheric Sounding Interferometer (IASI) on Meteorological Operational (MetOp 2014), Orbiting Carbon Observatory–2 (OCO-2 2014), Thermal And Near infrared Sensor for carbon Observation (TANSO) -FTS on Greenhouse Gases Observing Satellite (GOSAT 2014), and Carbon Monitoring Satellite (Carbonsat 2014). They scan the atmosphere of GHGs from top for (coarser-resolution) vertical profiling, boundary layer information, or sources and sinks determination.

Limb sounder provide higher vertical resolution of <1 km to 3 km with weak horizontal resolution $\sim$100 km to 300 km. So far they are limited to the free-atmosphere and cover the globe non-homogeneously or can not provide high repetition rates.

Nadir sounder provide weaker vertical resolution or mostly column content information but very high horizontal resolution. They may be even capable of detecting sources and sinks with a resolution of $2\times2\,\mathrm{km}^2$ as proposed for Carbon Monitoring Satellite (CarbonSat).

The missing gap of an active limb sounding system brings us to the proposed LEO–

LEO microwave and infrared-laser occultation (LMIO) mission concept introduced by Kirchengast and Schweitzer (2011), which presents a synergistic combination of the LEO–LEO microwave occultation (LMO) technique, which provides thermodynamic state variables, and the LEO–LEO infrared-laser occultation (LIO) technique, measuring the most important GHGs and line-of-sight wind velocity ($v_{\mathrm{l.o.s.}}$). All ECVs are provided in a long-term stable, self-calibrating, global coverage manner and with climate benchmark quality.

1.2 Concept of the LMIO mission and ACCURATE

The mission concept ACCURATE—Climate Benchmark Profiling of Greenhouse Gases and Thermodynamic Variables and Wind from Space combines two limb sounding measurement techniques to derive thermodynamic and chemical states of the free atmosphere, covering the upper troposphere–lower stratosphere (UTLS) between ∼5 km and ∼35 km.

The principle to measure the thermodynamic state variables, namely temperature (T), pressure (p) and specific humidity (q), is based on the LEO–LEO microwave occultation (LMO) technique.

To derive the chemical state of the free atmosphere, we profit from the absorption by molecules of quasi-monochromatic Infrared Laser (IRL) signals in the 2 μm to 2.5 μm range. In case of ACCURATE the following greenhouse gases (GHGs) are measured: water vapor (H_2O), carbon dioxide (CO_2) (carbon dioxide ($^{12}CO_2$), carbon dioxide first main isotope ($^{13}CO_2$), carbon dioxide second main isotope ($C^{18}OO$)), methane (CH_4), nitrous oxide (N_2O), ozone (O_3), semiheavy water (HDO), heavy-oxygen water ($H_2^{18}O$) and carbon monoxide (CO)) covering the LEO–LEO infrared-laser occultation (LIO). Additionally, line-of-sight wind velocity ($v_{\text{l.o.s.}}$) can be derived from wind induced Doppler-shift influencing the IRL absorption line frequencies.

These two measurement principles, LMO and LIO, are joined on aq pair of satellite platforms, a transmitter (Tx) and a receiver (Rx), performing an active limb-sounding of the atmosphere, to a single technique named LEO–LEO microwave and infrared-laser occultation (LMIO). The synergistic combination enables to derive a vector of thermodynamic and chemical state variables {T, p, q, $v_{\text{l.o.s.}}$; H_2O, CO_2, $C^{18}OO$, CH_4, N_2O, O_3, CO, HDO, $H_2^{18}O$} for the same profile location in the free atmosphere. The mission concept was introduced by Kirchengast and Schweitzer (2011), thoroughly described by Schweitzer (2010), and in the Earth Explorer 8 (EE-8) ACCURATE mission proposal to ESA by 2010 by Kirchengast et al. (2010a). The idea was born out of the occultation principle published by Phinney and Anderson (1968) and Kirchengast (2004).

A schematic overview of the LMIO concept is shown in Fig. 1.5. Here, one can see the two counter-clockwise rotating satellites, transmitting from a Tx MW signals and IRL signals simultaneously through the atmosphere to a Rx. While transmitting, the MW and IRL signals undergo a bending due to refraction in the atmosphere, which differs slightly between these two frequency ranges when passing the humid atmosphere (see later on refractivity (N) for MW and IRL signals in Sect. 1.2.1 and Sect. 1.2.2, respectively). These signals undergo various atmospheric effects besides refraction, like molecular absorption and defocusing for both signal ranges and Rayleigh scattering, turbulence, cloud extinction; $v_{\text{l.o.s.}}$-induced Doppler frequency shift is relevant for the IRL signals only.

The key advantage of the LMIO occultation technique, besides providing such a complete state vector of thermodynamic and chemical properties of the atmosphere, is

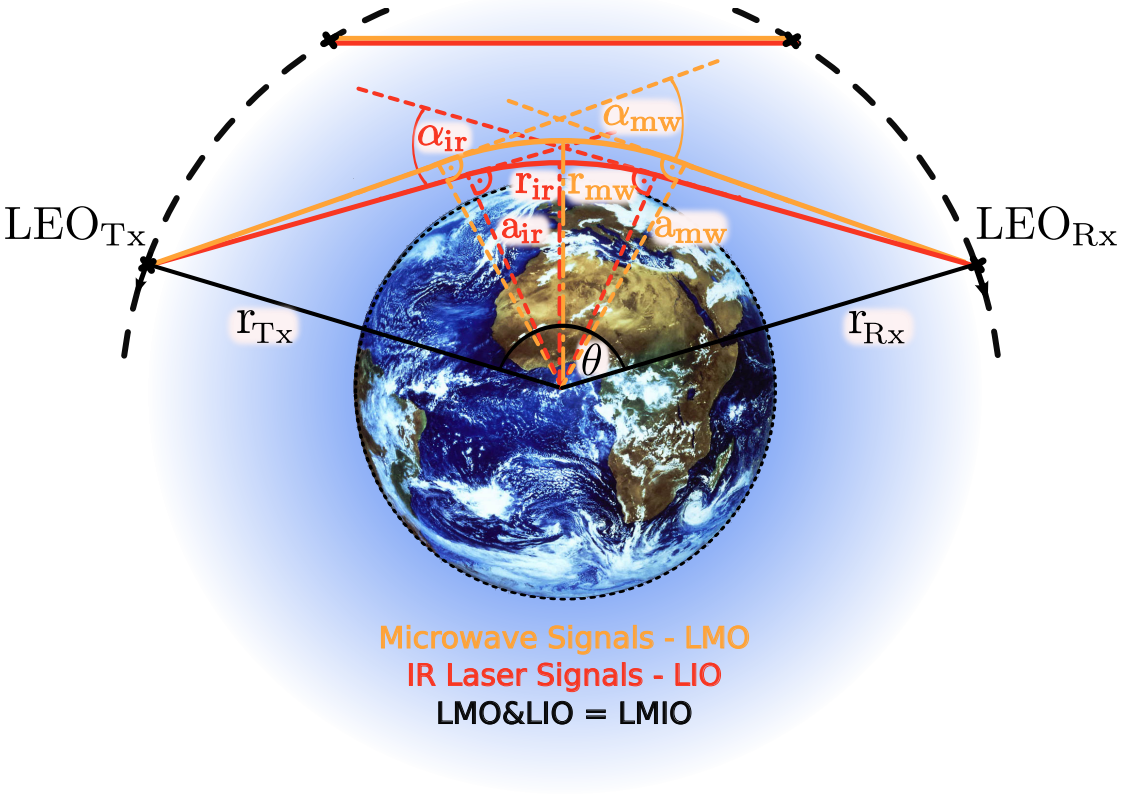

Figure 1.5: Schematic view of the LMIO measurement geometry, as a combination of LMO signals (MW, orange signal paths) and LIO signals (IR, red signal paths) which pass the vacuum as straight lines and are refracted by the atmosphere. The rays undergo different bending resulting in different α_{mw} and α_{ir}, a_{mw} and a_{ir}, and r_{mw} and r_{ir}, respectively. Detailed explanation is given in Chapt. 2 in Sect. 3.2.1 (Proschek, Kirchengast and Schweitzer 2011).

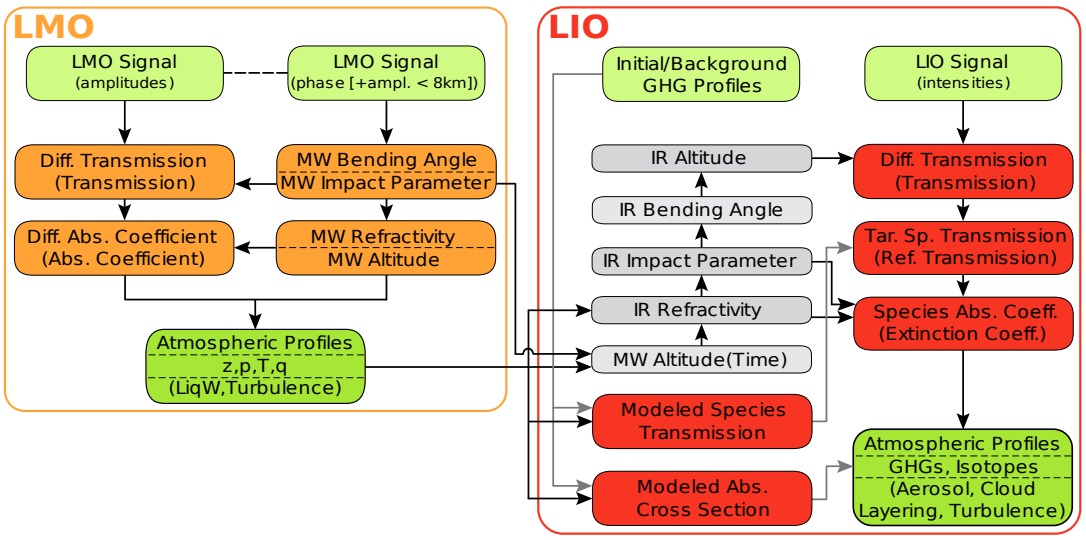

Figure 1.6: Schematic overview of the LMIO retrieval processing system, with its LMO (left, framed in orange) and LIO (right, framed in red) retrieval parts (Proschek, Kirchengast and Schweitzer 2011).

the global coverage, the high vertical resolution of ∼1 km, the long-term capability and the independent self-calibrating character, providing an ideal climate benchmark data set.

Figure 1.6 is pointing out the synergy of LMO and LIO in the retrieval algorithm. There we can see the MW part in the orange box as a precedent self-contained retrieval (more details see Schweitzer et al. (2011) and Subsection 1.2.1), providing the atmospheric parameters as p, T and q as function of altitude (z). Additional output is the MW impact parameter (a_{mw}) (geometric definition see Fig. 1.5). This parameter is provided on the sampling time grid, which will be the connecting variable to the IRL intensity (LIO retrieval shown in the red box). The latter is provided as well on the same sampling time grid. From the a_{mw}, the calculation of the IR altitude (z_{ir}) is possible with the relation over the time grid and the retrieved thermodynamic state variables. The LIO retrieval part is thus dependent on the LMO output parameter, which performs the retrieval for the GHGs, the line-of-sight wind velocity ($v_{\mathrm{l.o.s.}}$) and cloud layering product. These steps will be explained in detail later on in Subsection 1.2.2.

In the following two sections the LMO and the LIO retrieval concept are presented in an overview. The focus lies in the LIO section which mainly drives this thesis.

1.2.1 LEO–LEO microwave occultation

The LEO–LEO microwave occultation (LMO) mission concept is a heritage system based on the already very successful GNSS–LEO radio occultation (GRO) technique (Ware et al. 1996; Kursinski et al. 1997, e.g.). A Global Positioning System (GPS) signal in decimeter wavelength passes the Earth's atmosphere, undergoes bending and a phase-shift. The changed signal is recorded by an antenna on a Low Earth Orbit (LEO) satellite. From the so called *excess phase* one can derive the bending angle (α) of the transmitted signal, thus from it the N and finally the dry pressure (p_d) and dry temperature (T_d).

A couple of successful satellite missions have already shown the great advantage of the radio occultation (RO) method and are already integral part for Numerical Weather Prediction (NWP) models (Buontempo, Jupp and Rennie 2008). Some operational or planed satellite missions are e.g., Challenging Mini-Satellite Payload (CHAMP) (Wickert et al. 2001, 2004), Gravity Recovery and Climate Experiment (GRACE) (Beyerle et al. 2005), Constellation Observing System for Meteorology, Ionosphere, and Climate (COSMIC) (Anthes et al. 2008), Global Navigation Satellite Systems Receiver for Atmospheric Sounding (GRAS) on MetOp (Luntama et al. 2008) and Community Initiative for Continuing Earth Radio Occultation (CICERO) (McCormick et al. 2007). RO data sets are often used for comparison studies with other satellite or radiosonde data for calibration purposes due to their high vertical resolution capability and global coverage. Providing data for climate change investigations are not yet reliably significant, since the operational time period is too short to provide statistically trustworthy trend data.

The next step of occultation mission development leads us to the advantage of the LMO technique, which is transmitting signals at centimeter- and millimeter wavelengths. The signals are capable to let derive absorption of H_2O independently from external information. In comparison, RO can only lead to T_d and p_d without any external additional information. The technique is based on the amplitude of the H_2O absorption signal, which is tuned to H_2O peaks as close as possible, so that the amount of absorption allows an adequate signal-to-noise ratio (SNR). Thus the additional variable can independently decouple the T and q correlation to derive T, p and q (see retrieval algorithm details in Schweitzer et al. (2011) and scheme in Fig. 1.6, orange box). A channel close to an O_3 absorption peak enables the measurement of O_3 as a further additional variable (Herman et al. 2004).

The LMO technique was initially proposed by Lusignan et al. (1969), followed by an advanced proposal decades later by Yunck et al. (2000) and then further developed from Kursinski et al. (U.S.–NASA side; 2002, 2004); Herman et al. (as well NASA side; 2004); Kirchengast and Hoeg (from European–ESA side 2004). So far no LMO mission has ever flown, although on-going mission preparations for a first demonstration airplane-to-airplane experiment termed Active Temperature, Ozone, and Moisture Microwave Spectrometer (ATOMMS) led by Kursinski et al. (2009) were done recently.

The retrieval algorithm for the LMO method, as proposed by Kirchengast and Hoeg

(2004), is published in Schweitzer et al. (2011) and the algorithm flow is shown in the orange box of Fig. 1.6. A basic set of five frequency settings is used, with the frequencies being sensitive to T, p and H_2O (optional O_3) for different altitude ranges. The three K-band frequencies (17.25 GHz, 20.20 GHz and 22.60 GHz) are sensitive to H_2O from ∼5 km to 12 km and the two M-band frequencies (179.00 GHz and 181.95 km) are sensitive to H_2O at higher altitudes from ∼10 km to 18 km. Above about 18 km the atmosphere becomes rather dry (see Ph.D. thesis from Schweitzer 2010). Optional further M-band channels at 191.85 GHz and 195.35 GHz enable the O_3 measurement.

The basis of the retrieval is the calculation of the MW bending angle (α_{mw}) on an MW impact parameter (a_{mw}) grid from the excess phase (right parameter flow of Fig. 1.6 orange box), including filtering processes and statistical optimization (see Gobiet and Kirchengast (2004); Steiner et al. (2009)), to obtain an adequate profile. The MW refractivity (N_{mw}) is thus calculated from the α profile, by using tan Abel transform as following (in general from):

$$n(r) = \exp\left(\frac{1}{\pi}\int_{a_0}^{\infty}\frac{\alpha}{\sqrt{a^2-a_0^2}}\mathrm{d}a\right) = 1 + 10^{-6}\cdot N(r), \tag{1.1}$$

with refractive index (n) as function of tangent radius (r) and a_0 as impact parameter to the according r. For geometrical illustration see Fig. 1.5. This transformation is characteristic for deriving a scalar value from an integral value (Kursinski et al. 1997). Its principle applying it to occultations was invented by Pannekoek (1903) for stellar occultation and initially applied to satellite occcultaion measurements by Fjeldbo and Eshleman (1965) to study Venus's atmosphere.

The sensitivity to H_2O is determined with the absorption of the amplitude for different frequencies (left parameter flow of Fig. 1.6 orange box). Thus, absorption coefficients can be as well calculated from the known Abel transform, applying the principle after Fjeldbo and Eshleman (1965). The formula adapted for this purpose was published by Kursinski et al. (2002), for which a differential transmission (subtraction of an *Off-signal* from an H_2O sensitive *On-signal*) is used as the integral value and results in a differential absorption coefficient.

One core formula within the entire LMO retrieval is the Smith-Weintraub equation (Smith and Weintraub 1953), setting the empirical relation between N and the atmospheric parameters as T, p and q as function of altitude (z) and is written as follows:

$$N(z) = 77.60\frac{p(z)}{T(z)} + 3.73\cdot 10^5\frac{e(z)}{T(z)^2}. \tag{1.2}$$

The Smith-Weintraub equation with the differential absorption coefficient profile and the thermodynamic state equations, as the hydrostatic relation of pressure change with altitude and the relation of q with T and p (Schweitzer et al. 2011; Salby 1996),

respectively, build the basis for solving the equation system as described in detail in Schweitzer et al. (2011).

The study concerning the performance analysis of the LMO retrieval from Schweitzer et al. (2011) shows unbiased hydrostatic state results (p, T, q), except for tropical cases with very humid conditions with optimization potential in the weighting functions within the retrieval. The LMO root mean square (r.m.s.) error is improved compared to the accuracy of GNSS–LEO radio occultation (GRO) systems. The pressure is retrieved with an accuracy of $<0.2\,\%$, the temperature $<0.5\,\mathrm{K}$ and the specific humidity $<10\,\%$ on an individual-profile basis (Schweitzer et al. 2011). The latter parameter shows the biggest improvement to GRO missions, since they need background information to derive q profiles, compared to the independently retrievable T_d and p_d profiles.

Since the output of the LMO retrieval are the thermodynamic parameters with such high retrieval accuracy, and providing such high vertical resolution for the altitude level for 5 km to 35 km as target, we can benefit for the next retrieval (LIO) step to continue the process of independent measurements based on the occultation technique.

1.2.2 LEO–LEO infrared-laser occultation

This section is based on the previous, as the LEO–LEO microwave occultation (LMO) retrieval output is the input for the LEO–LEO infrared-laser occultation (LIO) retrieval, guaranteeing the self-calibrating and independent characteristics of the mission concept. Since this thesis, comprising papers Schweitzer, Kirchengast and Proschek (2011); Proschek, Kirchengast and Schweitzer (2011); Proschek et al. (2014a), is mainly driven by the Infrared Laser (IRL) occultation part, the explanations will be given in more detail compared to the microwave (MW) section.

The LIO is the novelty in the LEO–LEO microwave and infrared-laser occultation (LMIO) mission concept. It shows the occultation measurement concept of IRL signals in the $2\,\mu$m to $2.5\,\mu$m range, which lie in an atmospheric window of the Earth and the Sun radiation (see Schweitzer (2010); Salby (1996)). A first experiment proofing the differential transmission principle (subtracting an *Off-signal* from a greenhouse gas (GHG) sensitive *On-signal*), showing in the potential of IRL occultation measurements was done on the Canary Islands between La Palma and Tenerife in July 2011 (Brooke et al. 2012), realizing a 144 km IRL ground link. Detailed analysis results of this experiment are shown in Proschek et al. (2014b).

In the following subsections we discuss the influences of atmospheric effects on the IRL signal, the LIO retrieval under *clear-air* conditions, and the LIO retrieval under *cloudy-air* conditions. The detailed definitions of the two latter conditions will be given in the respective subsections.

Atmospheric Influences on the infrared-laser signals

During the feasibility study of the LEO–LEO microwave and infrared-laser occultation (LMIO) mission, an investigation of atmospheric influences on the IRL signal needed to be done. The resulting work was published by Schweitzer, Kirchengast and Proschek (2011) and is presented in Chap. 2. The IRL signals show multiple dependencies besides refraction of the ray paths, e.g., GHG absorption, aerosol extinction, Rayleigh scattering, defocusing loss and spreading, turbulence and cloud extinction. The Schweitzer, Kirchengast and Proschek (2011) study was performed based on Forward Modeling (FOM) with the software tools End-to-End Generic Occultation Performance Simulation and Processing System (EGOPS) and eXtended End-to-End Generic Occultation Performance Simulation and Processing System (xEGOPS), which were developed at the Wegener Center, University of Graz (Fritzer, Kirchengast and Pock 2009b; Fritzer et al. 2010b). The tools and the used settings for the end-to-end simulations will be explained in Chap. 1.3.

The atmospheric influences and their impact magnitude on the transmitted IRL signal are explained briefly in the following paragraphs.

The refractivity in the IR region plays an essential role in the LIO measurement concept and induces the bending of the ray paths. In xEGOPS/EGOPS, atmospheric condition and refractivity relation is based on a formula developed by Bönsch and Potulski (Bönsch and Potulski 1998) and reads as follows:

$$N = \left(c_1 + \frac{c_2}{d_1 - \frac{1}{\lambda^2}} + \frac{c_3}{d_2 - \frac{1}{\lambda^2}} \right) \cdot \frac{p}{T} - \epsilon \cdot e, \tag{1.3}$$

with constants $c_1 = 23.7104\,\mathrm{K\,hPa^{-1}}$, $c_2 = 6839.34\,\mathrm{K\,hPa^{-1}}$, $c_3 = 45.473\,\mathrm{K\,hPa^{-1}}$, $d_1 = 130.0$, $d_2 = 38.9$ and $\epsilon = 0.038\,\mathrm{hPa^{-1}}$, λ as the wavelength of a channel in μm, p the pressure in hPa, T the temperature in K and e the water vapour partial pressure in hPa. It describes an improved formula based on Edlén (1966), describing the wavelength, temperature and pressure dependency of the IR refractivity. The term containing the water vapour is very small. Comparing the MW refractivity (see Eq. 1.2) with the IR refractivity, the IR refractivity shows significant difference only at lower altitudes where water vapour is increasing and contributes to stronger bending of the MW ray path (up to relative refractive difference of 6 % at 5 km for tropics; see Fig. 2 in Schweitzer, Kirchengast and Proschek (2011)).

Since IRL signals are very sensitive to molecular absorption our laser system is using near monochromatic 1.5 ms-pulsed laser signals of emitted full-width at half maximum (FWHM) of $< 3 \cdot 10^{-8}$ (Kirchengast et al. 2010a; Schweitzer 2010). A careful selection of 13 channel pairs for a set of GHGs ({H_2O, $^{12}CO_2$, CH_4, N_2O, O_3, CO, and $^{13}CO_2$, $C^{18}OO$, HDO, $H_2^{18}O$} was done; see center frequency details in Tab.1 in Schweitzer, Kirchengast and Proschek (2011)). The selected channels show absorption for a target

GHG, a so called *On-Signal*, and hardly any GHG absorption for the *Off-Signal*, needed for broadband effects correction in the retrieval. To forward simulate the integrative absorption along the ray path for each IRL signal, we used the High-Resolution Transmission (HITRAN) (for this study High-Resolution Transmission (HITRAN)2008) database (a spectroscopic data base for several atmospheric constituents developed by Rothman et al. 2005, 2009) and the Reference Forward Model (RFM) developed by Dudhia (2008), integrated into the eXtended End-to-End Generic Occultation Performance Simulation and Processing System (xEGOPS). This integrated tool enables the simulation of the absorption coefficient along the ray path for a given thermodynamic and GHG state of atmosphere (for this study Fast Atmospheric Signature Code (FASCODE) thermodynamic and GHG atmosphere; Anderson et al. (1986)).

The target species absorption loss boundaries for absorption lines (On-signals) lie between 0.25 dB and 13 dB. Outside these limits the detector will not accurately resolve the signal as target species absorption signal anymore, since the signal-to-noise ratio (SNR) will be to weak. This implies that four H_2O channels needed to be used, sensitive to different altitude ranges. All other GHG On-signals, except for $H_2^{18}O$ exceeding the SNR boundary near 6 km, stay within these defined boundaries between about 5 km to 40 km.

The Off-signals, which should undergo very weak GHG absorption, show contributions of less then 0.25 dB down to a level of about 6 km to 7 km. But HDO and $H_2^{18}O$ Off-signals significantly exceed the 0.25 dB level up to 3 dB and 8 dB, near the target altitude of 5 km. The overall foreign GHG contributions for each channel pair, which means the differential foreign GHG contributions from an Off-signal and an On-signal, then stay below 0.25 dB down to the target altitudes of 5 km except for CO limited to ∼13 km, O_3 limited to ∼11 km and $H_2^{18}O$ limited to ∼9 km (for details see Schweitzer, Kirchengast and Proschek (2011)).

The aerosol extinction contribution along the ray path are simulated based on a semi-empirical model developed for the End-to-End Generic Occultation Performance Simulation and Processing System (EGOPS) (Schweitzer et al. 2008). This model includes three typical aerosol extinction coefficient climatologies (basic, medium and volcanic situations) based on the Stratospheric Aerosol and Gas Experiment II (SAGE II) measurements (Thomason and Peter 2006) at the wavelength of 1020 nm and is adapted with a wavelength dependency to the desired IRL signal extinction coefficients. The coefficients show no strong dispersity and result in a maximum differential aerosol extinction loss of 0.02 dB for volcanic load conditions (for details see Sect. 2.3.5 in Schweitzer, Kirchengast and Proschek (2011)).

The Rayleigh scattering coefficient is also integrated along the ray paths, with a dependency on the refractivity, thus the atmospheric parameters, and a wavelength dependency of the order of $1/\lambda^{-4}$. The differential Rayleigh scattering loss between the on- and off-signal does not exceed 0.001 dB and therefore shows very high correction potential due to the differential transmission principle. A detailed explanation on the

implementation of scattering in the xEGOPS system is given in Fritzer et al. (2010a) based on the definition by Salby (1996).

The defocusing and spreading effect of a beam with a certain laser beam divergence (in case of ACCURATE ∼3 mrad) results in an effective widened diameter of the beam at the tangent point (TP). The latter is the lowest point with respect to the Earth's surface of a single bended ray while passing the atmosphere. The effective diameter is produced due to refractive gradient differences within the atmosphere for the spreaded beam while passing different atmosphere layers. Strong refractivity gradient changes within the atmosphere can lead to defocusing and spreading loss of up to ∼5 dB for a single IRL signal. Since the effect is weakly dispersive, the differential transmission principle in the retrieval process will correct this effect completely (for details see Schweitzer et al. (2011); Schweitzer, Kirchengast and Proschek (2011)).

Turbulence plays a big role for IRL signals, since an atmosphere is never completely homogeneous and consists of small-scale atmospheric inhomogenities. So random diffraction of IRL propagating signals will show a certain fluctuation of the SNR at the receiver (Rx). Results from Sofieva (2009) and Horwath and Perlot (2008) showed that IRL signals with low frequency spacing, ideally $\Delta f/f$ <0.5 %, show a high correlation within the fluctuating intensity pattern at the Rx. This fact will later serve the differential transmission principle within the LIO retrieval to correct the effect to a worst case residual error of maximum 1.5 % near 10 km and 2.5 % near 5 km (for details see Schweitzer, Kirchengast and Proschek (2011) and retrieval results in Chap. 4 or Proschek et al. (2014a)).

Clouds show a non-homogeneous influence within the ray path for each atmosphere passing IRL signal. This is because clouds can be quasi-randomly distributed within the occultation ray path and the IRL signals can either be totally blocked or fairly perturbed sub-visible cirrus clouds. Clouds with liquid water content (LWC) show massive extinction effects and thus block the limb-sounding IRL signal (Emde and Proschek 2010), while ice water content (IWC) show a potential of weak extinction and can be corrected in the retrieval for intermittent penetrating IRL signals or extinctions below a <15 dB loss level (see later on Sect. 1.2.2, Chap. 4 or Proschek et al. (2014a)). Based on a study by Harrison and Bernath (2010), an estimation of the cloud influence on IRL signals and its penetration depths into the troposphere by investigation of solar occultation events from the Atmospheric Chemistry Experiment (ACE) came to the conclusion that about 40 % of the profiles reach down to 7.5 km and 20 % down to 5 km, while within a tropical band of ±15° only 20 % reach down to 7.5 km.

Influences due to wind induced Doppler-shift on the On- and Off-signal frequency play a significant role in the retrieval process and can produce biases in the retrieval results if not considered. An additionally developed wind retrieval part to the LIO core algorithm profits from the delta-differential transmission profiles between two selected $C^{18}OO$ wind channels, sitting on the inflection points of a quasi-super symmetric $C^{18}OO$ line, which is proportional to the $v_{\text{l.o.s.}}$ (Kirchengast and Schweitzer 2011). The wind retrieval uses also

an Abel transform. This retrieved wind information will serve as correction profile to reproduce the wind induced Doppler frequency shift on the IRL signals within the LIO retrieval. Detailed algorithm description for the $v_{\text{l.o.s.}}$ calculation is given in Syndergaard and Kirchengast (2013); Plach, Proschek and Kirchengast (2013), and detailed algorithm description on the LIO algorithm in xEGOPS and on its performance is given by Proschek, Plach and Kirchengast (2014); Plach, Proschek and Kirchengast (2014).

Scattered solar radiation and terrestrial thermal radiation are expected to be below the receiver noise level (Schweitzer, Kirchengast and Proschek 2011); residual scattered solar radiation is compensated by signal pulse design.

Figure 1.7 shows overall atmospheric influences for the entire set of thirteen on-channels and the according six off-channels of IRL signals under FASCODE standard (STD) atmosphere conditions with FASCODE GHGs and medium aerosol load (excluding scintillation and cloud effects; discussed later on in Sect. 1.2.2 and Proschek et al. (2014a)). The atmospheric influence limit is determined at 21 dB for a SNR margin of 13 dB to the absorption signal detection limit of the Rx. The vertical dotted and dashed lines symbolize the target and threshold, respectively.

In Figure 1.7 A the four H_2O profiles show a clear SNR altitude dependency, since two of the four channels exceed the detection limit above the threshold altitude of 7 km. Thus a combination of those four profile seems suitable and will be applied later on for the retrieval process. Figure 1.7 B with the $^{12}CO_2$ and the $^{13}CO_2$ profiles shows the possibility to a combined CO_2 due to a highly stable isotopic ratio $\delta^{13}C$ in the free atmosphere. HDO and $H_2^{18}O$ in Fig. 1.7 C show sensitivity only for low altitude levels of 5 km (threshold: 7 km) up to 12 km. O_3 in Fig. 1.7 D reflects a limited detection altitude range, since O_3 shows weak SNR below 15 km. CO shows hardly any absorption above 20 km and will thus not be well detectable above this altitude level. A list with detailed information about the observation requirements for all single target species are given in Tab. 3.2-1 and Tab. 3.2-2 in Kirchengast et al. (2010a).

Retrieval algorithm: The core algorithm

In the line of the feasibility study, we developed an algorithm to calculate GHG volume mixing ratio (VMR) profiles out of forward-simulated intensity profiles for the set of thirteen channels with their reference channels, covering ten target species (H_2O, $^{12}CO_2$, CH_4, N_2O, O_3, CO, $^{13}CO_2$, $C^{18}OO$, HDO and $H_2^{18}O$). The developments were first tested for *clear-air* conditions. The atmospheric background effects include Rayleigh scattering, medium aerosol extinction and defocusing loss in addition to the target-GHGs molecular absorption. This work is in detail explained in Chap. 3 and was published by Proschek, Kirchengast and Schweitzer (2011).

The core LIO algorithm, or so called Single-Line Trace Species Retrieval (SSR), is shown in Fig. 1.6 (red box). This algorithm flow shows the steps; every single On- and Off-channel intensity pair needs to undergo calculation of the target output volume

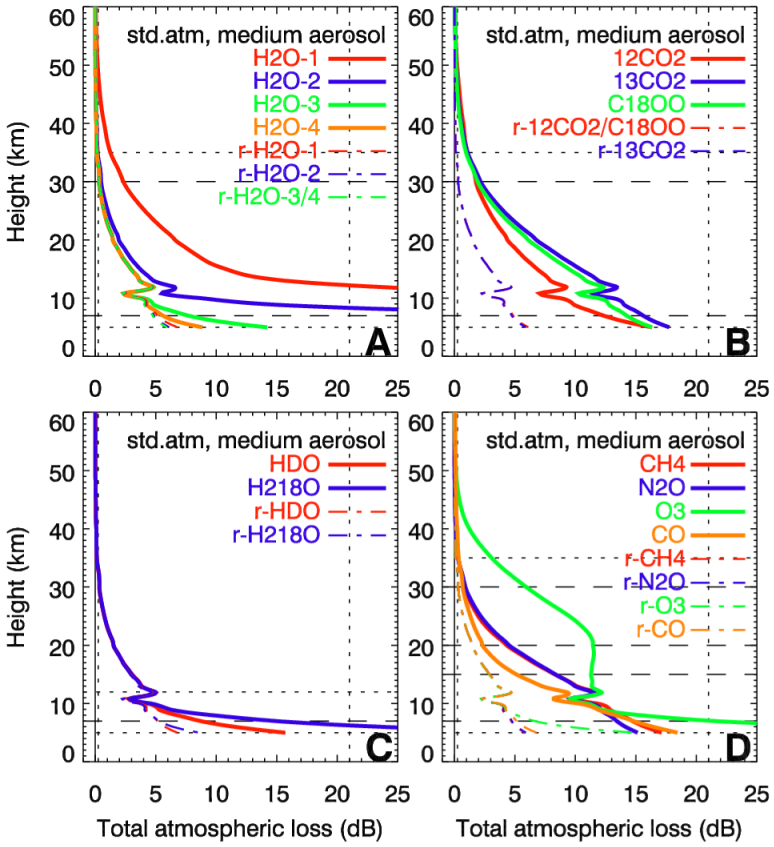

Figure 1.7: Total atmospheric loss for the thirteen absorption channels and the six reference channels, for the FASCODE STD atmosphere and medium aerosol load. The dotted and dashed lines determine the target and threshold scientific requirements. Figure taken from Schweitzer, Kirchengast and Proschek (2011)

mixing ratio (VMR). The orange box represents the LMO algorithm briefly described in Sect. 1.2.1. This atmospheric parameter, derived from the simultaneously measured MW amplitudes and phase delays, are needed for several steps within the LIO retrieval.

Additionally to this core algorithm, a dynamic structure of the LIO retrieval shown in Fig. 1.8 was co-developed, handling nested loops of a thoroughly defined consecutive SSR order of single target species (termed as inner loop or Multi-Line Trace Species Retrieval (MSR)), and the so called Basic-Update-Control Runs (BUC). The latter guarantee the convergence of the retrieval and will be explained later on.

In the red box of Fig. 1.6, the gray shaded boxes represent the preparatory calculation steps, which are the calculation steps of mainly geometric parameters such as the impact parameter, refractivity, bending angle and altitudes for each IRL signal. The arrows indicate the retrieval flow it self. Starting point is the MW altitude which can be derived from the MW impact parameter, existing on the measured sampling time grid and assigns the IR intensity profile with the according time stamps to the MW impact parameter. From there, the connection from MW to IR is set.

The calculation of the IR refractivity is performed after Eq. 1.3, with the thermodynamic parameters from the LMO retrieval on the MW altitude grid. On the same MW altitude grid, the IR impact parameter after Bouguer's rule (Born and Wolf 1964), based on the previously derived IR refractivity and the Earth's local radius of curviture (R_C), is calculated. At last the IR bending angle is derived from the Abel transform after Fjeldbo and Eshleman (1965) as well on the same MW altitude grid. Thus an iteration process as described in Sect. 3.3.5 in Chap. 3 or Proschek, Kirchengast and Schweitzer (2011) enables the calculation of the actual IR altitudes. The latter is thus set with the time grid in relation to the intensity value of the IRL signal.

The next steps are shown in the red boxes of the LIO retrieval process. Starting point is the IRL signal power profile of an On- and Off-channel pair on the measured sampling time grid. Figure 1.9 a shows an example signal power profile for an $^{12}CO_2$ On-signal (green solid) and its Off-signal (red dotted-dashed), or so-called reference signal, as function of sampling time. The IR altitude grid as function of sampling time is known from the preparatory step. The IR On- and Off-signal can thus be converted into transmissions on the IR altitude grid (see Fig. 1.9 b, green and red line, for the absorption and reference channel, respectively).

Applying the previously often mentioned *differential transmission principle*, which subtracts an Off-signal from an On-signal to correct all background effects, as Rayleigh scattering, aerosol extinction, defocusing loss or scintillation, is the next step in the SSR. To get the pure target species transmission, e.g. in Fig. 1.9 c the $^{12}CO_2$ target species, we need to correct the Off- and On-signal from its GHG foreign species influences. Therefore we simulate the transmission due to these foreign GHG contributions with the Reference Forward Model (RFM), termed as modeled species transmission in Fig. 1.6. The RFM was developed by Dudhia (2008) and integrated into our xEGOPS end-to-end simulation tool, by using the atmospheric parameters and initial background GHG concentration

(can be zero concentration) and the HITRAN2004 spectroscopic parameters. The output of this step is the target species absorption loss of the target species as shown in Fig. 1.9 c.

Applying the Abel transform on the target species absorption loss profile after Eq. 6 published in Schweitzer et al. (2011), one can calculate the absorption coefficient profile in m^{-1}. The example result is shown in Fig. 1.9 d.

The final step of the SSR is the calculation of the volume mixing ratio (VMR). The VMR is proportional to the absorption coefficient and the temperature and inverse proportional to the pressure and target species absorption cross section (Eq. 3.16 in Chap. 3). The latter is again modeled with the RFM utilizing the initialized background GHG profile. This results in the VMR as shown for the example target species $^{12}CO_2$ in Fig. 1.9 d as absolute value and in Fig. 1.9 f as relative value. The dotted and dashed lines mark the target and threshold values as proposed in Kirchengast et al. (2010a); Kirchengast and Schweitzer (2011). This process closes the SSR retrieval and is performed for each channel pair.

The SSR is nested into two loops, one loop considering the order of the retrieval for each single target species, named Multi-Line Trace Species Retrieval (MSR) and the second loop acts as convergence loop, termed Basic-Update-Control Runs (BUC). The embedding of the loops within the LIO core algorithm with the input-, initializing-, preparatory- and core algorithm steps is schematically shown in Fig. 1.8.

The inner loop follows the consecutive order of the following retrieved target species order {N_2O, CH_4, $^{13}CO_2$, $C^{18}OO$, H_2O-1, H_2O-2, H_2O-3, H_2O-4, $^{12}CO_2$, HDO, $H_2^{18}O$, CO, O_3} with the first listed retrieved first and to be continued till the O_3 is retrieved (for details see Tab. 3.1 in Chap. 3 or Proschek, Kirchengast and Schweitzer (2011)). The consecutive order is due to increasing foreign GHG influence on the single absorption- and reference channels. This means, the first target GHGs show the least foreign GHG influence and the last the highest, with consecutive dependency.

After a target species is retrieved, the so called background profile is updated with the newly retrieved GHG VMR values, so that the next SSR can profit from the previously retrieved target GHGs. Since H_2O provides four channels (H_2O-{1,2,3,4}) for different altitude ranges (see Tab. 3.1 in Chap. 3 or Proschek, Kirchengast and Schweitzer (2011)), we perform a combination of these four channels after the SSR. The combination follows a dynamic inverse error variance weighting and is in detail described in Sect.3.3.5 in Chap. 3 or Proschek, Kirchengast and Schweitzer (2011).

Additionally, the two isotopes $^{12}CO_2$ and $^{13}CO_2$ are retrieved. They can be combined with a static inverse error variance weighting to a single CO_2 profile, since their isotopic ratio $\delta^{13}C$ is rather stable in the free atmosphere (Allison and Francey 2007). $^{12}CO_2$ provides better VMR results above 10 km and $^{13}CO_2$ shows more accurate results below the 10 km altitude range (Proschek, Kirchengast and Schweitzer 2011); the combination thus improves the VMR of CO_2.

The BUC is a simple loop comprising three runs, termed basic-, update- and control-run over all target species from the inner loop of each SSR, to guarantee a convergence of

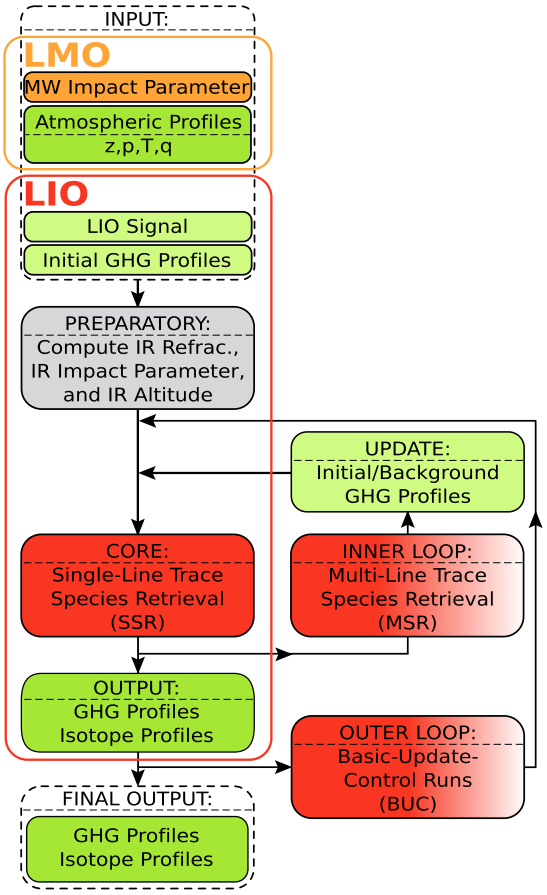

Figure 1.8: Overview of the dynamic structure and flow of the LIO retrieval algorithm, highlighting its preparatory part, establishing IR refractivity, impact parameter, and altitude profiles (grey box), its core part, the single-line trace species retrieval SSR (red box), and its dynamical part of envelope loops over the SSR, consisting of the multi-line trace species retrieval (MSR) loop and the basic-update-control run (BUC) loop, respectively (gradient-red boxes); see the text in Sect. 3.3.2 for further explanation.

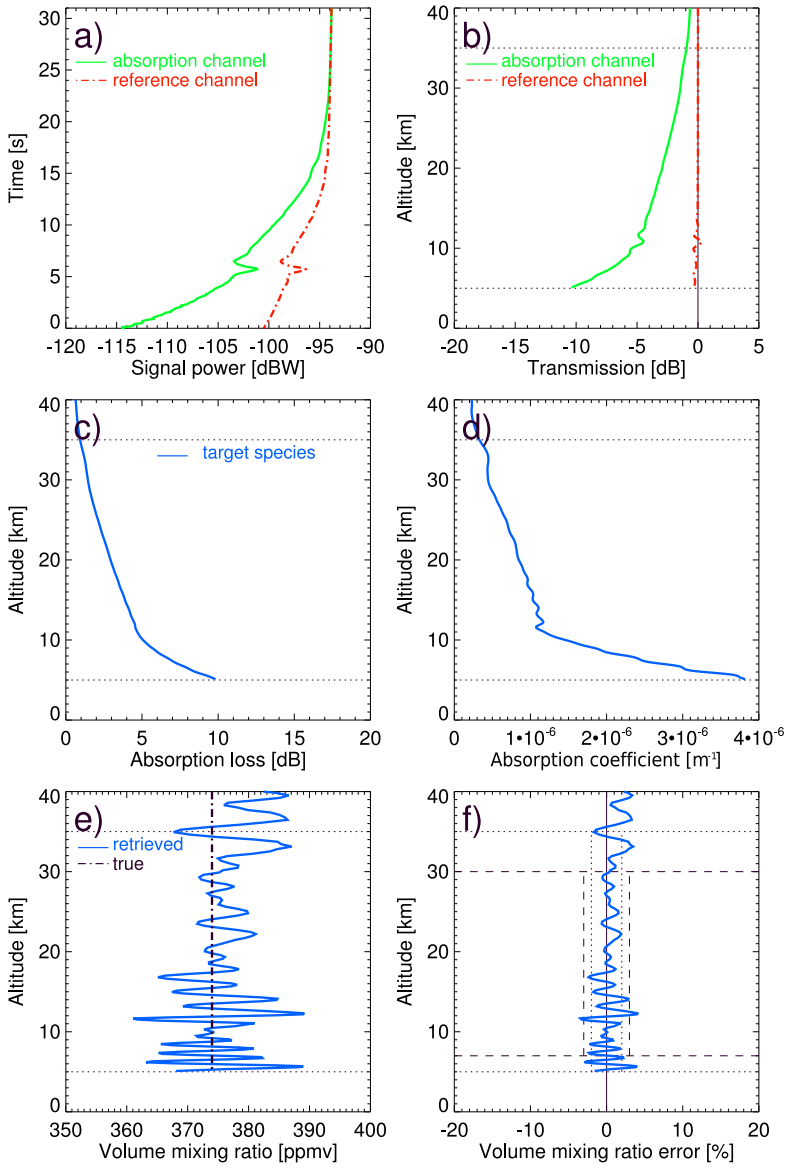

Figure 1.9: Illustration of the single-line trace species retrieval (SSR) algorithm for the single-line species $^{12}CO_2$. **(a)** LIO input profiles, simulated signal powers for the $^{12}CO_2$ absorption (green solid line) and reference (red dashed-dotted line) channel as a function of time. **(b)** Transmission profiles for the two channels after defocusing and spreading correction and allocation to the IR altitude grid. **(c)** $^{12}CO_2$ absorption loss profile after absorption-reference channel differencing and correction for all background effects. **(d)** $^{12}CO_2$ absorption coefficient profile after Abel transform retrieval. **(e)** Retrieved (blue solid) and true (black dashed-dotted) $^{12}CO_2$ volume mixing ratio (VMR) profile. **(f)** $^{12}CO_2$ VMR retrieval error profile (retrieved-minus-true relative to true). The horizontal and vertical dotted/dashed lines – especially used in panel **(f)** Indicate the target/threshold observational requirements for altitude domain and accuracy for the LMIO mission concept (Larsen, Kirchengast and Bernath 2009; Kirchengast et al. 2010a). Figure taken from Proschek, Kirchengast and Schweitzer (2011)

the entire LIO retrieval. Results are shown in Fig. 3.8 and Fig. 3.9 Chap. 3 or Proschek, Kirchengast and Schweitzer (2011).

The retrieval results under clear-air conditions for CH_4, H_2O, CO_2 and O_3 show unbiased relative VMR errors of 1 % to 3 % within their target altitude domain for different FASCODE atmospheres and GHG conditions (e.g., tropical (TRO), standard (STD) and subarctic winter (SAW)). This shows, besides the capacity of retrieving an entire set of GHGs, also a strong improvement of the H_2O result, compared to the LMO retrieval. The latter is only capable to retrieve H_2O with an accuracy of ∼10 %. Nevertheless, the necessity of the LMO retrieval is grounded in the need for the LIO preparatory algorithm steps to guarantee an independent, self-calibrating system for the entire LMIO concept. We expect results at an error level of <0.1 % for climatological averages.

Retrieval algorithm: Adaptations due to cloud influences

Clouds show a significant impact on the IRL signals compared to MW signals which are hardly influenced by them. An assessment on the influence of both wave length ranges of the occultation signals was done by Emde, Proschek and Kirchengast (2009) and Emde and Proschek (2010). Additionally, as mentioned above, solar occultation event analysis on the penetration depth into the troposphere showed that optical occultation events are significantly effected by clouds (see Harrison and Bernath (2010); Atmospheric Chemistry Experiment (ACE) mission study analysis). An advancement of the LIO algorithm for *cloudy-air* conditions is summarized in this section, detailed in Chap. 4 and published in Proschek et al. (2014a).

The potential to improve the number of tropospheric occultation events, i.e. those returning a retrieval profile down into the troposphere, lie in the bridging of intermittent cloud layers and sub-visible cirrus clouds. Since the IRL signals show a laser Fresnel diameter of about 3 m (see Kirchengast et al. (2010a)), the effective signal beams will be narrow and can pass through cloud layers and continue the profiling. However, such cloud-perturbed transmission profiles need to be reconstructed.

Therefore the core algorithm as briefly introduced in Sect. 1.2.2 needs to be extended as shown in Fig. 1.10. In this figure we can see two additional steps in the algorithm, emphasized in blue boxes. The first is the retrieval step of a cloud flagging profile. This process is crucial to determine the altitude levels at which clouds are present within the ray paths. Therefore, an Off-channel signal, with very weak foreign GHG absorption, is picked and smoothed from high frequent scintillation noise with a Blackman-Windowed-Sinc filter to keep the cloud-effected strongly varying transmission profile shape. Such profile is shown in Fig. 1.10 b, left panel, for the red line including the defocusing effect. The latter needs to be corrected as described in detail in Schweitzer et al. (2011), since defocusing can contribute ∼5 dB loss near 6 km.

Furthermore, a definition of a boundary at which cloud extinction starts to be relevant

is defined at a transmission level of -3 dB and thus a cloud flag is set to >0.0 for strong attenuation. This level is conservatively defined, since some atmospheric broad band effects like Rayleigh scattering, aerosol extinction and foreign GHG influence combined do not exceed this level. A signal is defined as blocked if it exceeds the -15 dB transmission level. The cloud flag is then set to 1.0. Intermittent transmission levels are set to adequate cloud flags between 0.0 and 1.0 within these boundaries.

From this step we get a cloud flagging profile as we can see for an example case in Fig. 1.10 b right panel (red dashed line), with a blocking cloud near ∼15 km, down to about 13 km, and weak extincting cloud features between ∼11.5 km and ∼10 km and near 7.5 km.

The second cloud algorithm step is the correction of the absorption loss profile (see cloud-perturbed absorption loss profile in Fig. 1.10 c left panel, dotted dashed green: $^{12}CO_2$, dashed blue: $H_2O(2)$) based on the previously retrieved cloud flagging profile.

The profiles are (log-)linearly interpolated, at cloud presence for cloud flags >0.0 and altitude gaps <3 km for all GHGs except H_2O. The latter profiles show strong transmission variations with altitude even for cloud regions with an extend of <3 km, so that we re-simulate these on the basis of the LMO humidity output, to reconstruct the H_2O absorption loss profiles. The latter provides an H_2O profile with accuracy of <10 %, which is helpful.

If the cloud interference continues down to the retrieval bottom altitude, the cloud top is set and the profile is cut at the altitude when the cloud flagging started to detect the cloud. Such reconstructed examples for $^{12}CO_2$ and $H_2O(2)$ lines are shown in Fig. 1.10 c, right panel. After these steps, the SSR can be normally continued as briefly explained in previous sections or for details see Proschek, Kirchengast and Schweitzer (2011).

For realistic simulations of cloud features within the ray paths, we used Cloud–Aerosol LIDAR Infrared Pathfinder Satellite Observations (CALIPSO) data to generate realistic clouds intersecting the IRL signals. The features are provided at a horizontal resolution of ∼300 m and vertical resolution of ∼60 m in perpendicular attenuated back-scatter (PAB) data. Since liquid water content (LWC) clouds are IRL signal blockers anyway, only ice water content (IWC) clouds were assumed, applying a simple linear relation between the PAB and IWC value, to realize realistic ice clouds at such high resolution.

Furthermore, a scan rate of 50 Hz was applied in a spherical symmetric gaseous atmosphere based on an European Centre for Medium-Range Weather Forecasts (ECMWF) analysis field and FASCODE GHG atmosphere. Scintillation effects were superimposed on the forward-simulated IRL signals. Additionally, the stepping of the ray tracer was set to 100 m to resolve the cloud features. The cloud extinction coefficients for the forward simulation are based on the empirical models for IWC clouds and effective radius calculation by Key et al. (2002)and Wyser (1998a), and for LWC clouds and effective particle size calculations we used the formulations by Hu and Stamnes (1993) and Wyser (1998b).

The retrieval results are promising and are shown and discussed in detail in Chap. 4 and

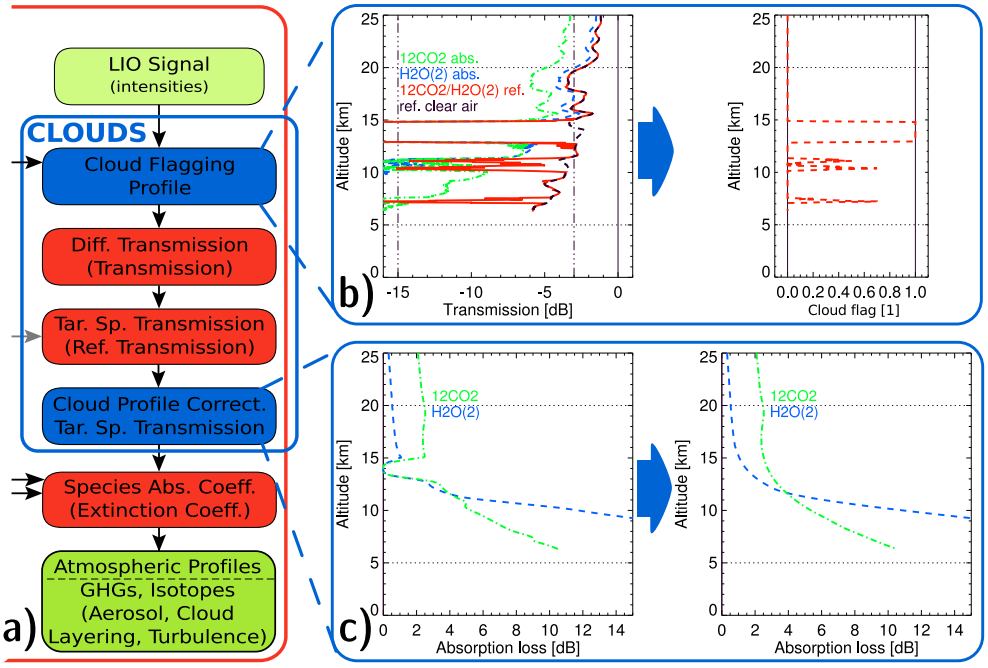

Figure 1.10: Overview of the cloud retrieval processes using $^{12}CO_2$ and $H_2O(2)$ channel pairs as examples. a) Illustrates the single retrieval steps and the intermediate steps for the cloud processing, i.e. the Cloud Flagging Profile and the Cloud Profile Correct. Tar. Sp. Transmission, in blue boxes. b) Shows the cloud flagging process; in detail the left panel shows the $^{12}CO_2$ absorption line in dotted green and the $H_2O(2)$ absorption line in dotted blue; the red solid line shows the reference line with cloud extinction the black-dashed line without cloud features; all include the defocusing effect and aerosol extinction besides GHG extinction. The vertical lines indicate the thresholds for the 0.0 cloud flag, for zero clouds above -3 dB, down to -15 dB for blocking clouds with a flag of 1.0; the horizontal lines symbolize the cloud relevant altitude region. The right panel shows the resulting cloud flagging profile derived from the reference absorption line, with vertical lines as cloud flagging boundaries. c) Shows the differential transmission profiles with cloud extinction layers at near 15 km and weaker cloud influences at near 10 km and near 7.5 km; the right panel shows the corrected differential transmission profile. Figure after Proschek et al. (2014a).

Proschek et al. (2014a). The cloud-perturbed transmission profiles could be reconstructed in a rather good way. The scintillation increased the noise level of the retrieval up to <1.5 % to 2.5 %. Some individual biases may occur for cloud-bridged regions, although they are assumed to level each out for profile averages, since clouds appear quasi-randomly in occultation events. The mean error is thus unbiased and stays within the level of 1 % to 3 %, except for H_2O profiles with very strong fluctuations within the profile, which are limited to a certain extend but still appear to well fulfill observational requirements.

1.3 End-to-end simulation framework xEGOPS/EGOPS

DEVELOPMENT of such a complex mission concept like the ACCURATE missions's LEO–LEO microwave and infrared-laser occultation (LMIO) method without a power-full and flexible software tool would not be possible. Therefore, the assessment work for the mission concept was built on the long-proven software tool End-to-End Generic Occultation Performance Simulation and Processing System (EGOPS) developed at the Wegener Center, serving as kernel library, and a prototype software environment termed eXtended End-to-End Generic Occultation Performance Simulation and Processing System (xEGOPS).

This following section will introduce the used and further developed software tool and gives an overview of the xEGOPS framework and the data flow, the algorithm implementation and an overview of setting possibilities used for the LMIO assessment studies and retrieval algorithm development. Due to the abundant structure and simulation possibilities in EGOPS and xEGOPS, covering GPS radio occultation (RO) real data processing, microwave (MW) and infrared (IR) ground-link, airborne-link occulation simulations, different options for satellite and instrument settings, etc., this section will only focus on simulation settings as usual in particular for the LEO–LEO infrared-laser occultation (LIO) basis algorithm description as published by Proschek, Kirchengast and Schweitzer (2011). Detailed description about the tool, the algorithm, setting possibilities and the input and output data are given in Fritzer, Kirchengast and Pock (2009b); Fritzer et al. (2010b); Fritzer, Kirchengast and Pock (2009a); Fritzer et al. (2010a).

The term end-to-end simulation denotes a closed process, wherein an entire occultation measurement process including the mission planning and preparation of the measurement, atmospheric influences, observational influences and the retrieval itself, are simulated. For the LMIO concept this are four main steps, termed Mission Analysis/Planning (MAP), Forward Modeling (FOM), Observation System Modeling (OSM) and Occultation Processing System (OPS), implemented as subsystems in the xEGOPS.

The end-to-end simulation process flow is schematically shown in Fig. 1.11 following the principle: *What you put in, you need to nominally get out!*. In this figure, the four subsystems with their parameter flow which is passed in between these subsystems, are shown in the middle column. The left side of the figure represents the input parameter and setting options to perform a simulation, the right side represents the various processes performed within the corresponding subsystem. The bottom panel shows the validation of the developed system, where the simulated input parameters are compared with the retrieved output parameters. The resulting errors determine the retrieval accuracy estimated by system. This includes, besides computational limits, the actual errors indueced by the Observation System Modeling (OSM) and by algorithm limits.

Each subsystem is explained in the following sections. The red highlighted input box in the Forward Modeling (FOM) subsystem with pressure (p), temperature (T), specific humidity (q), greenhouse gases (GHGs), and isotopes symbolise the variables of interest

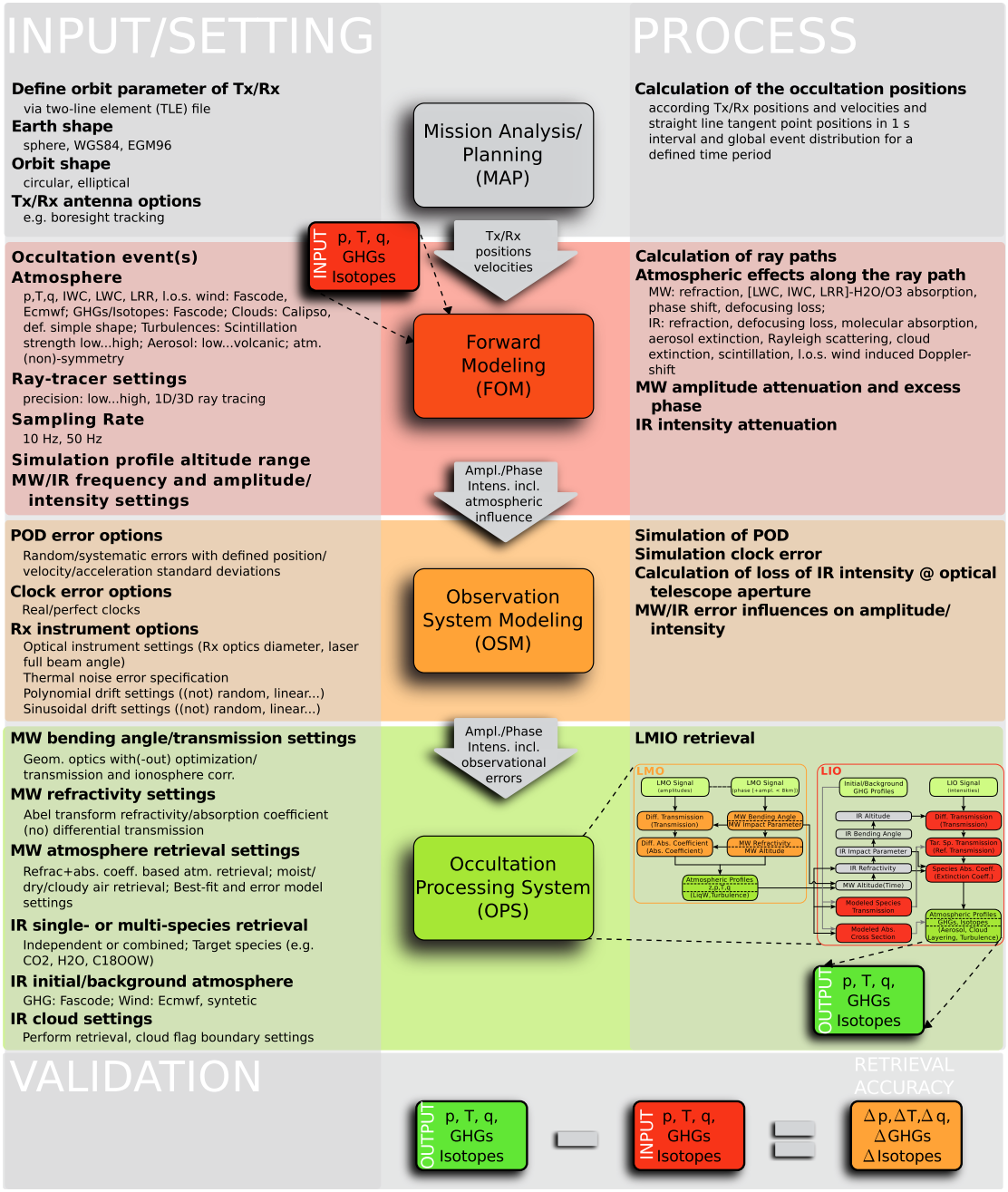

Figure 1.11: Schematic overview of the xEGOPS end-to-end simulation process with the xEGOPS sub-steps Mission Analysis/Planning (MAP), Forward Modeling (FOM), Observation System Modeling (OSM) and Occultation Processing System (OPS).

that serve as input in this subsystem. It is also the *desired* output after performing the retrieval in subsystem Occultation Processing System (OPS) and is shown in the green highlighted output parameter box. The validation (bottom line of Fig. 1.11) of the end-to-end system can be performed when subtracting the retrieved output parameters from the originally used input parameters, to determine the accuracy (errors, biases, standard deviations, etc.) of the retrieval and the system itself.

1.3.1 Mission analysis/planning

The Mission Analysis/Planning (MAP), xEGOPS subsystem gray part in Fig. 1.11, covers the orbiting of the satellites, the planning of the occultation events and the event distribution for rising and setting events over the Globe. The distribution is determined by minimally one pair of transmitter (Tx) and receiver (Rx) and their satellite orbiting altitude, the orbit inclination and the right ascension of the ascending node. The latter options are defined in a Two-Line Element (TLE) file. Additional options are the Earth- or Orbit shape and Tx/Rx antenna settings, which are set within the Mission Analysis/Planning (MAP) sub-process (e.g., World Geodetic System 1984 (WGS84), Landolt-Börnstein (1984)).

In Fig. 1.12 an example for such an occultation event distribution for sun-synchronous satellites with an inclination of ∼98° and orbiting altitudes of 800 km and 650 km for Tx and Rx satellites, respectively, covering 24 h for July 15, 2007 is shown. Highlighted in green is a standard (STD) atmosphere event, in red a tropical (TRO) event and in blue a subarctic winter (SAW) (settings are used in Proschek, Kirchengast and Schweitzer 2011).

More recent settings for the LMIO mission are defined in Kirchengast et al. (2010a) and show lower satellite orbiting heights (Tx: ∼595 km, Rx: ∼512 km) and an inclination of ∼80°. The latter settings show a better global coverage and a more accurate repetition rate with ideally ∼7200 occultation events within a month for two pairs of satellites (Kirchengast and Schweitzer 2011). For the cloud algorithm development (see Sect. 1.2.2 or Chap. 4) *Ideal Geometry* settings were used (a special option to feed the FOM), since there was the need of an occulation plane perpendicular to the Earth's surface without moving straight line tangent point (TP) within the occultation event to transform the realistic cloud data into the occultation plane rather easily and realistically since the cloud data are provided in such projections (for more details see Chap. 4).

The MAP calculates the positions ($\vec{x}_{\mathrm{Tx}}$, $\vec{x}_{\mathrm{Rx}}$) and the velocities ($\vec{v}_{\mathrm{Tx}}$, $\vec{v}_{\mathrm{Rx}}$) of the counter-rotating Tx and Rx, respectively, at every 1 s time step within the occultation event. Additionally, straight line TP positions for each time step are calculated realizing an occultation plane within the occultation event time, which is not necessarily normal to the Earth's surface. An occultation event is finished when the Tx and Rx loses the visibility when setting behind the Earth or are already above the atmosphere when rising. These calculated parameters are the necessary starting parameters for the next

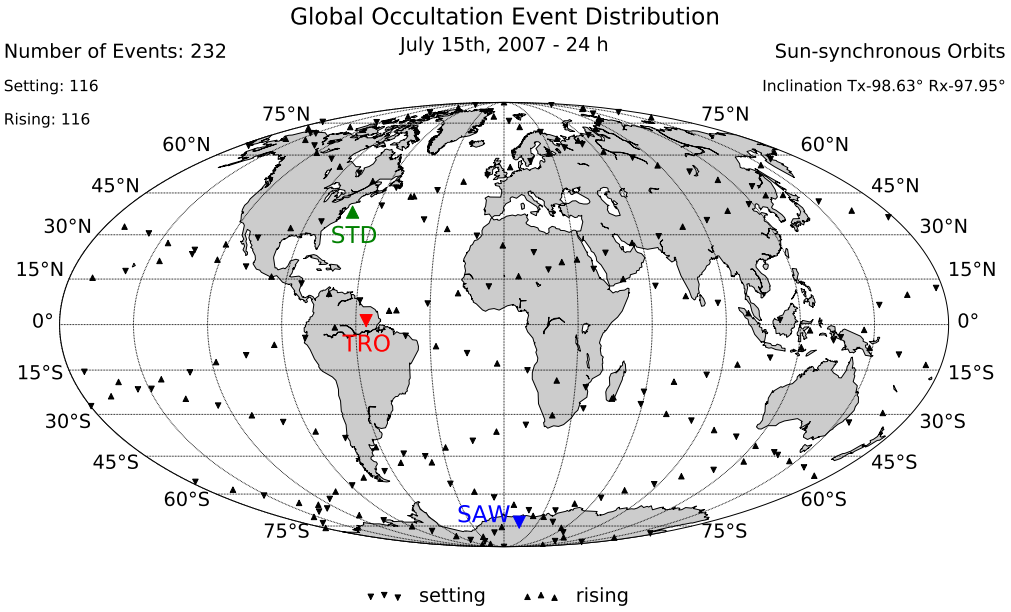

Figure 1.12: Occultation event distribution for sun-synchronous orbits for July 15, 2007 over a 24 h period and inclination of the Tx (orbit altitude at 800 km) and the Rx (orbit altitude at 650 km) of ∼98°. The standard (STD), tropical (TRO) and subarctic winter (SAW) event are chosen for the demonstration simulation of the LIO algorithm in clear-air conditions published in Proschek, Kirchengast and Schweitzer (2011) (plot courtesy of A. Plach, 2013).

sub-process, namely FOM.

1.3.2 Forward modeling

The process simulating atmospheric influences on actively transmitted signals between a Tx and a Rx is done in the Forward Modeling (FOM) subsystem of xEGOPS. An overview of the input, setting options and procedures is given in the red part of Fig. 1.11 and is explained in the following paragraphs.

It starts with the output, the positions and velocities of Tx/Rx for each occultation time step, from the MAP to simulate the MW excess phase, MW amplitude or IR intensity, while performing a limb-scan of the atmosphere. Such schematic view of the limb-scanning measurement procedure was shown in Fig. 1.5 above, transmitting an MW and Infrared Laser (IRL) signal simultaneously. A special option is *Ideal Geometry*, where simple circular orbits can be explicitly specified.

The atmosphere is assumed as spherical symmetric for all simulations and can either be a model atmosphere as the Fast Atmospheric Signature Code (FASCODE) (FASCODE 2008) or a more realistic one like an European Centre for Medium-Range Weather Forecasts (ECMWF) field, both taken for the calculated straight line TP position. The atmosphere, which contains the measured parameters of interest (red box highlighted in Fig. 1.11), provides p, T and q profiles for the refractivity and broadband effects calculations as well as line-of-sight wind velocity ($v_{\text{l.o.s.}}$), ice water content (IWC), liquid water content (LWC), liquid rain rate (LRR), aerosol concentrations and scintillation strength. And even greenhouse gas (GHG) profiles, needed for molecular absorption calculations, are defined by the atmosphere settings (currently only Fast Atmospheric Signature Code (FASCODE) GHG profiles are provided).

The sampling rate defines the data acquisition rate at which an amplitude/intensity profile is sampled during an occulation event. It is sufficient to work with a 10 Hz sampling rate for broadband effects simulation like Rayleigh scattering, defocusing loss or aerosol extinction, although 50 Hz are needed for scintillation simulations or realistic cloud-feature-influence simulation.

The tool enables simulations of realistic geometric optical ray paths between Tx and Rx as function of sampling time by a 3D ray-tracing algorithm developed by Syndergaard (1999). The ray tracing system needs the input atmosphere and the refractivity formulas, such as Eq. 1.2 developed by Smith and Weintraub (1953) covering the MW signal range and Eq. 1.3 based on Bönsch and Potulski (1998) covering the IR range (see Sect. 1.2.1 and 1.2.2). The ray path is tunable to a target accuracy up to ∼1 mm and a step size of ∼1 km, which is reduced to ∼100 m for more accurate stepping to sample realistic local features, in particular used in the cloud algorithm development (for more details see Chap. 4).

Along the ray, the developed FOM enables the simulation of several atmospheric influences. The effects are controlled via the input parameters and settings, with which

effects can be switched on and adapted to the needed strength of influences. The various processes, sucha as Rayleigh scattering (Salby 1996), aerosol extinction (Thomason and Peter 2006; Schweitzer, Kirchengast and Proschek 2011), scintillations due to atmospheric turbulence (Sofieva 2009; Horwath and Perlot 2008), cloud extinction (Key et al. 2002; Hu and Stamnes 1993; Wyser 1998a,b) and molecular absorption (Edwards 1996; Dudhia 2008; Rothman et al. 2005, 2009) for the IR signal were briefly described in Sect. 1.2.2 and are explained in more detail in Chap. 2.

Each IR related effect is calculated in a FOM sub-module and provides an absorption, scattering, or extinction coefficient for every step within the ray path. The absorption coefficient for the MW signal is based on Liebe's Millimeter Wave Propagation Model 1993 (MPM93) model (Liebe, Hufford and Cotton 1993; Schweitzer et al. 2011) and integrated into the EGOPS software tool. Such calculations are done for each MW or IR signal with a specified channel center frequency and an initial power at the Rx side (for LMIO channel settings and link budget see Kirchengast et al. (2010a)).

In general, such integrated attenuation influences along the ray path are described with the Bouguer-Lambert-Beer law which reads as follows:

$$I = I_0 \cdot \exp\left(-\tau\right) = I_0 \cdot \exp \int_{Tx}^{Rx} \epsilon\left(s\right) \mathrm{d}s. \tag{1.4}$$

The variable ϵ symbolizes the absorption/scattering/extinction coefficient for the single influences as described above, as function of the ray path (s). I is the intensity and I_0 the initial intensity, while τ defines the optical thickness. The ratio of I/I_0 can be easily converted into dB and thus every individual influence can be easily linearly summerized to the total atmospheric loss contribution.

The defocusing loss, accounting for the IR and MW range, as described by Kursinski et al. (2000) and Schweitzer et al. (2011), is calculated after the integration along the ray path of atmospheric broadband- and molecular loss, since defocusing shows only geometrical dependencies. It is essentailly proportional to the distance from the Rx to the limb (location of the TP), the bending angle (α) and the impact parameter (a). The definition of these geometric parameters are illustrated in Fig. 1.5 for the IRL signal in red and the MW signal in orange. The physical vertical resolution can reach from $\sim$3 m for the IRL signal up to $\sim$300 m for the MW signal, limiting the effective resolution of the entire LMIO concept; we generally apply filtering to $\sim$1 km resolutions.

The final output of the FOM is a MW excess phase, due to refraction and thus the prolonged ray path relative to tha straigth-line vacuum ray path, and an attenuated MW amplitude or IRL intensity signal, due to the atmospheric attenuation effects as function of sampling time.

1.3.3 Observation system modeling

The OSM subsystem simulates the observational errors. An overview with option settings and processes is shown in Fig. 1.11, orange highlighted part. The subsystem was newly implemented for the IR range, based on the MW routines with necessary adaptations to particular IR features, therefore the focus will be set here to the IR part. The input are the MW phase and amplitude and IR intensity data from FOM, respectively.

Since the observation instrument and the determination of the orbit precision play a significant role in the detection process and thus in the final power of the signal, such influences need to be accounted for. The following OSM influences can be flexibly activated and defined via an input file, when starting such simulations.

For the Precise Orbit Determination (POD) error simulation, which determines the position and velocity accuracy determination of the Rx and Tx, are simulated the same way on the MW phase and amplitude for as the IR intensity, as described in Steiner and Kirchengast (2005) and Schweitzer et al. (2011). Additionally, the clock inaccuracy on the excess phase is simulated with a relative stability of the worst clock with 1.0×10^{-13} s Allan (for more details see Ramsauer and Kirchengast (2001)).

The propergated signal, mainly influenced by MW/IR forward-simulated atmospheric losses as described in the previous section, is further influenced on the Rx side by geometrical optical loss and single observational influences, such as thermal Gaussian white noise and errors due to sinusoidal- or polynomial intensity signal drift.

The drift errors and thermal noise are the main errors for MW amplitudes and are thoroughly described in Fritzer, Kirchengast and Pock (2009a). An overview of the IR link budget simulations is explained below. Since all these factors are accounted for in units dB, a simple subtraction of losses and addition of gains or addition of noise/errors, can be performed.

First the geometric optical loss, depending on the distance between Tx and Rx, the divergence of the beam and the Rx telescope mirror diameter, need to be subtracted from the initial power, besides the forward simulated atmospheric loss from the previous step, resulting in the signal after the propagation (P_{prop}).

Then a Gaussian thermal white noise is added to the signal. The calculation of such is done in first subtracting the following terms from P_{prop}: the reception loss (∼-1.25 dB), which results from a receiver integration time greater than the pulse period, the total optical loss (∼-1.87 dB), defining the loss due to optical paths between front end of the Rx and the detector, and noise-equivalent-power (∼-121.4 [-124.9] dB at 50 [10] Hz), which defines the noise level of the detector, resulting into a signal-to-noise ratio (SNR) in DB, at the given sampling rate f_{s}.

A down-sampling gain for converting SNR at the given sampling rate to baseline 1 s, is added to the SNR and leads to an signal-to-noise density ratio ($\mathrm{S/N_0}$) in dBHz. Applying

then the following formula at a given sampling f_s,

$$\sigma = 10 \cdot \log \left(1 + \frac{\sqrt{0.5 \cdot f_s}}{10^{\frac{S/N_0}{10}}} \right). \tag{1.5}$$

the thermal noise standard error σ in dB can be calculated and is multiplied with a Gaussian random number and added to the propagated signal P_{prop}. For detailed description see Fritzer et al. (2010a); Schweitzer (2010).

The further error terms are finally added as well to the propagated signal. The errors, which follow the time, can be of the form of polynomial- and sinusoidal drift applying (non-)random drifts of linear, quadratic or higher order. The first model follows the suggestions of Silvestrin and Floury (2003) and both models are explained in detail in Kirchengast and Hoeg (2004); Schweitzer (2004); Fritzer, Kirchengast and Pock (2009a).

The final output is a quasi-realistic MW/IRL signal including observation system errors, and relevant gains and losses.

1.3.4 Occultation processing system

The last subsystem of the xEGOPS is the OPS. It closes the end-to-end loop and performs inversion of output data of the previous subsystems. This means, the retrieval of the atmospheric parameters such as p, T and q from the simulated MW excess phases and amplitudes and the retrieval of GHG volume mixing ratios (VMRs) from the IRL intensities and of other parameters, is the purpose of the OPS

This last step, with the retrieval options and settings, is shown schematically in the green part of Fig. 1.11. The MW amplitude and phase and the IRL intensities with superimposed observational errors are provided as input from the OSM. The retrieval algorithm is symbolically highlighted as LMIO process with the final output (p, T, q, GHGs, and isotopes) and shown in the green box.

A precedent process to LIO retrieval within the OPS is the retrieval of the atmospheric variables p, T and q described by the LMO algorithm as detailed by Schweitzer et al. (2011). The green part of Fig. 1.11 highlights the optional retrieval settings for the MW amplitude and phase gathered together and providing the atmospheric variables.

The LIO retrieval follows the LMO retrieval, and is described the two algorithm papers (Proschek, Kirchengast and Schweitzer 2011; Proschek et al. 2014a) presented in Chap. 3 and Chap. 4. These two papers describe very detailed both the basis LIO retrieval algorithm under clear-air conditions (Chap. 3), and advanced algorithm for cloudy-air conditions, considering broken cloudiness interacting with the IRL signal (Chap. 4).

The LIO retrieval is set up in a flexible way so that individual forward-simulated signals can be combined to an entire set, simulated for different frequencies (MW- and IR ranges) for the same occultation event to perform a Single-Line Trace Species Retrieval (SSR) or Multi-Line Trace Species Retrieval (MSR) as described in Proschek, Kirchengast

and Schweitzer (2011). The system can handle various sampling rates, nominally 10 Hz sampling rate is used or 50 Hz; the latter if higher sampling resolution is needed to capture local atmospheric effects like realistic cloud features.

Retrieval needs are implemented in a modular way, so that SSR, MSR or cloud flagging processes can be performed individually or in combination. SSR retrieval is in particular performed, if no combination options of GHGs are used or if no consecutive order of a set of GHGs set is employed.

Optionally, various background atmospheres, which serve as initial atmospheres at the beginning of the retrieval and which are updated within the MSR process line, can be used. They can comprise GHGs from FASCODE, European Centre for Medium-Range Weather Forecasts (ECMWF) data, or even *zero* atmosphere model initialization. The latter works without degradation in results, if a set of main GHGs from IRL signal profiles is available to perform a MSR. The atmospheric parameters as p, T and q are provided from the LEO–LEO microwave occultation (LMO) to guarantee independence of the LMIO measurement technique from external thermodynamic parameters.

The final output, highlighted in the green box of Fig. 1.11, is a state vector of atmospheric thermodynamic and trace species variables {p, T, q; water vapor (H_2O), carbon dioxide (CO_2), carbon dioxide second main isotope ($C^{18}OO$), methane (CH_4), nitrous oxide (N_2O), ozone (O_3), carbon monoxide (CO), semiheavy water (HDO), heavy-oxygen water ($H_2^{18}O$)}. Additional information such as the line-of-sight wind and cloud layering (cloud flagging profile) is available in addition if it was co-computed.

Altogether the xEGOPS/EGOPS system is therefore a powerful tool, well positioned to be the workhorse and key tool for the signal modeling and end-to-end simulations underlying the results of the three studies presented in Chap. 2 to Chap. 4 below.

CHAPTER 2

Atmospheric influences on infrared-laser signals used for occultation measurements between Low Earth Orbit satellites

This chapter presents work that was published in Atmospheric Measurement Techniques (AMT) by Schweitzer, Kirchengast and Proschek (2011). The work investigates the atmospheric influences on active limb-sounding Infrared Laser (IRL) signals mainly by forward-modeling simulations with eXtended End-to-End Generic Occultation Performance Simulation and Processing System (xEGOPS) software introduced in Sect. 1.3. The results support the definition of observational requirements of the LEO–LEO microwave and infrared-laser occultation (LMIO) technique and provide insights to the greenhouse gas (GHG) information contained in the IRL signals. Besides the co-editing of the paper text, my contribution to this work was the setup of the xEGOPS software framework, the adaptation of existing modules to the new framework and contributions to implementing new IRL relevant routines for the forward-modeling simulations.

ABSTRACT

LEO-LEO infrared-laser occultation (LIO) is a new occultation technique between Low Earth Orbit (LEO) satellites, which applies signals in the short wave infrared spectral range (SWIR) within 2 μ m to 2.5 μ m. It is part of the LEO–LEO microwave and infrared-laser occultation (LMIO) method, recently introduced by Kirchengast and Schweitzer (2011), that enables to retrieve thermodynamic profiles (pressure, temperature, humidity) and accurate altitude levels from microwave signals and profiles of greenhouse gases and further variables such as line of sight wind speed from simultaneously measured LIO signals. For enabling trace species retrieval based on differential

transmission, the LIO signals are spectrally located as pairs, one in the centre of a suitable absorption line of a target species (absorption signal) and one close by but outside of any absorption lines (reference signal). Due to the novelty of the LMIO method, detailed knowledge of atmospheric influences on LIO signals and of their suitability for accurate trace species retrieval did not yet exist. Here we discuss the atmospheric influences on the transmission and differential transmission of LIO signals. Refraction effects, trace species absorption (by target species, and cross-sensitivity to foreign species), aerosol extinction and Rayleigh scattering are studied in detail. The influences of clouds, turbulence, wind, scattered solar radiation and terrestrial thermal radiation are discussed as well. We show that the influence of defocusing, foreign species absorption, aerosols and turbulence is observable, but can be rendered small to negligible by use of the differential transmission principle and by a design with close frequency spacing of absorption and reference signals within 0.5 %. The influences of Rayleigh scattering and thermal radiation on the received signal intensities are found negligible. Cloud-scattered solar radiation can be observable under bright-day conditions but this influence can be as well made negligible by a design with a close time spacing (within 5 ms) of interleaved laser-pulse and background signals. Cloud extinction loss generally blocks SWIR signals, except very thin or sub-visible cirrus clouds, which can be addressed by a design allowing retrieval of a cloud layering profile from reference signals and its use in trace species retrieval when scanning through intermittent upper tropospheric cloudiness. Wind can have a small influence via Doppler shift resulting in a slightly modified trace species absorption in comparison to calm air, which can be made negligible by using a simultaneously retrieved wind speed profile or a moderately accurate (to about $10\,\mathrm{m\,s^{-1}}$) background wind profile. Considering all these influences, we conclude that the set of SWIR channels proposed for implementing the LMIO method (Kirchengast et al. 2010a; Kirchengast and Schweitzer 2011) provides adequate sensitivity to accurately retrieve eight greenhouse gas/isotope trace species of key importance to climate and atmospheric chemistry (H_2O, $^{12}CO_2$, $^{13}CO_2$, $C^{18}OO$, CH_4, N_2O, O_3, CO) in the upper troposphere–lower stratosphere region outside clouds under all atmospheric conditions. Two further isotope species (HDO, $H_2^{18}O$) can be retrieved in the upper troposphere.

2.1 Introduction

Recently, the satellite mission ACCURATE—Climate Benchmark Profiling of Greenhouse Gases and Thermodynamic Variables and Wind from Space—was proposed to the

European Space Agency by Kirchengast et al. (2010a) and received positive evaluation and recommendations for further study. This mission concept applies the occultation measurement principle (Phinney and Anderson 1968; Kirchengast 2004) in a novel way, called LMIO, recently introduced by Kirchengast and Schweitzer (2011). A graphical view of the concept is given in Figure 2.1. Laser signals in the short wave infrared (SWIR) spectral region (within 2 μ m to 2.5 μ m; pulsed signals) are used simultaneously with microwave (MW) signals at cm- and mm-wavelengths (within 8 GHz to 30 GHz and 175 GHz to 200 GHz; continuous-wave signals). These signals are transmitted between two Low Earth Orbit (LEO) satellites and thereby pass the Earth's atmosphere; the focus region is the upper troposphere–lower stratosphere (UTLS) (5 km to 35 km).

The signals are refracted and absorbed during propagation which enables to retrieve vertical profiles of thermodynamic and dynamic variables (refractivity, pressure, temperature, specific humidity, line of sight wind speed) and composition variables (greenhouse gas/isotope concentrations of H_2O, $^{12}CO_2$, $^{13}CO_2$, $C^{18}OO$, CH_4, N_2O, O_3, CO, HDO, $H_2^{18}O$) in the free atmosphere. By-products can be profiles of cloud liquid water (from the MW signals), cloud layering and aerosol extinction coefficient (from the short wave infrared (SWIR) signals) as well as turbulence strength (from both). The retrieved profiles are expected very accurate, have a high vertical resolution (about 1 km) and typically cover the whole UTLS region, which is an important region for climate and chemistry (Solomon et al. 2007b; Li, Austin and Wilson 2008; Steiner et al. 2009). For a detailed introduction of the LMIO method, and the proposed mission concept Climate Benchmark Profiling of Greenhouse Gases and Thermodynamic Variables and Wind from Space (ACCURATE) to implement it, see Kirchengast and Schweitzer (2011); Kirchengast et al. (2010a); Schweitzer (2010).

The part using the SWIR signals is called LEO–LEO infrared-laser occultation (LIO) and is suitable for retrieving profiles of trace species and line of sight (LOS) wind speed (besides the byproducts mentioned above; details on the trace species retrieval are given by Proschek, Kirchengast and Schweitzer 2011). The retrieval principle is based on *differential transmission* (Kursinski et al. 2002; Gorbunov and Kirchengast 2007), alternatively also called differential absorption principle. Regarding trace species, this means that each species is derived from the ratio of the transmissions of two signals (which corresponds to a difference in the dB space of log-transmission, proportional to optical thickness) termed a *channel pair*. One of these signals is primarily absorbed by the target species of interest and is called *absorption (on-line) signal*. The other signal is ideally not absorbed at all and only affected by broadband background effects; it is called *reference (off-line) signal*. Hence, most background effects can be eliminated by using differential transmission profiles. This and a self-calibration step in the retrieval algorithm, which is intrinsic to the occultation method since the transmitted intensities during an occultation event are generally normalised with the unattenuated intensity measured at the top of the atmosphere, are the reason why the LIO retrieval results are expected to be very accurate and essentially free of biases (Kirchengast and Schweitzer 2007; Schweitzer 2010;

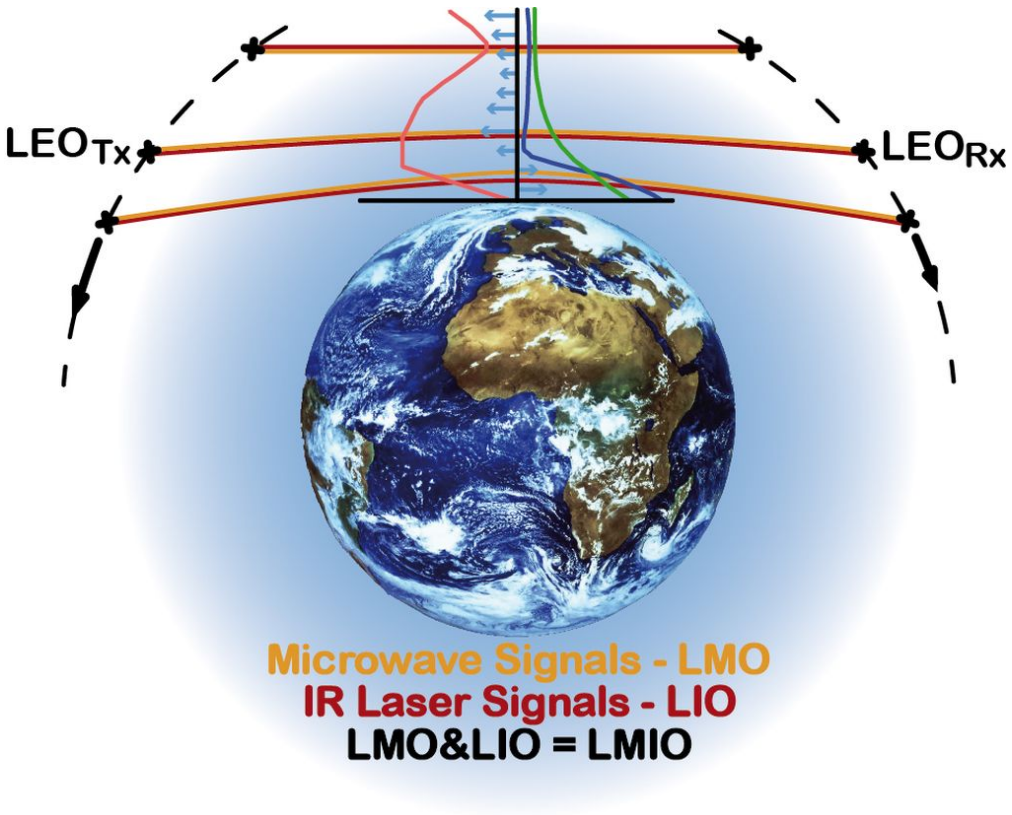

Figure 2.1: Overview of the measurement concept of the ACCURATE satellite mission applying the LMIO method.

Kirchengast and Schweitzer 2011; Proschek, Kirchengast and Schweitzer 2011). This means that the retrieval results are of high quality on a single-occultation-event basis, effectively independent of the specific LMIO mission that provides the measurements. It enables direct comparability of data from e.g., a series of successive missions, also without overlap. This long-term stability property of the data is very important in climate research.

The part using the MW signals is called LEO–LEO microwave occultation (LMO), which is well established already, even though it was not yet operated in space. More details on this technique, its capabilities and the quality of retrieval results can be found in Feng et al. (2002); Herman et al. (2004); Kursinski et al. (2002, 2004); Kirchengast and Hoeg (2004); Gorbunov and Kirchengast (2005, 2007); Kursinski et al. (2009); Schweitzer et al. (2011). A closely related occultation method is the GNSS–LEO radio occultation (GRO), which uses L-band signals from the Global Positioning System (GPS) system. GRO is meanwhile regularly operated in space and proved to be very useful for atmosphere and climate research and weather forecasting (e.g., Kursinski et al. 1997; Steiner et al. 2001; Hajj et al. 2002; Gobiet et al. 2005; Healy and Thépaut 2006; Anthes et al. 2008; Steiner et al. 2009; Ho et al. 2009; Cardinali 2009).

The LIO technique is the novel part of the LMIO method and was an original conception for the ACCURATE mission, adding to the LMO technique of the predecessor mission concept ACE+ (Kirchengast and Hoeg 2004). Hence, all scientific and technical characteristics of this technique needed to be assessed essentially from scratch. One important point for this assessment was the development of tools to simulate the measurements and to retrieve the atmospheric variables. For the simulation of the measurements, it was necessary to identify atmospheric and instrumental influences on the propagation of the signals. In this paper, we focus on investigation of the atmospheric influences which are of importance for the LIO technique and the utility of the LIO signals for accurate trace species retrieval. In particular, we analyse refractive effects (due to bending and defocusing) and components influencing the transmission (trace species absorption, aerosol extinction, Rayleigh scattering). We also show the total impact of these atmospheric influences on the received signal intensity; this total influence is an important ingredient for power-budget calculations along the LEO-LEO intersatellite link and is needed to determine power requirements in an LIO mission design. Likewise it is an important input to generate simulated measurements subsequently used in retrieval processing in the frame of end-to-end simulations (Proschek, Kirchengast and Schweitzer 2011). We also discuss other atmospheric effects like the influence of clouds, turbulence, wind, and solar and thermal radiation; details especially on clouds, turbulence, and wind will be published elsewhere.

As implemented by ACCURATE, LIO is nominally operated in combination with LMO, i.e., as a full LMIO approach. From the measurement of phase and amplitude of LMO signals, profiles of the thermodynamic variables pressure, temperature and humidity can be derived as well as accurate altitude levels. Hence, just the intensity of the SWIR signals

needs to be evaluated additionally to be able to derive the atmospheric trace species and the LOS wind speed from LIO measurements (Proschek, Kirchengast and Schweitzer 2011). LIO could in principle also be used stand-alone if very accurate instruments for measuring also the phase of these infrared signals are available. This would require robustly tracked continuous-wave signals, however, which need much more power than incoherent detection of the intensity of pulsed signals without active tracking. Another option would be to take pressure, temperature and altitude information, which are needed in the LIO retrieval process, from high-quality atmospheric fields (e.g., ECMWF analyses or short-term forecasts), but this compromises the independent benchmarking capability of the full LMIO method. Any of these implementations of LIO needs a careful characterisation and understanding of atmospheric influences on the propagating SWIR signals, which is therefore the focus of this study.

The paper is structured as follows. We first present the method used to investigate the atmospheric influences on LIO (see Section 2.2). Next we discuss each influence individually in Subsection 4.3.2, whereby the refractive effects are presented first (subsections 2.3.1 and 2.3.2), followed by the influences affecting the transmission and differential transmission of the signals (subsections 2.3.3 to 2.3.7). The influences discussed but not analysed in detail within this study are addressed in Subsection 2.3.8. Finally, results are summarised and conclusions drawn in Section 2.4.

2.2 Method

The influence of atmospheric processes on the transmission of LIO signals was studied by means of propagation simulations with the End-to-End Generic Occultation Performance Simulation and Processing System (EGOPS)+xEGOPS (Fritzer et al. 2010a,b). This system provides the framework for end-to-end simulations as well as processing of real data of occultation missions, the latter for GRO only. It was originally developed for studying and evaluating GRO and LMO satellite missions and more recently extended by capabilities needed for characterising the LIO method. Below, we describe the analysis layout used for this study (Subsection 2.2.1) and the algorithms applied in the simulations (Subsection 2.2.2).

2.2.1 Analysis layout

In the Earth's atmosphere, LIO signals experience several refractive influences and influences affecting the received intensity of the signal or, equivalently, the observed transmission. The most important refractive effects are bending and defocusing of the LIO signals, which are attributable to the vertical gradient and curvature structure of the atmospheric refractivity. Interesting influences affecting the received signal intensity and transmission are trace gas absorption (both from target species and foreign species with cross-sensitivity), aerosol extinction, Rayleigh scattering, cloud extinction, scintillations

Table 2.1: Channel pairs investigated in this paper. They are adopted from the ACCURATE satellite mission concept.

Species	Abs. Chan. $\bar{\nu}_{\mathrm{Abs}}$ (cm^{-1})	Ref. Chan. $\bar{\nu}_{\mathrm{Ref}}$ (cm^{-1})	Chan. Ratio (%) $100 \cdot \frac{\bar{\nu}_{\mathrm{Abs}} - \bar{\nu}_{\mathrm{Ref}}}{\bar{\nu}_{\mathrm{Ref}}}$
H_2O-1	4204.840290	4227.07	−0.5259
H_2O-2	4775.802970	4770.15	+0.1185
H_2O-3	4747.054840	4731.03	+0.3387
H_2O-4	4733.045010	4731.03	+0.0426
$^{12}CO_2$	4771.621441	4770.15	+0.0308
$^{13}CO_2$	4723.414953	4731.03	−0.1610
$C^{18}OO$	4767.041369	4770.15	−0.0652
CH_4	4344.163500	4322.93	+0.4912
N_2O	4710.340810	4731.03	−0.4373
O_3	4029.109610	4037.21	−0.2006
CO	4248.317600	4227.07	+0.5027
HDO	4237.016320	4227.07	+0.2353
$H_2{}^{18}O$	4090.871800	4098.56	−0.1876

induced by turbulence, and the influence of solar radiation scattered into the receiver and of the atmosphere's thermal radiation. Furthermore, LOS wind speed induces a frequency shift resulting in a slightly modified trace species absorption loss.

We investigate the influence of these effects on the transmission and differential transmission of LIO signals. We show most of them for the set of 19 LIO channels (resulting in 13 channel pairs for the retrieval of 10 different species) proposed by Kirchengast et al. (2010a) and Kirchengast and Schweitzer (2011), which have been selected on the basis of studies by Schweitzer (2010). The frequencies belonging to these channel pairs and their spectral separation are summarised in Table 2.1. Quasi-realistic propagation simulations with the EGOPS+xEGOPS system are used to discuss the influence of defocusing (Subsection 2.3.2), trace gas absorption (subsections 2.3.3 and 2.3.4), aerosol extinction (Subsection 2.3.5), Rayleigh scattering (Subsection 2.3.6) and the total influence of all of these atmospheric effects as well as the resulting received signal power in an LIO system (Subsection 2.3.7). The trace gas absorption is considered from two perspectives: on the one hand, the *target species absorption* is shown (Subsection 2.3.3), which is due to the influence of the desired absorber of an absorption channel; on the other hand, the *foreign species absorption* is investigated (Subsection 2.3.4), which is the sum of the influences of all unwanted background absorbers (which corresponds to all absorbers in a reference channel, and all absorbers except for the target species in an absorption channel).

The influences studied are inspected by means of the direct atmospheric losses resulting

from single channels, and/or by means of differential losses after computing differential transmission from channel pairs (note that atmospheric loss in units dB is the magnitude of atmospheric transmission in dB, which would have a negative sign). The direct loss is important for the power budget of the intersatellite link, since it degrades the signal-to-noise ratio (SNR) of the received signal. Hence it should be small for all unwanted background effects so that target species absorption is as dominating as possible. On the other hand, the loss due to target species absorption must be significant but also not excessive (which would again degrade SNR too much), in order to enable accurate retrieval of target species concentrations (Kirchengast and Schweitzer 2011; Proschek, Kirchengast and Schweitzer 2011). The differential loss reflects the residual influence of an effect after differencing the two transmissions (in units dB) of a channel pair, which is why it should be as small as possible for all unwanted background effects.

The favourable range of magnitudes of these losses depends on the mission design, above all on the available SNR at the receiver without atmospheric attenuation, i.e., on the ratio of received signal power to the noise-equivalent power (NEP) of the detection system. For the ACCURATE mission this is designed to be at least 34 dB at 1 Hz bandwidth (Kirchengast et al. 2010a; Kirchengast and Schweitzer 2011). The total atmospheric loss down to the UTLS bottom (5 km) should thus not exceed about 21 dB, leaving 13 dB SNR margin (5 % relative accuracy of signal). The target species absorption loss, the signal portion of interest, should be within about 0.25 dB and 13 dB, corresponding to an absorption of about 5 % to 95 % (cf. Schweitzer et al. 2011). This leaves about 8 dB for background losses of which defocusing will use up to about 5 dB (as seen further below), and 3 dB or more is thus the remaining margin for other effects like aerosol under post-volcanic conditions. Overall, the direct losses due to background influences should fit into these margins, ideally be below 0.25 dB (within 5 % perturbation), and in particular their impact in the differential transmission should be, or be correctable to, smaller than 0.005 dB (< 0.1 % residual error) in order to ensure that their influence on the accuracy of retrieved trace species is negligible. In the case that the direct loss of a background influence exceeds about 0.25 dB, it becomes a potential observable itself and information can be retrieved by applying a suitable algorithm to direct transmission profiles. For LIO signals this will enable to retrieve, for example, cloud layering (Schweitzer, Proschek and Kirchengast 2010), aerosol extinction (given significant aerosol load) and turbulence strength profiles.

The bending of the LIO signals is not discussed directly, since the refraction process behind is basically the same as for LMO and GRO signals, which is described by, e.g., Kursinski et al. (2000). Instead, we discuss the difference between the SWIR and MW refractivities, which is relevant for adequate processing of LIO measurements as part of the full LMIO method (Subsection 2.3.1).

The other atmospheric influences (clouds, turbulence, wind, scattered-solar and terrestrial radiation) are discussed in an introductory, semi-quantitative style in Subsection 2.3.8, referring to several grey literature reports related to which key results will be

published elsewhere. The reason is that except for thermal radiation these influences are more complex and therefore require separate papers. Moreover, since these influences exert, except for clouds, small to negligible effects in differential transmission (Schweitzer 2010; Kirchengast et al. 2010a; Kirchengast and Schweitzer 2011), they are not that fundamental in the context of this paper. Clouds will typically block the whole signal, leading to effectively zero transmission and no received SWIR-laser pulse signal at cloud-contaminated height levels. While it is important to keep this extreme attenuation by clouds in mind, which is separately addressed in mission design and processing, it is not relevant in the context here where we focus on exploitable signals in non-cloudy conditions.

The LIO propagation simulations were performed using the EGOPS+xEGOPS system. The atmosphere conditions (pressure, temperature, trace gas volume mixing ratios) underlying the simulations were taken from the Fast Atmospheric Signature Code (FASCODE) atmosphere model (Anderson et al. 1986, provided by A. Dudhia, Univ. of Oxford, UK, via http://www.atm.ox.ac.uk/RFM/atm); the volume mixing ratio (VMR) for $^{12}CO_2$ therein was updated to a more recent value of 380 ppmv. First, geometry data for three occultation events resulting from a constellation of two transmitter (Tx) and two receiver (Rx) satellites in counter-rotating orbits (receiver at 650 km, transmitter at 800 km, circular orbits at true-polar/90° inclination) were determined using the Mission Analysis/Planning (MAP) system of EGOPS. These events are located in three different latitude regions: one at mid latitudes, where FASCODE standard atmosphere conditions are used (STD: 39.7° N, 114.0° W), one at high latitudes with FASCODE subarctic winter conditions (SAW: 67.5° S, 7.3° E), and one in the tropics with FASCODE tropical conditions (TRO: 1.1° N, 86.0° W). These atmospheric conditions provide representative selections from the range of atmospheric variability (from dry and cold over medium to moist and warm conditions) and are thus suitable to indicate the variability of the atmospheric influences.

For these three occultation events, propagation simulations were performed using the geometric optical ray-tracing algorithm of the EGOPS+xEGOPS Forward Modeling (FOM) system (Syndergaard 1999, details in Fritzer et al., 2010a). The vertical simulation range was 3 km to 80 km and the sampling rate 10 Hz. The simulations were arranged for the 19 channels listed in Table 2.1. Atmospheric losses included in the simulations were those due to defocusing, trace gas absorption, aerosol extinction, and Rayleigh scattering. The atmosphere was assumed to be spherically symmetric and the Earth figure to be an ellipsoid (WGS84, Landolt-Börnstein 1984). A detailed description of the whole EGOPS+xEGOPS FOM system is contained in Fritzer et al. (2010a).

2.2.2 Algorithms for propagation simulation

Refractivity

The refractivity is described using a streamlined one-equation form of the more sophisticated empirical refractivity formulation of Bönsch and Potulski (1998), which is an improvement of the closely similar optical refractivity formula by Edlén (1966). This formula is accurately valid for optical frequencies including SWIR frequencies ($\lambda > 0.5\,\mu$ m) and reads, after Proschek, Kirchengast and Schweitzer (2011),

$$N = \left(c_1 + \frac{c_2}{d_1 - \frac{1}{\lambda^2}} + \frac{c_3}{d_2 - \frac{1}{\lambda^2}} \right) \cdot \frac{p}{T} - \epsilon \cdot e, \tag{2.1}$$

where the constants are $c_1 = 23.7104\,\mathrm{K\,hPa^{-1}}$, $c_2 = 6839.34\,\mathrm{K\,hPa^{-1}}$, $c_3 = 45.473\,\mathrm{K\,hPa^{-1}}$, $d_1 = 130.0$, $d_2 = 38.9$ and $\epsilon = 0.038\,\mathrm{hPa^{-1}}$. λ is the wavelength of a channel in μ m, p the pressure in hPa, T the temperature in K and e the water vapour partial pressure in hPa.

The refractivity is responsible for the bending of the LIO ray paths in the atmosphere as well as for the defocusing loss and is discussed below regarding its difference to microwave refractivity as felt by the LMO ray paths. How the refractivity is embedded in the propagation simulations using the geometric-optics ray tracer of EGOPS+xEGOPS is described in detail by Fritzer et al. (2010a).

Trace species absorption

The loss along the ray path due to trace species absorption is calculated by applying the Bouguer-Lambert-Beer law, which describes the attenuation of a signal when passing the absorbing air volumes:

$$I = I_0 \cdot \mathrm{e}^{-\tau} = I_0 \cdot \mathrm{e}^{-\int \alpha_\mathrm{m}(s)\mathrm{d}s}. \tag{2.2}$$

I_0 and I are the intensities before and after passing the atmosphere, respectively, and τ is the optical thickness, which is calculated via integration of the volume absorption coefficient $\alpha_\mathrm{m}(s)$ (in $\mathrm{m^{-1}}$) along the ray path s (in m). The integration in the EGOPS+xEGOPS system is done numerically by employing Simpson's trapezoidal rule in the ray tracer for approximating the integration along the path.

The absorption coefficient α_m at each ray path point is calculated by use of the Reference Forward Model (RFM), a line-by-line model which was developed under the lead of A. Dudhia, Univ. of Oxford, UK (Edwards 1996, http://www.atm.ox.ac.uk/RFM). This model was integrated via an interface subroutine into the xEGOPS system (Schweitzer, Kirchengast and Ladstädter 2007; Fritzer et al. 2010a, details in). It uses the absorption line parameters gathered in the High-Resolution Transmission (HITRAN) molecular absorption database (Rothman et al. 2005, 2009, distributed by the Harvard-Smithsonian Center for Astrophysics, Cambridge, MA, USA;) to model the absorption coefficients at

any given SWIR frequency. In the simulations prepared for this study, the HITRAN2004 database (Rothman et al. 2005) was used; the differences to the newer HITRAN2008 database (Rothman et al. 2009) have been checked and found very small and therefore not relevant for the results as discussed here. The pressure, temperature and trace species volume mixing ratio (VMR) profiles needed in the absorption coefficient modelling are taken from the FASCODE atmosphere model.

Aerosol extinction

The loss due to aerosol extinction is derived by integrating the aerosol extinction coefficient $\epsilon_{\mathrm{a}}(s)$ over the ray path following Equation 2.2 (practically by adding $\epsilon_{\mathrm{a}}(s)$ to $\alpha_{\mathrm{m}}(s)$ in the integrand). Thereby, $\epsilon_{\mathrm{a}}(s)$ is calculated using a semi-empirical model which we developed especially for xEGOPS (Schweitzer et al. 2008). Briefly, the model uses three climatologies for the aerosol extinction coefficient at a wavelength of 1020 nm, which we compiled on the basis of more than a decade of monthly data from the Stratospheric Aerosol and Gas Experiment II (SAGE II) instrument (Thomason and Peter 2006). The climatologies are two-dimensional fields containing 71 height levels (5 km to 40 km, 0.5 km steps) and 36 latitude bands (5° broad, 90° S to 90° N). The model interpolates to arbitrary latitude and height locations within these fields (and extrapolates beyond their boundaries in a meaningful way). The three climatologies reflect the atmospheric variability of the aerosol extinction coefficient in three typical aerosol conditions: background, medium, and volcanic aerosol load.

The extinction coefficient at other frequencies is derived from these climatologies by applying the so-called Ångström formula,

$$\epsilon_{\mathrm{a},\lambda} = \epsilon_{\mathrm{a},\lambda 0} \cdot \left(\frac{\lambda_0}{\lambda} \right)^{A}, \tag{2.3}$$

where $\epsilon_{\mathrm{a},\lambda}$ is the extinction coefficient (in m^{-1}) at the desired wavelength λ, $\epsilon_{\mathrm{a},\lambda 0}$ is the extinction coefficient tabulated/interpolated in the climatology (valid at $\lambda_0 = 1020\,\mathrm{nm}$), and A is the Ångström exponent. For the latter, we also developed a two-dimensional climatology (same latitude and height resolution as above) from the ratio of SAGE II extinction coefficient climatologies for the wavelengths of 525 nm and 1020 nm. Since the variation of this Ångström exponent depends comparatively weakly on the aerosol load, one climatology was considered sufficient.

With these settings, the empirical model is reasonably valid for calculation of aerosol extinction coefficients within 500 nm to 2500 nm; see in addition to (Thomason and Peter 2006) also Thomason and Taha (2003) for discussion of the SAGE II data. Details on how the climatologies have been compiled are presented by Schweitzer et al. (2008) and a detailed description of the aerosol model as implemented in xEGOPS can be found in Fritzer et al. (2010a).

Rayleigh scattering

The loss due to Rayleigh scattering is derived by integrating the respective scattering coefficient along the ray path following Equation 2.2 (practically by also adding the Rayleigh scattering coefficient $\sigma_r(s)$ to $\alpha_m(s)$). $\sigma_r(s)$ (in m^{-1}) is defined after Salby (1996) by

$$\sigma_r = \frac{32 \cdot \pi^3 \cdot (n-1)^2}{3 \cdot \lambda^4 \cdot N_{air}}, \tag{2.4}$$

where $n = 1 + 10^{-6}N$ is the refractive index, λ is the wavelength in m and N_{air} is the number density of the air in m^{-3}; details on how the Rayleigh scattering is implemented in xEGOPS are included in Fritzer et al. (2010a).

2.3 Results and discussion

2.3.1 Difference between IR and MW refractivity

As discussed in the introduction, the LMIO method exploits MW and SWIR signals which are simultaneously transmitted between two Low Earth Orbit (LEO) satellites. Since the atmospheric refractivity is slightly different for MW and SWIR frequencies, increasingly so in moist air, the signals propagate along somewhat different ray paths (as indicated in Figure 2.1). This leads to different tangent points (i.e., ray perigees) of the MW and SWIR propagation paths. Hence, profiles derived from LMO and LIO data are associated with a different tangent height grid when the measurements are taken at the same time grid. It is important to account for this difference in the retrieval of LIO products, which need the LMO retrieval results as input (Proschek, Kirchengast and Schweitzer 2011).

The main reason for the difference between the refractivities is that the MW refractivity significantly grows with increasing amount of water vapour while the SWIR refractivity is virtually independent of water vapour (Equation 2.1). This occurs because the water vapor (H_2O) molecules with their permanent electric dipole moment orientate themselves in the comparatively slowly oscillating electric field of the MW signals, leading to a significant orientation polarisation term (second term of Smith-Weintraub formula, see, e.g., Schweitzer et al. 2011), while the SWIR frequencies are too high for the dipole orientations to follow. As shown by Schweitzer (2010), presence of water vapour decreases the SWIR refractivity by less than 0.1 % at 5 km, even in very high moisture.

Favourably, the difference between the MW and SWIR refractivities is very small under most atmospheric conditions. This can be seen from Figure 2.2 which shows the relative difference of the refractivities in different representative atmospheric conditions for wavelengths between 1 μ m and 3 μ m. The MW refractivity is represented by the Smith-Weintraub formula (e.g., Schweitzer et al. 2011), the SWIR refractivity by the improved Edlén formula, Equation 2.1. The difference is very stable for wavelengths

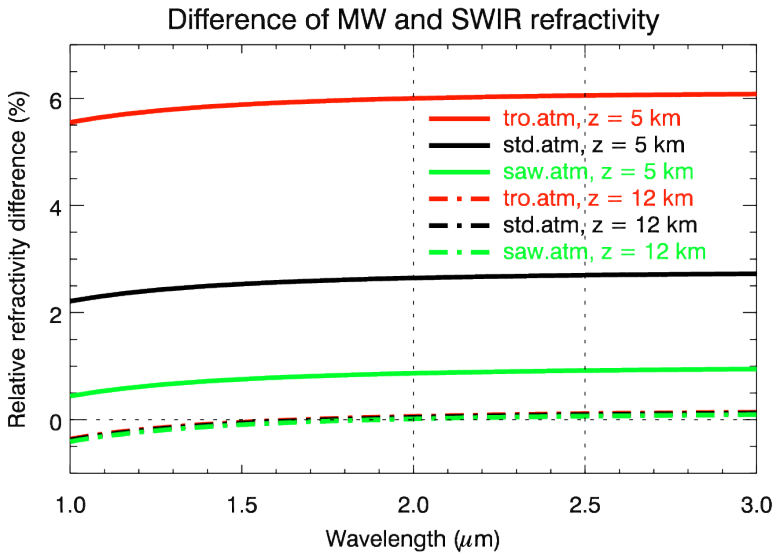

Figure 2.2: Relative difference between the MW refractivity (Smith-Weintraub formula) and the SWIR refractivity (improved Edlén formula). The differences are shown for the FASCODE TRO, STD and SAW atmospheres at 5 km and 12 km (atmospheric conditions, p/T/e in hPa/K/hPa, for TRO 5 km: 559.0/270.3/1.87; STD 5 km: 540.5/255.7/0.76; SAW 5 km: 515.8/240.9/0.22; TRO 12 km: 213.0/223.6/0.01; STD 12 km: 194.0/216.7/0.00; SAW 12 km: 176.6/217.2/0.00).

greater than about 1.6 μ m, which indicates that dispersive effects are minor in this spectral region. The region used by ACCURATE extends from 2 μ m to 2.5 μ m. The relative refractivity difference in this region is below 0.1 % for heights above about 9 km (high latitudes) to 13 km (tropics) (compare also Schweitzer 2010). Below, it grows depending on the moisture content up to about 1 % in subarctic winter (SAW) conditions, 2.75 % in standard (STD) and 6 % in tropical (TRO) conditions at 5 km.

These differences in the refractivities lead to different bending of the MW and SWIR ray paths. The MW rays are bent stronger than the SWIR rays (as depicted in Figure 2.1), which is why the MW tangent point heights are higher than the SWIR tangent point heights when comparing them at a specific time during the occultation event. In particular, the separation of the two tangent point heights at a given time related to a height of 5 km is about 0.15 km in SAW conditions, 0.5 km in STD conditions, and 1 km in TRO conditions. At a time related to around 10 km, the difference of the tangent point heights is already reduced to a few metres (about 5 m in SAW, 20 m in STD, 60 m in TRO). Above about 12 km to 13 km, the difference is negligible, i.e., within the vertical geolocation accuracy requirement of better than 10 m under all conditions (Kirchengast et al. 2010a).

Hence, the MW and SWIR parts of LMIO measurements can in principle be combined

directly above about 9 km to 13 km, using the MW heights also for the SWIR data. Below, the difference between the tangent point height profiles must be calculated and incorporated when retrieving LMIO products. Details of a respective algorithm are described by Proschek, Kirchengast and Schweitzer (2011), where, for completeness and for avoiding ad-hoc threshold heights near 13 km, the SWIR height grid is consistently determined over the complete occultation event height range, down to centimetre level differences of MW and SWIR heights. These residual differences of the slightly higher Smith-Weintraub refractivity in dry air compared to the improved-Edlén one (at the 5×10^{-4} level) are of no significant relevance since they are at the level of uncertainty of the empirical refractivity constants (see e.g., Healy 2011). Future refined estimates of the refractivity constants, or of the related molecular polarisabilities, at an accuracy of $< 1 \times 10^{-4}$ will be worthwhile in order to fully quantify the level of consistency of the MW and SWIR refractivities at this level of accuracy.

2.3.2 Influence of defocusing

Defocusing is attributable to changing vertical gradients, i.e., the second derivative, of the atmospheric refractivity. These changes cause differential bending and therefore divergence (sometimes, for limited time spans, convergence) of adjacent, initially parallel ray paths. Such divergence leads to an attenuation of the signal intensity (Kursinski et al. 2000), intermittent convergences lead to oscillations of defocusing loss.

Defocusing affects both, MW and SWIR signals, in the same way and leads to a significant loss reducing the SNR of the received intensity. Hence it is an important factor in computations of available SNR, especially in the troposphere. As visible in Figure 2.3, which shows examples of the defocusing loss in three representative atmospheric conditions, the loss typically reaches about 5 dB at 5 km and decreases upwards. Around 15 km, it is declined to about 3 dB and at about 30 km it falls below the lower useful-signal limit of 0.25 dB. The oscillating features in the profiles stem from strong temperature gradient changes around the tropopause leading to sharp changes of the vertical gradient of the refractivity. The dispersion of defocusing is negligible in the SWIR spectral range which is why the defocusing loss looks equal for all frequencies listed in Table 2.1. This negligible dependence on frequency is useful, since even though the SNR is somewhat degraded by the defocusing loss, its absolute influence can be eliminated in trace species retrieval simply by employing the differential transmission of channel pairs.

2.3.3 Influence of target species absorption

The term target species absorption names the portion of the molecular gas absorption in an LIO absorption channel induced by the species of interest (which is the species whose VMR shall be retrieved); all other species contribute to the unwanted, so-called foreign species absorption. Regarding LIO reference channels, all absorbing species are

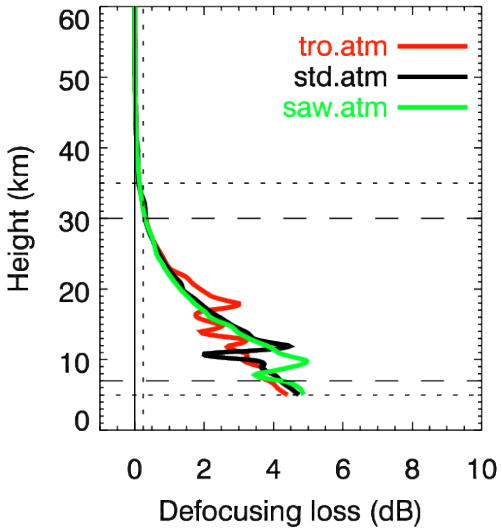

Figure 2.3: Defocusing loss for SWIR channels in the FASCODE SAW (green), STD (black), TRO (red) atmospheres. The vertical dotted line marks the boundary of the lower useful-signal limit of 0.25 dB. The horizontal dotted and dashed lines mark target and threshold requirements, respectively, regarding the vertical range within which trace species shall be retrieved (Kirchengast and Schweitzer 2011).

perturbing, which is why they are all considered foreign there, inducing foreign species absorption (which is in this case equal to the total gas absorption).

As discussed in Subsection 2.2.1, the target species absorption loss should fall within a certain favourable range (0.25 dB to 13 dB for the ACCURATE mission design) to ensure receiving good signal over noise, which can be exploited for accurate trace species retrieval. The lower boundary means to ensure sufficient signal (at least about 5 % absorption of transmitted signal), the upper boundary to ensure sufficient SNR (at least about 5 % of transmitted signal left after absorption). The total absorption of the reference channels should be as small as possible and contain the contribution of broadband far-line-wing or continuum absorption only, to minimise the influence of background absorption on retrieval products when using differential transmission.

Figure 2.4 presents the target species absorption for absorption channels and the total absorption for reference channels. Included are all 19 channels (13 channel pairs) listed in Table 2.1, which are part of the ACCURATE mission design.

Figure 2.4A shows the channels used to retrieve water vapour. Four absorption channels (H_2O-1, H_2O-2, H_2O-3, H_2O-4) are needed to cover the whole UTLS region and the atmospheric variability under all atmospheric conditions. The channel most sensitive to H_2O absorption, H_2O-1, is useful from about 13 km upwards to above 40 km under all atmospheric conditions. On the contrary, the least sensitive channel, H_2O-4, is useless in the UTLS in weakly moist conditions as SAW and STD. But it becomes important below about 7 km under wet TRO conditions (a detailed illustration of the sensitivities in different atmospheric conditions can be found in Schweitzer 2010). The medium-sensitive channels cover the region in between the outer channels, where H_2O-2 captures the altitudes from about 7 km to 10 km upwards (up to about 25 km), H_2O-3 becomes important below about 7 km to 10 km. Hence, the overlapping area of the medium sensitive channels is relatively small. This might result in slightly reduced but still high retrieval accuracy (within 4 % individual profile error; Proschek, Kirchengast and Schweitzer 2011) around 8 km to 10 km under unfavourable atmospheric conditions.

The reference channels used to retrieve water vapour (named by r-<species> in the figures) favourably show low sensitivity to atmospheric absorption. The absorption loss does not exceed 0.25 dB in the height ranges where they are employed. This applies also for the TRO and SAW conditions (cf. Schweitzer 2010).

Figure 2.4B shows the situation for the channels used to retrieve the three CO_2 isotopes carbon dioxide ($^{12}CO_2$), carbon dioxide first main isotope ($^{13}CO_2$) and carbon dioxide second main isotope ($C^{18}OO$). The sensitivities of the absorption channels cover the whole UTLS region, also in SAW and TRO conditions (Schweitzer 2010). Hence one channel for each species is sufficient to allow their retrieval under all atmospheric conditions. The sensitivities of the $^{13}CO_2$ and $C^{18}OO$ channels decrease very evenly with decreasing height and show very low sensitivity to ambient atmospheric (temperature, pressure) conditions. This behaviour is ideal from a scientific point of view since this minimises errors in the retrieval (e.g., errors from the LMO-retrieved pressure and temperature).

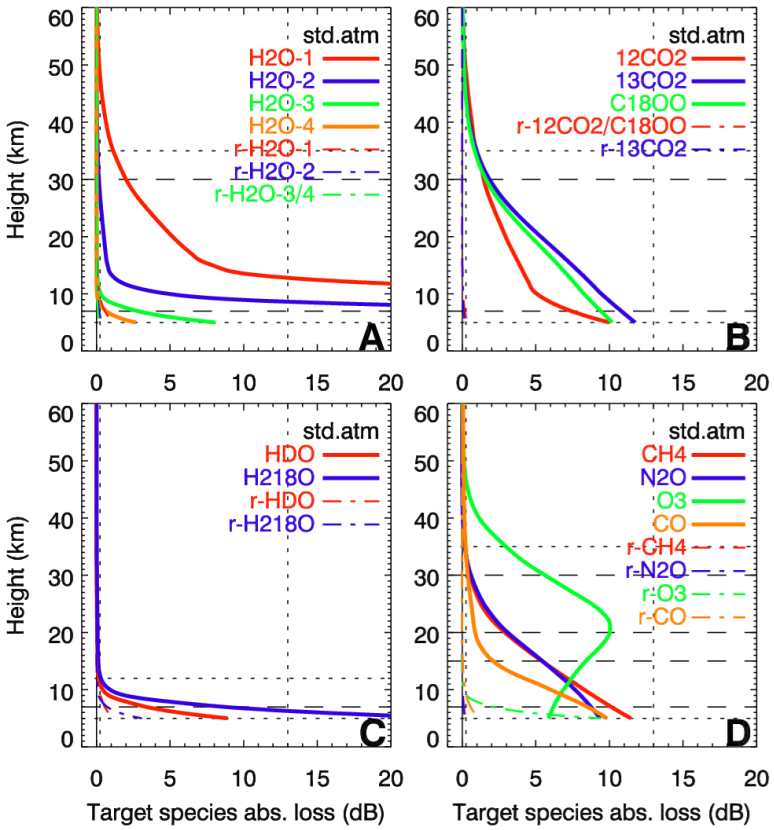

Figure 2.4: Target species absorption loss for the 13 absorption channels and total absorption loss for the six reference channels listed in Table 2.1. The situation is shown for the FASCODE STD atmosphere. Absorption channels are marked by solid lines, reference channels (at or near zero dB) by dashed-dotted lines. The vertical dashed lines mark the lower and upper boundary of favourable signal range. The horizontal dotted and dashed lines mark target and threshold requirements, respectively, regarding the vertical range within which trace species shall be retrieved.

The sensitivity of the $^{12}CO_2$ channel depends more significantly on the atmospheric conditions, especially on the temperature (Schweitzer 2010). This is because the lower state energy of the respective $^{12}CO_2$ absorption transition is rather high (it is still the best $^{12}CO_2$ line choice in the targeted SWIR range), which causes the transition to be notably dependent on pressure and temperature. Since pressure and temperature from LMO are expected to be very accurate (pressure better than 0.2 %, temperature better than 0.5 K; Schweitzer et al. 2011), the $^{12}CO_2$ VMR retrieval results will still be very accurate (Proschek, Kirchengast and Schweitzer (2011); for further improvement they can also be combined with $^{13}CO_2$ retrieval results).

The reference channels used to retrieve the three carbon dioxide (CO_2) isotopes have very low sensitivity to total atmospheric absorption. The loss exceeds 0.25 dB only very little below about 6 km to 7 km. The behaviour is very similar under all atmospheric conditions.

The channels used for retrieving the H_2O isotopes semiheavy water (HDO) and heavy-oxygen water ($H_2^{18}O$) are presented in Figure 2.4C. The vertical range of sensitivity of the absorption channels is quite limited in the STD atmosphere and also under SAW and TRO conditions (Schweitzer 2010). In particular, significant absorption only occurs below about 10 km to 12 km. This is due to the very low concentrations of HDO and $H_2^{18}O$ in the atmosphere and especially in the stratosphere. Below 10 km, the absorption steeply increases with decreasing height, for $H_2^{18}O$ a bit faster than for HDO. As a consequence, the absorption exceeds the upper limit of 13 dB already at heights slightly above 5 km and one must reckon that the signal is lost in moist air conditions. For example, the target species absorption of $H_2^{18}O$ exceeds the 13 dB limit at a height of about 8 km under TRO conditions.

The reference channels used for retrieving the H_2O isotopes also show a relatively high sensitivity to background absorption. This especially applies to the r-$H_2^{18}O$ channel, which reaches a loss of about 3 dB (SAW) to 8 dB (TRO) at 5 km (Schweitzer 2010). This absorption is mainly due to H_2O. The variability of the r-HDO channel is comparatively small; the absorption loss varies only within about 1 dB and 2 dB at 5 km, since the major part stems from the well-mixed species methane (CH_4).

All in all, the channels for measuring the H_2O isotopes are not ideal because of their vertical limitation in sensitivity and the relatively high influence of foreign species (cf. also Subsection 2.3.4). But these channels were the most suitable ones we could find for these isotopes in the SWIR 2 μ m to 2.5 μ m region. Therefore, the H_2O isotopes are considered as species of secondary interest in the ACCURATE mission concept. Meaningful retrieval of the VMR of these species is only possible within about 5 km to 12 km; this range is limited further in increasingly moist atmospheric conditions. However, since the upper tropospheric H_2O isotopes are important tracers of moistening and precipitation processes in the water cycle and measurements of them are rare, even these restricted profiles may have significant value for atmosphere and climate science.

Figure 2.4D shows the target species absorption losses for the channels used to retrieve

CH_4, nitrous oxide (N_2O), ozone (O_3) and carbon monoxide (CO). All four absorption channels show a very good sensitivity throughout the UTLS region under STD conditions. Since the variability is very small under different atmospheric conditions, this is also true in the SAW and TRO atmospheres (Schweitzer 2010). Characteristic is the behaviour of the O_3 absorption, which reflects the shape of the atmospheric O_3 concentration that peaks in the lower stratosphere.

The sensitivity of the reference channels r-CH_4 and r-N_2O to background absorption is very small. Their absorption loss is typically below 0.25 dB and exceeds this limit just marginally beneath about 6 km under TRO atmospheric conditions (Schweitzer 2010). In contrast, the r-O_3 and r-CO channels are significantly influenced by background absorbers. The r-CO is the same as the r-HDO channel and was already discussed above. The absorption of the r-O_3 channel is mainly caused by H_2O and therefore varies strongly under different moisture conditions; at 5 km from about 2.5 dB under SAW over 9.5 dB under STD to more than 20 dB under TRO conditions (see Subsection 2.3.4). Also the vertical variation is high and the loss steeply increases and exceeds the 0.25 dB boundary from about 10 km to 11 km downwards.

Overall the sensitivities of the absorption channels investigated here to the respective target species are very good (found most suitable by Schweitzer (2010) and Kirchengast and Schweitzer (2011) and used as the baseline for the ACCURATE mission; Kirchengast et al. (2010a)). They provide enough sensitivity to allow for accurate retrieval of eight trace species (H_2O, CO_2, $^{13}CO_2$, $C^{18}OO$, CH_4, N_2O, O_3, CO) throughout the UTLS region under all reasonable non-cloudy atmospheric conditions. Two further species, HDO and $H_2^{18}O$, which have a very low concentration in the atmosphere, can be retrieved within about 5 km to 12 km.

2.3.4 Influence of foreign species absorption

Regarding absorption channels, foreign species absorption means the portion of the molecular absorption which is induced by the sum of all foreign (background) species, which are all species except the target species of an absorption channel. Regarding reference channels, all absorbing species are foreign species, since in these channels any gas absorption should ideally be negligible.

Since foreign species disturb the absorptive signature of the target species, and thus may perturb the trace species retrieval, it is important to select channels which are as much as possible free from the influence of foreign species. In reality, however, foreign species absorption cannot be avoided entirely, which is why a second criterion for the selection of absorption and reference channels is that the influence of foreign species absorption is significantly reduced in the differential transmission. This means that the loss due to unavoidable foreign species absorption should be similar in the absorption and reference channels of a channel pair. The remaining differential foreign species losses should ideally be below 0.005 dB (corresponding to below 0.1 % differential absorption); a

hard criterion which can only be achieved at heights from about 15 km to 25 km upwards. In practice, one should therefore try to keep the differential foreign species absorption loss below 0.25 dB (below 5 %). The remaining influence can be co-modelled during the retrieval process to correct the residual foreign species absorption loss to the 0.01 dB level, with the remaining systematic error component below 0.005 dB (for details of this correction in trace species retrieval see Proschek, Kirchengast and Schweitzer 2011).

Figure 2.5 displays the foreign species absorption losses remaining in the differential transmissions for the selected channel pairs of Table 2.1. The behaviour is shown in the FASCODE STD atmosphere, which is well representative since dependence on ambient atmospheric conditions is weak for most species so that the losses are essentially the same as in the STD conditions (Schweitzer 2010). Differential foreign species absorption losses showing significant variability dependent on atmospheric conditions, which concerns O_3 and $H_2^{18}O$, are additionally illustrated in FASCODE SAW and TRO conditions in Figure 2.6.

Details which specific foreign species contribute to what degree to the foreign species losses are listed in Table 2.2. Practically speaking, for all those channel pairs being affected by no major influence of H_2O, the losses weakly depend on atmospheric conditions, since all other foreign species of relevance exhibit at any height level comparatively low variability of their concentration. O_3 and $H_2^{18}O$ channel pairs are those, where major influence of H_2O below about 10 km was unavoidable even for the best possible SWIR channel selections.

The residual foreign species absorption losses for the channel pairs used to retrieve H_2O are shown in Figure 2.5A. Their influence is negligible (i.e., losses below 0.005 dB) from about 20 km upwards. Below the losses gradually increase but stay within 0.25 dB in those height ranges, where the channels are used. That is the H_2O-2 channel pair, where the loss transgresses 0.25 dB at about 8 km, has its main range for contributing to H_2O retrieval from 8 km to 25 km (Proschek, Kirchengast and Schweitzer 2011). Dependence on ambient atmospheric conditions is weak for these channels as seen in Table 2.2; the major influence of HDO on H_2O-1 is restricted to below 10 km, which is outside the main range of this "stratospheric" H_2O channel that is exploited above 10 km only.

The residual foreign species losses for the channel pairs used to retrieve the CO_2 isotopes $^{12}CO_2$, $^{13}CO_2$ and $C^{18}OO$ are shown in Figure 2.5B. They are below 0.005 dB from about 15 km upwards. Below the losses increase but stay within the 0.25 dB boundary. The behaviour for the $^{13}CO_2$ and $C^{18}OO$ channel pairs is very stable under all atmospheric conditions (cf. Schweitzer 2010). Only the $^{12}CO_2$ channel shows a higher but limited sensitivity to atmospheric variability, leading to a differential foreign species absorption loss of up to 0.5 dB at 5 km under TRO conditions; the reason is some small influence of H_2O (Table 2.2).

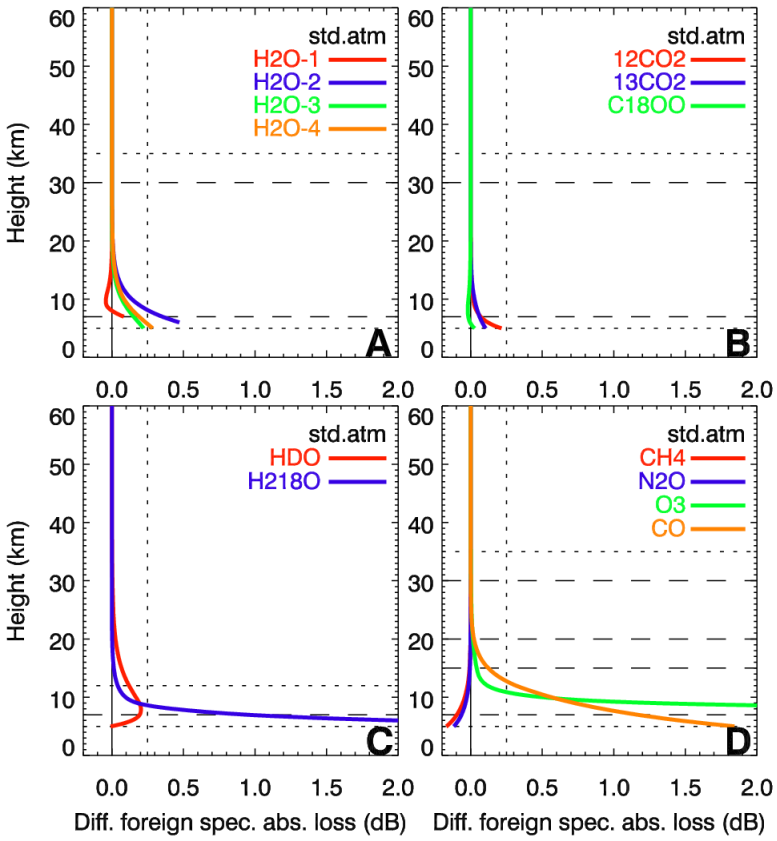

Figure 2.5: Differential foreign species absorption loss for the 13 channel pairs listed Table 2.1, for the FASCODE STD atmosphere. The vertical dotted line marks the boundary where the foreign species loss, if transgressing it, enters into the favourable range for target species loss. The horizontal dotted and dashed lines mark target and threshold requirements, respectively, regarding the vertical range within which trace species shall be retrieved.

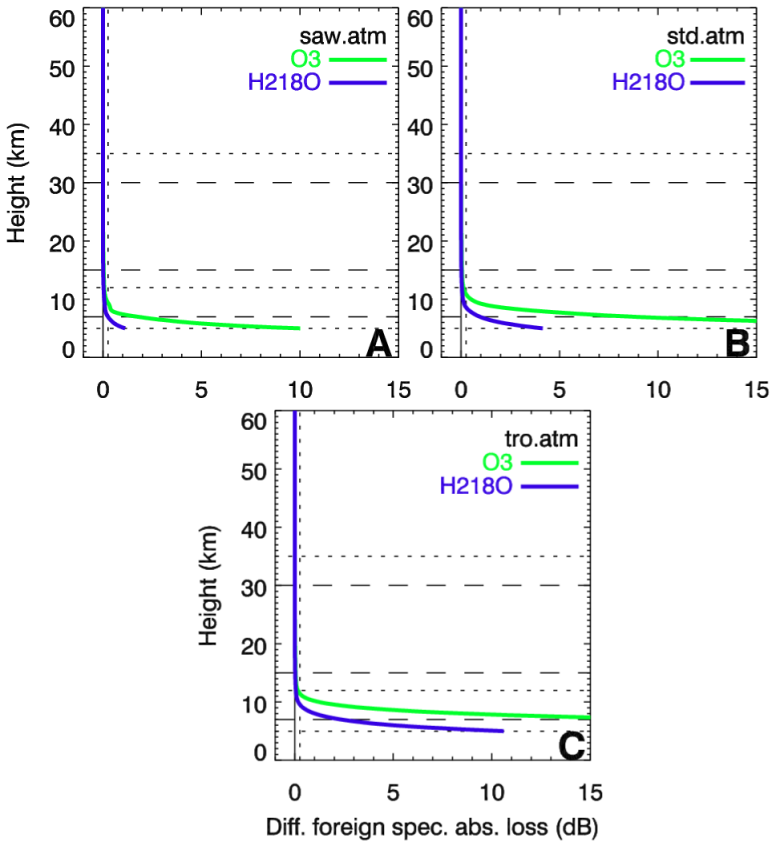

Figure 2.6: Differential foreign species absorption loss for channel pairs with significant sensitivity of foreign species loss to atmospheric conditions. The losses are shown in the FASCODE SAW, STD, and TRO atmospheres. The layout is the same as in Figure 2.5.

Table 2.2: Species mainly contributing to foreign species absorption, ordered according to their influence in FASCODE STD conditions at 5 km. Species without parentheses have major influence (larger or around 1 dB), squared brackets mark small influence (below 0.5 dB to 1 dB), round brackets very small influence (below 0.25 dB). These influence limits apply under all atmospheric conditions including TRO conditions.

Channel	Absorbing foreign species
H_2O-1	HDO, [CH_4], (CO)
H_2O-2	[$^{12}CO_2$, $C^{18}OO$]
H_2O-3	[N_2O], ($^{12}CO_2$)
H_2O-4	($^{12}CO_2$, $^{13}CO_2$, $C^{18}OO$)
$^{12}CO_2$	[H_2O, $C^{18}OO$]
$^{13}CO_2$	[$H_2{}^{18}O$], (H_2O)
$C^{18}OO$	($^{12}CO_2$, $^{13}CO_2$, H_2O)
CH_4	(H_2O)
N_2O	(H_2O)
O_3	H_2O, HDO, [$H_2{}^{18}O$], (CH_4)
CO	CH_4, [H_2O], (HDO)
HDO	CH_4, [H_2O]
$H_2{}^{18}O$	H_2O, [CH_4]
r-O_3	H_2O, (HDO)
r-$H_2{}^{18}O$	H_2O, [CH_4]
r-H_2O-1, r-HDO, r-CO	CH_4, [H_2O], (CO)
r-CH_4	(CH_4, H_2O)
r-N_2O, r-$^{13}CO_2$, r-H_2O-3/4	($^{12}CO_2$, $^{13}CO_2$, $C^{18}OO$)
r-$^{12}CO_2$, r-$C^{18}OO$, r-H_2O-2	($^{12}CO_2$, $C^{18}OO$, $^{13}CO_2$)

The residual foreign species losses for the water isotopes HDO and $H_2^{18}O$ are shown in Figure 2.5C. The loss resulting for the HDO channel pair is below 0.005 dB from about 25 km upwards, increases below to a maximum of about 0.2 dB near 7 km and decreases again beneath to near zero at 5 km. This is due to a different vertical behaviour of the foreign species absorption losses of the absorption and reference channel. Dependence on ambient atmospheric conditions is weak since the main influence stems from CH_4 (Table 2.2), which exhibits low variability globally. The foreign loss for the $H_2^{18}O$ channel pair stems mainly from H_2O, which is why this loss varies strongly under different atmospheric conditions as can be seen from Figure 2.6. The loss exceeds 0.005 dB from about 15 km downwards and reaches at 5 km about 1 dB under SAW, 4 dB under STD and 10.5 dB under TRO conditions. For this species it is thus particularly essential to co-model and correct the influence of the foreign species during the retrieval.

Figure 2.5D shows the residual foreign species losses for the channels used to retrieve CH_4, N_2O, O_3 and CO. The losses for CH_4 and N_2O are very small, exceeding the 0.005 dB boundary below about 15 km and reaching a maximum value of below 0.2 dB at 5 km. Dependence on atmospheric conditions is weak since cross-sensitivity to H_2O is very small (Table 2.2). The loss for CO is also very similar under all atmospheric conditions, even though this one exceeds the 0.25 dB boundary below about 13 km and reaches a value of near 1.9 dB under STD conditions (about 1.75 dB and close to 2 dB under SAW and TRO conditions; Schweitzer 2010), due to its cross-sensitivity to CH_4 (Table 2.2). The loss for O_3 is very small above about 9 km to 12 km but becomes very significant below, due to the strong cross-sensitivity of the O_3 channel pair to H_2O (Table 2.2). This strong foreign species absorption also reduces the SNR of these channels which is why in practice O_3 cannot reasonably be retrieved below about 10 km; highly accurate retrieval is possible above about 15 km which is the region of stratospheric ozone (Proschek, Kirchengast and Schweitzer 2011).

Overall we see that the differential foreign species absorption losses of most of the channel pairs is very small, with cross-sensitivities to foreign species being negligible in the stratosphere and generally still within 0.25 dB also at the UTLS bottom at 5 km. This is also a result of the substantial effort put into a careful SWIR channel selection process to find an ensemble of channel pairs as optimal as possible (Schweitzer 2010; Kirchengast and Schweitzer 2011). The residual influence of foreign species can be modelled and effectively corrected for, enabling very accurate trace species retrievals (individual-profile VMR errors within 1 % to 3 %), as discussed by Proschek, Kirchengast and Schweitzer (2011). For those species with substantial cross-sensitivities to H_2O below 10 km, $H_2^{18}O$ and O_3, the retrieval quality degrades in the upper troposphere, so that accurate $H_2^{18}O$ profiles may be bottom-limited to above about 7 km and accurate O_3 profiles to above about 10 km, respectively.

2.3.5 Influence of aerosol extinction

Aerosols, suspended non-H_2O particles in the atmosphere, can very effectively scatter and absorb radiation by Mie scattering/extinction (e.g., Salby 1996; Liou 2002). This results in some attenuation of LIO signals, though at the SWIR wavelength of interest $> 2\,\mu$ m the extinction is expected to be weak already since typical aerosol particle sizes are $< 1\,\mu$ m. The strength of the extinction depends on the concentration and size distribution of the aerosols. After major volcanic eruptions both concentration and sizes can significantly increase for a few months to about two years (Thomason and Peter 2006; Thomason and Taha 2003). Under non-volcanic conditions aerosol extinction of LIO signals in the UTLS will thus be weak but under post-volcanic conditions it may increase.

We used the aerosol extinction model described in Subsection 2.2.2 to assess the magnitude of aerosol extinction of LIO signals, which is one potentially important

background influence on top of defocusing (Subsection 2.3.2). Figure 2.7 shows the results from background aerosol load to post-volcanic load (top to bottom), both for the extinction loss in LIO channels directly (left column) and for the residual extinction loss in the differential transmission of channel pairs (right column). The selected channel pairs are representative of the SWIR range covered by LIO, from the low-wavelength end ($C^{18}OO$) to the the high-wavelength end (O_3), with one pair (CH_4) mid-range. The spectral spacing of the absorption and reference channel is smallest for the $C^{18}OO$ channel pair and highest for the CH_4 one (cf. Table 2.1).

As can be seen, the aerosol extinction loss as well as its signature in the differential transmission are very similar under background and medium aerosol load. The direct loss is small; it exceeds 0.25 dB only below about 8 km to 10 km and reaches a maximum of near 1 dB at 5 km. Since the wavelength dependence of the aerosol loss is weak (linear only; see Equation 2.3), the differential aerosol extinction loss stays negligible below 0.005 dB in all these non-volcanic conditions, including for the CH_4 channel pair with largest channel spacing (0.5 %). The influence of volcanic aerosol on direct LIO transmissions, however, is estimated to be clearly observable and to increase quickly from about 25 km downwards until it remains at a level of about 2 dB to 3 dB below about 15 km. The differential aerosol extinction loss can remain below 0.005 dB also in volcanic aerosol load, if the spectral spacing of absorption and reference channel is very small (< 0.1 %), as for the $C^{18}OO$ channel pair. If the spectral separation is higher, residual influences of the aerosol extinction under volcanic load reach up to about 0.02 dB as seen for the CH_4 channel pair that represents the largest spacing of LIO channel pairs of 0.5 % (cf. Table 2.1).

Since the direct aerosol loss transgresses into the favourable signal range of > 0.25 dB below about 7 km to 22 km (depending on the aerosol load), it is possible to retrieve aerosol extinction loss and extinction coefficient profiles under such higher load conditions by a suitable algorithm (exploiting transmissions of reference channels, especially of the ones of the CO_2 isotopes near 2.1 μ m which are both very clean from gas absorption and at the low-wavelength end with relatively best sensitivity to aerosol extinction). Any residual potentially bias-like influence on trace species retrieval that would be > 0.005 dB can then be corrected for based on the retrieved extinction loss profiles. Since we can reasonably expect an accuracy of at least about 20 % of these retrieved profiles, residual losses of about 0.02 dB under volcanic load conditions for channels with largest spacing of 0.5 % can thus be well corrected for to negligible residuals below 0.005 dB. The degradation of overall SNR by up to about 3 dB under volcanic load will increase the statistical error in retrieved trace species profiles only in a minor way and have no impact on residual systematic error.

In summary the LIO technique is thus expected to deliver robust trace species retrieval of climate benchmarking quality also through episodes of volcanic aerosol load in the UTLS such as occurred in the post-Pinatubo years (1992/1993, Thomason and Peter 2006). Given that we used an empirical model for scaling aerosol extinction coefficients measured

near 1 μ m to the 2 μ m to 2.5 μ m range (see model description in Subsection 2.2.2), it will be useful to undertake further assessments of aerosol influence with potentially more sophisticated models in the future. From the construction of the Ångström coefficient in our model we estimate the results here are tentatively conservative; future more sophisticated estimates may find somewhat less aerosol influence.

2.3.6 Influence of Rayleigh scattering

The influence of Rayleigh scattering on LIO signals is shown in Figure 2.8 both for direct-channel losses (left) and residual loss in differential transmissions (right). The same representative channel pairs are shown as used above for the aerosol extinction loss, located at the lower end ($C^{18}OO$), in the middle (CH_4) and at the upper end (O_3) of the SWIR wavelength range, and representing spectral spacings of channels from $< 0.1\,\%$ to $0.5\,\%$. Recall that Rayleigh scattering includes a λ^{-4} dependence on wavelength (Equation 2.4).

As can be seen, the losses due to Rayleigh scattering are very small. The direct loss increases with decreasing wavelength and reaches a maximum of about 0.04 dB to 0.08 dB at 5 km. This is far below the 0.25 dB boundary. In the differential transmissions, the influence is further reduced to about 0.001 dB or below; the residual becomes smaller, the smaller the spectral spacing of channels is. Since Rayleigh scattering depends on air density and refractivity which show at any height level fairly low variability globally, the behaviour under SAW and TRO conditions is closely the same as under the STD conditions shown.

Overall it is very clear from these results that the influence of Rayleigh scattering loss on trace species retrieval from LIO signals is negligible at all heights under all atmospheric conditions.

2.3.7 Total atmospheric loss and resulting intensity

The sum of all atmospheric influences investigated above, the so-called total atmospheric loss of LIO signals, is illustrated in Figure 2.9. As in Figure 2.4 for target species absorption loss, the total losses are shown here under FASCODE STD atmosphere conditions for all 19 channels listed in Table 2.1. Regarding aerosol extinction, medium aerosol load was assumed.

The total atmospheric loss profiles reflect very well the different atmospheric influences and at the same time neatly show the total signal. The main part of the loss of absorption channels stems from the target species absorption as is desired. Defocusing loss yields also a significant contribution, especially below about 25 km, and is the main loss in reference channels. The variability of the total atmospheric loss is mainly determined by the variability of the target species absorption loss and for some species partly also by the foreign species absorption loss. Hence, the absorption channels used to retrieve the CO_2

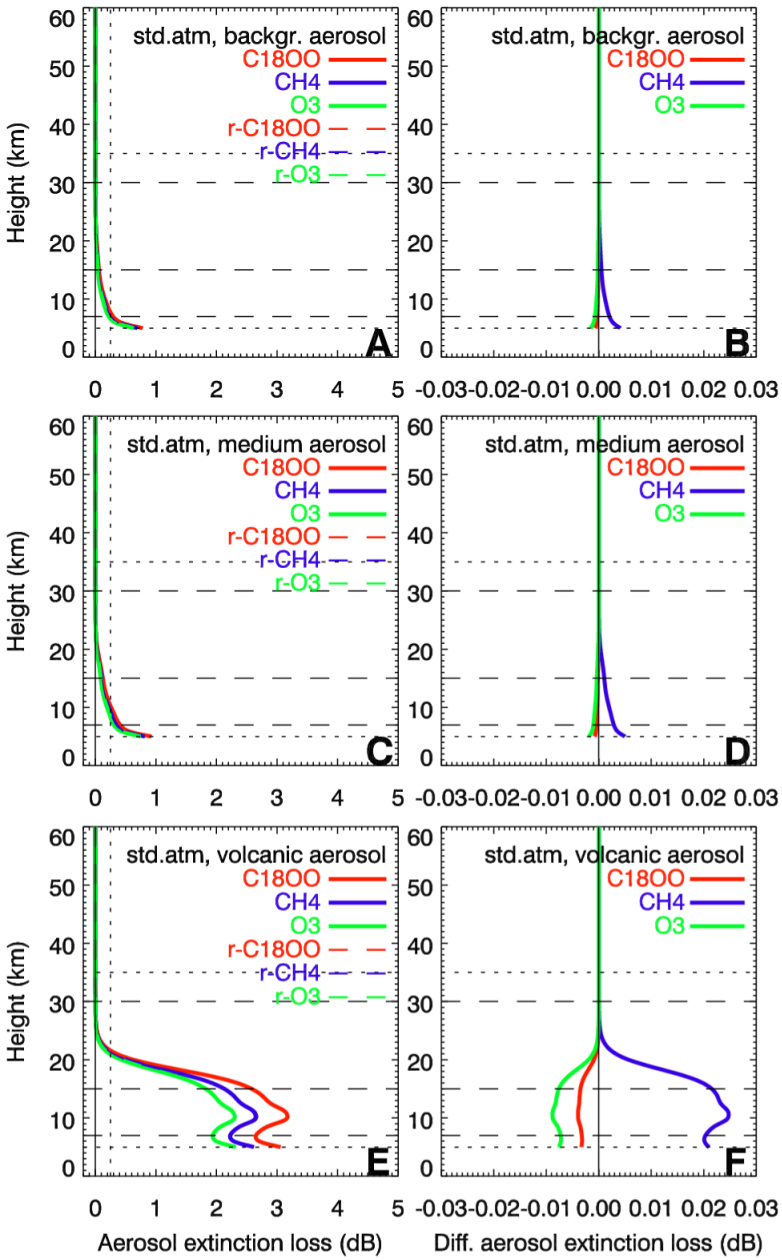

Figure 2.7: Aerosol extinction loss (A, C, E) and differential aerosol extinction loss (B, D, F) for three representative channel pairs with different spectral separation under FASCODE STD atmosphere conditions for background (A, B), medium (C, D), and volcanic (E, F) aerosol load. The vertical dotted line marks the boundary where the extinction loss, if transgressing it, enters into the favourable range for target species loss. The horizontal dotted and dashed lines mark target and threshold requirements, respectively, regarding the vertical range within which trace species shall be retrieved.

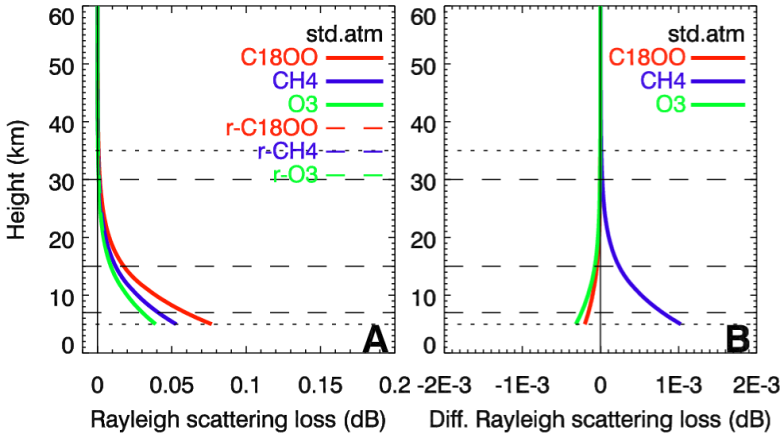

Figure 2.8: Rayleigh scattering loss (A) and differential Rayleigh scattering loss (B) for three representative channel pairs with different spectral spacings, for FASCODE STD atmosphere conditions. The layout of the panels is the same as in Figure 2.7.

isotopes, CH_4, N_2O, O_3 and CO show very weak atmospheric variability, whereas the other channels show medium to strong variability under different atmospheric conditions, which is primarily caused by H_2O variability (cf. Subsection 2.3.4); note that Schweitzer (2010) shows results regarding total atmospheric loss also for SAW and TRO conditions. The influence of the medium-load aerosol extinction is too small to be directly visible, the influence of Rayleigh scattering is negligible.

As discussed in Subsection 2.2.1, the total loss of the absorption channels should not exceed 21 dB (in compliancy with the ACCURATE mission design) to guarantee enough SNR of the LIO signals at the receiver. This requirement is evidently fulfilled by almost all channels under all atmospheric conditions in their designated height range (the H_2O-1 and H_2O-2 channels in Figure 2.9A have the bottom-limit of their main range at 13 km and 8 km, respectively, and are thus not needed below in retrievals; Proschek, Kirchengast and Schweitzer 2011). Therefore the respective target species can basically be retrieved within the whole UTLS region (5 km to 35 km), with bottom-limit constraints due to H_2O cross-sensitivity below 10 km for O_3 and $H_2^{18}O$ (cf. Subsection 2.3.4; visible also in Figure 2.9C and D), and top-limit constraints for the water isotopes HDO and $H_2^{18}O$ for which sensitivity reaches up to about 12 km only (cf. Figure 2.4).

Based on the total loss results, Figure 2.10 finally depicts the behaviour of the LIO signal power reaching the receiver detectors (upper panel axes) and the receiver SNR (lower panel axes). The signal power is the actual observable of interest from which also retrieval processing in an end-to-end simulation framework will start (after in addition accounting for observation system/instrumental errors; see, e.g., Proschek,

Kirchengast and Schweitzer 2011, Figures 4a and 5a therein). The received signal power is determined by subtracting the total atmospheric loss from the unattenuated top-of-atmosphere power reaching the receiver detectors, P_0, which is typically composed of the transmitted power minus all geometrical and instrumental losses caused by the observing system (e.g., propagation loss due to signal spreading, optical losses). The SNR at the receiver is then determined from the received signal power and the NEP of the detection system. Kirchengast et al. (2010a) and Kirchengast and Schweitzer (2011) discuss these LIO link budget aspects in detail and show that for the ACCURATE system design a top-of-atmosphere power $P_0 = -94\,\mathrm{dBW}$ (for each individual received laser pulse signal with the signals being received at a 50 Hz basic sampling rate) and a top-of-atmosphere $\mathrm{SNR}_0 = 34\,\mathrm{dB}$ (at 2 Hz sampling rate corresponding to about 1 km to 2 km vertical resolution) are adequate baseline values.

We thus adopted these values for Figure 2.10 here in order to discuss the results for the total atmospheric loss in terms of actual LIO observables, important to understand also the approach to mitigate the influence of some of the other atmospheric effects discussed below. From the P_0 and SNR_0 values we see that the unattenuated LIO laser pulse signal power detected is about 400 pW and that the associated signal-to-noise ratio is about 500 at the basic 50 Hz sampling rate (2500 at a 2 Hz sampling rate). This implies a detector noise level of only about 0.8 pW, providing even individual pulse signals at high SNR. In order to keep good basic accuracy, signal power should not fall below a few pW (say 3 pW, or −115 dBW, or 6 dB raw SNR) even if all atmospheric loss effects are in action below 10 km. This implies that the effective SNR at 2 Hz sampling rate, reflecting the final resolution for use of the data, should not fall below 13 dB as discussed in Subsection 2.2.1 and as marked in Figure 2.10C and D. As can be seen in Figure 2.10, all channels selected fall into the favourable range (with the upper-troposphere limitations for O_3 and the H_2O isotopes discussed above and visible in panels C and D).

Therefore, if the LIO technique is implemented to meet at least the specifications of the ACCURATE system design baselined here, the available SNR provides enough sensitivity to enable retrieval of the ten target trace species with high accuracy under all atmospheric conditions. In order to learn which level of retrieval performance can be achieved, Proschek, Kirchengast and Schweitzer (2011) started with LIO observables of the quality as discussed here. They found individual-profile retrieval errors within 1 % to 3 % and that the retrieved profiles are obtained essentially without biases. Kirchengast and Schweitzer (2011) estimated this performance already before using a simplified estimation process. See those studies for details.

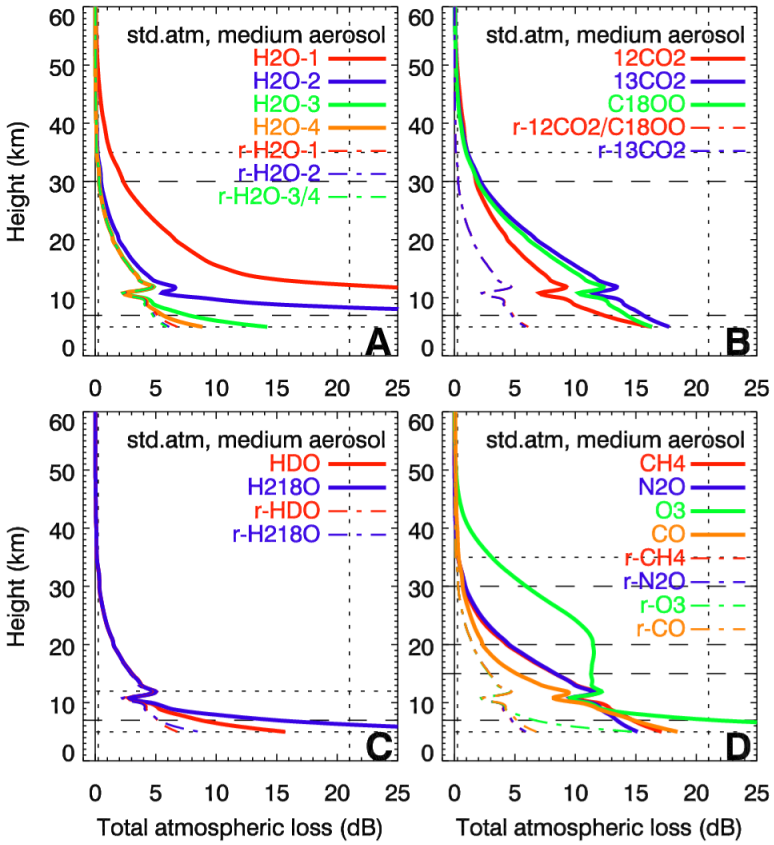

Figure 2.9: Total atmospheric loss for the 13 absorption channels and the six reference channels listed in Table 2.1, for the FASCODE STD atmosphere and medium aerosol load. The layout of the panels is the same as in Figure 2.4.

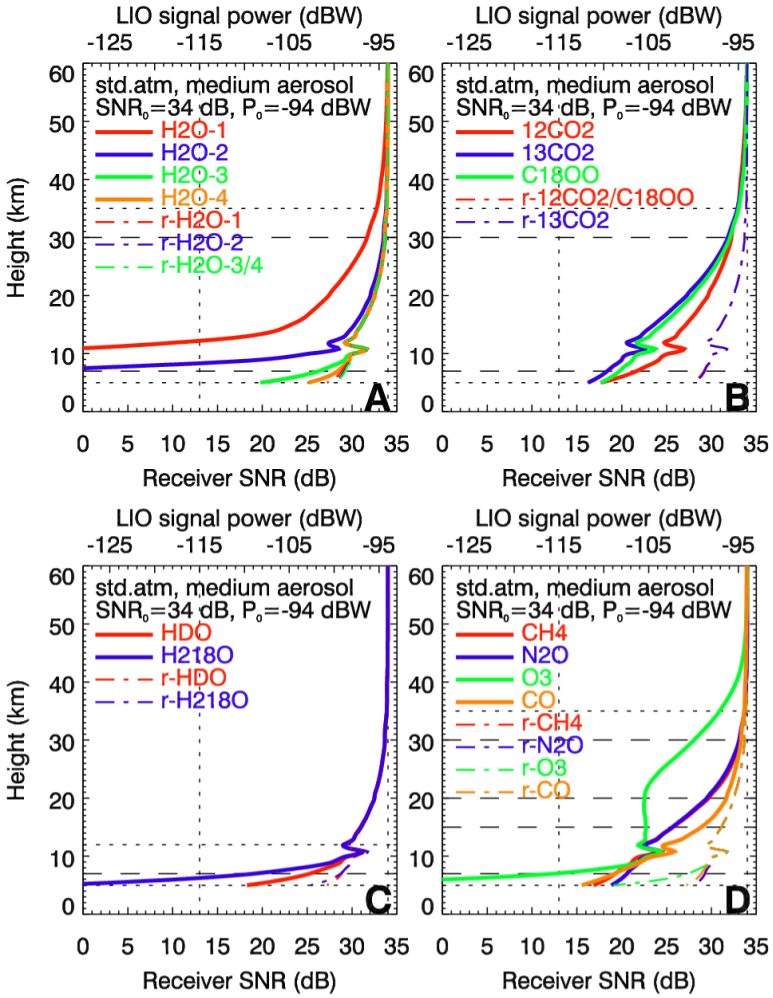

Figure 2.10: Received signal power (upper axes) and receiver SNR for the channels listed in Table 2.1 on the basis of adopting a top-of-atmosphere power of −94 dBW and a corresponding SNR of 34 dB, both being baseline values of the ACCURATE mission design. The results are shown for the FASCODE STD atmosphere and medium aerosol load. The layout of the panels is the same as in Figure 2.9.

2.3.8 Comments on further atmospheric effects

Clouds

Clouds affect the intensity of received LIO signals in two ways. On the one hand, their SWIR extinction coefficients are high, leading to strong cloud extinction loss which fully blocks the signals except for very thin or small (cirrus) clouds. On the other hand, clouds may scatter solar radiation towards the receiver, leading to an amplification of the detected signal, but this effect is very small (about 0.5 to 3.5 $\mathrm{mW\,m^{-2}\,nm^{-1}\,sr^{-1}}$; Emde and Proschek 2010); see the separate comments on scattered solar radiation below.

For liquid water clouds, the cloud extinction can be described by the Mie theory, since the microphysical properties of water clouds (like water content, size and shape of droplets) are not difficult to describe (Hu and Stamnes 1993). The extinction due to ice water clouds is more complicated, since ice particles can have many different sizes and shapes, which is why various parametrisations exist to describe their extinction coefficients and other optical properties (e.g., Key et al. 2002).

Investigations by Emde and Proschek (2010) showed that typical liquid water clouds induce a loss of much more than 30 dB in LIO intensities, which effectively corresponds to a full blocking of signals (see the requirements for adequate SNR in Subsection 2.3.7 above). Also ice water clouds are usually not transparent, except for very thin cirrus clouds with an ice water content at the $1 \times 10^{-3}\,\mathrm{g\,m^{-3}}$ level (assuming an along-path extension of several 10 km). They induce an extinction loss of up to about 10 dB and hence still allow to retrieve trace species through the clouds under degraded SNR. Details of these studies will be published elsewhere.

For the common cases in which clouds will block the LIO signals, the LMIO technique by design has the LMO signals continuing to track through clouds (so as to retrieve the thermodynamic variables through clouds) and also has the reception sequence of LIO signals continuing to work independent of clouds interfering in propagation paths of individual laser pulse signals. This is because the LIO receiver telescope has accurate pointing independent of received signal; the received LIO signal power will simply fall back to background levels for those pulse signals that have been blocked by cloud extinction. This also implies that the blocking of individual pulses does not affect the quality of pulses before and after so that any LIO pulse signal is received basically at clear-air quality if it somehow found a "hole" in intermittent cloudiness (note that the Fresnel diameter of the SWIR laser signals is about 3 m only so that the received power of individual pulse signals propagates along highly confined propagation "tubes"; Kirchengast and Schweitzer 2011). In this way, high-quality target species transmission values can be retrieved, with gaps, across layered cloudiness, where profiles of cloud layering are a byproduct flagging the gaps. Interpolating over limited gaps then allows trace species retrieval of still high quality. An overview of cloudy air retrieval, the developments of which are currently on-going, is provided by Schweitzer, Proschek and Kirchengast (2010).

The influence of clouds on the tropospheric penetration of atmospheric profiles retrieved from LIO was so far roughly estimated, as a worst case limit, from analysing solar occultation data of the Canadian Atmospheric Chemistry Experiment (ACE) satellite (Harrison and Bernath 2010, including G. C. Toon, Jet Propulsion Lab., CA, USA, pers. communications, 2009). These data show that about 40 % of all measured profiles reach down to about 7.5 km, 20 % reach even down to about 5 km. Exception is a tropical band within 15° of the equator, where only 20 % of the profiles reach down to about 7.5 km. It is expected that LIO data have an improved vertical coverage into the upper troposphere due to their capability to penetrate intermittent cloudiness as outlined above.

Turbulence

Atmospheric turbulence is associated with random variations of the refractive index, which in turn affect optical beams. This occurs because the intensity of a beam is multiply diffracted on small-scale air density irregularities. One relevant effect is intensity fluctuations of the beam, also called scintillation, which is caused by random redistribution of the energy within the cross section of the beam, another one additional spreading of the beam (beyond the spreading caused by the pure refraction).

First estimations by Sofieva (2009) and Horwath and Perlot (2008), details of which will be published elsewhere, show that the influence of scintillation on single LIO channels is rather high, as is for example known from stellar occultation data like the GOMOS instrument on Envisat (Kyrölä et al. 2004). In particular, the relative intensity fluctuations rapidly grow with decreasing altitude, nearly proportional to air density, from about 0.05 near 30 km up to the saturation level of about 1 below about 20 km. Saturation occurs, when a signal is repeatedly scattered along a (long) propagation path.

Fortunately the correlation of the scintillations at closely spaced frequencies is very high since spectrally adjacent channels essentially avoid dispersive effects and therefore signals pass through the same air density irregularities. The adverse influence of scintillation can thus be largely removed by application of the differential transmission retrieval approach with sufficiently closely spaced channels. Sofieva (2009) recommends a frequency separation of a channel pair of up to 0.5 % only, which could be realised in the ACCURATE design by careful channel selection (Table 2.1). This strict closeness is required because the relative error in the differential transmission rapidly grows with increasing wavelength separation, due to the slight chromatic shift of the signal path of the absorption relative to the reference channel, since the infrared refractivity is still slightly dispersive at $> 2\,\mu$ m (Subsection 2.2.2, Equation 2.1). For example, at a 50 Hz sampling rate the residual scintillation error in the differential transmission for channels near $2.1\,\mu$ m with a separation of 0.1 % was estimated to be at an acceptable level of only about 1 % to 1.5 % near 10 km and about 1.5 % to 2.5 % near 5 km, while at a separation of 1 % it would already be about 10 times as large. This error is a statistical error with negligible bias component. Most of the channel pairs of the ACCURATE design have a spectral

separation of less than 0.1 % to 0.25 %, the largest separations are 0.5 % (Table 2.1); the latter implying about five times the error of 0.1 %.

The residual scintillation error can be mitigated further by a factor of 5 or more if the slight chromatic shift between the ray paths of the channels is compensated for based on a slight time shift of transmitting the absorption channel pulses relative to the reference channel pulses, to ensure close alignment of the ray paths and thus higher correlation of the scintillation noise (Sofieva 2009). This can be implemented using knowledge on the atmospheric refraction profile during occultation events, where the required 20 % accuracy is readily achievable (or outperformed) in the UTLS (Kirchengast et al. 2010a). The chromatic shift compensation is estimated to effectively reduce the residual error for channels spaced by 0.5 % to at least the error level of channels spaced 0.1 % only.

Wind

Wind sets air molecules in motion, which is why they are moved towards or away from the transmitter. Hence the frequency seen by the molecules differs slightly from the one being transmitted, according to the Doppler effect. The molecules thus absorb this slightly shifted frequency. Since absorption lines in the SWIR spectrum are very narrow, this shift is visible for absorption channels in form of slight transmission changes.

Practically the effect is very small when considering the centre of absorption lines, which is why the influence of wind needs only be very roughly accounted for when working with line centres as done for trace species retrieval. Typical meridional winds, the winds dominating for polar or near-polar LEO-LEO configurations, have speeds of less than $30\,\mathrm{m\,s^{-1}}$. This leads to a relative frequency shift of about 10^{-7}. As a representative example, such a line of sight wind speed would in case of the $C^{18}OO$ line lead to a reduction of the transmission by about 0.03 dB at 10 km and 0.01 dB at 30 km, relative to the centre of the line probed in case of zero wind speed. Background knowledge of the wind speed with about $10\,\mathrm{m\,s^{-1}}$ uncertainty (available, e.g., from atmospheric analyses or short-range forecasts) is thus estimated to be sufficient to enable accurate trace species retrieval with systematic error residuals below 0.005 dB.

The effect is about 10 times larger when considering the inflection points of an absorption line where the spectral gradient of transmission is strongest. Using dedicated LIO signals at such inflection points of a highly symmetric absorption line, which is at the same time stable under different atmospheric conditions, can thus be used to retrieve the line-of-sight wind speed (Kirchengast and Schweitzer 2011). This capability is an integral part of the ACCURATE concept (Kirchengast et al. 2010a). In essence, it is the differential transmission between the two inflection points that is exploited, where the $C^{18}OO$ line turned out as a particularly suitable line (Schweitzer 2010; Kirchengast and Schweitzer 2011). The retrieved LOS wind speed profile can then be used to correct the small off-centre Doppler shifts in the trace species retrieval discussed above, eliminating the need for background knowledge of wind speed from an external atmospheric field.

More details on the LIO wind capability can be found in Schweitzer (2010).

Scattered solar radiation

Solar radiation can be scattered into the receiver telescope either by Rayleigh scattering due to clear air or by particle (Mie-type) scattering due to clouds. Since the SWIR range of interest ($2\,\mu$ m to $2.5\,\mu$ m) is intentionally located as far as possible in the long-wavelength tail of the solar Planck radiation spectrum, the intensity is already low (see, e.g., Liou 2002) and scattering influences are thus to be expected very small. Aerosol-scattered solar radiation is negligible since concentrations are significantly too small and wavelengths too long.

From error budget analyses we estimated that the Rayleigh-scattered solar radiation captured by the telescope during any single pulse measurement is, for the ACCURATE design described by Kirchengast et al. (2010a), below the receiver noise level (about 0.8 pW; cf. Subsection 2.3.7) and thus negligible. This holds over the whole UTLS also during all conditions of bright day; it reaches the 0.1 pW level but stays below 0.5 pW also at the UTLS bottom near 5 km for the shortest relevant wavelengths near $2.1\,\mu$ m. Details will be published elsewhere. We note for completeness that also scattering (or other radiation) from surface sources is negligible, since the telescope will observe downwards to minimum tangent altitudes of 2.5 km only where no surface radiation can enter the Field of View (FOV) of the telescope. Likewise, in the case of direct sun, a geometrical situation which rarely occurs when using near-polar orbiting satellites as in the ACCURATE concept, the receiver will be shielded from this strong signal to protect the instruments. This will ensure that indeed only scattered solar radiation can enter the telescope.

Other than for Rayleigh scattering, cloud-scattered solar radiation is estimated to be observable under certain conditions (Kirchengast et al. 2010a; Emde and Proschek 2010). Relevant influence can arise in particular from clouds fractionally covering the FOV of the telescope, e.g., from cloud edges near cloud top or bottom (if there is full cloud blocking of the LIO signal, the influence will not be relevant). During bright day, this scattering could sometimes exceed the detector noise level of about 0.8 pW, but is estimated to stay within a factor of ten of this level. Such an influence is still small given a basic signal strength at the 100 pW level (cf. Subsection 2.3.7). Moreover it is foreseen to be rigorously controlled, and as necessary corrected for, by a receiver design including a close time spacing of interleaved laser-pulse and background signals within 5 ms (Kirchengast et al. 2010a).

Briefly, this design includes that before and after each laser pulse signal measurement also a background measurement is performed within ± 2.5 ms. This corresponds to a vertical shift of within ± 5 m, given typical scan velocities of occultation events, so that the receiver telescope with a FOV of about 3 km vertical extend at atmospheric tangent point sees essentially the same scattering scene both for the pulse and background

measurement. The background measurement thus enables rigorous control of the SNR of each single received pulse, for optimal quality independent of whether scattered radiation is available above receiver noise level or not. The background measurement is furthermore planned at multiple detection pixels adjacent to the pulse measurement so that in case the background power is needed to be subtracted an average can be subtracted which only insignificantly increases the noise in the background-corrected pulse signal. Also on this topic of cloud scattering details will be published elsewhere.

Terrestrial thermal radiation

The SWIR spectral range is located at the short-wavelength side of the Planck spectrum of Earth's thermal radiation (e.g., Liou 2002). Since these short wavelengths see an exponential falloff of the thermal radiation spectrum with its maximum near $10\,\mu$ m, the radiation at $< 2.5\,\mu$ m is already very small. We estimated its influence by means of worst case values of the thermal radiation entering the receiver telescope, where we used a temperature of 280 K, because UTLS temperatures are typically below, and an upper-end wavelength of $2.5\,\mu$ m. The estimated power turns out to be always at most near 0.01 pW, which is far below receiver noise level (0.8 pW). Hence, terrestrial thermal radiation is negligible in a mission design like ACCURATE.

2.4 Summary and conclusions

In this study we discussed atmospheric influences on SWIR laser signals which are transmitted between two LEO satellites in occultation geometry. Such an occultation system is called LIO and primarily aims at providing accurate profiles of atmospheric trace species, especially of greenhouse gases, and of LOS wind speed. Other retrieval products can be profiles of cloud layering, aerosol extinction coefficient, and turbulence strength. LIO is part of the LMIO method, recently introduced by Kirchengast and Schweitzer (2011), where the above profiles are determined in synergy and consistent with thermodynamic profiles (pressure, temperature, humidity) from LMO signals. A detailed mission concept for implementing the LMIO method, the ACCURATE mission proposed by Kirchengast et al. (2010a), was used as baseline mission design for this study.

Quasi-realistic propagation simulations have been used to investigate the atmospheric influences on LIO signals and their implications for the total received LIO signal power. The EGOPS/xEGOPS simulation system (Fritzer et al. 2010a,b) was used for this purpose, where we recently included algorithms and databases for modelling the infrared refractivity, trace species absorption, aerosol extinction, and Rayleigh scattering that we used in this study. Functionality for simulating the influence of clouds, wind, and turbulence has been included as well; it aided understanding of related effects briefly discussed in this study but details will be published elsewhere.

Most of the influences have been assessed by means of simulation results for the set of 19 SWIR channels that are the basis for the ACCURATE mission design. Defocusing loss, target species absorption loss, foreign species absorption loss, aerosol extinction loss, Rayleigh scattering loss as well as the sum of all these losses were mainly shown for FASCODE STD atmosphere conditions, which represents average atmospheric conditions, and compared with the results in more extreme atmospheric conditions, namely the dry and cold FASCODE SAW and the warm and moist FASCODE TRO atmospheres. These three atmosphere settings served to represent the basic range of atmospheric variability.

The influence of refractivity was considered in view of its different effect on MW and SWIR ray paths, resulting in different ray bending and thus tangent point heights of LIO and LMO signals. Further atmospheric effects—the influence of clouds, turbulence, wind, scattered solar radiation and atmospheric thermal radiation—were discussed in an introductory manner, referring to several recent grey literature reports; detail results to these ends will be published elsewhere.

We established that the set of SWIR channels of the ACCURATE mission provides very good sensitivity to target species absorption. In particular, eight species (H_2O, CO_2, $^{13}CO_2$, $C^{18}OO$, CH_4, N_2O, O_3, CO) can be acquired within the whole UTLS region under all atmospheric conditions, except for lower-limit constraints for O_3 the signal of which can become obscured below 10 km. For two further species, HDO and $H_2^{18}O$, which have a very low concentration in the atmosphere (especially in the stratosphere), sensitivity is available within about 5 km to 12 km only.

The cross-sensitivity of most of the channels to the absorption by foreign species is favourably small; the influence of foreign species even falls below 0.25 dB down to 5 km for most of the channel pairs when considering the differential transmissions. Exceptions are the channel pairs used for the retrieval of CO, O_3 and $H_2^{18}O$. For CO, the influence does reach near 2 dB in the differential transmission but is stable, which is why it can be robustly corrected for in the retrieval as part of the foreign species correction (see Proschek, Kirchengast and Schweitzer 2011). The O_3 channels are substantially affected by foreign species absorption due to H_2O below about 10 km, wherefore the retrieval of O_3 is limited to heights above. Also the $H_2^{18}O$ intensity is significantly affected by H_2O absorption below about 7 km, which as well reduces the retrieval range for this species under moist conditions.

The aerosol extinction loss can transgress the limit of 0.25 dB into the favourable signal range of target species absorption loss below about 7 km to 22 km, depending on the aerosol load. In this case it is possible to retrieve aerosol extinction by a suitable algorithm. In the differential transmission, aerosol influence is significantly reduced and essentially negligible in its influence for trace species retrieval. Only under volcanic aerosol load at post-Pinatubo levels a small influence can remain (estimated to reach about 0.02 dB), which can be corrected for in this case by use of the retrieved aerosol extinction profiles.

Defocusing loss has a significant influence on the signal intensity and reduces it by

up to about 5 dB near 5 km, which is to be taken into account in the power budget of the intersatellite link in order to ensure sufficient SNR of received signal power in the upper troposphere. The direct effect of defocusing on the trace species retrieval is negligible, however, since due to its independence of frequency it is eliminated in the differential transmission. The influence of Rayleigh scattering is negligible in both direct and differential transmission signals.

The difference in the MW and SWIR refractivities leads to different tangent point heights of LIO and LMO ray paths, with the degree of tangent point separation determined by the presence of water vapour. Around 5 km, where moisture is strongest, the difference is about 0.15 km in SAW conditions, 0.5 km in STD and 1 km in TRO conditions. Following the decrease of water vapour, it strongly decreases with increasing altitude and becomes negligible from about 9 km to 13 km upwards. It is thus important in the trace species retrieval to compute correct LIO height levels in the upper troposphere, supported by LMO information (Proschek, Kirchengast and Schweitzer 2011).

Clouds generally block SWIR signals, except for very thin or small (Cirrus) clouds, which attenuate the signal significantly but not completely (Emde and Proschek 2010). This blocking or partial extinction is addressed in the ACCURATE mission concept by a design allowing retrieval of a cloud layering profile from reference signals and its use in trace species retrieval when scanning through intermittent upper tropospheric cloudiness. Since LIO is used in combination with LMO, accurate height levelling can be maintained through clouds, which is why also top and bottom heights of (layered) cloudiness can be determined, and atmospheric variables at these top and bottom heights.

Atmospheric turbulence induces major intensity fluctuations of the LIO signals, also called scintillations. Favourably, these fluctuations are highly correlated when considering closely spaced frequencies; close spacing of absorption and reference signals within 0.5 % is thus part of the ACCURATE design, combined with compensation of chromatic shift of ray paths between the channels (Sofieva 2009). In this way, the influence of residual scintillation noise becomes small, comparable to receiver thermal noise, in the differential transmission.

Wind along ray paths causes air to move and induces absorption at slightly shifted wavelengths due to Doppler shift. By using the centre of absorption lines for the trace species retrieval, this change in transmission is very small and hence can be corrected for by a moderately accurate (to about $10\,\mathrm{m\,s^{-1}}$) background wind profile. However, the influence becomes useful as an observable when regarding the inflection points of a highly symmetric absorption line. This is the basis for line of sight wind retrieval, effectively from the differential transmission between the infection points (Schweitzer 2010; Kirchengast and Schweitzer 2011). Using these retrieved wind profiles also eliminates the need for background wind profiles supporting the trace species retrieval.

In principle, the received signal power could also be increased due to atmospheric influences, by solar-scattered radiation and terrestrial thermal radiation collected within the FOV of the receiver telescope. We find these influences generally negligible, however,

since the chosen SWIR range intentionally is located in the "hole" between the solar Planck spectrum and the terrestrial Planck spectrum. Cloud-scattered solar radiation is the only process found to potentially provide signal above receiver noise level. This is addressed in the ACCURATE design by a close time spacing of interleaved laser-pulse and background signals within 5 ms, which enables to correct for such radiation while only insignificantly increasing received signal noise.

Putting the total atmospheric loss into context with the ACCURATE design of top-of-atmosphere received power and SNR (baseline −94 dBW and 34 dBHz; Kirchengast et al. 2010a), we found the available LIO signal level throughout the atmosphere down to 5 km adequate for enabling accurate trace species retrieval. Overall we find the set of LIO channels, and the ACCURATE design for implementing the full LMIO method, to be a new observing system of high promise for measuring greenhouse gas profiles, and other atmospheric variables, with unprecedented quality over the UTLS. First retrieval performance analysis results based on a realistic retrieval processing chain and end-to-end simulations underpin this promise (Proschek, Kirchengast and Schweitzer 2011).

In future work we intend to advance the simulation capabilities and assessment of atmospheric influences on LIO signals by the EGOPS/xEGOPS system by broader variability of atmospheric trace gas fields (atmospheric analysis fields complemented by composition analysis fields) and also by employing the capabilities for cloud, wind, and turbulence modelling, including in ensemble-based statistical analyses. This will allow to consolidate this first assessment by a statistical analysis that can also be linked to an ensemble-based retrieval performance analysis. As a specific issue we consider to investigate the region within 1.9 μ m and 2 μ m for absorption lines sensitive to the water isotopes HDO and $H_2^{18}O$, attempting to increase the vertical range of sensitivity for these species so that they may become useful for troposphere/stratosphere exchange studies. Finally there is currently a ground-based LIO experiment prepared, for a 144 km link at about 2.4 km height between observatories at the Canary Islands (by Univ. of York, Univ. of Manchester, and Univ. of Graz; P. F. Bernath et al., 2010–2011), which we use to learn about atmospheric influences based on real data somewhat similar to a LEO-to-LEO link.

CHAPTER 3

Greenhouse gas profiling by infrared-laser and microwave occultation: retrieval algorithm and demonstration results from end-to-end simulations

The focus of this chapter is the development of a greenhouse gas (GHG) retrieval algorithm for the LEO–LEO microwave and infrared-laser occultation (LMIO) technique under clear-air conditions. The output is a set of multiple species of accurately retrieved GHG volume mixing ratio (VMR) profiles. The content of this chapter was published in Atmospheric Measurement Techniques (AMT) by Proschek, Kirchengast and Schweitzer (2011). My contribution to this publication was the main manuscript text work, implementation of the algorithm into the eXtended End-to-End Generic Occultation Performance Simulation and Processing System (xEGOPS) and data analysis and result-figures generation. The work builds upon the work by Schweitzer et al. (2011) described in Chap. 2 above.

ABSTRACT

MEASURING greenhouse gas (GHG) profiles with global coverage and high accuracy and vertical resolution in the upper troposphere and lower stratosphere (UTLS) is key for improved monitoring of GHG concentrations in the free atmosphere. In this respect a new satellite mission concept adding an infrared-laser part to the already well studied microwave occultation technique exploits the joint propagation of infrared-laser and microwave signals between Low Earth Orbit (LEO) satellites. This synergetic combination, referred to as LEO-LEO microwave and infrared-laser occultation (LMIO) method, enables to retrieve thermodynamic profiles (pressure, temperature, humidity) and accurate altitude levels from the microwave signals and GHG profiles from the simultaneously measured infrared-laser signals. However, due to the novelty of

the LMIO method, a retrieval algorithm for GHG profiling is not yet available. Here we introduce such an algorithm for retrieving GHGs from LEO-LEO infrared-laser occultation (LIO) data, applied as a second step after retrieving thermodynamic profiles from LEO-LEO microwave occultation (LMO) data. We thoroughly describe the LIO retrieval algorithm and unveil the synergy with the LMO-retrieved pressure, temperature, and altitude information. We furthermore demonstrate the effective independence of the GHG retrieval results from background (a priori) information in discussing demonstration results from LMIO end-to-end simulations for a representative set of GHG profiles, including carbon dioxide (CO_2), water vapor (H_2O), methane (CH_4), and ozone (O_3). The GHGs except for ozone are well retrieved throughout the UTLS, while ozone is well retrieved from about 10 km to 15 km upwards, since the ozone layer resides in the lower stratosphere. The GHG retrieval errors are generally smaller than 1 % to 3 % r.m.s., at a vertical resolution of about 1 km. The retrieved profiles also appear unbiased, which points to the climate benchmarking capability of the LMIO method. This performance, found here for clear-air atmospheric conditions, is unprecedented for vertical profiling of GHGs in the free atmosphere and encouraging for future LMIO implementation. Subsequent work will examine GHG retrievals in cloudy air, addressing retrieval performance when scanning through intermittent upper tropospheric cloudiness.

3.1 Introduction

The LEO-LEO microwave and infrared-laser occultation (LMIO) method is a thoroughly defined synergistic combination of LEO-LEO microwave occultation (LMO) and LEO-LEO infrared-laser occultation (LIO), as schematically shown in Fig. 3.1 and introduced in detail by Kirchengast et al. (2010a), Schweitzer (2010), and Kirchengast and Schweitzer (2011). This proposed inter-satellite active limb sounding technique would enable the synergy of deriving thermodynamic variables, including pressure, temperature and humidity, from LMO phase and amplitude data, and at the same time trace species concentrations and the line-of-sight wind speed from LIO intensity data. The primary altitude domain of the measurements is the upper troposphere and lower stratosphere (UTLS; ~5 km to 35 km) where all main greenhouse gases (GHGs) except the synthetic chlorine-flourine-containing species can be retrieved, i.e., water vapor, carbon dioxide, methane, nitrous oxide, ozone, and carbon monoxide.

As described by Kirchengast and Schweitzer (2011), the LMIO method can be considered as a next generation of the well established and successful GNSS-LEO radio occultation (GRO) method (Ware et al. 1996; Kursinski et al. 1997; Steiner et al. 2001; Anthes et al. 2008; Luntama et al. 2008; Steiner et al. 2009; Ho et al. 2009). LMIO and GRO share the

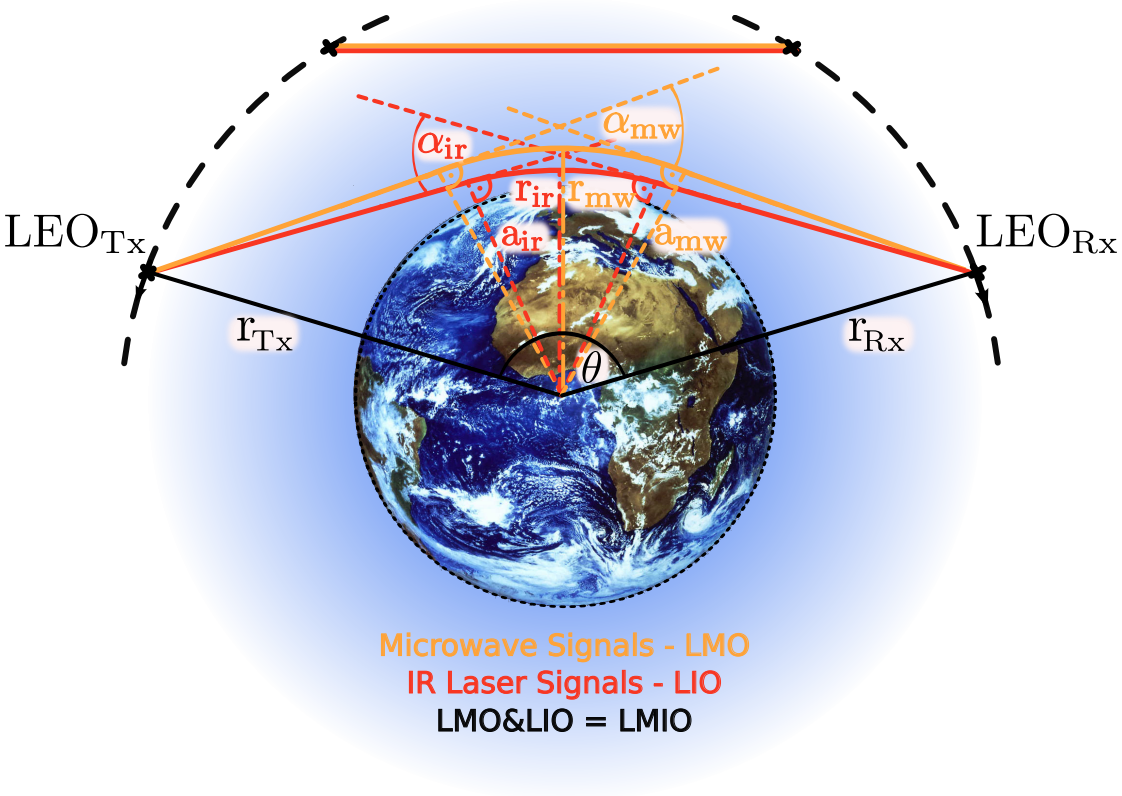

Figure 3.1: Schematic view of the LEO-LEO microwave and infrared-laser occultation (LMIO) measurement geometry, as a combination of LMO signals (MW, orange signal paths) and LIO signals (IR, red signal paths) which pass the vacuum as straight lines and are refracted by the atmosphere. Characteristic MW and IR parameters defining this geometry are marked; see the text in Sect. 3.2.1 for further explanation.

occultation measurement principle (Phinney and Anderson 1968; Kirchengast 2004) and the use of highly coherent and stable inter-satellite signals, and therefore the potential of providing accurate, long-term, consistent benchmark data with high vertical resolution and global coverage. However, while GRO uses decimeter-wave navigation signals from the Global Positioning System GPS, and of other future navigation satellites, LMIO will use specifically developed centimeter- and millimeter-wave (LMO) and micrometer-wave signals (LIO). These vastly expand the accessible atmospheric variables from the GRO focus on refractivity-related variables to the full suite of thermodynamic, composition, and wind variables noted above (for more details see Kirchengast and Schweitzer (2011)).

The LMO part of LMIO has substantial heritage from a range of studies over the recent decade (Kursinski et al. 2002, 2009; Herman et al. 2004; Kirchengast 2004; Gorbunov and Kirchengast 2005, 2007) and very recently a detailed LMO algorithm description and performance analysis was provided by Schweitzer et al. (2011). This heritage work established well the expected performance of LMO for accurate thermodynamic state profiling in the UTLS, which serves as the basis for the LIO-related GHG profiling introduced here.

We implemented the LIO retrieval as a complementary, subsequent part to the LMO retrieval of Schweitzer et al. (2011), completing the LMIO retrieval algorithm introduced in a brief overview form in Kirchengast and Schweitzer (2011). We describe in this study the detailed steps of the algorithm, which can be applied for single species (single-line trace species retrieval, SSR) or a set of several trace species (multi-line trace species retrieval, MSR), and include a demonstration of its capabilities by end-to-end performance simulation results. The synergy between LMO and LIO is pointed out, since the LMO retrieval with its thermodynamic profiles as output serves as a necessary provider of input information for the LIO retrieval. In addition, the effective independence from external (a priori) information and the high accuracy of the LIO retrieval results, i.e., of the GHG and isotope profiles, is emphasized.

The paper is structured as follows. We start with introducing the geometry, the main atmospheric effects relevant to the retrieval algorithm, and the simulation and retrieval demonstration setup in Sect. 3.2. This preparatory information is followed by a detailed LIO algorithm description in Sect. 3.3, describing the core elements and necessary systematic update loops over the core. In Sect. 3.4 the demonstration results are discussed. Finally, Sect. 3.5 presents a summary and conclusions of the study.

3.2 Geometry and setup

3.2.1 Geometry and atmospheric effects

Figure 3.1 illustrates the LMO and LIO signal propagation paths, with all signals transmitted from one joint platform, LEO_{Tx}, and received at another joint platform, LEO_{Rx}. Both LMO and LIO signals follow closely similar but not identical paths, i.e.,

the refraction becomes somewhat different for the microwave (MW) and infrared (IR) signals, proportional to the amount of water vapor in the air (Thayer 1974; Bönsch and Potulski 1998; Kirchengast and Schweitzer 2011; Schweitzer, Kirchengast and Proschek 2011). The corresponding difference in bending of MW and IR ray paths is practically negligible above about 8 km to 12 km, a highly favorable property, and gradually increases downwards into the troposphere (Schweitzer, Kirchengast and Proschek 2011), leading to a difference of the tangent altitude of about 0.5 km near 5 km in moist conditions (Kirchengast et al. 2010a).

Figure 3.1 highlights that this different bending of MW and IR rays, despite generally being a very small effect, formally leads to different bending angles (α_{MW}, α_{IR}) at any given time during an occultation event and as well also different impact parameters (a_{MW}, a_{IR}) and radial distances from the center of curvature to the tangent points (r_{MW}, r_{IR}), the latter implying as well different tangent point altitudes. The radial distances from the center of curvature to the satellite platforms are given by r_{Tx} and r_{Rx}, with θ being the opening angle between the two satellite vectors. This geometric setup of the LIO signal propagation on top of the LMO signal propagation is, in addition to the LMO heritage summarized in the introduction, a key basis for formulating the LIO-related GHG profiling algorithm.

The influences of absorption by atmospheric trace species and of other atmospheric processes on the carefully selected quasi-monochromatic LIO signals are essential for the LIO method. Besides the absorption of the target greenhouse gas, also other influences due to the atmospheric background such as defocusing, foreign species absorption, Rayleigh scattering, aerosol extinction, cloud extinction, signal scintillations from turbulence, Doppler shift of signal frequencies due to line-of-sight winds, and Rayleigh as well as cloud scattering of solar radiation into the receiver are potentially relevant. The effects from these background influences, except for cloud extinction, are practically either negligibly small under most conditions or can be reduced to very small levels of residual error (typically $< 0.1\,\%$) as discussed by other studies (Emde and Proschek 2010; Schweitzer 2010; Kirchengast et al. 2010a; Schweitzer, Kirchengast and Proschek 2011). In the LIO forward simulations of the received intensity signals for this study we account for the main effects of attenuation, namely target and foreign species absorption, and defocusing (plus for the small Rayleigh scattering loss since easily co-modeled). Cloudy air and a suitable retrieval will be treated in a separate study; a brief discussion of cloud influences, including limitations to tropospheric penetration of part of the events especially in the tropics, is given by Schweitzer, Kirchengast and Proschek (2011). The other effects can be assumed negligible, or are sufficiently corrected to the level of thermal noise that we include. This is sufficient in the context here to demonstrate the new retrieval algorithm.

To isolate the absorption due to the target GHG from the absorption of foreign species and broadband atmospheric effect, an adjacent pair of signals, one “absorption signal” (at the center of an absorption line of a target species) and one “reference signal”

(off-line of any trace species absorption) is employed using a differential absorption principle (Kursinski et al. 2002; Gorbunov and Kirchengast 2007; Kirchengast et al. 2010a; Kirchengast and Schweitzer 2011; Schweitzer, Kirchengast and Proschek 2011), which will be explained in detail in Sect. 3.3. In the retrieval presented in Sects. 3.3 and 3.4, the target species H_2O, CO_2, CH_4, O_3, N_2O, and CO are specifically taken into account, with focus on the first four. But we note that the retrieval algorithm itself is generically valid for any group of LIO target species.

3.2.2 Simulation and retrieval demonstration setup

For the simulation of the LMIO measurements, which we produced for demonstrating the new retrieval algorithm, we used the End-to-End Generic Occultation Performance Simulation and Processing System (EGOPS5.5) and the eXperimental End-to-End Generic Occultation Performance Simulation and Processing System (xEGOPS5.5) (Fritzer, Kirchengast and Pock 2009b; Fritzer et al. 2010b). The EGOPS system development started for GRO end-to-end simulations more than a decade ago (Kirchengast 1996, 1998; Ramsauer and Kirchengast 2000; Kirchengast, Fritzer and Ramsauer 2002), was then extended to also enable LMO simulations (Kirchengast et al. 2007; Fritzer, Kirchengast and Pock 2009b), and proved useful in a myriad of GRO and LMO-related studies, including the recent study by Schweitzer et al. (2011). The complementary xEGOPS system (Fritzer et al. 2010b) was developed more recently and extends EGOPS by LIO end-to-end simulation capabilities. We use EGOPS/xEGOPS here in the same way and logic for LMIO simulations as Schweitzer et al. (2011) used EGOPS for LMO simulations.

We start with the Mission Analysis Planning (MAP), a subsystem of EGOPS, to generate occultation events for a low-, mid- and high latitude region for 15 July 2007 (an arbitrary example day). We used LEO satellites in sun-synchronous orbits, two transmitters and two counter-rotating receivers, with the transmitters at an orbital height of 800 km and the receivers at 650 km, yielding about 230 globally well distributed occultation events per day (same as Schweitzer et al. (2011)). The MAP calculates occultation event locations and related positions of the transmitter and receiver satellites during the event. The occultation events chosen for further forward modeling are a tropical (TRO, 1.3° N/55.6° W), a standard (STD, 38.0° N/71.2° W) and a sub-arctic winter event (SAW, 72.8° S/13.7° E), together allowing to span a representative range of atmospheric conditions.

The Forward Modeling (FOM) subsystem of EGOPS/xEGOPS uses the MAP results (satellite positions and velocities) to simulate excess phase, amplitude (LMO) and intensity (LIO) profiles as a function of time for each occultation event. For the simulation of realistic ray paths a highly accurate geometric optical ray-tracing algorithm is used at a sampling rate of 10 Hz (Syndergaard 1999). We assume a spherical symmetry of the atmosphere about the occultation event location (to avoid including representativeness errors; cf. Schweitzer et al. (2011)) and an ellipsoidal Earth shape (WGS84, Landolt-

Table 3.1: Trace species retrieval order, associated absorption and reference wavenumbers, and their frequency spacing.

Retrieval order	Target species [valid range]	Absorption wavenumber cm^{-1}	Reference wavenumber cm^{-1}	(Abs-Ref)/Ref freq. spacing %
1	N_2O	4710.340810	4731.03	−0.4373
2	CH_4	4344.163500	4322.93	+0.4912
3	$^{13}CO_2$	4723.414953	4731.03	−0.1610
4	$C_{18}OO$	4767.041369	4770.15	−0.0652
5	$H_2O(1)$ [13–48 km]	4204.840290	4227.07	−0.5259
6	$H_2O(2)$ [8–25 km]	4775.802970	4770.15	+0.1185
7	$H_2O(3)$ [5–10 km]	4747.054840	4731.03	+0.3387
8	$H_2O(4)$ [4–8 km]	4733.045010	4731.03	+0.0426
9	$^{12}CO_2$	4771.621441	4770.15	+0.0308
10	HDO	4237.016320	4227.07	+0.2353
11	$H_2^{18}O$	4090.871800	4098.56	−0.1876
12	CO	4248.317600	4227.07	+0.5027
13	O_3	4029.109610	4037.21	−0.2006

Börnstein (1984)). The ray-tracing uses for the LMO channels the microwave refractivity formula of Smith and Weintraub (1953) and for the LIO channels an accurate but simplified approximation of the visible/infrared refractivity formula by Bönsch and Potulski (1998) (more details in Sect. 3.3.3). Absorption by trace species is integrated along these ray paths. The relevant absorption coefficients for the LMO channels are computed by an advanced version of Liebe's Millimeter Wave Propagation Model MPM93 (Liebe, Hufford and Cotton 1993; Schweitzer et al. 2011), those for the LIO channels by the Reference Forward Model (RFM) (Edwards 1996; Dudhia 2008), which uses the spectroscopic parameters from the HITRAN2004 database (Rothman et al. 2005) pages.

The atmospheric model used is the Fast Atmospheric Signature Code (FASCODE) model (in the form supplied online by FASCODE (2008)), including the US standard atmosphere (Anderson et al. 1986). In line with the latitudes of occultation events selected above we use the tropical (TRO), standard (STD), and sub-arctic winter (SAW) atmospheres (STD atmosphere for the example cases illustrating the algorithm steps in Sects. 3.3.4 and 3.3.5, all three atmospheres for the demonstration results in Sect. 3.4). Each FASCODE atmosphere comprises profiles of the thermodynamic variables, namely pressure (p), temperature (T), and humidity (q), as well as the concentration of all needed trace species profiles ($X = N_2O$, CH_4, $^{12}CO_2$, $^{13}CO_2$, $C^{18}OO$, H_2O, HDO, $H_2^{18}O$, CO,

O_3), where the concentrations of the secondary isotopes are estimated from the main isotope via isotopic fractional abundances following Rothman et al. (2005). The outdated FASCODE value for CO_2 (330 ppmv up to about the mesopause) was updated to a more recent value of 380 ppmv (see also Kirchengast and Schweitzer (2011)). The atmosphere is assumed to be free from clouds and aerosols (cf. discussion in Sect. 3.2.1); hence refraction, defocusing and GHG trace species absorption are the processes effectively contributing to the simulated LMO excess phase, LMO amplitude loss, and LIO intensity loss data (Rayleigh scattering loss is formally co-integrated along the rays but is negligible). The vertical simulation range is set to cover altitudes between 3 km and 80 km. The frequency channels used for LMO are those of Schweitzer et al. (2011) (5 channels, 17.25 GHz, 20.2 GHz, 22.6 GHz, 179 GHz and 182 GHz), the LIO channels used follow Schweitzer (2010) and Kirchengast and Schweitzer (2011) and are summarized in Table 3.1.

The simulation of quasi-realistic observation system errors is done with the EGOPS subsystem Observation System Modeling (OSM). Link budget computation accounting for transmitter power, free space loss, total atmospheric loss, and instrument-related losses are employed to model amplitude and intensity profiles in absolute terms (in dBW) and to model thermal noise for adequate signal-to-noise ratios at the receiver (67 dBHz C/N_0 for LMO amplitudes at top-of-atmosphere, 34 dBHz SNR for LIO intensities; cf. Kirchengast et al. (2004); Schweitzer et al. (2011); Kirchengast and Schweitzer (2011)). Residual linear drift errors over the occultation event, reflecting expected short-term stability limitations of measured LMO and LIO amplitudes/intensities, are superimposed as well; for LMO in the same way as by Schweitzer et al. (2011), for LIO according to the system requirement specifications in Kirchengast et al. (2010a). Clock errors and precise-orbit-determination (POD) errors, affecting the LMO excess phase, and thermal noise on the phase are modeled in the same way as was done for GRO simulations by Steiner and Kirchengast (2005) and adopted for LMO simulations by Schweitzer et al. (2011). Errors in spectroscopic parameters are not considered in this study because, on the one hand, they lead to essentially time-constant retrieval errors only with negligible effects on observing GHG variability and, on the other hand, their reduction is a separate matter of spectroscopic laboratory work. Kirchengast and Schweitzer 2011, section S2 therein, and Harrison, Bernath and Kirchengast 2011 discuss the requirements and needs for reducing spectroscopic errors to within ~0.1 % in detail.

In order to finally provide the retrieved thermodynamic variables from LMO based on the simulated signals from the OSM subtool, we use the retrieval algorithm described by Schweitzer et al. (2011), which is implemented in the Occultation Processing System (OPS) subsystem of EGOPS. As Schweitzer et al. (2011) conclude, the LMO-retrieved thermodynamic profiles are essentially unbiased and achieve r.m.s. errors of < 0.2 % for the pressure, <0.5 K for the temperature and <10 % for the specific humidity; the related altitude levels are determined to within 10 m accuracy. LMO is thus evidently very suitable to provide the needed thermodynamic state and altitude information to the LIO retrieval.

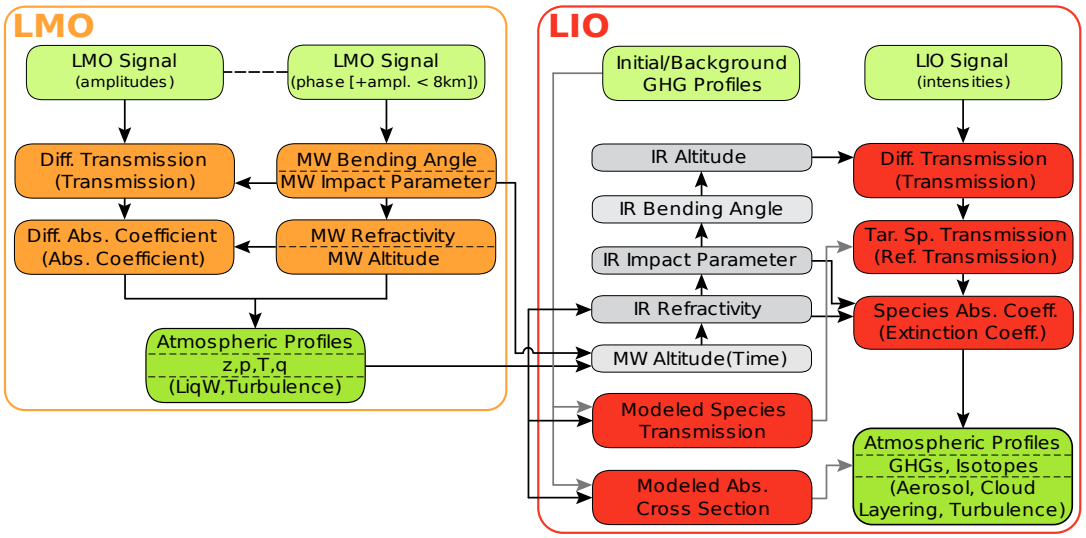

Figure 3.2: Schematic overview of the LMIO retrieval processing system as implemented in the EGOPS/xEGOPS software, with its LMO (left, framed in orange) and LIO (right, framed in red) retrieval parts; see the text in Sect. 3.3.1 for further explanation.

The LIO retrieval is then performed applying the OPS part of xEGOPS. It needs an array of initial/background GHG profiles as input. The latitude-dependent FASCODE GHG profiles are used for this purpose when demonstrating the single core steps of the SSR process in Sect. 3.3.4 and for the demonstration results in Sect. 3.4. The array is, for test purposes, also set to zero initial values for the GHG species H_2O, CO_2, CH_4 and O_3 in the MSR process. This latter setting will demonstrate the importance of the order in which the trace species are retrieved, as discussed in Sect. 3.3.5.

3.3 Retrieval algorithm

In this section we discuss in detail the LIO retrieval algorithm methodically supported by quasi-realistic end-to-end simulations. The main goal is to clearly describe the retrieval steps and processing flow and to show the utility of the combined LMO and LIO observations. We show the effective independence of the LMIO retrieval results from external/background/first guess information and demonstrate the high accuracy of the GHG profiles.

3.3.1 Algorithm overview and context

The retrieval flow of the LMO to the LIO variables is illustrated in Fig. 3.2, which visually emphasizes the synergy of LMO and LIO in the combined LMIO method.

In the left orange-bordered part of the scheme in Fig. 3.2, the LMO retrieval input (bright green), main calculation steps (orange) and final outputs (dark green) are shown. The detailed algorithm to derive the output variables from the LMO excess phase and amplitudes is described by Schweitzer et al. (2011). The required variables of the LMO retrieval for the LIO retrieval are pressure (p) and temperature (T) on a given grid (z), plus the MW impact parameter grid of the MW occultation rays that is associated with the original time grid of the transmitter and receiver positions. Since it is co-available, we also formally use the humidity (q) in computing the IR refractivity but because its contribution is practically negligible at UTLS altitudes in the IR domain (Bönsch and Potulski 1998; Schweitzer 2010) it could as well be disregarded.

The right red-bordered part of Fig. 3.2 illustrates the flow and inner-dependencies of the LIO SSR parameters. The direct LIO-observed input parameters are the received LIO intensity signals on the time grid shared with LMO signals and the transmitter and receiver positions. This input is complemented by first guess (initial/background) GHG profiles (bright green) used for convenience on the z grid shared with p, T, and q from LMO. From the MW impact parameter, combined with the thermodynamic variables, the "refractive" IR quantities are calculated (grey boxes), i.e., those quantities that are directly retrievable in the MW domain from the phase measurements but not from the IR intensity-only measurements.

Based on first preparing an auxiliary MW altitude grid as a function of time from the LMO input, these quantities include the IR refractivity (Bönsch and Potulski 1998), followed by the IR impact parameter (cf. Bouguer's rule in Born and Wolf (1964)), the IR bending angle as auxiliary profile (using the Abel transform, e.g., Fjeldbo and Eshleman (1965); Fjeldbo, Kliore and Eshleman (1971)) and the IR tangent point altitude. These parameters are necessary to tie the LIO intensity signals measured as a function of time to their associated IR altitude levels (recall from Fig. 3.1 that the propagation path differences between MW and IR occultation rays are essentially negligible in the stratosphere but need to be accounted for in the upper troposphere where humidity increases downwards, in order to ensure accurate retrievals within 20 m altitude geolocation accuracy down to 5 km).

After the preparatory calculations of the "refractive" quantities, the core steps (red symbols in Fig. 3.2) of the SSR process are performed. First, a correction for defocusing loss is performed (an option not strictly needed if proceeding with differential transmissions) and the differential transmission is calculated from a pair of the LIO intensity profiles comprising one absorption and its corresponding reference channel (Table 3.1; Schweitzer (2010); Kirchengast and Schweitzer (2011)), and the result allocated to the IR altitude grid. Subsequently, the differential transmission and the modeled species

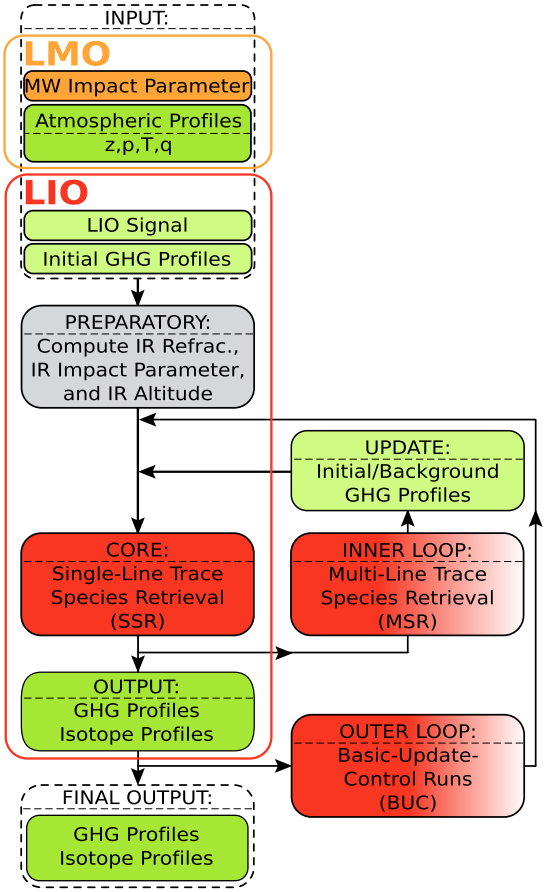

Figure 3.3: Overview of the dynamic structure and flow of the LIO retrieval algorithm, highlighting its preparatory part, establishing IR refractivity, impact parameter, and altitude profiles (grey box), its core part, the single-line trace species retrieval SSR (red box), and its dynamical part of envelope loops over the SSR, consisting of the multi-line trace species retrieval (MSR) loop and the basic-update-control run (BUC) loop, respectively (gradient-red boxes); see the text in Sect. 3.3.2 for further explanation.

transmissions, which are derived by employing the RFM (Edwards 1996; Dudhia 2008) based on the initial/background GHG profiles, are used to isolate the target species transmission of the absorption channel. This target species transmission is the pure transmission due to a single GHG (e.g., $^{12}CO_2$), with effectively negligble influence of foreign species. The target species transmission is then used, together with the IR impact parameter and the IR refractivity, to retrieve the target species absorption coefficient on the IR altitude grid by use of the "absorptive" Abel transform (Kursinski et al. 2002; Schweitzer et al. 2011). Finally, the GHG/isotope volume mixing ratio profile is derived from the target species absorption coefficient and a modeled absorption cross section of the target species for which we employ RFM based on the initial/background target species profile and the p and T profiles from LMO; likewise it could also be the mole fraction profile. Optionally, also the absolute concentrations of GHGs/isotopes could be computed as needed.

3.3.2 Algorithm dynamic structure and flow

While we focused above on an overview of the SSR core process of the LIO retrieval we focus in this subsection on an overview of the dynamic structure of the LIO algorithm before we then proceed to explain it step by step. Overall the LIO algorithm is a sequential order of retrieval calculation steps and two nested loops over the core retrieval algorithm as illustrated in Fig. 3.3. The input parameters are the retrieved LMO profiles, the LIO intensities and a set of initial/background GHG profiles as discussed above.

The first step in the LIO retrieval flow is to prepare the "refractive" quantities, where we then need IR refractivity, IR impact parameter, and IR altitude profiles (details in Sect. 3.3.3). The core part of the retrieval is then the SSR process (details in Sect. 3.3.4), which estimates the GHG/isotope profiles starting from the LIO intensity signals attributed to the IR impact parameter and IR altitude grid. This SSR core part is included in two nested loops, namely an inner MSR (multi-species retrieval) and an outer BUC (basic-update-control) loop.

The inner MSR loop, an envelope process over the SSR process (details in Sect. 3.3.5), performs a carefully defined consecutive order of single species retrievals. After every single inner loop step, the initial/background GHG profiles are updated with the output from the SSR. This results in a step-wise improved set of GHG profiles. The order in which the species are retrieved is important; first the most independent species is retrieved (meaning the species which is derived from a channel pair which includes the smallest amount of foreign species absorption), followed by the other ones which are gradually more and more dependent on the target species already retrieved before. These are available to the later profiles as background profiles that have already superseded the initial profiles in the array of initial/background GHG profiles. Additionally, in this MSR loop suitable single-line trace species outputs are combined, i.e., $^{12}CO_2$ and $^{13}CO_2$, as well as $H_2O(X)$ with $X = \{1, 2, 3, 4\}$, which further improves the initial/background

GHG profiles for CO_2 and H_2O for the next inner loop step.

The outer BUC loop comprises Basic-Update-Control runs and is an envelope loop over the SSR and MSR processes (details in Sect. 3.3.6). This loop performs two iterations of the basic GHG/isotope profiles retrieval of the first completed MSR loop. The converged retrieval results after the BUC control run are then used as final best estimate of the GHG/isotope profiles, as schematically shown in Fig. 3.3. We note that the control run results in practice (in our end-to-end simulations) turn out to negligibly differ from the update run result. Thus in case of real LMIO data it likely will serve just as a quality control whether any problem with convergence has occurred at any altitude level with any GHG.

3.3.3 Computation of IR refractivity, impact parameter, and altitude

From the LIO measurements we do not get any information on the tangent point altitude of each ray as this measurement information only comprises the received IR-laser intensities in dBW as a function of time. Also, related to this, we have no information about the thermodynamic conditions (p, T, q) affecting the LIO signal at this altitude. Therefore, since the LIO retrieval requires refractivity, impact parameter and altitude information for the IR occultation rays (cf. Fig. 3.2), a first algorithm step is necessary to calculate these IR parameters on the basis of the MW parameters. For this algorithm step we proceed as follows.

First, from the MW impact parameter level as a function of time t_j, $a_{\mathrm{MW}}(t_j)$, the according MW altitude level $z_j(t_j)$ is calculated via an iterative process (iteration index k). The starting profile of the MW altitude, $z_{j,k=0}(t_j)$, is derived by using the MW impact height for the purpose, i.e., we subtract the Earth's local radius of curvature R_{C} from the MW impact parameter, $z_{j,k=0}(t_j) = a_{\mathrm{MW}}(t_j) - R_{\mathrm{C}}$ (R_{C} is available as part of standard auxiliary output parameters from the LMO retrieval). At each iteration the MW refractive index $n_{\mathrm{MW}}(z_{j,k})$ at any MW altitude level $z_{j,k}(t_j)$ is obtained by log-linear interpolation from the known MW refractive index profile. It is calculated based on the formula by Smith and Weintraub (1953) using p, T, q from LMO. Bouguer's rule of the relation of impact parameters to the radial distance of rays from the curvature center (Born and Wolf 1964) is then used to calculate an updated MW altitude $z_{j,k+1}(t_j)$ in the form

$$z_{j,k+1}(t_j) \;=\; \frac{a_{\mathrm{MW}}(t_j)}{n_{\mathrm{MW}}(z_{j,k}(t_j))} \;-\; R_{\mathrm{C}}, \tag{3.1}$$

where the iteration is accepted converged and stopped when the change of the MW altitude per iteration step, $|z_{j,k+1}(t_j) - z_{j,k}(t_j)|$, becomes <0.1 m. The iteration algorithm is robust and fast and convergence is reached within a single or very few iterations.

The IR refractivity, impact parameter, and altitude computation now can use this MW altitude level as a function of time $z_j(t_j)$ in a form strictly consistent with the retrieved MW impact parameters and p, T, q from LMO. Note that in principle one might use the

retrieved MW altitude from LMO directly. Dependent on algorithmic implementation of LMO retrieval this may not be directly related to the time grid of the occultation rays, however, while the impact parameters are formally related based on geometric-optical formulation of ray paths. Furthermore, the LIO computations will base the IR refractivity computation on p, T, q, so that the same way of using the information is advisable also for MW refractivity. This will ensure strict consistency of final differences of MW and IR altitudes despite the small extra errors that have been incurred when retrieving p, T, q from MW refractivity. Therefore a preparation of $z_j(t_j)$ as introduced here is better than a direct use of MW altitudes, even if the latter are kept related to the original time grid in the LMO retrieval (as we currently also do in the EGOPS LMO retrieval; Schweitzer et al. (2011)). In principle also a different altitude grid than the MW grid used here could be employed as starting point but this one was found clearly most suitable for a reliable and fast subsequent derivation of the IR impact parameter and altitude grid.

Since we use the index j for the MW altitude at times t_j, and later the index i for the IR level at the same times $t_i = t_j$, the MW altitude notation is used in the simplified form z_j hereafter. We can now compute the IR refractivity, impact parameter, and bending angle at the z_j level. We formulate the IR refractivity (in N-units) based on Bönsch and Potulski (1998) as

$$N\,(z_j) \;=\; \left(c_1 \;+\; \frac{c_2}{d_1 \;-\; \frac{1}{\lambda^2}} \;+\; \frac{c_3}{d_2 \;-\; \frac{1}{\lambda^2}} \right) \frac{p\,(z_j)}{T\,(z_j)} \;-\; \varepsilon_1\; e\,(z_j)\,, \tag{3.2}$$

where the constants are $c_1 = 23.7104\,\mathrm{K\,hPa^{-1}}$, $c_2 = 6839.34\,\mathrm{K\,hPa^{-1}}$, $c_3 = 45.473\,\mathrm{K\,hPa^{-1}}$, $d_1 = 130.0$, $d_2 = 38.9$, and $\varepsilon_1 = 0.038\,\mathrm{hPa^{-1}}$. λ is the wavelength of the IR-laser signals in units μm, for our LIO signals in the range of $2\,\mu$m to $2.5\,\mu$m, p the pressure in hPa, T the temperature in K, and e the water vapor partial pressure in hPa. This refractivity expression at the z_j level is computed after first interpolating p, T, q from their native LMO grid to the z_j level. Equation (3.2) is a streamlined single-equation form of the more sophisticated empirical formulation of Bönsch and Potulski (1998). It follows very closely the Bönsch and Potulski (1998) formulation (at $\lambda > 0.5\,\mu$m) and can be considered an improved version of the classical very similar optical refractivity formula developed by Edlén (1966). Different from the Smith-Weintraub formula of microwave refractivity used in LMO (Schweitzer et al. 2011), the water vapor term in this optical refractivity formula is essentially negligible because the frequencies are much too high for the permanent dipole moments of the water vapor molecules to contribute an orientation polarization term (the "wet term" in the microwave formula; e.g., Kursinski et al. (1997)). The difference of the MW refractivity and the IR refractivity is illustrated over the range $2\,\mu$m to $3\,\mu$m by Schweitzer, Kirchengast and Proschek (2011). Based on $N\,(z_j)$, the IR refractive index n_j (dimensionless) is

$$n_j \;=\; n\,(z_j) \;=\; 1 \;+\; 10^{-6}\; N\,(z_j)\,, \tag{3.3}$$

which is used in the further calculations.

The IR impact parameter a_j is subsequently, again using Bouguer's rule (Born and Wolf 1964), computed as

$$a_j \;=\; a\,(z_j) \;=\; n\,(z_j)\;r\,(z_j) \;=\; n\,(z_j)\;(z_j \;+\; R_{\rm C})\,, \tag{3.4}$$

where $r\,(z_j) = r_j = z_j + R_{\rm C}$ is the radial distance from the Earth's curvature center at the mean tangent point location of the occultation event.

Based on the n_j, r_j, and a_j profiles, the IR bending angle profile $\alpha\,(a_j)$ corresponding to the z_j level is then computed as

$$\alpha\,(a_j) \;=\; 2\;a\,(z_j) \int\limits_{r(z_j)}^{r_{\rm top}} \frac{1}{\sqrt{n^2\,(z)\;r^2\,(z) \;-\; a^2\,(z_j)}} \frac{{\rm d}\;\ln\;(n\,(z))}{{\rm d}r} {\rm d}r, \tag{3.5}$$

which is the classical Abel transform for converting refractive index to bending angle (Fjeldbo and Eshleman 1965; Fjeldbo, Kliore and Eshleman 1971). For computing it, we employ a standard numerical implementation of this Abel integral in EGOPS (setting $r_{\rm top}$ to 80 km, leaving negligible residual error at the altitudes of interest up to 40 km; Steiner, Kirchengast and Ladreiter (1999)).

With the IR refractive index, impact parameter, and bending angle profiles available at the MW altitude grid $z_j(t_j)$, we can now compute the impact parameter grid of the IR occultation rays, $a_i(t_i = t_j)$. We do this by exploiting the unique geometrical relation which the bending angle and impact parameter have to fulfill for representing a valid occultation ray at any joint LIO and LMO measurement time $t_i = t_j$ between the corresponding joint LIO and LMO transmitter and receiver positions, $r_{{\rm Tx},i} = r_{{\rm Tx},j}$ and $r_{{\rm Rx},i} = r_{{\rm Rx},j}$. This geometrical relation reads (Melbourne et al. 1994; Syndergaard 1999; Kirchengast et al. 2006)

$$\alpha_{\rm g}\,(a_i) \;=\; \theta_i \;-\; \arccos\,\left(\frac{a\,(z_i)}{r_{{\rm Tx},i}}\right) \;-\; \arccos\,\left(\frac{a\,(z_i)}{r_{{\rm Rx},i}}\right), \tag{3.6}$$

where $\alpha_{\rm g}\,(a_i)$ and $a\,(z_i)$ denote the desired point on the (interpolated) IR bending angle profile $\alpha\,(a_j)$ (Eq. 3.5) that represents the IR occultation ray. The angle θ_i is the opening angle between the transmitter and the receiver at time t_i (see Fig. 3.1). Since this is no explicit formulation, we must find the desired point iteratively for which we also use the (analytically available) derivative of Eq. (3.6), $\alpha_{\rm g}^{'}(a_i)$, which reads

$$\alpha_{\rm g}^{'}\,(a_i) \;=\; \frac{{\rm d}\;\alpha_{\rm g}}{{\rm d}a}\,(a_i) \;=\; \frac{1}{r_{{\rm Tx},i}\,\sqrt{1 \;-\; \left(\frac{a(z_i)}{r_{{\rm Tx},i}}\right)^2}} \;+\; \frac{1}{r_{{\rm Rx},i}\,\sqrt{1 \;-\; \left(\frac{a(z_i)}{r_{{\rm Rx},i}}\right)^2}}. \tag{3.7}$$

We use an implementation of Newton's method for the iteration process (iteration index k), searching for the desired impact parameter a_i by updating the bending angle

difference of $\alpha_g(a_i)$ (Eq. 3.6) and $\alpha(a_i)$ (interpolated from Eq. 3.5), and the subsequently estimated impact parameter difference, until convergence is achieved. In this process according to the update rules given below, $\alpha(a_i)$ is log-linearly interpolated from the profile $\alpha(a_j)$ and the derivative $\alpha_g'(a_i)$ supports the impact parameter difference estimate and provides the direction of the iterative difference minimization process. As initial value for any time $t_i = t_j$ we use the MW impact parameter, $a_{k=0} = a(z_i) = a_j$, which is a good initial guess since the IR and MW ray path differences $a_i - a_j$ and $z_i - z_j$ are small. The update rules for the iteration are given by

$$\Delta\alpha_{k+1} = \alpha_g(a_k) - \alpha(a_k) \tag{3.8}$$

$$\Delta a_{k+1} = \frac{1}{\eta(z_j)} \frac{\Delta\alpha_{k+1}}{\alpha_g'(a_k)} \tag{3.9}$$

$$a_{k+1} = a_k - \Delta a_{k+1}. \tag{3.10}$$

In Eq. (3.9), the altitude-dependent relaxation factor $\eta(z_j)$ ensures robust convergence despite the iteration problem is one-sided convergent for the larger MW and IR ray separations into the troposphere (un-relaxed iteration can lead to convergence to a spurious oscillating bi-stable solution, beyond the first bifurcation in the state space of the given iteration problem). We formulated $\eta(z_j)$ as

$$\eta(z_j) = \eta_{top}\left(1 + \frac{3}{2}\exp\left[-\frac{(z_j - z_{base})}{H_{atm}}\right]\right), \tag{3.11}$$

where the minimum relaxation factor at high altitudes η_{top} is set to 2, the base altitude z_{base} to 5 km and the atmospheric scale height H_{atm} to 7 km. This provides robust and at the same time still fast convergence within a few iterations. The iteration is accepted converged and stopped when the change of the IR impact parameter per iteration step, $|\Delta a_{k+1}|$, becomes <0.1 m. Based on GRO and LMO experience with bending angle and impact parameter retrieval, an additional criterion back-checks the impact parameter solution for vertical monotony (i.e., next downward ray to always have impact parameter lower than the previous ray). The processing is terminated at the altitude level where the monotony is first violated if that occurs before the bottom of the z_j grid. This safeguards from potential errors in the LMO-retrieved input data at lowest tropospheric altitude levels.

The final converged values a_{k+1} at all measurement times $t_i = t_j$ of the occultation event provide the resulting a_i levels of IR impact altitudes. We can now log-linearly interpolate the IR refractive index from the a_j grid corresponding to the z_j grid (Eqs. 3.3 and 3.4) to this a_i level, yielding the resulting IR refractive index profile $n(a_i)$. Using Bouguer's rule again (as in Eq. 3.1), we finally also obtain the resulting z_i level of IR altitudes. All subsequent LIO retrieval steps can thus now use together with the t_i grid also its associated a_i or z_i grids.

3.3.4 Single-line trace species retrieval (SSR)

The SSR algorithm is the core of the LIO trace species retrieval. In this step, one absorption-reference channel pair of measured LIO intensities is used to derive one trace species profile (cf. Figs. 3.2 and 3.3, red boxes). The detailed steps are explained in the following sections, accompanied by illustration of the steps. Example results are illustrated for the trace species $^{12}CO_2$ (Fig. 3.4) and $H_2O(2)$ (Fig. 3.5); for a full list of single-line trace species see Table 3.1 (for details on the related LMIO mission design see Kirchengast et al. (2010a); Schweitzer (2010); Kirchengast and Schweitzer (2011)).

Defocusing correction

The starting point are the raw, quasi-realistically simulated LIO signal power profiles in dBW reaching the receiver detectors, as shown in Figs. 3.4a and 3.5a. These panels show the signal power profiles as a function of time for the absorption channel (solid green line) and for the reference channel (dashed-dotted red line). The atmospheric settings are defined in Sect. 4.2. In practice, power normalized to a reference power value, $\tilde{P}$ in $\mathrm{W\,W^{-1}}$, is then used. For real data the reference generally is the noise-equivalent power of the detection system (Schweitzer, Kirchengast and Proschek 2011), leading to the signal-to-noise ratio, and for simulated data in EGOPS we use the power value at the top-altitude level. From the previous preparatory step (cf. Sect. 3.3.3) we can allocate to every power value $\tilde{P}(t_i)$ an IR impact parameter a_i and IR altitude z_i, respectively.

The defocusing correction clears the signal powers from the influence of spherical signal spreading and differential bending, which reduces the signal power increasingly from top to bottom by up to a maximum defocusing loss of near 5 dB at 5 km (cf. Schweitzer, Kirchengast and Proschek 2011). The "bump" on the power profiles visible within 5 s to 7 s in Figs 3.4a and 3.5a is a feature of the defocusing around the tropopause height, due to the sharp change of the vertical gradient of the refractive index there. The defocusing correction is based on equations developed by Jensen et al. (2003). A detailed algorithmic description of the defocusing correction for LMO, which we identically use in the LIO retrieval, is given by Schweitzer et al. (2011) who also address its limitations in non-spherically symmetric atmospheres; residual effects of horizontal gradients only cancel in differential transmissions between neighbor frequencies as formed in Sect. 3.3.4 below. As top-of-atmosphere (TOA) reference power, needed in the algorithm, we use the measured LIO signal powers at an altitude of 65 km with an averaging interval of 4 km. At these high altitude levels negligible absorption takes place at the channel frequencies selected so that we have essentially unity transmission and otherwise only noise contributions. In the LMO retrieval (Schweitzer et al. 2011), the defocusing loss is applied to amplitudes but it is equally valid for powers (with dB-conversion factor of 10 instead of 20). For LIO the corrected power profiles in dB, applying a defocusing

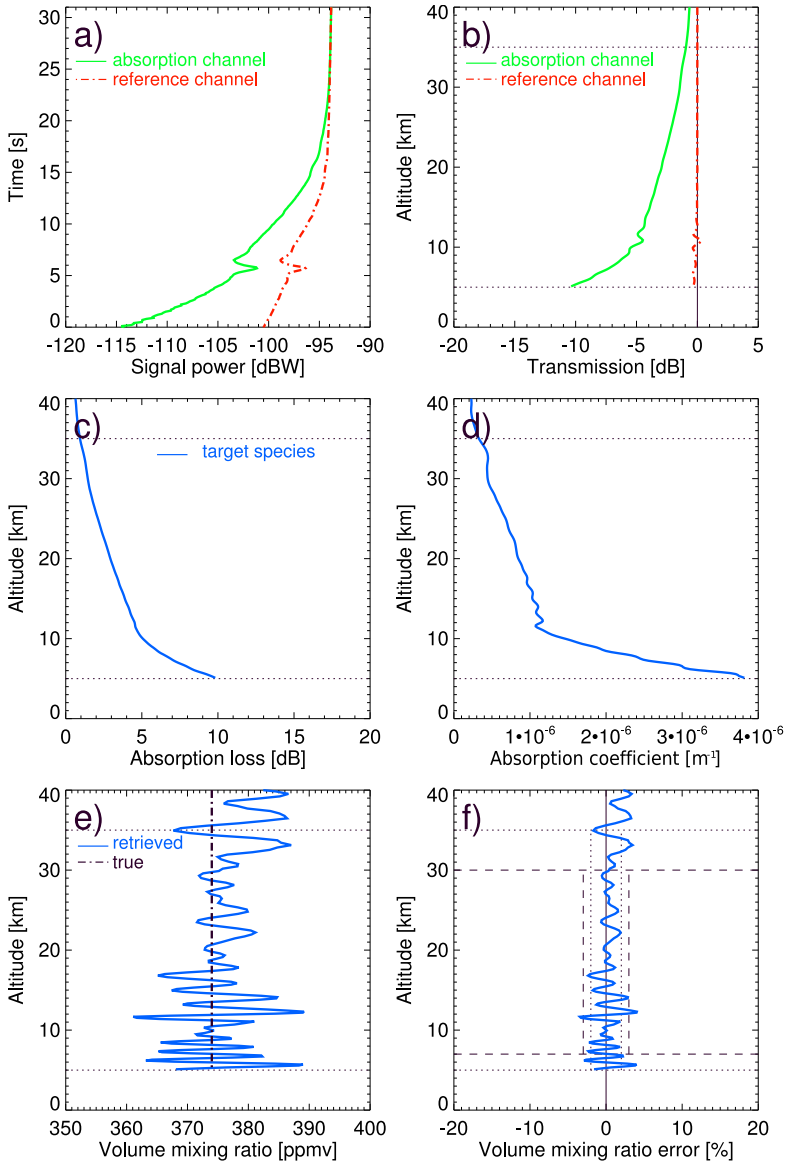

Figure 3.4: Illustration of the single-line trace species retrieval (SSR) algorithm for the single-line species $^{12}CO_2$. **(a)** LIO input profiles, simulated signal powers for the $^{12}CO_2$ absorption (green solid line) and reference (red dashed-dotted line) channel as a function of time. **(b)** Transmission profiles for the two channels after defocusing and spreading correction and allocation to the IR altitude grid. **(c)** $^{12}CO_2$ absorption loss profile after absorption-reference channel differencing and correction for all background effects. **(d)** $^{12}CO_2$ absorption coefficient profile after Abel transform retrieval. **(e)** Retrieved (blue solid) and true (black dashed-dotted) $^{12}CO_2$ volume mixing ratio (VMR) profile. **(f)** $^{12}CO_2$ VMR retrieval error profile (retrieved-minus-true relative to true). The horizontal and vertical dotted/dashed lines – especially used in panel **(f)** indicate the target/threshold observational requirements for altitude domain and accuracy for the LMIO mission concept (Larsen, Kirchengast and Bernath 2009; Kirchengast et al. 2010a).

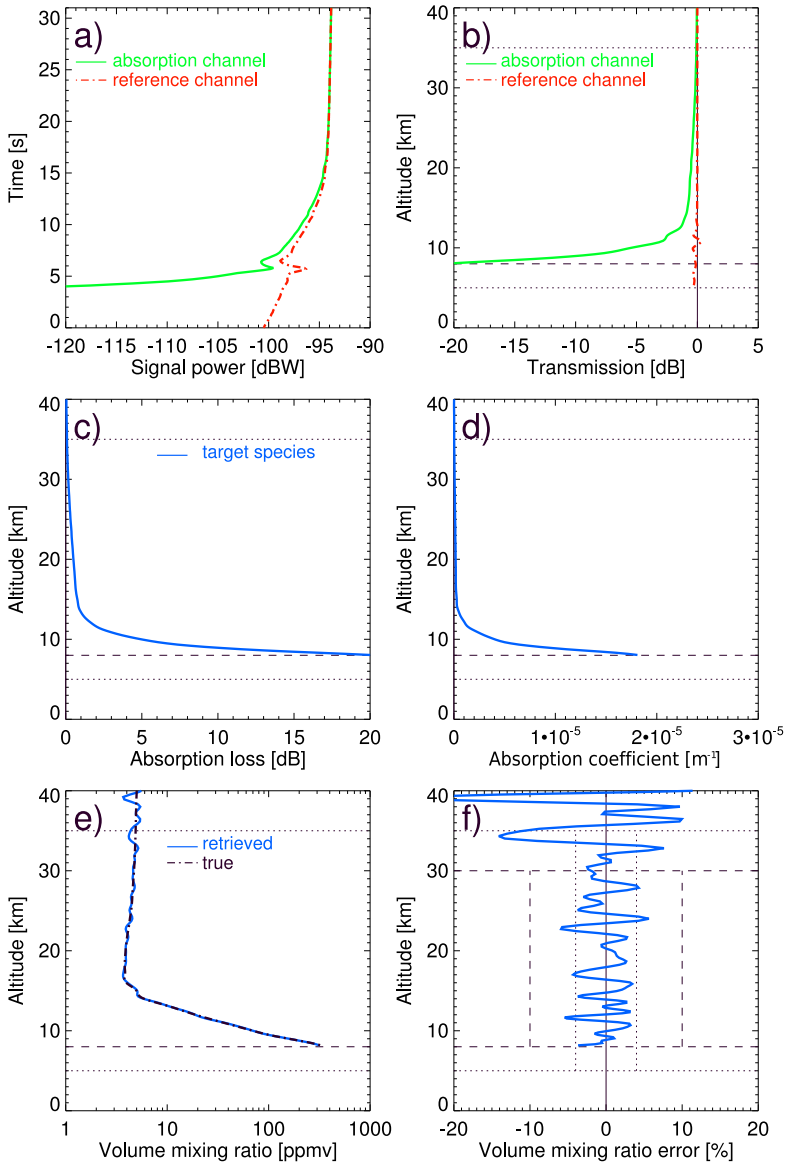

Figure 3.5: Illustration of the single-line trace species retrieval (SSR) algorithm for the single-line species $H_2O(2)$. The layout is the same as in Fig. 3.4; see that caption for explanation.

correction term ($\tilde{P}_{\mathrm{dc}}(a_i)$) analogously to Schweitzer et al. (2011), are given by

$$\mathcal{T}(a_i) \;=\; -10\;\left[\log\left(\tilde{P}(a_i)\right) \;-\; \log\left(\tilde{P}_{\mathrm{dc}}(a_i)\right)\right]. \tag{3.12}$$

The resulting transmission profiles for absorption and reference channel after the defocusing correction are illustrated in Figs. 3.4b and 3.5b. We note that the defocusing correction is not necessarily needed if differential transmission is used, such as we will use here for the GHG profiling. This applies because the very closely spaced LIO absorption and reference channel frequencies experience the same defocusing and beam spreading, which is thus automatically corrected for simply by the use of differential transmissions. However, differential transmissions can generally not be used when targeting information such as aerosol extinction, scintillation strength, or cloud layering profiles. These require the use of single-channel transmissions directly and in those cases the defocusing correction will thus be needed.

Target species transmission retrieval

The starting point for the target species transmission retrieval are the transmissions of a channel pair consisting of an absorption and a reference channel (either raw transmissions or defocusing-corrected transmission as explained in Sect. 3.3.4). Such transmissions can be seen in Fig. 3.4b for the retrieval of $^{12}CO_2$ and in Fig. 3.5b for the retrieval of $H_2O(2)$, respectively. In this section we discuss how these transmission profiles are corrected from further atmospheric influences, such as scintillation noise, aerosol extinction, Rayleigh scattering and absorption due to foreign species. The output will be the pure transmission profile due to the target species only.

Correction for broadband atmospheric effects

Since the transmissions of the absorption-channel signal $\mathcal{T}_{\mathrm{Abs}}(a_i)$ and the reference-channel signal $\mathcal{T}_{\mathrm{Ref}}(a_i)$, both given in dB, experience very similar broadband atmospheric influences (in air without clouds especially scintillation, aerosol extinction, broadband/-continuum absorption, and Rayleigh scattering; cf. Schweitzer, Kirchengast and Proschek (2011); Schweitzer (2010)), a simple difference of the two channel transmission profiles eliminates these influences to a high degree

$$\Delta\mathcal{T}(z_i) \;=\; \Delta\mathcal{T}(a_i) \;=\; \mathcal{T}_{\mathrm{Abs}}(a_i) \;-\; \mathcal{T}_{\mathrm{Ref}}(a_i). \tag{3.13}$$

This differential transmission profile $\Delta\mathcal{T}(z_i)$ in dB at the z_i level (applicable interchangeably with the a_i level) is corrected for potentially remaining absorption effects from absorption lines of foreign species that are not broad and overlap the target species absorption line.

Correction for foreign species absorption

As the absorption and/or reference signal have, despite a careful channel selection process (Kirchengast and Schweitzer 2011), some small but non-negligible sensitivity to line absorption by foreign species (Schweitzer 2010; Schweitzer, Kirchengast and Proschek 2011), these residual foreign species absorptions need be eliminated as well. Their influence is modeled by use of the initial/background GHG trace species profiles. Specifically, the absorption channel needs to be corrected for the absorption of all foreign species, the reference channel for the absorption of all foreign species plus the target species (the latter being in the reference channel, where absorption ideally should be truely zero, also a type of foreign species; therefore we use here the simplified generic terminology "foreign species correction"). The set of foreign species accounted for is composed of the potentially relevant foreign species $\{M : X \setminus \{\text{Target} : \text{Target} \in X\}\}$ where $X = \{N_2O$, CH_4, $^{12}CO_2$, $^{13}CO_2$, $C^{18}OO$, H_2O, HDO, $H_2^{18}O$, CO, $O_3\}$; all others are negligible at the selected LIO channel frequencies.

The transmissions for the foreign species were calculated in the xEGOPS system with the Reference Forward Model (RFM) (Edwards 1996; Dudhia 2008), using the spectroscopic parameters from HITRAN2004 (Rothman et al. 2005) and user-supplied atmospheric profiles (see RFM introduction in Sect. 4.2). Here we supply RFM with the LMO profiles p, T and the initial/background GHG profiles to obtain the ensemble of modeled species transmissions needed (see Fig. 3.2). For the absorption channel we use the ensemble $\{M\}$ for computing the background transmission $\mathcal{T}_{\text{Abs,bgr}}(z_i)$ from the foreign species, for the reference channel we use the ensemble of all species $\{X\}$ to compute the background transmission $\mathcal{T}_{\text{Ref,bgr}}(z_i)$. The difference of these two modeled background transmission profiles yields the differential background transmission profile from the foreign species, $\Delta\mathcal{T}_{\text{bgr}}(z_i)$, given by

$$\Delta\mathcal{T}_{\text{bgr}}(z_i) \;=\; \mathcal{T}_{\text{Abs,bgr}}(z_i) \;-\; \mathcal{T}_{\text{Ref,bgr}}(z_i)\,. \tag{3.14}$$

The pure target species transmission in the absorption channel, $\mathcal{T}_{\text{tgt}}(z_i)$, can thus be obtained by subtracting the differential background transmission profile $\Delta\mathcal{T}_{\text{bgr}}(z_i)$ (Eq. 3.14) from the differential transmission profile $\Delta\mathcal{T}(z_i)$ (Eq. 3.13),

$$\mathcal{T}_{\text{tgt}}(a_i) \;=\; \mathcal{T}_{\text{tgt}}(z_i) \;=\; \Delta\mathcal{T}(z_i) \;-\; \Delta\mathcal{T}_{\text{bgr}}(z_i)\,, \tag{3.15}$$

where the resulting target species transmission profile (in units dB) can again be alternatively used at the a_i level, which is needed for the next step of absorption coefficient retrieval.

The magnitude of $\mathcal{T}_{\text{tgt}}(z_i)$, the target species absorption loss profile, is illustrated for the $^{12}CO_2$ and $H_2O(2)$ channels in Figs. 3.4c and 3.5c, respectively. The $H_2O(2)$ absorption loss exceeds the upper bound of favorable dynamic range ($0.25\,\text{dB} < |\mathcal{T}_{\text{tgt}}(z_i)| < 13\,\text{dB}$, corresponding to about 5 % to 95 % absorption; Kirchengast and Schweitzer (2011);

Schweitzer, Kirchengast and Proschek (2011)) at altitudes below about 8.5 km. This indicates why for H_2O, with its very high dynamic range of concentrations over the UTLS, several single-line species are needed to properly cover the full UTLS. The absorption loss for $^{12}CO_2$ is within the favorable dynamic range from top to bottom over the UTLS, reaching about 10 dB at an altitude of 5 km. Typical sizes of the target species and foreign species transmissions of all other GHG species according to Table 3.1 are found in Schweitzer, Kirchengast and Proschek (2011) for a set of representative atmospheric conditions.

Absorption coefficient retrieval

The next important step is the retrieval of the (volume) absorption coefficient $\kappa(z_i)$ in units m^{-1} from the target species transmission profile $\mathcal{T}_{tgt}(a_i)$. For this purpose we employ the same absorptive Abel transform as used and described in detail by Schweitzer et al. (2011) for the LMO absorption coefficient retrieval. This type of Abel transform leads to noise amplification by about a factor of 2 to 2.5 (Sofieva and Kyrölä 2004). The absorptive Abel transform implementation in EGOPS is very robust, however, and designed to minimize this noise amplification (Schweitzer et al. 2011).

The resulting example absorption coefficient profiles for $^{12}CO_2$ and $H_2O(2)$ are shown in Figs. 3.4d and 3.5d, respectively. It is seen, best visible for the $^{12}CO_2$ case, that the noise increases from the absorption loss profile to the absorption coefficient profile due to the noise amplification discussed above. Future more special filtering may slightly reduce this noise further; regarding resolution the filtering is currently set to yield a high vertical resolution of about 1 km (Schweitzer et al. 2011). In terms of absorption coefficient magnitudes, profiles are useful for subsequent atmosperic profiles retrieval with high accuracy (1 % level) within an absorption coefficient range of about $10^{-7}\,m^{-1}$ to $10^{-5}\,m^{-1}$ as also discussed by Schweitzer et al. (2011). Consistent with the respective behavior of the absorption loss profile, the $^{12}CO_2$ absorption coefficient profile fully fits this range while the $H_2O(2)$ one begins to exceed it near 8 km and other H_2O channels will have to complement it in the lowest part of the UTLS towards 5 km.

Atmospheric profiles retrieval

The last step of the SSR process is the retrieval of atmospheric profiles, in particular of the volume mixing ratio (VMR) profile of the GHG or minor isotope target species, $\chi(z_i)$ in units ppmv, from the absorption coefficient profile $\kappa(z_i)$ in units m^{-1}. In addition (see Fig. 3.2) we need a modeled molar absorption cross section of the target species $\epsilon(z_i)$ (units $m^2\,mol^{-1}$). This is computed again with RFM, based on the initial/background target species profile (units ppmv) and the p (units Pa) and T (units K) profiles from LMO interpolated to the z_i level.

With these input profiles, the VMR profile $\chi(z_i)$ is then calculated as

$$\chi(z_i) \;=\; 10^6 \; R^* \; \frac{\kappa(z_i)}{\epsilon(z_i)} \; \frac{T(z_i)}{p(z_i)}, \tag{3.16}$$

where $R^* = 8.3145\,\mathrm{J/(K\,mol)}$ is the universal molar gas constant and the factor 10^6 is the conversion factor from dimensionless fraction to ppmv (e.g., Salby (1996)). We note that alternatively or additionally we also could compute the target species dry air mole fraction and/or the target species absolute concentration, likely preferable for some applications in case of real data. In this end-to-end simulation framework we can refrain from computing these additional profiles, however, since the VMR profile is well representative and convertible with the help of the thermodynamic profiles to any other representation.

The resulting example VMR profiles for $^{12}CO_2$ and $H_2O(2)$ are shown in Figs. 3.4e and 3.5e, and the relative VMR error is displayed in Figs. 3.4f and 3.5f, respectively. It can be seen that $^{12}CO_2$ is retrieved to higher accuracy than H_2O. The relative error of CO_2, looked at as a standard deviation, is within 2 % over the ULTS due to the good absorption signal at all altitudes (Fig. 3.4c and d). The $H_2O(2)$ is more at a standard deviation near 3 %, and beyond above about 32 km, since the absorption signal (Fig. 3.5c and d) is less favorably distributed over the UTLS.

Generally these single-line example retrievals appear unbiased and at fairly high accuracy, within the target observational requirements (marked on the panels) that were set by scientific objectives of atmosphere and climate research planned to be supported by LMIO data (Larsen, Kirchengast and Bernath 2009; Kirchengast et al. 2010a). More details on the performance are discussed in the sections below.

3.3.5 Multi-line trace species retrieval (MSR)

This section discusses the inner loop of the LIO retrieval, called multi-line trace species retrieval (MSR) (cf. Fig. 3.3). This MSR loop handles the consecutive retrieval of the multiple species. Its purpose is to ensure that the set of trace species is retrieved in a well defined order and to update the set of the initial/background GHG profiles so that the SSR core process finds this set improved by a new retrieved profile after every step of the MSR loop (details in Sect. 3.3.5). The set is needed in the SSR for the foreign species correction (Sect. 3.3.4) within the target species transmission retrieval and for the molar absorption cross section calculation (Sect. 3.3.4) within the atmospheric VMR profile retrieval. Additionally, the composite VMR profiles of CO_2 and H_2O are improved at each step of the MSR loop by combining adequate retrieved single-line species profiles (details in Sect. 3.3.5).

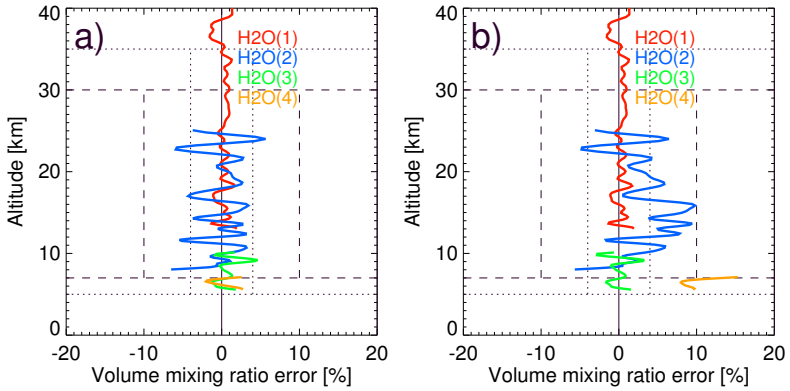

Figure 3.6: Demonstration of the influence of the single-line trace species order in the MSR loop on VMR retrieval errors of the four single-line species $H_2O(X)$ ($X = \{1, 2, 3, 4\}$). VMR errors from a correct and sensible order **(a)** are shown compared to VMR errors for an intentionally sub-optimal order, where no CO_2 retrieval was placed before the H_2O retrievals **(b)**; see the text in Sect. 3.3.5 for further explanation.

Trace species retrieval order

Generally, the SSR process requires the VMR profiles of the main atmospheric absorbers to be able to assess the contribution of foreign species absorption on the transmission of the absorption and reference channels (as explained in Sect. 3.3.4). At the very start of the MSR process (at the start of the basic run of the outer loop), the array of retrieved trace species profiles of the relevant atmospheric absorbers (which are H_2O, CO_2, CH_4, N_2O, O_3, CO for our channels) is set to initial values, which might be a priori VMR profiles from an atmospheric model or even just zero. In the LIO retrieval these initial/background GHG profiles (cf. LIO auxiliary input in Fig. 3.2) are either taken from a FASCODE atmosphere that is somewhat adjacent in atmospheric conditions to the FASCODE atmosphere used as "true" one in the forward modeling (e.g., standard atmosphere as initial if tropical is the "true"), or set to zero for test purposes.

After the first SSR step, one obtains the VMR profile of the target species (see Sect. 3.3.4) that is first in the order. The respective initial/background GHG profile is then updated by this retrieved one. All other species remain at the initial values. In this spirit the MSR proceeds to perform a full chain of SSRs, consecutively retrieving the target species in a sensible order, and after each SSR step the set of initial/background GHG profiles gets improved by a new retrieved profile. Hence, the foreign species correction for the absorption and reference channel in the SSR (cf. Sect. 3.3.4) gets improved every step as more and more initial profiles are superseded by actual retrieved profiles. Thus overall the MSR is an envelope process over the SSR, which after a complete first MSR

loop (complete basic run) has entirely superseded the original set of initial/background GHG profiles by retrieved profiles. Even if the intial values were zero, this first full set of retrieved profiles can be expected to be very accurate already since the foreign species interference is very small thanks to the careful selection of the LIO channels (Kirchengast and Schweitzer 2011; Schweitzer, Kirchengast and Proschek 2011).

To ensure such accurate retrieval results, it is key to employ a well defined sequence in which the VMR profiles of the single gases are retrieved by the SSR process. Since the channels used for retrieving the species have different sensitivity to foreign species absorption, those gases need to be retrieved first the channels of which exhibit least sensitivity to any other species. In the case of the set of channels used in this study, a very suitable sequence that we found based on the studies of atmospheric influences on LIO signals by Schweitzer (2010) and Schweitzer, Kirchengast and Proschek (2011) is listed in Table 3.1. That is, in Table 3.1 the sensitivity to foreign species absorption is generally lowest to highest from top to bottom and at the same time the foreign influence on species coming later is generally highest to lowest from top to bottom. This ensures accurate retrieval results even if one starts with an initial concentration of the foreign species of zero, since the top listed ones are themselves fairly insensitive and on the other hand precede the later ones which they influence. In this way the MSR-computed set of VMR profiles is effectively independent of a priori information, enabling – together with other favorable properties from using the occultation principle with coherent signals – its climate benchmarking capability (Kirchengast et al. 2010a; Kirchengast and Schweitzer 2011).

An illustrative example result of the dependency of the retrieval on the species order in the set of initial/background GHG profiles is given in Fig. 3.6. In these panels VMR errors are shown for the $H_2O(X)$ single-line retrievals with $X = \{1, 2, 3, 4\}$. The individual $H_2O(X)$ channels are suitable for different altitudes as indicated in Table 3.1. Figure 3.6a shows the SSR error results for the four $H_2O(X)$ cases when using the correct initial/background GHG profile order according to Table 3.1 (N_2O, CH_4, CO_2, etc.). In contrast, Fig. 3.6b shows the VMR error profiles for the four $H_2O(X)$ cases when using a zero-valued initial/background CO_2 profile, i.e., when not retrieving CO_2 before H_2O. The concentrations of N_2O and CH_4 were set to the correct values. It can be seen that the $H_2O(2)$ and $H_2O(4)$ channels show a significant dependence on the CO_2 VMR profile (while the $H_2O(1)$ and $H_2O(3)$ channels show nearly no dependence). Although less ambitious remote sensing systems would not care too much about errors still not higher than about 10 % (that in addition would be largely part of random rather than systematic error in ensembles of profiles), these $H_2O(2)$ and $H_2O(4)$ test results are clearly at the margin of the demanding requirements for the LMIO method. It is therefore encouraging to see in Fig. 3.6a that a sensible order of species in the MSR does a highly effective job in keeping results unbiased and in terms of standard deviation keeping them well within target requirements already in a single basic run of the MSR loop.

Composite CO_2 and H_2O profiles

An important further part of the MSR process is the meaningful combination of suitable VMR profiles from the SSR in order to improve the overall VMR error of a species. This is done for ${}^{X}CO_2$ channels for two different isotopes and for the four $H_2O(X)$ single-line species to merge the individual profiles covering the UTLS piecewise into a composite profile covering the full UTLS.

As the general approach any composite species VMR profile $\chi_c(z_i)$ is derived via summation of a number of n single-line species VMR profiles $\chi_m(z_i)$, scaled by their isotopic fractional abundances a_m and weighted by inverse-variances $w_m(z_i)$ representing their relative uncertainty,

$$\chi_c(z_i) = a_c \sum_{m=1}^{n} \left(w_m(z_i) \frac{\chi_m(z_i)}{a_m} \right), \tag{3.17}$$

where the additional factor a_c is the assigned fractional abundance of the composite (usually set to unity for representing the full abundance of all isotopes of a species). Note that for the single-line species other than CO_2 and H_2O such as CH_4 and O_3 we also employ Eq. (3.17) in its simplest form ($n = 1$, $a_c = 1$, $w_m(z_i)$ is unity), just for dividing the single-species result from Eq. (3.16) by the respective isotopic abundance to obtain the VMR for the full species abundance.

The inverse-variance weight $w_m(z_i)$ in Eq. (3.17) is defined by

$$w_m(z_i) = \frac{1}{\sum_{m=1}^{n} \left(\frac{1}{\varepsilon_m^2(z_i)} \right)} \frac{1}{\varepsilon_m^2(z_i)}. \tag{3.18}$$

where the normalization factor of $1/\varepsilon_m^2$ ensures that the sum of all weights w_m is unity.

The isotopic fractional abundances a_m are taken from Rothman et al. (2005). The standard error profiles $\varepsilon_m(z_i)$ utilized to build the variances express the altitude-dependent errors of the individual VMR profiles (in units %), which determine the weight of any individual profile relative to the other profiles; their formulation for our specific CO_2 and H_2O composites is summarized below. The performance improvement derives from the fact that the error of the composite profile from the simple optimal estimation formulated by Eqs. (3.17) and (3.18) will at any altitude level always be smaller than the smallest individual profile error at that level. For example, combining two profiles with equal errors would lead to a composite profile with the error reduced by a factor of $1/\sqrt{2}$. On the other hand, with two significantly unequal errors the composite profile error would be only very slightly reduced against the smaller of the two errors.

CO_2 composite profile and its weighting:

The composite CO_2 VMR profile $\chi_{CO_2}(z_i)$ is derived by combining the two isotopes ${}^{12}CO_2$ and ${}^{13}CO_2$ via inverse-variance weighting including static standard errors. The

rationale for combining just these two isotopes is their known highly stable isotopic ratio δ^{13}C in the free atmosphere, which can thus be relied on in the combination of the profiles over the UTLS (δ^{13}C ratio variations <0.05 %; Allison and Francey (2007)). Employing Eq. (3.17) with the composite abundance a_c set to unity, $\chi_{CO_2}(z_i)$ is given by

$$\chi_{CO_2}(z_i) = w_{^{12}CO_2}(z_i) \frac{\chi_{^{12}CO_2}(z_i)}{a_{^{12}CO_2}} + w_{^{13}CO_2}(z_i) \frac{\chi_{^{13}CO_2}(z_i)}{a_{^{13}CO_2}}, \tag{3.19}$$

where $a_{^{12}CO_2} = 0.98420$ and $a_{^{13}CO_2} = 0.01106$ (Rothman et al. 2005).

The needed relative VMR error profiles $\varepsilon_{CO_2}(z_i)$ in % for $^{12}CO_2$ and $^{13}CO_2$ (we suppress the index m for brevity in formulating $\varepsilon_{CO_2}(z_i)$ but it clearly applies to both profiles) are specified from experience with simulated LIO retrieval performance for these two species so far. This indicated a characteristic height dependence of the two errors relative to each other. This dependence can be embodied into a simple static error model following the empirical vertical error modeling approach developed in the GRO context by Steiner and Kirchengast (2005) and recently also adopted by Scherllin-Pirscher et al. (2011). This simple model can be written as

$$\varepsilon_{CO_2}(z_i) = \begin{cases} \varepsilon_0 + q_0 \left[\frac{1}{z_i^p} - \frac{1}{z_{\mathrm{Ttop}}^p} \right], & \text{for } z_{\min} < z_i \leq z_{\mathrm{Ttop}} \\ \varepsilon_0, & \text{for } z_{\mathrm{Ttop}} < z_i \leq z_{\mathrm{Sbot}} \\ \varepsilon_0 \exp \left[\frac{(z_i - z_{\mathrm{Sbot}})}{H_S} \right], & \text{for } z_{\mathrm{Sbot}} \leq z_i < z_{\max} \end{cases} \tag{3.20}$$

It models the errors as constant (ε_0 in %) in an UTLS core region, with an exponential increase defined by an error scale height H_S above this region, and with an increase by an inverse altitude law, defined in shape by q_0 and by the power parameter p of z, below this region. For a more detailed discussion see Steiner and Kirchengast (2005) and Scherllin-Pirscher et al. (2011). Roughly reflecting the $^{12}CO_2$ and $^{13}CO_2$ VMR errors estimated in initial performance analyses we set the model parameters to $z_{\min} = 0.5$ km, $z_{\mathrm{Ttop}} = 15$ km, $z_{\mathrm{Sbot}} = 25$ km, $z_{\max} = 80$ km, $\varepsilon_0 = 1.0$ % for $^{12}CO_2$ and 0.5 % for $^{13}CO_2$, $q_0 = 10$ % for $^{12}CO_2$ and 15 % for $^{13}CO_2$, $p = 0.5$ for both isotopes, and $H_S = 18$ km for $^{12}CO_2$ and 12 km for $^{13}CO_2$. Additionally, the resulting error $\varepsilon_{CO_2}(z_i)$ is bounded to a maximum of 10 %, which is a reasonable bound becoming effective below a height of 1 km (practically irrelevant in the context here) and above 60 km.

The two error profiles are illustrated in Fig. 3.7a for the altitude range of main interest. Figure 3.7b shows the corresponding errors of the retrieved VMR profiles of $^{12}CO_2$, $^{13}CO_2$, and of the composite CO_2 VMR profile obtained according to Eqs. (3.19) and (3.20). The effect of more equal weighting is visible in particular at altitudes below about 10 km, where the two individual errors are comparable. At higher altitudes, the composite is dominated by the lower $^{13}CO_2$ VMR error but the $^{12}CO_2$ VMR error is clearly seen to aid as well, especially if the two errors are incidentally opposite in sign such as above 30 km. Overall the quality of the composite CO_2 profile is clearly improved over either

individual profile, staying unbiased with a standard deviation of less than 1 % over most of the altitude range.

H_2O composite profile and its weighting

The VMR profile of H_2O is composed of the four $H_2O(X)$ ($X = \{1, 2, 3, 4\}$) single-line species VMR profiles, which exhibit their respective best sensitivities in different height ranges. Hence the composite H_2O profile can be expected to be very accurate throughout the whole UTLS whereas a single profile is accurate only in a limited height range (cf. Table 3.1; typical validity height range per H_2O channel quoted in brackets). Since the composite H_2O profile consists of profiles having the same isotope abundance, Eq. (3.17) turns for $\chi_{H_2O}(z_i)$ into the simple form

$$\chi_{H_2O}(z_i) \;=\; \frac{1}{a_{H_2^{16}O}} \sum_{m=1}^{4} \left(w_m(z_i) \;\; \chi_{H_2O(m)}(z_i) \right), \tag{3.21}$$

where $a_{H_2^{16}O} = 0.997317$ after Rothman et al. (2005).

In this case, the relative VMR error profiles $\varepsilon_{H_2O}(z_i)$ in % for the four individual profiles need a dynamical error model, since H_2O is a highly variable species (also here we supress the index m in formulating $\varepsilon_{H_2O}(z_i)$ but it clearly applies to all four profiles). We follow the semi-analytical retrieval error propagation modeling in the simplified LIO performance simulator tool ALPS (Kirchengast et al. 2010b), which was described most accurately recently by Kirchengast and Schweitzer (2011). In particular, a reasonable simple estimate of the error profiles is given by the ratio of an empirically approximated absolute error profile ($\mathcal{E}_{\mathcal{T}}(z_i)$) in dB and the retrieved target species absorption loss profile $|\mathcal{T}_{tgt}(z_i)|$ in dB (cf. Sect. 3.3.4) in the form

$$\varepsilon_{H_2O}(z_i) \;=\; 100 \; \frac{\mathcal{E}_{\mathcal{T}}(z_i)}{|\mathcal{T}_{tgt}(z_i)|}, \tag{3.22}$$

where the factor 100 is to provide units %. The absolute error profile $\mathcal{E}_{\mathcal{T}}(z_i)$ in Eq. (3.22) is formulated as

$$\mathcal{E}_{\mathcal{T}}(z_i) \;=\; c_{f2dB} \left[10^{-\left(\frac{SNR_{Abs}(z_i)}{10}\right)} \;+\; \mathcal{E}_{\mathcal{T},resid} \right], \tag{3.23}$$

where $SNR_{Abs}(z_i)$ in dB is an estimate of the signal-to-noise ratio profile of the absorption channel, $\mathcal{E}_{\mathcal{T},resid}$ is a fractional residual error set to 0.003 (lower bound error at high altitudes), and $c_{f2dB} = 4.3429\,dB/1$ is the conversion factor from fractional values to units dB. The SNR profile $SNR_{Abs}(z_i)$ in Eq. (3.23) is dynamically estimated as

$$SNR_{Abs}(z_i) \;=\; SNR_{TOA} \;-\; \mathcal{L}_{bgr}(z_i) \;-\; |\mathcal{T}_{tgt}(z_i)|, \tag{3.24}$$

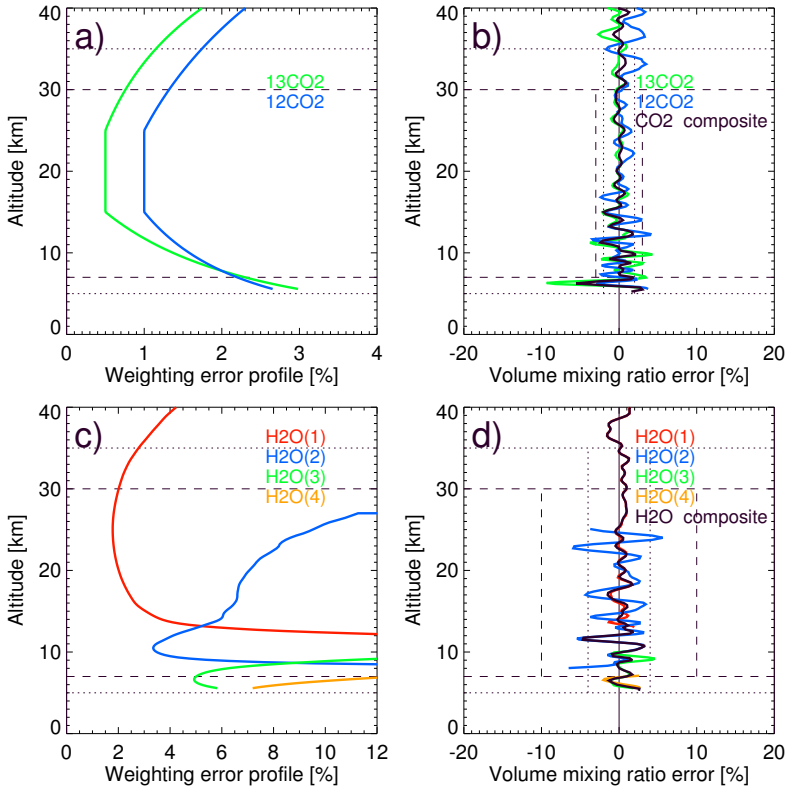

Figure 3.7: Ilustration of combining the $^{12}CO_2$ and $^{13}CO_2$ VMR profiles into a composite CO_2 profile (top panels), and of the four $H_2O(X)$ ($X = \{1, 2, 3, 4\}$) VMR profiles into a composite H_2O profile (bottom panels). The left panels **(a, c)** show the weighting error profiles used within the respective weighting functions for inverse-variance-weighted combination of the profiles (different color per single-line species). The right panels **(b, d)** show the VMR retrieval error results of the individual single-line species (colored lines) overplotted by the error of the composite profile (black line).

where $\mathrm{SNR}_{\mathrm{TOA}}$ is the top-of-atmosphere value of the SNR set to 33 dB (an adequate value at TOA where transmission is unity; e.g., Kirchengast et al. (2010a); Kirchengast and Schweitzer (2011)), $\mathcal{L}_{\mathrm{bgr}}(z_i)$ in dB is a simple estimate of the total background loss profile, and definitely also the target species absorption loss profile $|\mathcal{T}_{\mathrm{tgt}}(z_i)|$ needs to be subtracted to have a reasonable estimate of the total SNR profile $\mathrm{SNR}_{\mathrm{Abs}}(z_i)$. The background loss profile $\mathcal{L}_{\mathrm{bgr}}(z_i)$ can be approximated by the dominating contribution of defocusing loss (cf. Schweitzer, Kirchengast and Proschek 2011) for which a simple exponential model in units dB following Kirchengast et al. (2010b) is

$$\mathcal{L}_{\mathrm{bgr}}(z_i) \;=\; \mathcal{L}_0 \;\exp\left[-\frac{(z_i \;-\; z_0)}{H_{\mathrm{loss}}}\right], \tag{3.25}$$

where $\mathcal{L}_0$ set to 10 dB is the estimated value of $\mathcal{L}_{\mathrm{bgr}}$ at the base height $z_0 = 0$ km and where the defocusing loss scale height H_{loss} is set to 11 km.

Briefly to explain the behavior of the model $\varepsilon_{\mathrm{H_2O}}(z_i)$ according to Eqs. (3.22) to (3.25), the absolute error profile $\mathcal{E}_{\mathcal{T}}(z_i)$ in the numerator is basically dominated by the (decaying) background loss profile $\mathcal{L}_{\mathrm{bgr}}(z_i)$ at higher altitudes and by the increasingly growing absorption loss profile $|\mathcal{T}_{\mathrm{tgt}}(z_i)|$ at lower altitudes. The absorption loss in the denominator does not grow as fast downwards as the absolute error in the numerator, however, so that also the relative error $\varepsilon_{\mathrm{H_2O}}(z_i)$ strongly increases downwards when absorption in a channel becomes strong. On the other hand $\varepsilon_{\mathrm{H_2O}}(z_i)$ increases as well towards higher altitudes since the absorption loss in the denominator becomes small upwards faster than the absolute error. In order to limit the error below and above the height range where a particular channel is most sensitive, we keep $\varepsilon_{\mathrm{H_2O}}(z_i)$ in practice constant at altitudes, where the respective absorption loss profile is outside 0.25 dB to 17 dB (setting the constant to the error value at the altitudes associated with these two threshold values). This ensures sufficient overlap between the channels at all heights and at the same time overall robustness of this dynamical composite profile estimation.

Figure 3.7c shows the resulting error profiles for the four $\mathrm{H_2O}(X)$ profiles with $X = \{1, 2, 3, 4\}$. The altitude regions with the best sensitivity of the channels are clearly visible as is the general altitude-dependent behavior described above; the contribution of the $\mathrm{H_2O}(4)$ channel is limited in this STD atmosphere case, its value is to support the very moist tropical conditions. An illustration of the corresponding errors of the VMR profiles of the four $\mathrm{H_2O}$ single-line retrievals and of the composite $\mathrm{H_2O}$ VMR profile is given in Fig. 3.7d. The benefit of the weighted profile combination is well visible, since it is clearly seen that the composite profile is very effective in exploiting at all altitude levels the best possible information. In this way the overall quality of the composite $\mathrm{H_2O}$ profile is substantially improved over either individual profile, staying unbiased and reaching a standard deviation of within 2 % essentially everywhere in the altitude range.

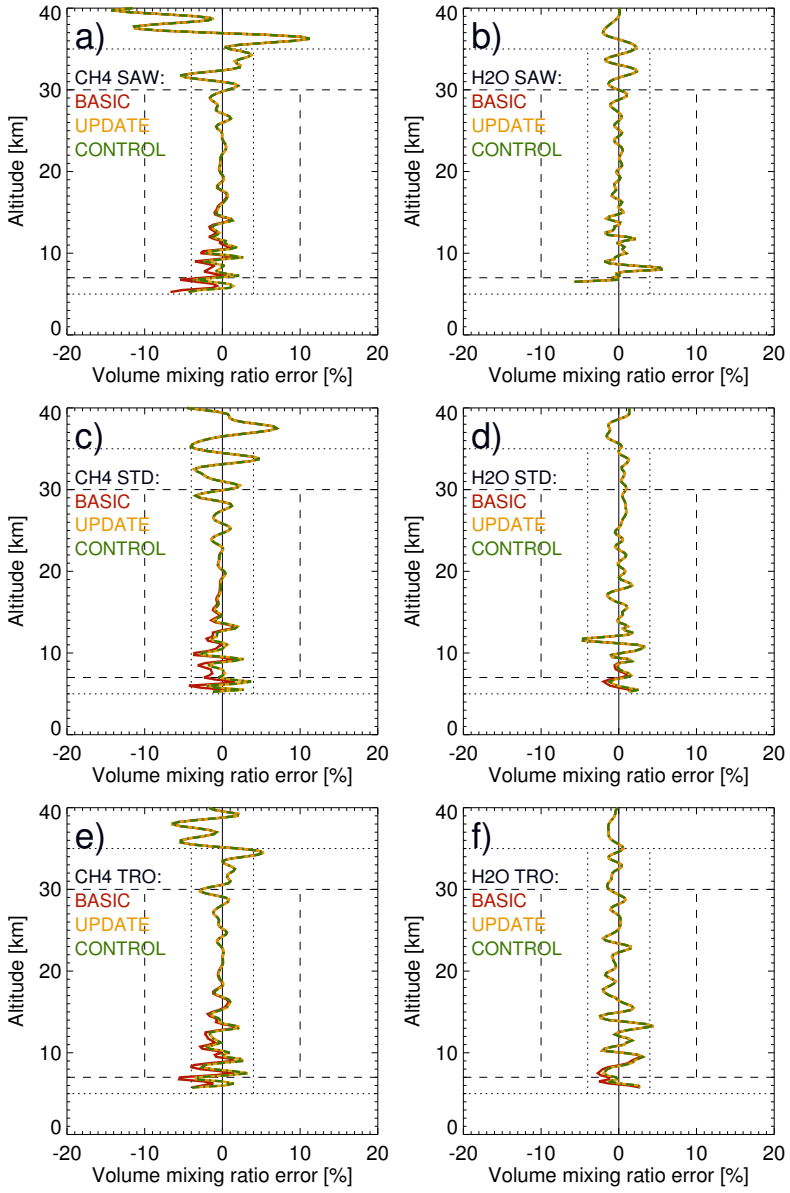

Figure 3.8: Retrieval performance results of the LMIO end-to-end simulations for CH_4 (left column) and H_2O (right column). VMR retrieval errors are shown for sub-arctic winter (top), standard (middle), and tropical (bottom) atmosphere conditions, for GHG retrieval results after the basic run (red line), update run (yellow line) and control run (green dashed-dotted line) of the basic-update-control run (BUC) loop.

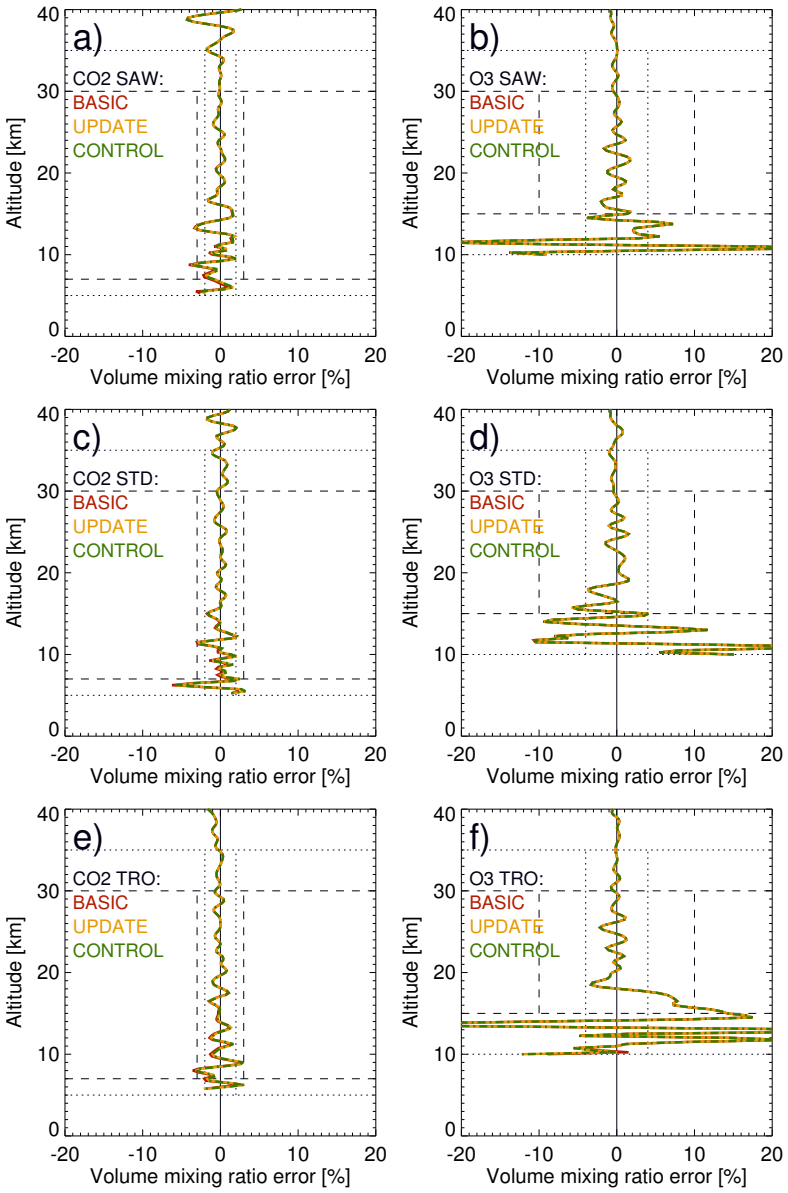

Figure 3.9: Retrieval performance results of the LMIO end-to-end simulations for CO_2 (left column) and O_3 (right column). The layout is the same as in Fig. 3.8; see that caption for explanation.

3.3.6 Basic-update-control (BUC) runs

The last step of the LIO retrieval is the outer loop, also called Basic-Update-Control run (BUC) loop. This loop is a simple envelope loop over the MSR process, as shown in Fig. 3.3, to guarantee (update run) and cross-check (control run) the convergence of the retrieved set of GHG/isotope profiles beyond the first complete step of the loop (basic run). Each of these runs consists of a full MSR process, including all trace species retrieved by the SSR core process in the well defined order presented in Sect. 3.3.5, and including the generation of the composite CO_2 and H_2O profiles. After the basic run, all initial/background GHG profiles are replaced by the retrieved GHGs, followed by the update run after which the GHG/isotope profiles are improved and the retrieval results have nominally fully converged. The control run provides quantitative quality control of the convergence of every single retrieved GHG profile over the full altitude range.

To provide an example of the effectiveness of the BUC loop, the output VMR profiles after each step of the loop are illustrated for CH_4 and H_2O in Fig. 3.8 and for CO_2 and O_3 in Fig. 3.9, for three representative atmospheric conditions. It is clearly seen that already the update run ensures full convergence for all species, which is verified by the control run result; details on these demonstration results are discussed in Sect. 3.4.

Regarding finally the computational efficiency of the complete LMIO retrieval algorithm in the EGOPS/xEGOPS system (LMO thermodynamic state retrieval and afterwards LIO multi-species retrieval with full BUC loop), it currently takes without any dedicated speed optimization effort and without compiler optimization about 30 min on a standard Linux workstation of the 2 GHz CPU class (the most demanding part being the RFM transmission computations for foreign species correction). Given the multi-parameter retrieval power and substantial room for speed improvements, this computational performance is very encouraging. It is clear that all data of any real LMIO mission could be readily processed within adequate time slots with a very moderate number of processors.

3.4 Demonstration results

Here we discuss the retrieval demonstration results of the set of representative example species of this study (CO_2, H_2O, CH_4, O_3); a more complete analysis comprising all LIO species and statistical retrieval performance estimates from ensemble simulations is on-going and will be published elsewhere. Figures 3.8 and 3.9 illustrate the GHG profiles retrieval performance achieved for CH_4, H_2O, CO_2, and O_3 by the LMIO retrieval after each run of the BUC loop in terms of VMR retrieval errors against the “true” VMR profiles used in the forward modeling. Intentionally the order of showing the results of the four species follows the sequence as they are retrieved within the MSR loop, facilitating to see (small) influences of whether a species is retrieved earlier or later. Three representative atmospheric conditions are considered (top to bottom in Figs. 3.8 and 3.9), the sub-arctic winter (SAW), standard (STD), and tropical (TRO) atmospheres

of the FASCODE model (Anderson et al. (1986); FASCODE (2008); with the CO_2 VMR updated to 380 ppmv as noted in Sect. 4.2).

For these demonstration cases, we subsequently retrieved the single-line species CH_4, $^{13}CO_2$, $H_2O(X)$ ($X = \{1, 2, 3, 4\}$), $^{12}CO_2$, and O_3 by use of the MSR process, with the SSR process embedded, in each run of the BUC loop. While CH_4 and O_3 are single-line species, i.e., derived from a single channel pair utilizing a single absorption line, CO_2 and H_2O are composite profiles as discussed in Sect. 3.3.5. The initial values for the four GHG profiles demonstrated here were set to zero to illustrate a "worst case" initialization. The other two initial/background GHG profiles needed (N_2O, CO) were set to their GHG values from the respective FASCODE atmosphere as we did not focus on these two here; their influence as foreign species is very small anyway (Schweitzer 2010) and their effects on the retrieval of the four example species generally negligible even if only rough knowledge of their concentrations is used.

CH_4 is the species retrieved first in the sequence and Fig. 3.8 (left column) shows the performance. Since the initial/background GHGs profiles at start of the basic run were zero, the foreign species correction necessarily yielded no appropriate estimate and indeed the CH_4 error from the basic run shows a slight negative bias within 1 % to 2 % below about 12 km under all atmospheric conditions (red profile). That this bias is relatively small despite the foreign species effects are not corrected at all indicates the careful selection of very "clean" channels. However, as the LMIO method targets to keep biases within 0.1 % to 0.2 %, a correction is clearly needed. It is seen that this correction is very effectively done by the update run (yellow dashed profile), for which all other GHGs are already available from the basic run. The control run (green dotted-dashed profile) then confirms that the CH_4 error has converged to within the 0.1 % level.

The single-line species next in sequence is $^{13}CO_2$, since it is helpful to have a first CO_2 profile estimate (that itself is not sensitive to H_2O) before retrieving H_2O (cf. the discussion of the sensitivity of H_2O to CO_2 in Sect. 3.3.5 and the related Fig. 3.6). This intermediate auxiliary single-line retrieval is followed by the retrieval of all four H_2O single-line profiles and the computation of the related H_2O composite profile for which the retrieval performance is shown in Fig. 3.8 (right column). Since for H_2O the initial/background GHG profiles for CH_4 and CO_2 are available during the basic run, the performance of this basic run is very good already. Small biases are visible only below about 9 km, especially for the moist tropical atmosphere, but staying within 1 % even there. In the dry sub-arctic winter case, where the first two single-line retrievals $H_2O(1)$ and $H_2O(2)$ favorably reach with their sensitivity deeper into the upper troposphere, the retrieval is already fully converged in the basic run. As for CH_4 the update run effectively corrects the remaining biases in the lowest part of the UTLS and leads to convergence to within the 0.1 % level as confirmed by the control run.

The CO_2 composite profile, which finishes retrieval as the third species next after H_2O, exhibits already very good performance from the basic run as illustrated in Fig. 3.9 (left column). Remaining biases relative to full convergence are at the order of 0.1 % also

everywhere below 10 km. This is possible for CO_2 because the foreign species correction can use the retrieved CH_4 and H_2O profiles as background in the basic run already. Only the initial/background GHG profile for O_3 is still zero, but there is no relevant cross-sensitivity of CO_2 to O_3 (cf. Schweitzer 2010; Schweitzer, Kirchengast and Proschek 2011). The update run very slightly changes the results from the basic run below about 10 km only and the control run again confirms the update run.

The species retrieved last is O_3, the retrieval performance of which is shown in Fig. 3.9 (right column). Here the O_3 VMR error resulting from the basic run is already fully converged as confirmed by the update and the control run; there is only one small bias visible from the basic run near 10 km in the tropical atmosphere, which points to the foreign influence of H_2O, being the key cross-sensitivity of the O_3 channels used. The lower bound altitude domain requirements of O_3 are higher than for the other species, since the ozone layer resides in the stratosphere and the concentration becomes weak towards the troposphere. Based on this the noise level starts to increase below about 15 km and further down below about 10 km also the H_2O influence begins to mask the O_3 absorption (Schweitzer 2010; Schweitzer, Kirchengast and Proschek 2011). The O_3 channels thus focus on accurate profiling of stratospheric ozone from about 10 km to 15 km upwards.

Considering finally the overall GHG retrieval performance indicated by these intial demonstration results of the new LMIO algorithm it looks very encouraging. The results from these quasi-realistic end-to-end simulations are consistent with and confirm the basic estimates from simplified error propagation modeling by Kirchengast and Schweitzer (2011). The retrieval errors appear to be essentially unbiased over the full height range of interest and the r.m.s. errors appear to lie well within target requirements. Since the errors are essentially random, climatological averages will enable very high accuracy at the 0.1 % level, given sufficient care is taken related to avoiding or mitigating potential systematic errors in all relevant elements of an LMIO mission design as dicussed by Kirchengast et al. (2010a) and Kirchengast and Schweitzer (2011).

Favorably CO_2 appears to be the GHG that can be retrieved most accurately, within 1 % to 2 % of VMR error, but also the other species H_2O, CH_4 and O_3 are retrieved to within 1 % to 3 % of VMR error almost everywhere in their targeted altitude domain. Specifically regarding H_2O, the results indicate that it can be retrieved in clear air from LIO with significantly more accuracy than from LMO (the latter yields to within about 10 %; e.g., Schweitzer et al. (2011)). Thus LIO could also help to further improve the accuracy of the thermodynamic state p, T, q. For O_3 the retrieval strength lies in the stratosphere from about 15 km upwards.

3.5 Summary and conclusions

In this study we introduced a retrieval algorithm for the LIO part of the LMIO satellite mission concept, which is a proposed occultation observing system that combines LIO and LMO to retrieve thermodynamic profiles (pressure, temperature, humidity) as a function of altitude from LMO and GHG profiles from simultaneously measured LIO data. The LMO algorithm part for thermodynamic state retrieval was recently introduced by Schweitzer et al. (2011), the novel LMIO method as a whole by Kirchengast and Schweitzer (2011). The LIO algorithm, completing the full LMIO retrieval, is applied as a second step after the LMO algorithm. We described the LIO algorithm in detail and showed its performance – and the effective independence of the GHG retrieval results from external (a priori) information – via demonstration results from LMIO end-to-end simulations by the EGOPS/xEGOPS software system for a representative set of GHG profiles (CO_2, H_2O, CH_4, and O_3) under three representative clear-air atmospheric conditions (tropical, standard, sub-arctic winter).

We showed how the LIO algorithm benefits from the LMO output, more precisely from the thermodynamic profiles (pressure, temperature, humidity) and the impact parameter profile, the latter enabling acccurate geolocation of altitude levels. The LIO intensity signals as a function of time, complemented by initial/background GHG profiles which can even be set to zero initially, are the LIO observational input to the algorithm. The algorithm itself consists of a preparatory part, establishing IR refractivity, impact parameter, and altitude profiles from LMO output, a core part, the single-line trace species retrieval (SSR), and a dynamic part of envelope loops over the SSR, consisting of the multi-line trace species retrieval (MSR) loop and the basic-update-control run (BUC) loop, respectively.

The preparatory part establishes the IR refractivity, IR impact parameter, and IR altitude profiles corresponding to the transmitter and receiver positions and the LIO intensity profiles available as a function of time. The SSR provides trace species volume mixing ratio (VMR) profiles from single absorption lines, i.e., from the LIO intensities of a single pair of absorption and reference channel, by exploiting the differential absorption principle which enables high-accuracy retrievals. The MSR loop, an envelope process over the SSR process, performs single-line species retrievals in a carefully defined order and updates the set of initial/background GHG profiles after each SSR step, resulting in a step-wise improved set of GHG profiles. A proper order provides highly effective retrieval and enables to start even with initial profiles set to zero: we first retrieve the most independent species (in terms of minimal absorption influence in their channels from other species), followed by the less independent ones that can then already benefit from the previously retrieved ones in their correction for residual foreign species absorption. In addition, the MSR combines suitable single-line species profiles into composite profiles, which we employed for a composite CO_2 profile from $^{12}CO_2$ and $^{13}CO_2$ and for a composite H_2O profile from the four H_2O single-line profiles of which each only partially covers the

UTLS altitude range. The BUC loop is a simple envelope loop over the MSR process to complete (update run) and cross-check (control run) the convergence of the retrieved set of GHG profiles after the first MSR run (basic run).

Regarding the EGOPS/xEGOPS end-to-end simulations, the GHG retrieval performance indicated by the intial demonstration results of the LMIO algorithm were found very encouraging. The results are consistent with and confirm the basic estimates from simplified error propagation modeling by Kirchengast and Schweitzer (2011). The retrieval errors appear to be essentially unbiased over the full height range of interest and the r.m.s. errors appear to lie well within target requirements set by scientific objectives of atmosphere and climate research to be supported by the data. Carbon dioxide appears to be the GHG that can be retrieved most accurately, within 1 % to 2 % of VMR error, but also the other species H_2O, CH_4 and O_3 are retrieved to within 1 % to 3 % of VMR error almost everywhere in their targeted altitude domain. The H_2O results indicate that water vapor can be retrieved in clear air from LIO with higher accuracy than from LMO so that LIO could also potentially help this way to further improve the accuracy of the thermodynamic state. For O_3 the retrieval strength is on the stratospheric ozone from about 15 km upwards as the O_3 signal-to-noise ratio becomes small below about 10 km to 15 km. Since the individual-profile errors found here are essentially random, climatological averages will enable very high accuracy at the 0.1 % level, given sufficient care is taken related to avoiding or mitigating potential systematic errors in all relevant elements of an LMIO mission design as dicussed by Kirchengast et al. (2010a) and Kirchengast and Schweitzer (2011).

Overall the LMIO retrieval performance, found here for clear-air atmospheric conditions, is unprecedented for vertical profiling of GHGs in the free atmosphere and encouraging for future LMIO implementation. On-going subsequent work includes a more complete performance analysis, comprising all LIO species and statistical retrieval error estimates from end-to-end ensemble simulations, also using a greater variety of atmospheric conditions. Further work addresses the advancement of the present GHG retrieval algorithm to cloudy air, for best-possible retrieval performance also when scanning through intermittent upper tropospheric cloudiness, as well as the advancement of the retrieval to also determine line-of-sight wind speed beyond the simple approach introduced by Schweitzer (2010) and Kirchengast and Schweitzer (2011). On the experimental side a ground-based LIO demonstration experiment is prepared for a 144 km link between high-altitude observatories at the Canary Islands, Spain (ESA project by Univ. of York, Univ. of Manchester, and Univ. of Graz, P. F. Bernath et al., 2010–2011). This work aims at a first experimental demonstration of the LIO technique for CO_2, CH_4, and H_2O measurements under field conditions somewhat akin to a space link.

CHAPTER 4

Greenhouse gas profiling by infrared-laser and microwave occultation in cloudy air: results from end-to-end simulations

This chapter deals with the advancement and performance assessment of the LEO–LEO microwave and infrared-laser occultation (LMIO) retrieval algorithm introduced in Chap. 3 above to cloudy-air conditions. The chapter presents work that is published in the Journal of Geophysical Research (JGR) by Proschek et al. (2014a). My contributions to this work were the main manuscript text work, the implementation of the forward-modeling of cloud extinction and of the cloud-related retrieval algorithm advancements into the eXtended End-to-End Generic Occultation Performance Simulation and Processing System (xEGOPS) and the main work on data analysis and result-figures generation.

ABSTRACT

The new mission concept of microwave and infrared-laser occultation between Low Earth Orbit satellites (LMIO) is capable to provide accurate, consistent, and long-term stable measurements of many essential climate variables. These include temperature, humidity, key greenhouse gases (GHGs) such as carbon dioxide and methane, and line-of-sight wind speed, all with focus on profiling the upper troposphere and lower stratosphere. The GHG retrieval performance from LMIO data was so far analyzed under clear-air conditions only, without clouds and scintillations from turbulence. Here we present and evaluate an algorithm, built into an already published clear-air algorithm, which copes with cloud and scintillation influences on the infrared-laser transmission profiles used for GHG retrieval. We find that very thin ice clouds fractionally extinct the infrared-laser signals, thicker

but broken ice clouds block them over limited altitude ranges, and liquid water clouds generally block them so that their cloud top altitudes typically constitute the limit to tropospheric penetration of profiles. The advanced algorithm penetrates through broken cloudiness. It achieves this by producing a cloud flagging profile from cloud-perturbed infrared-laser signals, which then enables bridging of transmission profile gaps via interpolation. Evaluating the retrieval performance with quasi-realistic end-to-end simulations, including high-resolution cloud data and scintillations from turbulence, we find a small increase only of GHG retrieval RMS errors due to broken-cloud scenes and the profiles remain essentially unbiased as in clear air. These results are encouraging for future LMIO implementation, indicating that GHG profiles can be retrieved through broken cloudiness, maximizing upper troposphere coverage.

4.1 Introduction

The mission concept ACCURATE—Climate Benchmark Profiling of Greenhouse Gases and Thermodynamic Variables and Wind from space—comprises a synergistic usage of the Low Earth Orbit (LEO-LEO) microwave occultation (LMO) and the LEO-LEO infrared-laser occultation (LIO) technique (Kirchengast et al. 2010a; Schweitzer 2010). Together, these methods allow to measure the thermodynamic variables pressure, temperature and humidity from LMO (Schweitzer et al. 2011) simultaneously with greenhouse gas concentrations and line-of-sight wind speed from LIO, joining to the LEO-LEO microwave and infrared-laser occultation (LMIO) method (Kirchengast and Schweitzer 2011). The LMIO method is meanwhile a well understood mission concept (Kirchengast and Schweitzer 2011; Schweitzer, Kirchengast and Proschek 2011; Proschek, Kirchengast and Schweitzer 2011; Harrison, Bernath and Kirchengast 2011; Brooke et al. 2012) and received positive evaluation for further study and development in the framework of European Space Agency (ESA) Earth Explorer mission calls (Kirchengast et al. 2010a).

The LMIO focus altitude range for profiling of greenhouse gases (GHGs) covers the upper troposphere and lower stratosphere (UTLS; ∼5 km to 35 km), where the most important GHGs (CO_2, CH_4, N_2O, H_2O, O_3, CO; incl. key isotopes $^{13}CO_2$, $C^{18}OO$) can be retrieved with an individual-profile error within 1 % to 3 % RMS, and in an essentially unbiased manner, at a vertical resolution of ∼1 km (Kirchengast and Schweitzer 2011). This was demostrated for clear-air conditions, meant here to denote no influence of clouds and atmospheric turbulence but accounting for the influence of other main atmospheric features like defocusing loss, aerosol extinction, and Rayleigh scattering (Schweitzer, Kirchengast and Proschek 2011; Proschek, Kirchengast and Schweitzer 2011).

The key step of the GHG retrieval from LMIO data is to apply the *differential transmission* principle between an *on-signal* (channel on a GHG absorption line) and an

off-signal (adjacent channel outside GHG absorption line) in order to cancel out broadband background effects, such as defocusing loss (Kursinski et al. 2000), Rayleigh scattering and aerosol extinction (Salby 2012; Liou 2002), and scintillations from turbulence (Andrews and Philips 2005; Gurvich et al. 2012). The residuals from these effects are negligible or very small in the differential transmission as discussed in detail by Schweitzer, Kirchengast and Proschek (2011).

The LMIO method can be viewed as an advancement of the well known radio occultation method in the L-band region (Ware et al. 1996; Kursinski et al. 1997), but with a transmitting LEO satellite actively sending microwave and infrared-laser signals through the atmosphere to a receiving LEO satellite, while the two satellites are counter-rotating in near polar orbits. This setup enables a combined measurement of thermodynamic variables and GHGs, providing these observations as independent, self-calibrating, long-term data with high vertical resolution for climate change monitoring and research.

Building on other pioneering work on the LMIO method and the ACCURATE mission concept as cited above, Proschek, Kirchengast and Schweitzer (2011) introduced a novel algorithm for GHG retrieval from infrared (IR)-laser signal data, as part of LMIO data, and proved it to work well under clear-air conditions. IR-laser signals are very sensitive to clouds, however, from semitransparent thin cirrus clouds that already perturb the signals to liquid water clouds that fully block them. Given this sensitivity, cloud presence strongly influences the GHG retrieval capability and limits the tropospheric penetration depth of GHG profiles. Therefore an improved algorithm, capable of handling IR-laser signal profiles under cloudy-air conditions, is highly useful. Here we introduce such an improved algorithm and evaluate its retrieval performance by end-to-end simulations.

Some heritage information on cloud influences in atmospheric occultation is available from the stellar occultation instrument GOMOS (Global Ozone Monitoring by Occultation of Stars) on the European environmental satellite Envisat (Kyrölä et al. 2004; Kyrölä et al. 2010) and, in particular, the solar occultation infrared measurements by the Atmospheric Chemistry Experiment ACE (Bernath et al. 2005). On the basis of ACE data, Harrison and Bernath (2010) estimated the fraction of solar occultation events that are altitude limited by clouds. They concluded that, outside a tropical band within about 15 ° of the equator, the tropospheric penetration of occultation events reaches down to about 7.5 km for about 40 % of the events and down to about 5 km for about 20 % of the events; within the tropical band only about 20 % reach down to 7.5 km.

Due to limitations in vertical resolution and/or signal-to-noise ratio, such solar and stellar occultation instruments are not capable to provide accurate data into broken cloudiness, however, while the LMIO technique by design, and thanks to the highly confined propagation "tubes" of its IR-laser signals, provides this capability (see Schweitzer, Kirchengast and Proschek (2011), section 3.8 therein). It is therefore expected that LMIO profiling data provide improved vertical coverage into the upper troposphere due to their capability to penetrate intermittent cloudiness. The present study focuses on quantitatively assessing the validity of this expectation, including under conditions of

signal scintillations due to turbulence which will always prevail to some degree in the real atmosphere (Schweitzer, Kirchengast and Proschek 2011).

A schematic view of the LMIO signal propagation under cloudy-air conditions is shown in Figure 4.1. It illustrates the propagation between transmitter platform, $\mathrm{LEO_{Tx}}$, and receiver platform, $\mathrm{LEO_{Rx}}$, along refracted signal ray paths indicated by bending angle α as function of impact parameter a, through broken cloudiness. The LIO signals feeding the GHG retrieval can be considered intermittently disturbed or blocked by clouds, while the LMO signals are essentially unaffected by clouds (Emde, Proschek and Kirchengast 2009) and therefore enable retrieval of thermodynamic profiles (pressure, temperature, humidity) and altitude leveling information also into and through clouds (Schweitzer et al. 2011). Otherwise the measurement geometry and setup are identical as for clear-air conditions and have been discussed in detail by Kirchengast and Schweitzer (2011) and Proschek, Kirchengast and Schweitzer (2011).

We structured the paper as follows. Section 4.2 introduces the quasi-realistic forward modeling in cloudy air, including high-resolution cloud scenes from the CALIPSO satellite (Winker et al. 2009), and the end-to-end simulation setup. Section 4.3 describes the cloudy-air retrieval algorithm and the GHG retrieval performance results obtained based on the new algorithm, including for coinfluence of signal scintillations due to turbulence. Finally, a summary and conclusions are provided in section 4.4.

4.2 Forward modeling in cloudy air and simulation setup

Building on the LMIO forward modeling and retrieval capabilities in clear air, presented in detail by Proschek, Kirchengast and Schweitzer (2011), we developed appropriate capabilities for cloudy air. In this section we describe how we parameterized cloud influences in the forward modeling, how these influences affect the LIO signals, and how we set up and carried out the LIO forward simulations.

4.2.1 Cloud parameterization in LIO forward simulations

To simulate the influence of liquid and ice water clouds on LIO signals, we used the End-to-End Generic Occultation Performance Simulation and Processing System (EGOPS) and eXtended EGOPS (xEGOPS) version 5.5 (Fritzer, Kirchengast and Pock 2009b; Fritzer et al. 2010b) as basis—the latter operates with the EGOPS as kernel and serves as developer environment for the new LIO algorithms—and expanded the xEGOPS forward modeling with capabilities for the simulation of the influence of clouds.

Based on careful literature study and testing, we chose parameterizations for cloud extinction coefficients of ice water and liquid water clouds, which are formulated as functions of the effective radius of the cloud particles r_{eff}, the ice water content (IWC) ρ_{ice} or liquid water content (LWC) ρ_{liq}, respectively, the cloud temperature T_{C} (for ice water clouds), and the frequency ν of the propagating signal. We did not use a more

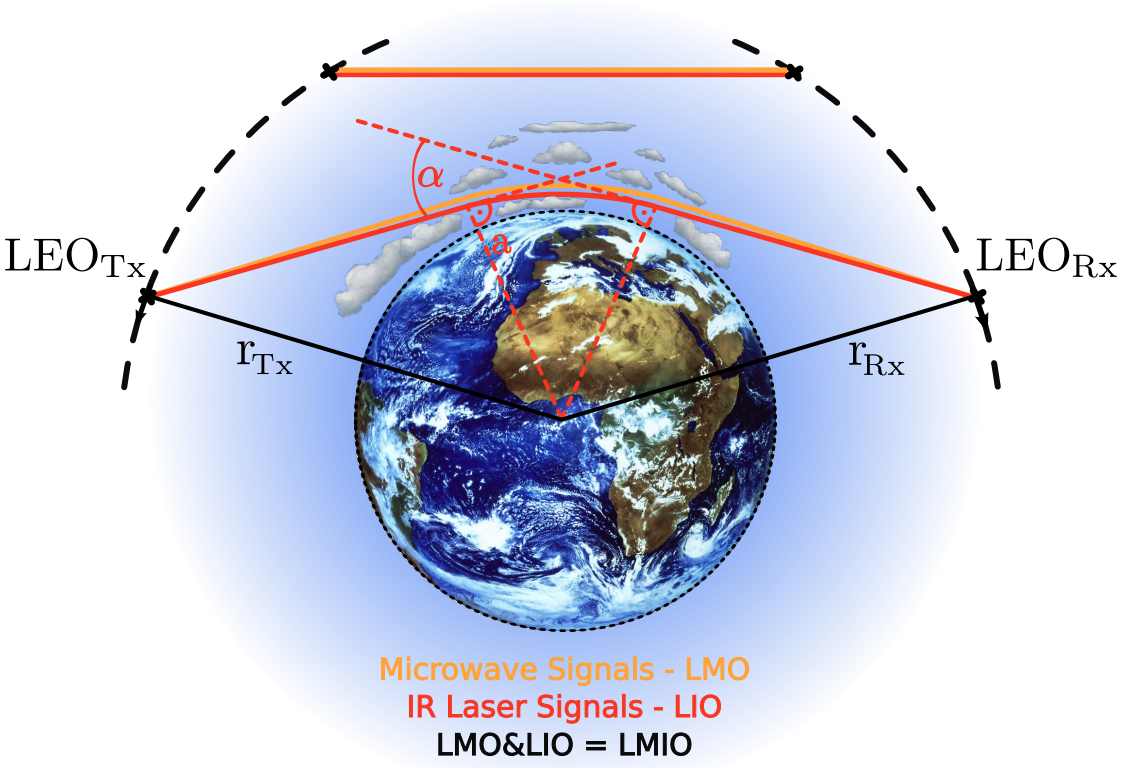

Figure 4.1: Schematic illustration of the LMIO measurement technique under cloudy air conditions (symbolic broken clouds), with the combined infrared-laser signals (LIO, red) and microwave signals (LMO, orange). The bending angle of an IR-laser raypath is denoted α, the corresponding impact parameter is denoted by a, and the radial positions of transmitter and receiver satellite are denoted by r_{Tx} and r_{Rx}, respectively.

sophisticated way of cloud extinction modeling, such as Mie theory and full particle size distributions (e.g., McFarquhar and Heymsfield 1997), since our algorithm does not depend on a very accurate quantitative estimation of extinction loss; raypaths with total loss higher than 3 dB are, regardless of magnitude of loss, flagged and treated as cloud perturbed (details in section 4.3). Therefore, a physically sound but not too sophisticated parameterization is sufficient for the purpose.

For ice water clouds, we parameterized the extinction coefficient $\beta\left(\rho_{\mathrm{ice}}, \nu, T_{\mathrm{C}}\right)$ (in m^{-1}) after Key et al. (2002),

$$\beta\left(\rho_{\mathrm{ice}}, \nu, T_{\mathrm{C}}\right) = \left[\sum_{n=0}^{3} a_n(\nu) \frac{1}{r_{\mathrm{eff}}^n(\rho_{\mathrm{ice}}, T_{\mathrm{C}})}\right] \cdot \rho_{\mathrm{ice}}, \tag{4.1}$$

where $a_n(\nu)$ are predefined parameters, which differ for different frequency bands (though the IR-laser signals used in this study lie all in the same band so that the same parameters apply to all of them). In this relation r_{eff} (in μm) is a function of ice water content ρ_{ice} (in $\mathrm{g\,m}^{-3}$) and cloud temperature T_{C} (in K) and was calculated after Wyser (1998a),

$$r_{\mathrm{eff}}\left(\rho_{\mathrm{ice}}, T_{\mathrm{C}}\right) = 377.4 + 203.3 \cdot B + 37.91 \cdot B^2 + 2.3696 \cdot B^3, \tag{4.2}$$

with the parameter $B = B(\rho_{\mathrm{ice}}, T_{\mathrm{C}})$ formulated as

$$B\left(\rho_{\mathrm{ice}}, T_{\mathrm{C}}\right) = -2 + 10^{-3} \cdot (273 - T_{\mathrm{C}})^{1.5} \cdot \log\left(\frac{\rho_{\mathrm{ice}}}{\rho_{\mathrm{ice},0}}\right), \tag{4.3}$$

where the empirical reference value $\rho_{\mathrm{ice},0}$ is 50 $\mathrm{g\,m}^{-3}$. This parameterization is valid for r_{eff} values from 6 μm to 84 μm for the widely applicable solid-columns particle shape (Key et al. 2002) and was implemented in xEGOPS as an additional ice cloud extinction coefficient term complementing the existing absorption, scattering, and extinction terms described by Schweitzer, Kirchengast and Proschek (2011). It was also used for producing Figure 4.2.

For liquid water clouds, we parameterized the extinction coefficient $\beta(\rho_{\mathrm{liq}}, \nu)$ (in m^{-1}) after Hu and Stamnes (1993),

$$\beta(\rho_{\mathrm{liq}}, \nu) = \left(a_1(\nu) \cdot r_{\mathrm{eff}}^{b_1(\nu)}(\rho_{\mathrm{liq}}) + c_1(\nu)\right) \cdot \rho_{\mathrm{liq}}, \tag{4.4}$$

where $a_1(\nu)$, $b_1(\nu)$, and $c_1(\nu)$ are frequency-dependent parameterization coefficients. In this relation r_{eff} (in μm) is a function of liquid water content ρ_{liq} (in $\mathrm{g\,m}^{-3}$) and was calculated after Wyser (1998b),

$$r_{\mathrm{eff}}\left(\rho_{\mathrm{liq}}\right) = 10^6 \cdot \left(\frac{3 \cdot \rho_{\mathrm{liq}}}{4\pi \cdot \rho_w \cdot k \cdot N_{\mathrm{d}}}\right)^{\frac{1}{3}}, \tag{4.5}$$

with the water density ρ_w used at 273.15 K being set to 999839 g m^{-3}, an empirical constant k being set to 0.8 (free troposphere value, i.e., above the boundary layer), and N_d (in m^{-3}) being an empirical droplet number density (free troposphere value) formulated as,

$$N_d = \hat{N}_d \cdot \log\left(1 + \frac{N_a}{\hat{N}_a}\right), \tag{4.6}$$

where the empirical reference value $\hat{N}_d$ was set to $140 \cdot 10^6$ m^{-3}, the empirical aerosol number density N_a to $150 \cdot 10^6$ m^{-3}, and the empirical aerosol reference value $\hat{N}_a$ to $100 \cdot 10^6$ m^{-3}, respectively. These values reflect some typical number densities as for example described by Salby (2012).

As for the ice clouds, this liquid cloud extinction coefficient term was implemented in xEGOPS as additional extinction term to complement the existing terms described by Schweitzer, Kirchengast and Proschek (2011). Tests confirmed that LIO transmission simulation results are essentially insensitive to detailed settings for the empirical values in the r_{eff} parameterization, since liquid clouds generally block IR-laser signals.

4.2.2 The influence of clouds on LIO signals

When clouds are prevailing, they show strong influence on the transmissions of the LIO signals. Therefore, they are best accounted for in the retrieval at the point where the LIO transmissions are derived (details in section 4.3 below). As summarized in section 4.1 above, it is to be expected that tropospheric penetration depth of GHG profiles will be limited by clouds, due to their strong attenuation, or complete extinction, of the LIO transmission signals.

More quantitatively, as determined by Emde and Proschek (2010) and Proschek, Schweitzer and Kirchengast (2011), liquid water clouds typically lead to extinction loss of more than 30 dB for LIO signals, even for fairly low liquid water content (LWC). Hence, liquid water clouds will lead to total blocking of the signals and their cloud tops will limit the penetration depth of LIO signals. Fortunately, most of the liquid water clouds reside in the lower troposphere (below 5 km), which is below the primary altitude range for the LMIO method which focuses on profiling over the UTLS (5 km to 35 km).

Ice water clouds, which typically prevail at heights above 5 km, are sometimes semitransparent for LIO signals, depending on whether their ice water content (IWC) along the raypath is sufficiently low and the ice particle size is sufficiently large. Figure 4.2 shows the LIO signal extinction loss from ice water clouds as a function of path length of the signal within such clouds, for different representative IWCs and two very different values of the ice particle effective radius (r_{eff}) of the clouds (the boundary values of the Key et al. (2002) parameterization).

As introduced in section 4.2.1, the extinction is influenced by the IWC itself and the temperature in the ice clouds, with colder clouds leading to smaller particle sizes. In the

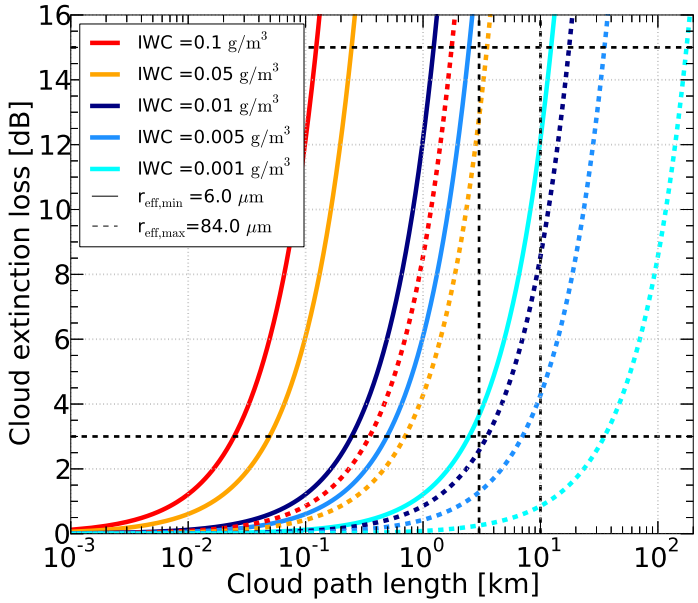

Figure 4.2: Cloud extinction loss as function of path length through clouds for different levels of ice water content (IWC) of these clouds (see inset legend), either for an effective radius of 6.0 μm (solid lines) or 84.0 μm (dotted lines). The loss is shown here for the $^{12}CO_2$ absorption channel near 2.1 μm, but it is very weakly depending on frequency (see section 4.2.1 that describes the extinction parameterization used). The dotted horizontal lines mark extinction loss boundaries for cloud flagging, with 3 dB marking the start of significant cloud contribution and 15 dB the start of blocking the signal (see sections 4.2.2 and 4.3.1). The dotted vertical lines indicate typical path lengths for small cirrus clouds (3 km) and more extended patches of ice clouds (10 km).

algorithm implementation we consider extinction losses of higher than 3 dB as significant contribution of cloud extinction already, and more than 15 dB as blocking the signal; these extinction levels are therefore marked as dotted lines in Figure 4.2.

More precisely speaking, while this is a reasonable approximation, the level of actual signal blocking will depend for any given IR-laser signal channel on the available signal-to-noise ratio (SNR), which varies somewhat from channel to channel as shown and discussed in detail by Schweitzer, Kirchengast and Proschek (2011). That is, the level of cloud extinction needs to be considered on top of all other atmospheric extinction influences (like defocusing and species absorption losses), which is why additional extinction levels of 3 dB upward are already considered significant. For example, the $^{12}CO_2$ absorption channel, underlying the computations for Figure 4.2, is one that exhibits medium sensitivity to the clear-air atmospheric loss effects (Schweitzer, Kirchengast and Proschek 2011).

As can be seen from Figure 4.2, the cloud extinction is higher, the higher the IWC of the clouds is and the smaller the effective radius of the ice particles. Ice water clouds with a high IWC of 0.1 g/m^3 or 0.05 g/m^3 and a small particle effective radius of 6 μm (solid red and orange lines) block LIO signals very strongly; blocking occurs for cloud path lengths of less than 1 km already. The other extreme is represented by very thin ice clouds (IWC=0.001 g/m^3) with a large particle effective radius of 84 μm (dotted turquoise line), which are far more optically transparent; they become significant for LIO signal loss only when the path length exceeds 30 km (and they block only if it reaches 200 km).

Since real conditions of broken upper tropospheric cloudiness will be highly variable, both in IWC and in particle sizes, Figure 4.2 implies that we need quasi-realistic forward modeling using high-resolution cloud information in order to get a reasonable quantitative evaluation from end-to-end simulations of the performance and effectiveness of GHG retrievals in broken cloudiness.

4.2.3 LIO forward simulations for the retrieval analysis

The Forward Modeling (FOM) and Observation System Modeling (OSM) subsystems of the xEGOPS/EGOPS system were used to quasi-realistically simulate the LMIO measurements in the atmosphere, including the cloud parameterizations described above.

The basic settings for the simulations were taken to be the same as described in section 2.2 of Proschek, Kirchengast and Schweitzer (2011), which is why we focus here on the differences to those settings needed for the present end-to-end simulations. In the FOM simulations, we used the so-called "Ideal Geometry" mode for the LEO orbits, providing for vertical occultation event planes at user-specified tangent-point locations with user-specified azimuthal orientation that enable to well match high-resolution cloud cross sections from CALIPSO nadir scans. Reflecting the baseline orbits of Kirchengast et al. (2010a), we put the LEO_{Tx} platform in a 590 km orbit and the LEO_{Rx} platform in a 510 km counter-rotating orbit, both circular, and with north-south orientation of the occultation plane.

The vertical simulation range was set from 3 km to 80 km, fully covering the UTLS and a retrieval intialization region above. The data sampling rate of the 3-D ray tracing and along-ray extinction integration was set to 50 Hz (i.e., 50 simulated rays per second leading to 50 atmospheric loss values per second), in line with the specifications of the ACCURATE mission concept. Since the vertical scanning velocity over the upper troposphere is about 1 km/s to 1.5 km/s, this implies a vertical resolution of the sampled data of about 20 m to 30 m. In order to be able to capture high-resolution cloud fields also in the horizontal dimension, the step size along the raypaths was set to 100 m for altitudes below 20 km. Clouds were foreseen to be simulated below 20 km, above cloud extinction coefficients were set to zero.

For the basic thermodynamic variables, pressure, temperature, and humidity (H_2O), we used a global analysis field provided by the European Centre for Medium-Range Weather Forecasts (ECMWF), from 23 May 2011, 12 UTC, approximately matching selected CALIPSO cloud scenes in time (analysis resolution T1279L91, corresponding to ∼16 km horizontal resolution, and 91 vertical hybrid-pressure levels up to 0.01 hPa). In particular, we employed vertical profiles extracted at defined occultation event locations and assumed spherical symmetry about this location, in order to avoid (representativeness) errors due to horizontal variability in the gaseous atmosphere, as also done by Schweitzer, Kirchengast and Proschek (2011). Regarding all other GHGs (beyond H_2O), we used the Fast Atmosphere Signature Code (FASCODE) atmosphere model (FASCODE 2008; Anderson et al. 1986) in the same way as Proschek, Kirchengast and Schweitzer (2011), also applying spherical symmetry. FASCODE includes representative sets of GHG profiles for a few latitude bands (e.g., tropical band used here) (see Kirchengast and Schweitzer 2011, , Figure S2 therein).

For realistic representation of clouds, we used, as mentioned above, two-dimensional cloud data from the Cloud-Aerosol Lidar and Infrared Pathfinder Satellite (CALIPSO) (Winker et al. 2009). CALIPSO is a joint mission of NASA and the French space agency CNES, combining three instruments on the satellite, a backscatter lidar with orthogonal polarization, an imaging infrared radiometer, and a wide field camera. For our purpose we used the lidar data.

We selected both a nighttime and a daytime example cloud scene, representative of broken cloudiness in the upper troposphere, on 23 May 2011 during near-meridional nadir scans of the CALIPSO backscatter lidar (CALIPSO LID L1 ValStage V3 T21 data; nighttime scene 12:39 UTC, latitude range −39.38° to +9.32°, longitude ∼168°W; daytime scene 21:40 UTC, latitude range −20.09° to +28.72°, longitude ∼124°W). For the simulations we projected the near-meridional CALIPSO data into the meridional occultation plane, i.e, we used them with accounting for their latitude variation but at a fixed longitude that we set for the underlying ECMWF analysis field's meridional cross section; see below. The high-resolution variability of these data in the occultation plane was thus fully accounted for in the simulations, for capturing realistic influences of the clouds on the propagating LIO signals.

Because liquid water clouds generally lead to full attenuation of the LIO signals, implying that their cloud top defines the penetration depth of GHG retrievals, we used ice water clouds only in this study. This enables to compare the impact of various broken cloud conditions, including different thicknesses and shapes of the ice water content (IWC) distribution of these clouds, on the GHG retrieval. For the selected cloud scenes, the CALIPSO database indicated that liquid water clouds would anyway have become relevant below about 5 km only or would have induced blocking only lower than the ice clouds.

Computational expenses of such high-resolution end-to-end simulations demand a limited ensemble, so we chose eight representative occultation events: four at locations matching the CALIPSO nighttime scene (tangent point latitudes 18°S, 12°S, 7°S, 3°S) and four matching the daytime scene (tangent point latitudes 13°S, 5°S, 1°N, 12°N). The tangent point longitude was set to 168°W for all cases (so that the underlying ECMWF analysis field's meridional cross section is the same).

Due to the fact that the available CALIPSO Level 2 IWC data have a lower resolution than the underlying Level 1B data, we decided to use the Level 1B perpendicular attenuated back-scatter (PAB) data instead in our simulations, which feature ∼330 m horizontal resolution and ∼60 m vertical resolution. These PAB data were converted into IWC data by using a simple linear relationship, which we empirically determined from scatter plots comparing Level 2 IWC data with Level 1B PAB data. We found that the IWC (in gm^{-3}) is reasonably approximated by 5.3×PAB (in $\mathrm{km}^{-1}\mathrm{sr}^{-1}$) and therefore used this simple conversion. The results are only weakly sensitive to the exact factor used in this conversion, since the total along-ray cloud extinction is generally strong if clouds interfere while it is small if signals manage to pass through broken clouds along clear-air paths.

Given some basic noise level in the CALIPSO backscatter data, a lower-threshold value for the PAB data was used to isolate this noise; a threshold of $0.0045\,\mathrm{km}^{-1}\mathrm{sr}^{-1}$ / $0.0001\,\mathrm{km}^{-1}\mathrm{sr}^{-1}$ was found suitable for the daytime / nighttime scene. All PAB values below the threshold were set to zero and then the PAB values were converted to IWC values by the factor above. The higher threshold needed during daytime inevitably leads to somewhat finer cloud structures compared to nighttime, due to eliminating also some small cloud structures that are potentially real; nevertheless, all main cloud structures remain.

Figure 4.3 shows the resulting IWC fields for nighttime (Figure 4.3a) and daytime (Figure 4.3b), with illustrative raypaths of the chosen occultation events overplotted. As can be seen, we selected the occultation event tangent point (TP) locations in a way that we have different representative broken cloud situations along the raypaths, like thin patches of cirrus clouds (e.g., nighttime TP 12°S and TP 7°S events below 12 km, daytime TP 13°S and TP 1°N events above 10 km), cloud layers inducing signal gaps (e.g., nighttime TP 7°S event, daytime TP 5°S event), and comparatively larger clouds limiting by their cloud top (e.g., nighttime TP 18°S event, daytime TP 12°N event).

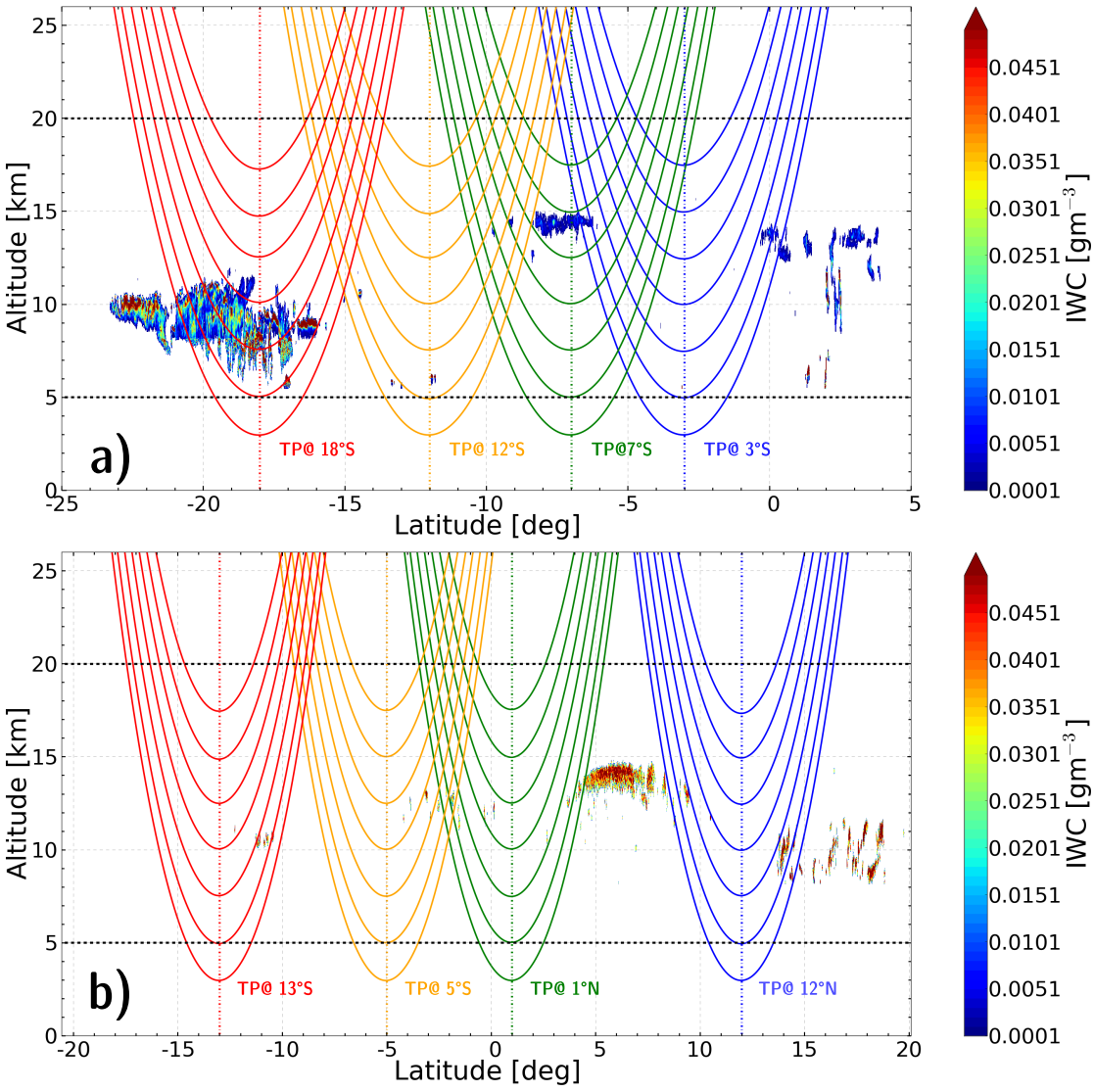

Figure 4.3: Ice water content (IWC) data derived from CALIPSO perpendicular attenuated backscatter data, for one nighttime (a) and one daytime (b) near-meridional CALIPSO nadir scan recorded on 23 May 2011 over the tropical Pacific. For each of these two example cloud scenes, illustrative ray paths of four selected occultation events, with tangent point (TP) locations as annotated (and TP altitudes of 3, 5, 7.5, 10, 12.5, 15, 17.5 km), are overplotted to indicate the diversity of potential interference of broken clouds with propagating IR-laser signals. The horizontal dotted lines mark the altitude range of core interest for potential cloud effects in retrievals.

In addition to the influence of clouds, we also accounted for the influence of defocusing, aerosol extinction, and Rayleigh scattering, in the same manner as done by Proschek, Kirchengast and Schweitzer (2011), using the modeling in xEGOPS for these influences as described by Schweitzer, Kirchengast and Proschek (2011).

Furthermore, to perform simulations as realistically as possible, we optionally also added the influence of atmospheric turbulence, producing scintillations in the LIO signals, in the FOM simulations. We included a LIO scintillation model in xEGOPS for this purpose, superposing scintillation fluctuations on the forward modeled signals, which is based on scintillation data from the GOMOS (Global Ozone Monitoring by Occultation of Stars) instrument (Sofieva et al. 2009). The model for the xEGOPS was developed by Sofieva (2009) in compliance also with the theoretical analyses of Horwath and Perlot (2008). The model assumes stratified altitude-dependent scintillations that saturate below about 20 km, corresponding to GOMOS observations and satisfying also experimental results by Gurvich, Kan and Fedorova (1996).

Figure 4.4 shows typical examples of forward-simulated atmospheric loss profiles for clear-air and cloudy-air signal propagation, in the cloudy-air case with and without turbulence-induced scintillations. It can be seen that clouds strongly influence the signals, up to complete blocking. It can also be seen that such individual signals of single frequency channels are strongly influenced by turbulence resulting in scintillation noise on the transmission profiles; as discussed by Schweitzer, Kirchengast and Proschek (2011), the fluctuations relative intensity (their RMS level relative to the mean intensity) rapidly grows with decreasing altitude, from about 0.05 (RMS) near 30 km up to the saturation level of about 1 (RMS) below about 20 km.

However, scintillations are correlated over frequency so that the narrow relative spacing of absorption and reference channels, $<0.5\,\%$ in the ACCURATE mission design (Kirchengast et al. 2010a; Kirchengast and Schweitzer 2011), strongly limits the fluctuation noise on the differential transmission profiles. Including, moreover, the optional chromatic shift compensation (Sofieva 2009) allows to obtain differential transmission profiles where the scintillation noise is always mitigated to levels of 1 % or smaller. For more detailed information see Schweitzer, Kirchengast and Proschek (2011, , section 3.8 therein). The residual scintillation error is further decreased when compiling a composite of retrieved profiles, as done for CO_2 and H_2O in the GHG retrieval algorithm (Proschek, Kirchengast and Schweitzer 2011).

Finally, we included errors due to the observation system, such as from receiver thermal noise and small intensity drifts during an occultation event. These errors are superposed on the forward modeled signals by the OSM subsystem of xEGOPS/EGOPS. They were modeled in the same way in this study as by Proschek, Kirchengast and Schweitzer (2011), where they are described in detail.

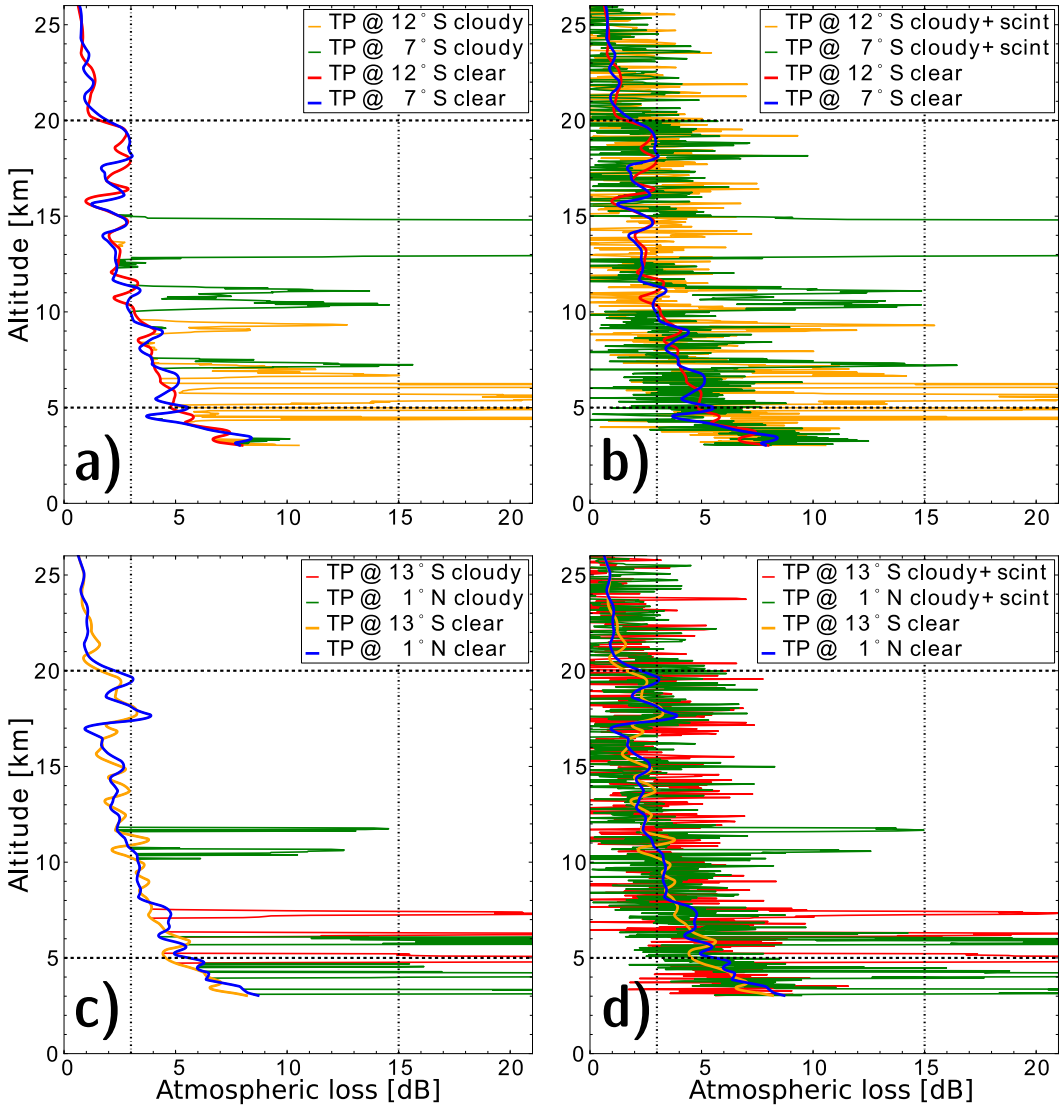

Figure 4.4: Atmospheric loss profiles of selected occultation events as function of tangent point altitude, from those events illustrated in Figure 4.3 (see inset legends), under (a–d) clear-air conditions as well as perturbed profiles under cloudy-air conditions (Figure 4.4a and 4.4c) and under cloudy-air conditions plus scintillations (Figure 4.4d and 4.4d). Two selected events are illustrated for the nighttime cloud scene (Figure 4.4a and 4.4b) and two for the daytime scene (Figure 4.4c and 4.4d), respectively. All profiles shown are from simulations for the reference channel at 4770.15 cm^{-1} (cf. Table 4.1), serving as a typical example.

4.3 Retrieval algorithm and demonstration results

The previous section demonstrated that clouds, which typically are small-scale structures that are distributed inhomogeneously along the raypaths, have significant influence on IR-laser signals, much stronger than the influence of other effects such as defocusing, aersol extinction, Rayleigh scattering, and (differential transmission-mitigated) scintillations. Therefore, the influence of clouds needs to be carefully accounted for in the retrieval process.

Figure 4.5, building on Figure 2 of Proschek, Kirchengast and Schweitzer (2011) that showed the clear-air algorithm scheme, recalls the basic steps executed in the LMIO algorithm for retrieving profiles of GHGs (and of isotopes; included in the term GHGs hereafter). This is necessary background information to understand how the cloudy-air advancements are integrated into the basic retrieval algorithm. The LIO part of the algorithm is the crucial one for retrieval of the GHG profiles as well as of the cloud layering profiles and associated cloud gap interpolations in GHG transmission profiles being introduced in this study.

Briefly explaining Figure 4.5, the main input variables for the LIO retrieval are the received LIO signal intensity profiles and the initial/background profiles for the relevant GHGs (green boxes). Furthermore, atmospheric profiles and the impact parameter, transferring the altitude leveling information, from the simultaneously measured LMO signals are used, which are provided by the LMO retrieval (orange frame on top). The LMO input is primarily needed for the geometrical calculation process, yielding accurate refractivity, impact parameter, bending angle, and tangent altitude profiles (gray boxes) for the LIO signal paths, as well as for the calculation of modeled species transmissions and modeled absorption cross sections (bottom left). These variables are used to help derive differential transmission, target species transmission, and absorption coefficient profiles (red boxes, right), and finally volume mixing ratio (VMR) profiles of all target GHGs of interest (bottom right).

Two iterations over this retrieval sequence, termed update and control runs after a basic run, ensure accurate GHG multispecies results even if initial GHG profiles are artificially set to a VMR of zero. We refer for further details, including on retrieval performance results in clear air, to the in-depth description by Proschek, Kirchengast and Schweitzer (2011).

In this section we describe the cloudy-air retrieval steps, which are necessary to complement the clear-air LIO retrieval. The two main processes needed to treat the influence of clouds in LIO transmission profiles are, (i) a so-called cloud flagging process (yielding a cloud flagging profile) and, (ii) a corresponding target species transmission profile correction process, both of which complement the clear-air algorithm as schematically shown in Figure 4.6.

Furthermore, based on this advanced algorithm, we will demonstrate and evaluate the GHG retrieval performance by comparing retrieval results in clear air, clear and turbulent

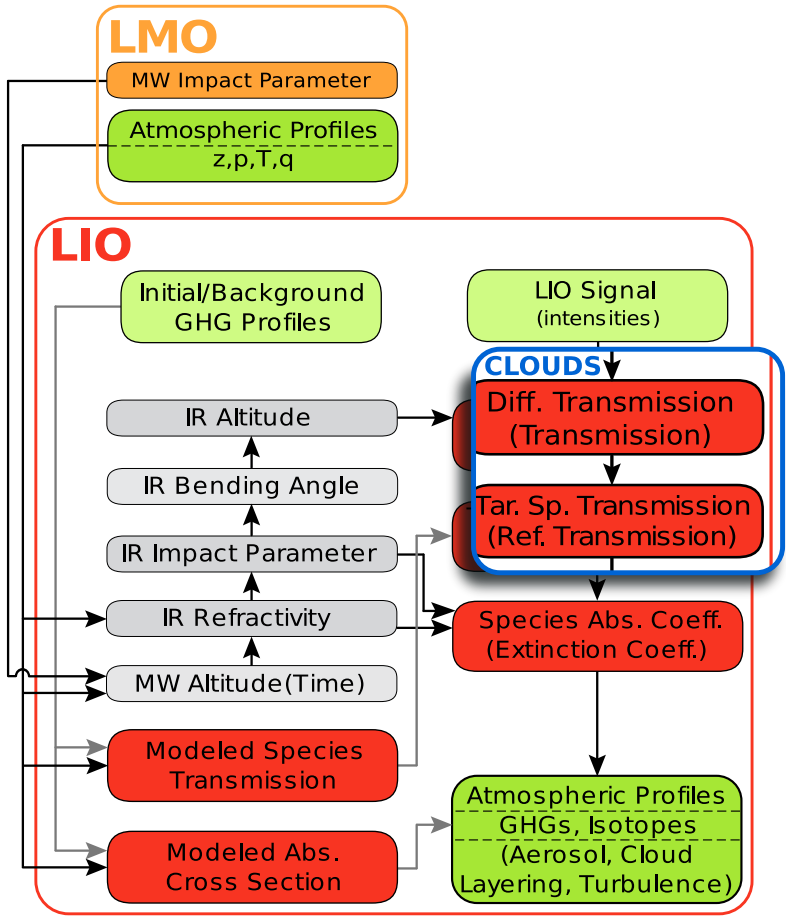

Figure 4.5: Scheme of the LMO input parameters and the LIO core retrieval algorithm, highlighting the schematic location were cloud algorithm processes are involved ("CLOUDS"); see the introductory text in section 4.3 for further explanation.

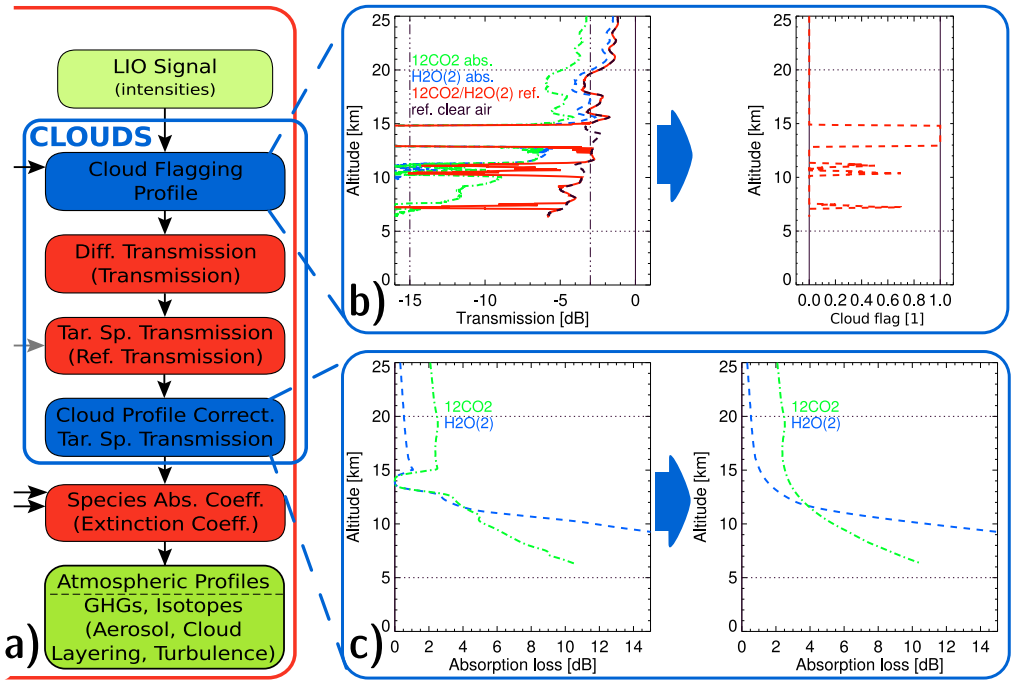

Figure 4.6: Overview of the cloudy-air retrieval processes. (a) Scheme of individual LIO retrieval steps with the additional two cloud-related steps highlighted in blue, i.e. the *Cloud Flagging Profile* step and the *Cloud Profile Correct. Tar. Sp. Transmission* step. (b) Illustration of the cloud flagging process, showing example transmission profiles of $^{12}CO_2$ and $H_2O(2)$ absorption channels and of the corresponding reference channel, both for cloudy and clear-air, in the left subpanel (see in-panel legend for identification), and the resulting cloud flagging profile in the right subpanel. (c) Illustration of the cloud correction process, showing example target species absorption loss profiles for $^{12}CO_2$ and $H_2O(2)$, with the cloud-perturbed ones in the left subpanel and the resulting cloud-corrected ones in the right subpanel.

Table 4.1: Suitable reference channels for the cloud flagging process.

Channel utility	**Wavenumber** [cm^{-1}]	**Frequency** [THz]
Ref[H_2O-1, HDO, CO]	4227.07	126.7244
Ref[N_2O, $^{13}CO_2$, H_2O-3, H_2O-4]	4731.03	141.8327
Ref[$C^{18}OO$, $^{12}CO_2$, H_2O-2]	4770.15	143.0055

air (including scintillations), and cloudy and turbulent air (including cloud interferences and scintillations).

4.3.1 Cloudy-air retrieval algorithm

The first cloud-related step in the retrieval, yielding a *cloud flagging profile*, is dedicated to determine the altitudes in LIO transmission profiles that are affected by cloud extinction. This is an early step in the retrieval chain, which is executed even before differencing the transmissions between absorption and reference channels and computing the target species transmission (see Figure 4.6).

We use LIO signals from the three most suitable reference channels for this step, which are summarized by Table 4.1. Their main characteristic for the purpose ist that they are essentially insensitive to GHG absorption losses, i.e., the total influence due to GHG absorption is $< 0.25\,\mathrm{dB}$ (see Schweitzer, Kirchengast and Proschek 2011, , section 3.4 therein).

An example transmission profile for such a reference channel suitable for cloud flagging is shown in Figure 4.6b (red profile; for comparison black-dashed clear-air profile). This transmission profile includes, besides examplary cloud extinction features, defocusing loss (up to about 5 dB at UTLS bottom near 5 km), aerosol extinction loss ($< 0.25\,\mathrm{dB}$ usually, maximum $\sim$1 dB for the case of volcanic aerosol contribution), Rayleigh scattering loss (always $< 0.1\,\mathrm{dB}$) and weak GHG absorption loss ($<$0.25 dB) (Schweitzer, Kirchengast and Proschek 2011). Scintillation effects are disregarded in this example and discussed separately below (see also Figure 4.5 for illustration of reference channel profiles including scintillations).

All these atmospheric broadband effects together contribute less than 1.5 dB (on top of defocusing loss) in the reference transmission profile. Scintillations will result in a noise profile superimposed on the broadband effects and would therefore not contribute an effective additional loss on the transmission profile, as can be seen from Figure 4.4. For comparison to the reference channel, also the respective transmission profiles for the $^{12}CO_2$ and $H_2O(2)$ absorption channels are shown in Figure 4.6b (blue and green profiles), as examples showing the additional influence of GHG absorption that would

degrade reliable cloud flagging.

The first step of the cloud flagging process is a filtering of the reference transmission profile, which we implemented by applying a Blackman-Windowed Sinc (BWS) low-pass filter operated effectively as a moving average (smoothing to a resolution of ∼200 m). This results in mitigation of scintillation noise, and of other smaller effects inducing high-frequency fluctuations such as receiver thermal noise, while the strongly pronounced transmission features due to cloud extinction persist in the profile.

Next the defocusing loss is corrected (subtracted) from the reference transmission profile, which is done as described by Schweitzer et al. (2011), based on the method introduced by Jensen et al. (2003). As a result, a noise-filtered and defocusing-corrected profile remains, which includes only small remaining broadband effects together with the prominent cloud extinction features. Note that the defocusing correction needs to be done only for the reference channel(s) used for the cloud flagging; for all other channels the step of transmission differencing between absorption and reference channels will automatically also correct the defocusing, since its frequency dependence over such narrow channel spacings is negligible (Proschek, Kirchengast and Schweitzer 2011).

The noise-filtered and defocusing-corrected reference transmission profile is now used as basis for the cloud flagging, where we apply empirically determined limits of −3 dB and −15 dB as lower and upper transmission limits from initial cloud detection to full cloud blocking, respectively (as discussed in section 4.2.2 along with Figure 4.2 above). Table 4.2 summarizes the cloud flags assigned for sensible ranges of extinction loss $|\mathcal{T}|$ (magnitude of transmission $\mathcal{T}$), from flag 0 for $|\mathcal{T}|$ below 3 dB (margin for other residual atmospheric losses and noise) to flag 1 for $|\mathcal{T}|$ exceeding 15 dB (full cloud blocking degrading the SNR of LIO signals too much for exploitation in retrievals), with the flags in between assigned in increments of 0.1 to regular $|\mathcal{T}|$ increments of 1.333 dB.

We defined these incremental stepwise values from zero to unity in order to make sure that the cloud flagging can reflect in a simple manner the strength of cloud interference along the raypaths, in particular for limited cloudiness which is not yet fully blocking. A cloud flagging profile defined in this way is therefore a useful auxiliary information to retrieved GHG profiles, indicating the severity of cloud presence as a function of (ray tangent point) altitude.

Assigning cloud flag values to the reference transmission profiles according to the extinction loss ranges in Table 4.2 provides the cloud flagging profile as a function of altitude. Such a profile is illustrated in the right subpanel of Figure 4.6b for the example shown in the left subpanel; both the couple of cloud extinction spikes and the cloud-induced gap with full blocking over about 13 km to 15 km are clearly visible. Since the BWS filter applied can effectively isolate the high-frequency noise, the vertical resolution of the cloud flagging profile remains at ∼200 m, allowing determination of sharp cloud features. Note that the cloud flagging process is performed as a preparatory step, before the GHG retrieval algorithm as described by Proschek, Kirchengast and Schweitzer (2011) enters into its basic-update-control (BUC) loop and its multispecies retrieval inner loop

Table 4.2: Cloud flagging scheme as function of extinction loss. Minimum and maximum values of extinction loss for the cloud flagging, and extinction increment per flag increment, as well as definition of cloud flag values from 0 to 1 as function of extinction loss values.

$\lvert\mathcal{T}\rvert_{\text{cloud;Min}}$ [dB]	$\lvert\mathcal{T}\rvert_{\text{cloud;Max}}$ [dB]	$\lvert\Delta\mathcal{T}\rvert_{\text{cloud}}$ [dB]
3.0	15.0	1.333

Feature	**Cloud Flag** [1]	**Extinction Loss** $\lvert\mathcal{T}\rvert$ [dB]
non	0.0	$\lvert\mathcal{T}\rvert < 3.0$
weak	0.1	$3.0 \leq \lvert\mathcal{T}\rvert < 4.33$
	0.2	$4.33 \leq \lvert\mathcal{T}\rvert < 5.67$
	0.3	$5.67 \leq \lvert\mathcal{T}\rvert < 7.0$
medium	0.4	$7.0 \leq \lvert\mathcal{T}\rvert < 8.33$
	0.5	$8.33 \leq \lvert\mathcal{T}\rvert < 9.67$
	0.6	$9.67 \leq \lvert\mathcal{T}\rvert < 11.0$
strong	0.7	$11.0 \leq \lvert\mathcal{T}\rvert < 12.33$
	0.8	$12.33 \leq \lvert\mathcal{T}\rvert < 13.67$
	0.9	$13.67 \leq \lvert\mathcal{T}\rvert \leq 15.0$
blocking	1.0	$\lvert\mathcal{T}\rvert > 15.0$

embedded in this BUC loop.

The second key step in the cloudy-air GHG retrieval is a correction of the target species transmission profiles from the cloud perturbations signaled by the cloud flagging profile. This step (named *Cloud Profile Correct. Tar. Sp. Transmission* in Figure 4.6a), follows the retrieval of the target species transmission profile $\mathcal{T}_{\text{tgt}}$, or equivalently the absorption loss profile $|\mathcal{T}_{\text{tgt}}|$ (magnitude of $\mathcal{T}_{\text{tgt}}$), which was described in detail by Proschek, Kirchengast and Schweitzer (2011, , section 3.4.2 therein). The step uses the cloud flagging profile to perform a correction of the $\mathcal{T}_{\text{tgt}}$ profiles of all GHGs to be retrieved over altitude levels perturbed by clouds.

We apply cloud correction for perturbed layers of vertical extent up to 3 km; larger cloud-induced gaps are not corrected both for not locally degrading the resolution of individual GHG profiles too much against the nominal retrieved-profile resolution of ∼1 km and for keeping the bridging of $\mathcal{T}_{\text{tgt}}$ gaps (discussed below) sufficiently accurate over the gaps. Figure 4.6c, left subpanel, illustrates the cloud-perturbed absorption loss profiles $|\mathcal{T}_{\text{tgt}}|$ derived from the raw profiles in Figure 4.6b; they are to be corrected for their degradations at certain altitudes which are clearly related to the cloud interferences.

We implemented this correction as follows. Altitude ranges with cloud flag 0 may contain weak noise effects in the $\mathcal{T}_{\text{tgt}}$ profile if small cloud perturbation effects were

present (below the 3 dB limit described in section 4.2.2); this noise is due to slightly non-identical paths of the absorption and reference signals, since the refraction is sligthly dispersive for the LIO signals (Schweitzer, Kirchengast and Proschek 2011). In addition some residual numerical errors can contribute to the noise, which is due to the need to interpolate within the forward modeling the ice water content (IWC) to slightly different raypaths (an effect that would not occur in real data). We mitigate any such possible small noise in altitude ranges with cloud flag 0 by performing a low-pass filter on the $\mathcal{T}_{\rm tgt}$ profile (BWS filter operated effectively as moving average, smoothing to a resolution of ∼400 m or smaller, down to ∼200 m for narrow flag 0 ranges between cloud-perturbed layers).

If stronger clouds are present, or even blocking clouds leading to gaps in the IR-laser signals, a bridging of $\mathcal{T}_{\rm tgt}$ across the cloud-perturbed layers is required. For this purpose, we determine the perturbed layers from the nonzero flags of the cloud flagging profile and a bridging is done for any cloud-induced gap of vertical extent smaller than 3 km where at least ∼400 m of flag 0 range is available at both sides of the gap. The bridging is implemented as an interpolation of the $\mathcal{T}_{\rm tgt}$ profile and the interpolation process starts and ends ∼400 m above and below the bridged gaps, since we take 15 data points from the flag 0 profile as basis at each side. For profiles with an essentially (log)linear shape as function of altitude, like $^{13}CO_2$ and CH_4 profiles, (log)linear interpolation is applied, while for profiles changing more strongly, like the $^{12}CO_2$ profile, cubic-spline interpolation is applied. These interpolation choices ensure a good approximation of the shape of $\mathcal{T}_{\rm tgt}$ over any gaps.

An exception are the strongly varying $H_2O(X)$ (X={1, 2, 3, 4}) transmission profiles, for which the above interpolation shapes are found to be not accurate enough for avoiding biases under all conditions tested. We therefore took benefit for this species from the H_2O profile obtained from the LMO retrieval preceding the LIO retrieval. Even though the LMO-retrieved H_2O profile is of lower accuracy than LIO can provide (Schweitzer et al. 2011; Proschek, Kirchengast and Schweitzer 2011), we can use it to forward simulate the LIO H_2O transmission profiles across the gap. Except for replacing the H_2O profile from the set of initial/background profiles by the LMO-derived H_2O profile, this LIO forward modeling is the same as described by Proschek, Kirchengast and Schweitzer (2011) for foreign species correction, i.e., it uses the Reference Forward Model (RFM), which is fed by the HITRAN2008 molecular spectroscopic database and the initial GHG profiles from the FASCODE model (Edwards 1996; Dudhia 2008; Rothman et al. 2009; FASCODE 2008). The forward simulated piece of H_2O transmission is then used across the gap and the H_2O transmission profile is further improved in course of the BUC runs of the multi-species GHG retrieval Proschek, Kirchengast and Schweitzer (2011, , section 3.6 therein).

To be precise, since the forward simulated H_2O transmission piece across the gap may show some offset to the H_2O transmissions ∼400 m above and below the gap, which could occur due to LMO retrieval errors, we smoothly retify the simulated transmission

piece over the gap to match the transmission data above and below. In detail, the mean offsets of the simulated transmission piece from the 15-data-point samples above and below are computed and a linear offset function is determined for all levels across the gap connecting the offset values above and below. Subtracting this linear offset function, the simulated transmission piece over the gap is then rectified in its shape to match the 15-data-point samples above and below. It is this rectified simulated transmission piece that is actually used for the bridging as described above.

Figure 4.6c, right subpanel, illustrates the cloud-corrected absorption loss profiles $|\mathcal{T}_{\mathrm{tgt}}|$ after applying the correction measures described above to the cloud-perturbed $|\mathcal{T}_{\mathrm{tgt}}|$ shown in the left subpanel. The result profiles are now found of a quality similar to clear-air profiles, although, depending on the character of the cloud perturbations, the vertical resolution may be degraded (up to 3 km locally) at some altitudes, compared to genuine clear-air profiles (retrieved-profile resolution ∼1 km throughout).

Having the cloud-corrected $|\mathcal{T}_{\mathrm{tgt}}|$ profiles available, the remaing steps in the GHG retrieval process are again the same as in the clear-air algorithm described by Proschek, Kirchengast and Schweitzer (2011); an Abel transform (Fjeldbo, Kliore and Eshleman 1971; Schweitzer et al. 2011) provides retrieved absorption coefficient profiles from which finally the GHG volume mixing ratio (VMR) profiles are derived. Note that this whole cloud correction process is carried out within the BUC loop, and its multispecies retrieval inner loop, so that also the cloud bridging can benefit from the iterative improvements due to these loops.

In the postprocessing and use of the data, we know from the cloud flagging profile the altitudes where the profiles were bridged and thus need to be used carefully because the retrieval error might be higher in these ranges. The better the approximation of the transmission bridging performs, the better the VMR profile will be, since the Abel integration will extend residual perturbations of the $|\mathcal{T}_{\mathrm{tgt}}|$ profile from interfering cloud layers further downwards.

4.3.2 Demonstration results

For demonstration and assessment of the GHG retrieval performance in cloudy-air and under the influence of scintillations due to turbulence, we performed LMIO end-to-end simulations in clear air, clear air plus scintillations, cloudy air, and cloudy air plus scintillations. We performed the forward simulations in the quasi-realistic manner as described in section 4.2.3, for all eight occultation events illustrated in Figure 4.3, and the retrieval processing as described in the previous subsection 4.3.1. We performed a multispecies retrieval focusing on the main GHGs carbon dioxide (CO_2), methane (CH_4), and water vapor (H_2O); the results for N_2O and CO would be of similar quality as for CH_4, high-quality O_3 is limited to above 15 km (Proschek, Kirchengast and Schweitzer 2011), and the water vapor isotopes HDO and $H_2^{18}O$ are limited to below 12 km (Kirchengast and Schweitzer 2011; Schweitzer, Kirchengast and Proschek 2011).

Figures 4.7–4.9 illustrate the GHG retrieval performance results, mainly in terms of volume mixing ratio (VMR) errors. We show the profiles from 5 km up to 25 km since our focus interest is the potentially cloud-influenced upper troposphere and tropopause region below 20 km. Each plot panel illustrates four events (day cases or night cases) and the associated individual retrieval error profiles shown were computed as (relative or absolute) difference of retrieved VMR profile from the 'true' VMR profile used in the forward modeling. In the panels showing relative errors, the mean error (heavy green profile near zero) and the standard deviations (heavy blue profiles left/right from zero) were obtained by estimating them in a moving window of 5 km width (i.e., within ±2.5 km at any altitude level) from all the individual error values in the window.

We show the results without clouds (Figure 4.7) for the four nighttime occultation events only, since for the daytime events the retrieval performance is essentially the same. Furthermore, we do not show the cloudy-air results without scintillations, since above the cloud-influenced altitudes in the lower stratosphere they are essentially the same as the clear-air results (Figure 4.7a, 4.7c, and 4.7e), and at the cloud-influenced upper tropospheric altitudes they show similar added-error characteristics as the cloudy-air cases plus scintillations (Figures 4.8a, 4.8c, 4.8e, 4.9a, 4.9c, and 4.9e). Also, in the real atmosphere scintillations will always occur.

Figure 4.7 compares, for the nighttime events (Figure 4.3a), the VMR retrieval error results for CO_2, CH_4, and H_2O (top to bottom) for clear air (Figure 4.7a, 4.7c, and 4.7e) with the results for clear air plus scintillations (Figure 4.7b, 4.7d, and 4.7f). The clear-air results provide backlink to the performance demonstration results of Proschek, Kirchengast and Schweitzer (2011) (though produced here with a sampling rate of 50 Hz rather than 10 Hz, which should only lead to small differences for clear air, however). We find the clear-air results consistent with the Proschek, Kirchengast and Schweitzer (2011) results, as expected.

Furthermore, we find the influence of scintillations from atmospheric turbulence to dominate the random error budget for all species and throughout the UTLS, as is clearly seen in Figure 4.7b, 4.7d, and 4.7f. That is, the receiving system noise from the finite SNR, governing the random errors in clear air without scintillations (Kirchengast and Schweitzer 2011; Schweitzer, Kirchengast and Proschek 2011), is adequately below the estimated turbulence-induced errors. This confirms that the ACCURATE mission design and system specifications (Kirchengast et al. 2010a) are sensible and not technically limiting the performance more than residual errors from natural atmospheric processes.

The total RMS error (heavy blue profiles), including estimated scintillation influence, is still found within target observational requirements for all species over most of the UTLS, and well within threshold requirements overall. Also, the retrieved profiles are found statistically unbiased (heavy green profiles), which is key to their climate benchmarking data quality (Goody, Anderson and North 1998; Leroy, Dykema and Anderson 2006).

Regarding the tropospheric penetration depths reached by the GHG profiles for these end-to-end simulations without clouds, they are limited by the bottom altitude achieved

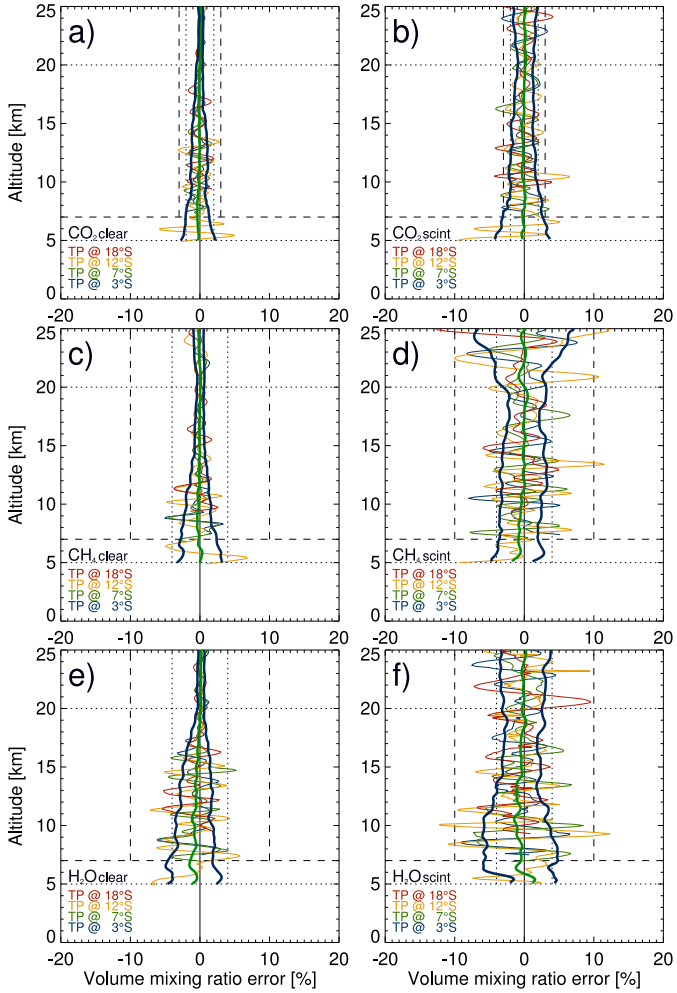

Figure 4.7: Volume mixing ratio (VMR) retrieval errors of CO_2 (a and b), CH_4 (c and d), and H_2O (e and f) for clear-air conditions (Figure 4.7a, 4.7c, and 4.7e) and clear-air conditions plus scintillations (Figure 4.7b, 4.7d, and 4.7f), for the four nighttime occultation events of Figure 4.3a; see the in-panel legends for the tangent point (TP) locations (latitudes) and for the color of the respective profiles. The solid green/blue lines represent mean and standard deviation estimates as explained in the introductory part of section 4.3.2. The horizontal and vertical dotted/dashed lines indicate the target/threshold observational requirements for altitude domain and accuracy for the ACCURATE/LMIO mission concept (Larsen, Kirchengast and Bernath 2009; Kirchengast et al. 2010a) (except for the line at 20 km, indicating the top of the cloudy-air domain).

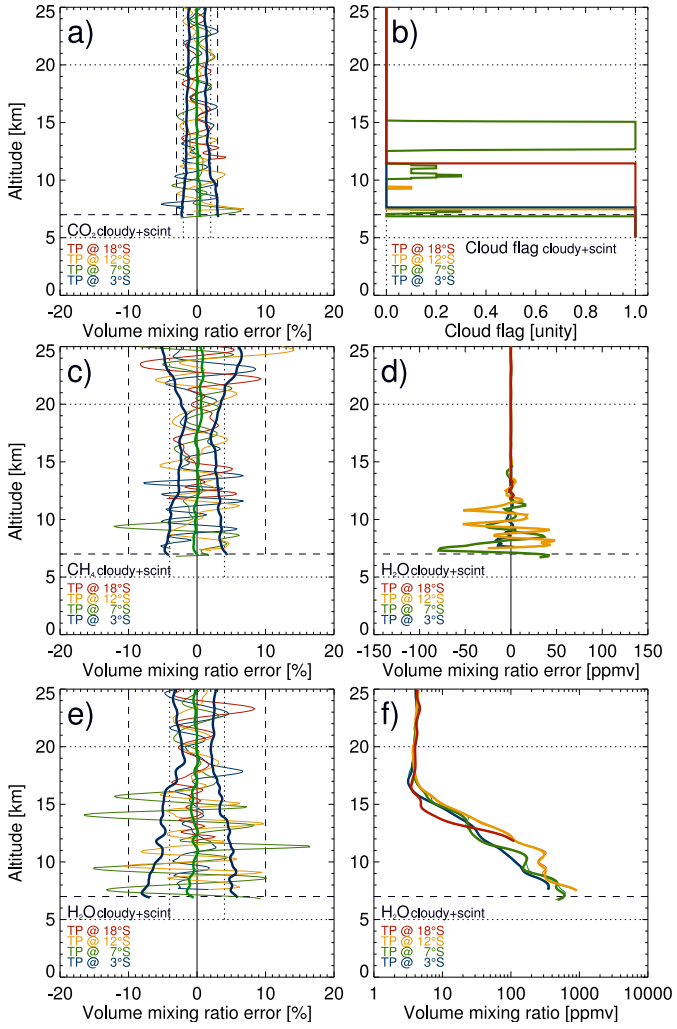

Figure 4.8: Volume mixing ratio (VMR) retrieval errors of CO_2 (a), CH_4 (c), and H_2O (e relative, d absolute), cloud flagging profiles (b), and H_2O VMR profiles (f), for cloudy-air conditions plus scintillations, for the four nighttime occultation events of Figure 4.3a; see the in-panel legends for the tangent point (TP) locations (latitudes) and for the color of the respective profiles. The layout of panels Figure 4.8a, 4.8c, and 4.8e is the same as in Figure 4.7 (see that caption); the vertical dotted lines in Figure 4.8b indicate the cloud flag bounds 0 and 1.

by the LMO retrieval, which in the current EGOPS implementation depends on various settings as described in detail by Schweitzer et al. (2011); typically the LMO profiles reach down to about 7 km to 5 km or even lower.

Figure 4.8 (for the nighttime events, Figure 4.3a) and Figure 4.9 (for the daytime events, Figure 4.3b) illustrate the VMR retrieval error results for CO_2, CH_4, and H_2O for cloudy-air conditions plus scintillations (Figure 4.8a, 4.8c, and 4.8e). They also include complementary illustration of the corresponding cloud flagging profiles (Figure 4.8b) and, for the highly variable species H_2O, of the VMR retrieval error (Figure 4.8d) and the retrieved VMR profiles (Figure 4.8f) in absolute terms (units ppmv).

Comparing Figure 4.8a, 4.8c, and 4.8e to the corresponding Figure 4.7b, 4.7d, and 4.7f, we can see that the retrieval through broken cloudiness is fairly successful for all three species and is fairly similar in performance to the clear-air plus scintillations case, which is a very encouraging result. The RMS error at the cloud-influenced upper tropospheric altitudes is increased by a small amount only (most for H_2O), and the profiles remain statistically unbiased. Clearly, though, depending on individual cloudiness conditions, the tropospheric penetration depth of the GHG profiles is limited if reaching a cloud top below which the LIO signals are fully cloud-blocked. As the cloud flagging profiles indicate (Figure 4.8b), this occurs for the given example events for three of four cases (orange, green, blue) only near 7 km, for one case (red) near 11 km.

The corresponding Figure 4.9a, 4.9c, and 4.9e confirm these findings for the separately simulated daytime events. The results show that cloud interferences were reliably bridged by the cloudy-air retrieval in three cases, near 7 km and 6 km for the red case, near 10 km and 8 km for the orange case, and near 12 km and 11 km for the green case; the blue case reached a cloud top near 10 km that limited further penetration. Overall, the retrieval performance for these events is essentially the same as for the nighttime events, indicating that the LMIO capability of supplying data that enable accurate GHG retrieval through broken cloudiness is a robust result.

H_2O as a highly variable species is the relatively most sensitive species to be affected by broken cloudiness. This can be seen in Figures 4.8e and 4.9e and in back-comparison of Figure 4.8e to Figure 4.7f. Figures 4.8d and 4.8f and 4.9d and 4.9f illustrate the strong vertical variations of the H_2O profiles, also over short altitude scales where the vertical resolution limits of the retrieval are reached. This will generally lead to somewhat more "spiky" behavior of the VMR errors (as, for example, seen for the light green profile in Figure 4.8e). The care needed to avoid residual biases under these challenging conditions justifies the cloud-bridging approach for H_2O, invoking LMO-derived H_2O as background, as discussed in section 4.3.1.

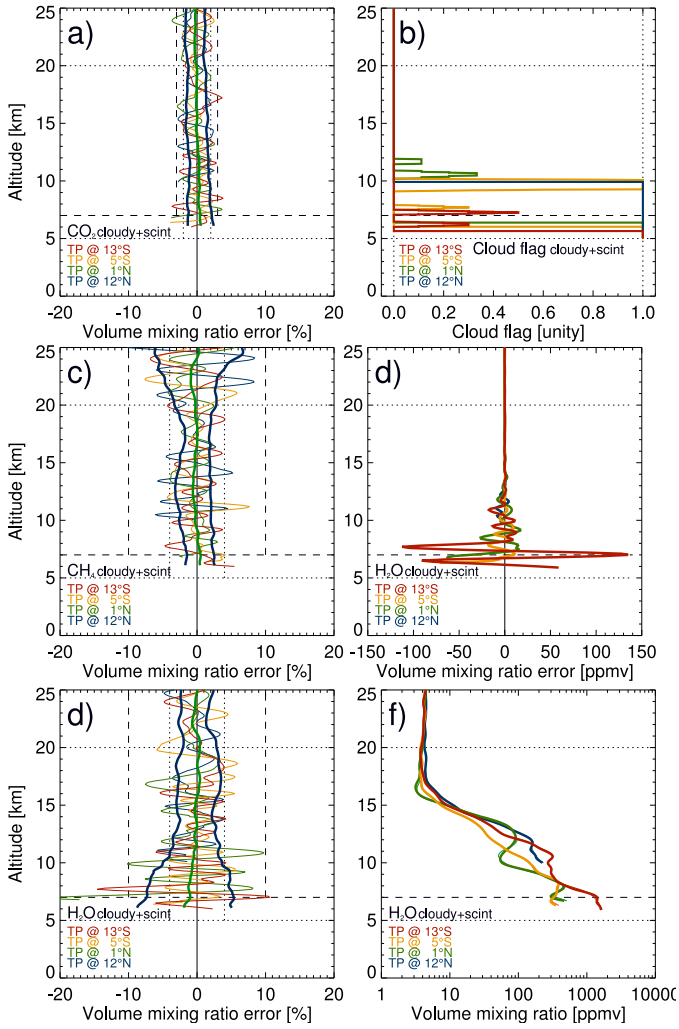

Figure 4.9: Volume mixing ratio (VMR) errors for CO_2, CH_4, and H_2O, cloud flagging profiles, and H_2O VMR profiles for the four daytime occultation events of Figure 4.3b. The layout is the same as in Figure 4.8; see that caption for explanation.

4.4 Summary and conclusions

In this study we introduced an extension of the LMIO retrieval algorithm under clear-air conditions, presented by (Proschek, Kirchengast and Schweitzer 2011), namely algorithm advancements enabling a GHG retrieval under cloudy-air conditions. We also assessed the coinfluence of scintillations due to atmospheric turbulence. The main interest of the new cloudy-air GHG retrieval is to benefit from improved tropospheric penetration of retrieved GHG profiles through broken cloudiness; without the advancements the retrievals would be limited by the highest ice water cloud tops reached despite they might only block over a limited altitude range. If the GHG profiles under broken cloudiness can be restored, while keeping them essentially unbiased and with only a modest increase in RMS error, they can valuably contribute to long-term GHG monitoring over the upper troposphere.

We performed quasi-realistic LMIO end-to-end simulations with the xEGOPS/EGOPS software, including high-resolution cloud data from the CALIPSO satellite and scintillations from turbulence in the forward simulations, on top of all other relevant effects already included by Proschek, Kirchengast and Schweitzer (2011). We included the cloudy-air algorithmic advancements in the xEGOPS/EGOPS retrieval processing system and described these new algorithmic steps in detail as part of this study.

We find that sub-visible cirrus and very thin cirrus clouds fractionally extinct the IR-laser signals, thicker but broken patches of ice clouds block them over limited altitude ranges, and liquid water clouds generally block them so that their cloud top altitudes typically constitute the limit to tropospheric penetration of retrieved GHG profiles. The advanced algorithm achieves the penetration of GHG retrievals through broken cloudiness by first determining a cloud flagging profile from perturbed IR-laser signals, which then enables bridging of cloud-perturbed IR-laser transmission profile gaps via interpolation. For postprocessing and use of the data, the cloud flagging profile rigorously conserves the knowledge where the GHG profiles needed to be bridged, enabling clear and traceable quality control.

For a demonstration and evaluation of the GHG retrieval performance in cloudy air and under the influence of scintillations due to turbulence, we performed end-to-end simulations of eight representative occultation events in clear air, clear air plus scintillations, cloudy air, and cloudy air plus scintillations and assessed the volume mixing ratio (VMR) retrieval error results obtained for the main GHGs carbon dioxide (CO_2), methane (CH_4), and water vapor (H_2O).

We find the clear-air results consistent with the Proschek, Kirchengast and Schweitzer (2011) results, as expected. Furthermore, we find the influence of scintillations from atmospheric turbulence to dominate the GHG's random error budget throughout the UTLS. This implies that the receiving system noise from finite signal-to-noise ratio, governing the random errors in clear air without scintillations, is adequately smaller than the estimated turbulence-induced errors. This confirms that the ACCURATE/LMIO

mission design and system specifications are sensible and not technically limiting the performance more than residual errors from natural atmospheric processes. The total error, including estimated scintillation influence, is still found within target observational requirements for the GHGs over most of the UTLS, and well within threshold requirements overall. Also, the retrieved profiles are found statistically unbiased, which is key to their benchmark data quality.

For the cloudy-air results, including scintillation influence, we find that the retrieval through broken cloudiness is fairly successful for all GHGs, which is a very promising result. The VMR retrieval RMS error at cloud-influenced upper tropospheric altitudes is increased by a small amount only and the profiles remain statistically unbiased and well within observational requirements. Depending on the character of the cloud perturbations, the vertical resolution may be degraded (up to 3 km locally) at some altitudes, compared to clear-air profiles (resolution ∼1 km throughout). Also, depending on the specific cloudiness conditions for an occultation event, the tropospheric penetration depth of the GHG profiles will be limited if reaching a cloud top below which the LIO signals are fully blocked. Such cloud tops were encountered, in the example cases analyzed, for two of eight cases around 10 km but for the remaining six cases near 7 km or lower only.

Overall these results are encouraging for future ACCURATE/LMIO mission implementation, indicating that GHG profiles can be reliably retrieved through broken cloudiness, maximizing upper troposphere coverage. The advanced algorithm therefore valuably contributes to the climate benchmarking capability of the LMIO method, which can provide global, accurate, and long-term stable atmospheric profiling of thermo-dynamic variables and GHGs for climate monitoring and research and other applications.

Summary and Conclusions

IMPROVING measurement techniques or developing new methods for better climate benchmark profiling is an on-going and needed process within the climate research community.

The goal of this thesis was to contribute to the LEO–LEO infrared-laser occultation (LIO) measurement technique of the ACCURATE—Climate Benchmark Profiling of Greenhouse Gases and Thermodynamic Variables and Wind from Space mission concept with assessment work on atmospheric influences on Infrared Laser (IRL) signals and with retrieval algorithm development and related greenhouse gas (GHG) retrieval performance analyses.

In chapter 1 a short overview on the historical and current situation regarding climate change with respect to temperature and greenhouse gas changes was given. The current research shows with high confidence that the contemporary climate change is primarily a man-made process and shows strong anomaly to the natural climate variability. For a better understanding of dynamical processes and for more reliable projections of future climate scenarios an improvement in measurement techniques is needed. We need long-term stable Essential Climate Variables (ECVs) with high accuracy and global coverage, including independence from model or external information.

This need motivated the mission concept ACCURATE, applying the Low Earth Orbit (LEO–LEO) microwave and infrared-laser occultation (LMIO) measurement technique, a synergistic combination of the LEO–LEO microwave occultation (LMO) and the LIO technique for which an overview was given as well.

An overview was also given of the eXtended End-to-End Generic Occultation Performance Simulation and Processing System (xEGOPS), developed for the purpose of the LMIO assessment work in this thesis and beyond, and based on the End-to-End Generic Occultation Performance Simulation and Processing System (EGOPS) software tool. The software is composed of four subsystems, namely the Mission Analysis/Planning (MAP) as preparation for the occultation event global distribution, the Forward Modeling (FOM), as simulation tool to quasi-realistically simulate the atmospheric processes acting on microwave (MW) and IRL signals, the Observation System Modeling (OSM), superposing the observational errors on the forward-propagated signals, and the retrieval tool named Occultation Processing System (OPS).

Based on the above mission concept and tools, first a detailed study into the atmospheric effects on the IRL signals was performed, which defined the observational requirements of an LMIO mission and provided insight to the GHG information contained in the signals.

An assessment of relevant atmospheric influences, like molecular absorption, defocusing loss, aerosol extinction, Rayleigh scattering and scintillation, was performed for the entire set of IRL on-absorption and off-channels of H_2O-(1, 2, 3, 4), $^{12}CO_2$, $^{13}CO_2$, $C^{18}OO$, CH_4, N_2O, O_3, CO, HDO and $H_2^{18}O$. Within the whole upper troposphere–lower stratosphere (UTLS) focus range (5 km to 35 km) all channel total absorption losses stay below 21 dB signal-to-noise ratio (SNR) boundary and are thus suitable channel selections for the LIO measurement technique. The water vapor channels exceed this boundary outside their specific target altitude range (sub-ranges of the UTLS), but can be combined within the retrieval process to an entire water vapor (H_2O) altitude profile covering the UTLS. The altitude range for ozone (O_3) is limited to above about 10 km and semiheavy water (HDO) and heavy-oxygen water ($H_2^{18}O$) are only detectable between about 5 km and about 12 km, respectively.

Furthermore, the synergistic combination of the LMO and LIO in the LMIO method was used to develop an algorithm for multi-species GHG retrieval from IRL signals, first for clear-air conditions. This basis algorithm covers the process flow using a set of on-absorption and off-channels for the retrieval of GHG volume mixing ratio (VMR) profiles from quasi-realistic forward-simulated IRL signals. A detailed description of the geometric parameter calculations as preparatory step, the so-called Single-Line Trace Species Retrieval (SSR) and the Multi-Line Trace Species Retrieval (MSR), was given. The retrievals show unbiased results and VMR root mean square (r.m.s.) errors within 1 % to 3 % for carbon dioxide, water vapor, methane and ozone, within the UTLS altitude range.

Building on the clear-air algorithm, an extension to cloudy-air was then performed. These extensions of the LIO algorithm, treating cloud-perturbed IRL signals, enable a retrieval process under conditions of broken cloudiness. Bridging processes, (log-)linear interpolation for all GHGs except H_2O, the latter using re-simulation of transmission profiles within cloud-induced gaps from LMO water vapor output, enable a recovery over intermittent cloud gaps or thin-cirrus-perturbed altitude ranges. The cloudy-air algorithm improves the troposphere penetration depth of retrieved GHG profiles and prevents the profiles to be terminated first by broken-cloud presence. The VMR results under such challenging conditions, including error due to scintillation from atmospheric turbulence, show unbiased results and appear to essentially remain within the target observational requirement range.

The three core publications cited in the Preface (Schweitzer, Kirchengast and Proschek 2011; Proschek, Kirchengast and Schweitzer 2011; Proschek et al. 2014a) were the basis for Chap. 2 – Chap. 4, wherein the above summarized studies are described in detail.

These published studies are essential and integral parts of the ACCURATE mission concept assessment. We can conclude from the results that the ACCURATE concept

indeed shows promising prospects to provide climate benchmark capability for GHG profiling and thermodynamic profiles covering the UTLS and beyond.

Currently on-going follow-on work to the Ph.D. thesis studies is in the final phase to publication of (encouraging) results also for line-of-sight wind profiling, the remaining key climate variable available from IRL signals that was not yet assessed before. Complementary work on the pioneering ground-based IRL occultation demonstration experiment in the Canary Islands has provided a first successful experimental proof of concept measuring GHGs by long-path IRL signals, over 144 km between the islands of La Palma and Tenerife. Publications from both this ground-based demonstration work and the wind profiling assessment work are included as complementary references in the Preface.

Altogether the results point to a bright future of the LMIO technique and underpin its enormous scientific utility. It is therefore hoped that an ACCURATE satellite mission will be implemented over the next few years.

List of Figures

List of Tables

Acronyms

Symbols

N Refractivity. 15, 17, 19

N_{mw} MW Refractivity. 19

R_{C} Earth's local radius of curviture. 26

T Temperature. 15, 17–19, 26, 33, 37, 40, 41, 151

T_{d} Dry temperature. 17–19

α Bending angle. 17, 19, 38

α_{ir} IR Bending angle. 15

α_{mw} MW Bending angle. 15, 19

a Impact parameter. 38

a_{ir} IR Impact parameter. 15

a_{mw} MW Impact parameter. 15, 17, 19

n Refractive index. 19

p Pressure. 15, 17–19, 26, 33, 37, 40, 41

p_{d} Dry Pressure. 17–19

q Specific humidity. 15, 17–19, 33, 37, 40, 41

r Tangent radius. 19

r_{ir} IR Radial distance. 15

r_{mw} MW Radial distance. 15

$v_{\mathrm{l.o.s.}}$ Line-of-sight wind velocity. 13, 15, 17, 23, 37

z Altitude. 17

z_{ir} IR Altitude. 17

CH_4 Methane [target species of Climate Benchmark Profiling of Greenhouse Gases and Thermodynamic Variables and Wind from Space (ACCURATE)]. 2, 5, 6, 15, 21, 24, 27, 41, 43, 45, 60–62, 65–67, 70, 78, 152

CO_2 Carbon dioxide [target species of ACCURATE]. 1, 2, 5, 6, 15, 24, 27, 41, 58, 60–62, 67, 70, 78, 152

CO Carbon monoxide [target species of ACCURATE]. 15, 21, 22, 24, 27, 41, 43, 45, 61, 65, 70, 78, 79, 152

$C^{18}OO$ Carbon dioxide isotope with one heavy-oxygen atom ^{18}O [target species of ACCURATE]. 15, 21, 23, 24, 27, 41, 43, 45, 58, 61, 62, 66, 67, 76, 78, 152

H_2O Water vapor [target species of ACCURATE]. 2, 15, 18, 19, 21, 22, 24, 27, 31, 41, 43, 45, 54, 58, 60–62, 65, 66, 70, 71, 78, 79, 152

HDO Semiheavy Water isotope of water vapour with one heavy-hydrogen atom ^{2}H [target species of ACCURATE]. 15, 21, 22, 24, 27, 41, 43, 45, 60–62, 70, 78, 80, 152

$H_2^{18}O$ Heavy-oxygen water isotope of water vapour with one heavy-oxygen atom ^{18}O [target species of ACCURATE]. 15, 21, 22, 24, 27, 41, 43, 45, 60–62, 66, 70, 78–80, 152

N_2O Nitrous oxide [laughing gas (target species of ACCURATE)]. 5, 6, 15, 21, 24, 27, 41, 43, 45, 61, 65, 70, 78, 152

O_3 Ozone [target species of ACCURATE]. 2, 15, 18, 21, 22, 24, 27, 41, 43, 45, 61, 62, 65–67, 70, 71, 78, 79, 152

$^{12}CO_2$ Carbon dioxide main CO_2 isotope [target species of ACCURATE]. 15, 21, 24, 26, 27, 31, 43, 45, 51, 58, 62, 152

$^{13}CO_2$ Carbon dioxide main isotope with one heavy-carbon atom ^{13}C [target species of ACCURATE]. 15, 21, 24, 27, 43, 45, 58, 61, 62, 78, 152

A

ACCURATE Climate Benchmark Profiling of Greenhouse Gases and Thermodynamic Variables and Wind from Space. iii, v, vii, 1, 2, 15, 22, 33, 44, 45, 47, 49, 50, 54, 58, 61, 70, 71, 75–80, 151–153

ACE Atmospheric Chemistry Experiment [Canadian solar occultation mission]. 13, 23, 30, 74

AIRS Atmospheric Infrared Sounder. 13

AMT Atmospheric Measurement Techniques. 43, 83

AOGCM Atmosphere-Ocean Global Circulation Model. 8

Aqua NASA Science Satellite [Latin word for water]. 13

AR5 IPCC Fifth Assessment Report [Climate Change 2013]. 6, 8

ASAP Austrian Space Applications Programme [programme within the Österreichische Forschungsförderungsgesellschaft (FFG) funded by the Ministry of Innovation and Transport]. vii

ATOMMS Active Temperature, Ozone, and Moisture Microwave Spectrometer. 18

B

BUC Basic-Update-Control Runs. 24, 27

C

CALIPSO Cloud–Aerosol LIDAR Infrared Pathfinder Satellite Observations. 31

CarbonSat Carbon Monitoring Satellite [proposed to EE-9]. 13

CHAMP Challenging Mini-Satellite Payload. 18

CICERO Community Initiative for Continuing Earth Radio Occultation. 18

CMIP-3 Coupled Model Intercomparison Project – Phase 3. 8, 10

CMIP-5 Coupled Model Intercomparison Project – Phase 5. 8, 10

Copernicus The European Earth Observation Programme [formerly Global Monitoring for Environment and Security (GMES)]. 10

COSMIC Constellation Observing System for Meteorology, Ionosphere, and Climate. 18

E

ECMWF European Centre for Medium-Range Weather Forecasts. 31, 37, 41, 47

ECV Essential Climate Variable [As defined by GCOS]. 10, 13, 151

EE-8 Earth Explorer 8 [mission call from the LPP]. 15

EGOPS End-to-End Generic Occultation Performance Simulation and Processing System. vii, 2, 20–22, 33, 38, 41, 48, 51, 52, 151

ENVISAT Environmental Satellite. 13

EOS Earth Observation System. 13

ESA European Space Agency. vii, 15

F

FASCODE Fast Atmospheric Signature Code [simple atmospheric model]. 21, 24, 27, 31, 37, 41, 51, 52, 54, 56, 58, 62, 67, 69, 71, 78

FOM Forward Modeling. 20, 33, 35, 37, 38, 51, 151

FOV Field of View. 76, 77, 80

FTS Fourier Transform Spectrometer. 13

FWHM Full-Width at Half Maximum. 21

G

GCM General Circulation Model. 10

GCOS Global Climate Observing System. 10

GHG Greenhouse Gas. vii, 2, 5, 6, 8, 10, 20–22, 24, 26, 27, 30, 31, 37, 40, 43, 83, 151, 152

GHGs Greenhouse Gases. iii, v, 2, 5, 6, 8, 10, 13, 15, 17, 24, 27, 33, 40, 41, 152, 153

GOSAT Greenhouse Gases Observing Satellite. 13

GPS Global Positioning System. 17, 33, 47

GRACE Gravity Recovery and Climate Experiment. 18

GRAS Global Navigation Satellite Systems Receiver for Atmospheric Sounding. 18

GRO GNSS–LEO radio occultation. 17, 19, 47, 48, 50

GRUAN GCOS Reference Upper-Air Network. 10

H

HadCRUT4 Hadley Centre/Climatic Research Unit gridded surface temperature data set 4. 8, 10

HITRAN High-Resolution Transmission [molecular spectroscopic database]. 21, 26, 52

I

IASI Infrared Atmospheric Sounding Interferometer. 13

IR Infrared. 15, 21, 26, 33, 37–40

IRL Infrared Laser. iii, v, 2, 15, 17, 20–24, 26, 30, 31, 37, 38, 40, 41, 43, 151–153

IWC Ice Water Content. 23, 31, 37

J

JGR Journal of Geophysical Research. 121

L

LEO Low Earth Orbit. 1, 17, 43, 44, 53, 76, 78, 80, 151

LIO Low Earth Orbit (LEO–LEO) infrared-laser occultation. iii, v, 1, 2, 13, 15, 17, 20, 21, 23, 24, 26, 27, 30, 33, 35, 40, 43, 45, 47, 48, 50–53, 56, 66, 67, 69–71, 74, 76–80, 151, 152

LMIO Low Earth Orbit (LEO–LEO) microwave and infrared-laser occultation [(synergistic use of LIO and LMO)]. iii, v, vii, 1, 2, 13, 15, 20, 27, 33, 35, 38, 40, 41, 43–45, 47, 50, 53, 56, 74, 78, 80, 83, 121, 151–153

LMO Low Earth Orbit (LEO–LEO) microwave occultation. iii, v, 1, 2, 13, 15, 17–20, 24, 26, 27, 31, 40, 41, 47, 48, 50, 52, 53, 58, 74, 78, 79, 151, 152

LOS Line of Sight. 43, 45, 47, 48, 76, 78, 80

LRR Liquid Rain Rate. 37

LWC Liquid Water Content. 23, 31, 37

M

MACC-II Monitoring Atmospheric Composition and Climate - Interim Implementation. 10

MAP Mission Analysis/Planning. 33, 35, 37, 51, 151

MetOp Meteorological Operational [satellite series]. 13, 18

MIPAS Michelson Interferometer for Passive Atmospheric Sounding. 13

MPM93 Millimeter Wave Propagation Model 1993. 38

MSR Multi-Line Trace Species Retrieval. 24, 27, 40, 41, 152

MW Microwave. 15, 17, 20, 21, 24, 26, 30, 33, 37–40, 44, 45, 47, 50, 53, 54, 56, 78, 79, 151

N

NASA National Aeronautics and Space Administration. 13

NEP Noise-Equivalent Power [a measure of the sensitivity of optical detectors]. 50, 70

NH Northern Hemisphere. 8

NWP Numerical Weather Prediction. 18

O

OCO-2 Orbiting Carbon Observatory–2. 13

OPS Occultation Processing System. 33, 40, 151

OSM Observation System Modeling. 33, 38–40, 151

P

PAB Perpendicular Attenuated Back-scatter. 31

POD Precise Orbit Determination. 39

R

r.m.s. Root Mean Square. iii, 19, 152

RFM Reference Forward Model. 21, 26, 52

RO Radio Occultation. 18, 33

Rx Receiver. 15, 23, 24, 35, 37–39, 51

S

S/N$_0$ Signal-to-Noise Density Ratio. 39

SAGE II Stratospheric Aerosol and Gas Experiment II [a solar occultation instrument aboard the ERBS satellite of NASA]. 22, 52, 53

SAW Subarctic Winter [used in context with the FASCODE atmospheres]. 27, 35, 51, 54, 56, 58, 60–62, 69, 70, 78, 79

SCIAMACHY Scanning Imaging Absorption Spectrometer for Atmospheric Cartography. 13

SciSat-1 Scientific Satellite–1. 13

SH Southern Hemisphere. 8

SNR Signal-to-Noise Ratio. 18, 22–24, 39, 49, 50, 56, 58, 65, 67, 70, 71, 74, 77, 79, 80, 152

SSR Single-Line Trace Species Retrieval. 24, 26, 27, 31, 40, 152

STD Standard [used in context with the FASCODE atmospheres]. 24, 27, 35, 51, 54, 56, 58, 60–62, 65, 67, 69, 71, 78, 79

SWIR Short Wave Infrared [spectral region (1.5 μm to 2 μm; here referring to the 2 μm to 2.5 μm region)]. 13, 43–45, 47, 50–54, 56, 58, 60, 62, 66, 67, 71, 75–80

T

TANSO Thermal And Near infrared Sensor for carbon Observation. 13

TCCON Total Carbon Column Observing Network. 10

TLE Two-Line Element. 35

TP Tangent Point. 22, 35, 37, 38

TRO Tropical [used in context with the FASCODE atmospheres]. 27, 35, 51, 54, 56, 58, 60–62, 69, 70, 78, 79

Tx Transmitter. 15, 35, 37, 39, 51

U

UTLS Upper Troposphere–Lower Stratosphere [region]. iii, v, 1, 15, 43–45, 50, 58, 61, 66, 67, 70, 75–78, 80, 152

UV Ultraviolet. 13

V

VMR Volume Mixing Ratio. iii, 2, 24, 26, 27, 40, 51, 52, 56, 58, 60, 66, 83, 152

W

WGS84 World Geodetic System 1984. 35

WMO World Meteorological Organization. 10

X

xEGOPS eXtended End-to-End Generic Occultation Performance Simulation and Processing System. vii, 2, 20–23, 26, 33, 35, 40, 41, 43, 48, 51–53, 83, 121, 151

Bibliography

AQUA (2014). *website last visited 2014-03-29*. URL: http://aqua.nasa.gov/ (cit. on p. 13).

Allison, C. E. and R. J. Francey (2007). 'Verifying southern hemisphere trends in atmospheric carbon dioxide stable isotopes'. In: *J. Geophys. Res.* 112, D21304. DOI: 10.1029/2006JD007345 (cit. on pp. 27, 109).

Ammann, C. M. et al. (2003). 'A monthly and latitudinally varying volcanic forcing dataset in simulations of 20^{th} century climate'. In: *Geophys. Res. Lett.* 30. ISSN: 1944-8007. DOI: 10.1029/2003GL016875 (cit. on p. 8).

Anderson, G. P. et al. (1986). *AFGL atmospheric constituent profiles (0–120 km)*. Environ. Res. Papers, Tech. Rep. 954, AFGL-TR-86-0110. Hanscom AFB, Massachusetts, USA: Optical Phys. Div., Air Force Geophys. Lab. (cit. on pp. 22, 51, 89, 116, 130).

Andrews, L. C. and R. L. Philips (2005). *Laser Beam Propagation through Random Media*. 2nd Edn. Bellingham, Washington D. C., USA: SPIE Press (cit. on p. 123).

Anthes, R. A. et al. (2008). 'The COSMIC/FORMOSAT-3 mission: Early results'. In: *Bull. Amer. Meteorol. Soc.* 89, pp. 313–333. DOI: 10.1175/BAMS-89-3-313 (cit. on pp. 18, 47, 84).

Arrhenius, S. (1896). 'On the influence of carbonic acid in the air upon the temperautre of the ground'. In: *Philos. Mag. and J. Sci.* 42, pp. 237–276 (cit. on pp. 1, 6).

Aschbacher, J. and M. P. Milagro-Pérez (2012). 'The European Earth monitoring (GMES) programme: Status and perspectives'. In: *Remote Sens. Environ.* 120, pp. 3–8. ISSN: 0034-4257. DOI: 10.1016/j.rse.2011.08.028 (cit. on p. 13).

Barnett, T. P. et al. (2000). 'Uncertainty levels in predicted patterns of anthropogenic climate change'. In: *J. Geophys. Res. Atmos.* 105, pp. 15525–15542. ISSN: 2156-2202. DOI: 10.1029/2000JD900162 (cit. on p. 6).

Bernath, P. F. et al. (2005). 'Atmospheric Chemistry Experiment (ACE): Mission overview'. In: *Geophys. Res. Lett.* 32. ISSN: 1944-8007. DOI: 10.1029/2005GL022386 (cit. on p. 123).

Beyerle, G. et al. (2005). 'GPS radio occultation with GRACE: Atmospheric profiling utilizing the zero difference technique'. In: *Geophys. Res. Lett.* 32. ISSN: 1944-8007. DOI: 10.1029/2005GL023109 (cit. on p. 18).

Bindoff, N. L. et al. (2013). '2013: Detection and Attribution of Climate Change'. In: *Climate Change 2013: The Physical Science Basis. Contribution of Working Group I to the Fifth Assessment Report of the Intergovernmental Panel on Climate Change*. Ed. by T. F. Stocker et al. United Kingdom and New York, NY, USA: Cambridge University Press (cit. on pp. 8, 11).

Blunier, T. et al. (1994). 'Variations in atmospheric methane concentration during the Holocene epoch'. In: *Nature* 374, pp. 46–49. DOI: 10.1038/374046a0 (cit. on p. 6).

Bönsch, G. and E. Potulski (1998). 'Measurements of the refractive index of air and comparison with modified Edlén's formulae'. In: *Metrologia* 35, pp. 133–139. DOI: 10.1088/0026-1394/35/2/8 (cit. on pp. 21, 38, 52, 87, 89, 92, 96).

Born, M. and E. Wolf (1964). *Principles of Optics*. New York: Pergamon Press (cit. on pp. 26, 92, 95, 97).

Brohan, P. et al. (2006). 'Uncertainty estimates in regional and global observed temperature changes: A new data set from 1850'. In: *J. Geophys. Res. Atmos.* 111. ISSN: 2156-2202. DOI: 10.1029/2005JD006548 (cit. on p. 6).

Brooke, J. S. A. et al. (2012). 'Greenhouse gas measurements over a 144 km open path in the Canary Islands'. In: *Atmos. Meas. Tech.* 5, pp. 2309–2319. DOI: 10.5194/amt-5-2309-2012. URL: http://www.atmos-meas-tech.net/5/2309/2012/ (cit. on pp. ix, 20, 122).

Buontempo, C., A. Jupp and M. Rennie (2008). 'Operational NWP assimilation of GPS radio occultation data'. In: *Atmos. Sci. Lett.* 9, pp. 129–133. ISSN: 1530-261X. DOI: 10.1002/asl.173 (cit. on p. 18).

Carbonsat (2014). *website last visited 2014-03-29*. URL: http://www.iup.uni-bremen.de/carbonsat/ (cit. on p. 13).

Cardinali, C. (2009). *Forecast Sensitivity to Observation (FSO) as a diagnostic tool*. Tech. Memorandum 599. Reading, United Kingdom: European Centre for Medium-Range Weather Forecasts (cit. on p. 47).

Ciais, P. et al. (2013). '2013: Carbon and Other Biogeochemical Cycles'. In: *Climate Change 2013: The Physical Science Basis. Contribution of Working Group I to the Fifth Assessment Report of the Intergovernmental Panel on Climate Change*. Ed. by T. F. Stocker et al. United Kingdom and New York, NY, USA: Cambridge University Press (cit. on pp. 6, 7).

Dudhia, A. (2008). 'Reference Forward Model RFM: Inst. of Atmos., Oceanic and Planet. Phys., Univ. of Oxfor, Oxford, UK'. In: http://www.atm.ox.ac.uk/RFM/.last access: 3 April 2014 (cit. on pp. 22, 26, 39, 89, 94, 103, 141).

ENVISAT (2014). *website last visited 2014-03-29*. URL: https://earth.esa.int/web/guest/missions/esa-operational-eo-missions/envisat (cit. on p. 13).

Edlén, B. (1966). 'The refractive index of air'. In: *Metrologia* 2, pp. 71–80. DOI: 10.1088/0026-1394/2/2/002 (cit. on pp. 21, 52, 96).

Edwards, D. P. (1996). *High level algorithm definition document*. Tech. Rep. ESA/ESTEC PO-TN-OXF-GS-0004, Contract No. 11886/96/NL/GS. Oxford, UK: Inst. of Atmos., Oceanic and Planet. Phys., , Univ. of Oxford. URL: http://www.atm.ox.ac.uk/RFM/ (cit. on pp. 39, 52, 89, 94, 103, 141).

Emde, C. and V. Proschek (2010). *Atmospheric impacts on ILO signals: Impact of cloud scattering*. Tech. Rep. ESA/ESTEC TN2—Part of TR-IRPERF Report. Wessling, Germany: DLR Oberpfaffenhofen (cit. on pp. 23, 30, 74, 77, 80, 87, 127).

Emde, C., V. Proschek and G. Kirchengast (2009). *Atmospheric impacts on MWO signals: Impact of cloud scattering at 175–200 GHz*. Tech. Rep. ESA/ESTEC TN-Clouds—Part of TR-MWPERF Report. Wessling, Germany: DLR Oberpfaffenhofen (cit. on pp. 30, 124).

FASCODE (2008). 'RFM website—FASCODE model atmospheres: Inst. of Atmos., Oceanic and Planet. Phys., Univ. of Oxford, Oxford, UK'. In: last access: 3 April 2014. URL: http://www.atm.ox.ac.uk/RFM/atm (cit. on pp. 38, 89, 116, 130, 141).

Feng, D. D. et al. (2002). 'Deriving atmospheric water vapour and ozone profiles from active microwave occultation measurements'. In: *Sensors, Systems and Next-Generation Satellites IV*. Ed. by H. Fujisada et al. Vol. 4169. SPIE Proceedings Series. Bellingham, USA: SPIE - Int. Soc. Optical Engineering, pp. 299–308. ISBN: 0-8194-3825-1 (cit. on p. 47).

Fischer, H. et al. (1999). 'Ice core records of atmospheric CO_2 around the last three glacial terminations'. In: *Science* 283, pp. 1712–1714. DOI: 10.1126/science.283.5408.1712. URL: http://www.sciencemag.org/content/283/5408/1712.abstract (cit. on p. 5).

Fjeldbo, G. and V. R. Eshleman (1965). 'The bistatic radar-occultation method for the study of planetary atmospheres'. In: *J. Geophys. Res.* 70, pp. 3217–3225 (cit. on pp. 19, 26, 92, 97).

Fjeldbo, G., A. J. Kliore and V. R. Eshleman (1971). 'The neutral atmosphere of venus as studied with the Mariner V radio occultation experiments'. In: *Astron. J.* 76, pp. 123–140 (cit. on pp. 92, 97, 142).

Flückiger, J. et al. (2002). 'High-resolution Holocene N_2O ice core record and its relationship with CH_4 and CO_2'. In: *Global Biogeochem. Cycles* 16, pp. 10–1–10–8. ISSN: 1944-9224. DOI: 10.1029/2001GB001417 (cit. on p. 6).

Forster, P. M. et al. (2013). 'Evaluating adjusted forcing and model spread for historical and future scenarios in the CMIP5 generation of climate models'. In: *J. Geophys. Res. Atmos.* 118, pp. 1139–1150. ISSN: 2169-8996. DOI: 10.1002/jgrd.50174 (cit. on p. 8).

Francey, R. J. et al. (1999). 'A 1000-year high precision record of δ^{13}C in atmospheric CO_2'. In: *Tellus B* 51, pp. 170–193. ISSN: 1600-0889. DOI: 10.1034/j.1600-0889.1999.t01-1-00005.x (cit. on p. 6).

Fritzer, J. M., G. Kirchengast and M. Pock (2009a). *End-to-End Generic Occultation Performance Simulation and Processing System version 5.5 —Detailed Design Document*. Tech. Rep. ESA-ESTEC 2/2009. Graz, Austria: Wegener Center, Inst. for Geophys., Astrophys., and Meteorol., Univ. of Graz (cit. on pp. 34, 40, 41).

– (2009b). *End-to-End Generic Occultation Performance Simulation and Processing System version 5.5 (EGOPS 5.5) Software User Manual*. Tech. Rep. ESA-ESTEC 1/2009. Graz, Austria: Wegener Center, Inst. for Geophys., Astrophys., and Meteorol., Univ. of Graz (cit. on pp. 21, 34, 88, 124).

Fritzer, J. M. et al. (2010a). *End-to-End Generic Occultation Performance Simulation and Processing System version 5.5 (EGOPS 5.5 and xEGOPS)—Detailed Design Document*. Tech. Rep. ESA-ESTEC 2/2010. Graz, Austria: Wegener Center, Inst. for Geophys., Astrophys., and Meteorol., Univ. of Graz (cit. on pp. 23, 34, 41, 48, 51–54, 78).

– (2010b). *End-to-End Generic Occultation Performance Simulation and Processing System version 5.5 (EGOPS 5.5 and xEGOPS) Software User Manual*. Tech. Rep. ESA-ESTEC 1/2010. Graz, Austria: Wegener Center, Inst. for Geophys., Astrophys., and Meteorol., Univ. of Graz (cit. on pp. 21, 34, 48, 78, 88, 124).

From, E. and C. D. Keeling (1986). 'Reassessment of late 19th century atmospheric carbon dioxide variations in the air of western Europe and the British Isles based on an unpublished analysis of contemporary air masses by G. S. Callendar'. In: *Tellus B* 38B, pp. 87–105. ISSN: 1600-0889. DOI: 10.1111/j.1600-0889.1986.tb00092.x (cit. on p. 1).

GOSAT (2014). *website last visited 2014-03-29*. URL: http://www.gosat.nies.go.jp/index_e.html (cit. on p. 13).

Gobiet, A. and G. Kirchengast (2004). 'Advancement of GNSS radio occultation retrieval in the upper stratosphere'. In: *Occultations for Probing Atmosphere and Climate*. Ed. by G. Kirchengast, U. Foelsche and A. K. Steiner. Graz, Austria: Springer, Berlin-Heidelberg, pp. 137–148. ISBN: 978-3540223504 (cit. on p. 19).

Gobiet, A. et al. (2005). 'Climatological validation of stratospheric temperatures in ECMWF operational analyses with CHAMP radio occultation data'. In: *Geophys. Res. Lett.* 32, p. L12806. DOI: 10.1029/2005GL022617 (cit. on p. 47).

Goody, R., J. Anderson and G. North (1998). 'Testing Climate Modesl: An Approach'. In: *Bull. Amer. Meteorol. Soc.* 79, pp. 2541–1549. DOI: 10.1175/1520-0477(1998)079<2541:TCMAA>2.0.CO;2 (cit. on p. 143).

Gorbunov, M. E. and G. Kirchengast (2005). 'Processing X/K band radio occultation data in the presence fo turbulence'. In: *Radio Sci.* 40, RS6001. DOI: 10.1029/2005RS003263 (cit. on pp. 47, 86).

– (2007). 'Fluctuations of radio occultation signals in X/K band in the presence of anisotropic turbulence and differential transmission retrieval performance'. In: *Radio Sci.* 42, RS4025. DOI: 10.1029/2006RS003544 (cit. on pp. 45, 47, 86, 88).

Gurvich, A. S., V. Kan and O. V. Fedorova (1996). 'Refraction angle fluctuations in the atmosphere from space observations of stellar scintillations'. In: *Atmos. Ocean. Phys.* 31. Englisch Version, pp. 742–749 (cit. on p. 133).

Gurvich, A. S. et al. (2012). 'Spatiotemporal structure of a laser beam over 144 km in a Canary Islands experiment'. In: *Appl. Opt.* 51, pp. 7374–7383. DOI: 10.1364/AO.51.007374. URL: http://ao.osa.org/abstract.cfm?URI=ao-51-30-7374 (cit. on pp. ix, 123).

Gurvich, A. S. et al. (2014). 'Spatiotemporal structure of a laser beam at a path length of 144 km: comparative analysis of spatial and temporal spectra'. In: *Appl. Opt.* 53.12, pp. 2625–2631. DOI: 10.1364/AO.53.002625. URL: http://ao.osa.org/abstract.cfm?URI=ao-53-12-2625 (cit. on p. ix).

Hajj, G. A. et al. (2002). 'A technical description of atmospheric sounding by GPS occultation'. In: *J. Atmos. Sol.-Terr. Phys.* 64, pp. 451–469 (cit. on p. 47).

Harrison, J. J. and P. F. Bernath (2010). *Spectroscopic properties of greenhouse gases from 2.0 to 2.5 μm*. Tech. Rep. UoY/ESA-IRDAS/Greenhouse/ Jan. 2010. York, UK: Dept. of Chemistry, Univ. of York (cit. on pp. 23, 30, 75, 123).

Harrison, J. J., P. F. Bernath and G. Kirchengast (2011). 'Spectroscopic requirements for ACCURATE, a microwave and infrared-laser occultation satellite mission'. In: *J. Quantit. Spectr. Radiat. Transfer* 112, pp. 2347–2354 (cit. on pp. 90, 122).

Healy, S. B. (2011). 'Refractivity coefficients used in the assimilation of GPS radio occultation measurements'. In: *J. Geophys. Res.* 116, p. D01106. DOI: 10.1029/2010JD014013 (cit. on p. 56).

Healy, S. B. and J.-N. Thépaut (2006). 'Assimilation experiments with CHAMP GPS radio occultation measurements'. In: *Q. J. R. Meteorol. Soc.* 132, pp. 605–623. DOI: 10.1256/qj.04.182 (cit. on p. 47).

Hegerl, G. C. et al. (2007). '2007: Understanding and Attributing Climate Change'. In: *Climate Change 2007: The Physical Science Basis. Contribution of Working Group I to the Fourth Assessment Report of the Intergovernmental Panel on Climate Change*. Ed. by S. Solomon et al. United Kingdom and New York, NY, USA: Cambridge University Press. URL: https://www.ipcc.ch/publications_and_data/ar4/wg1/en/ch9.html (cit. on p. 8).

Herman, B. M. et al. (2004). 'An overview of the University of Arizona ATMOS project'. In: *Occultations for Probing Atmosphere and Climate*. Ed. by G. Kirchengast, U. Foelsche and A. K. Steiner. Berlin-Heidelberg: Springer Verlag (cit. on pp. 18, 47, 86).

Ho, S.-P. et al. (2009). 'Estimating the uncertainty of using GPS radio occultation data for climate monitoring: Inter-comparison of CHAMP refractivity climate records 2002–2006 from different data centers'. In: *J. Geophys. Res.* 114, D23107. DOI: 10.1029/2009JD011969 (cit. on pp. 47, 84).

Horwath, J. and N. Perlot (2008). *Atmospheric impacts on ILO signals: Scintillation*. Tech. Rep. ESA/ESTEC TN4—Part of TR-IRPERF Report. Oberpfaffenhofen, Germany: DLR Oberpfaffenhofen (cit. on pp. 23, 39, 75, 133).

Hu, Y. X. and K. Stamnes (1993). 'An accurate parameterization of the radiative properties of water clouds suitable for use in climate models'. In: *J. Climate* 6, pp. 728–742 (cit. on pp. 31, 39, 74, 126).

Immler, F. J. et al. (2010). 'Reference quality upper-air measurements: Guidance for developing GRUAN data products'. In: *Atmos. Meas. Tech.* 3, pp. 1217–1231. DOI: 10.5194/amt-3-1217-2010. URL: http://www.atmos-meas-tech.net/3/1217/2010/ (cit. on p. 13).

Jensen, A. S. et al. (2003). 'Full spectrum inversion of radio occultation signals'. In: *Radio Sci.* 38, 1040. DOI: 10.1029/2002RS002763 (cit. on pp. 99, 139).

Jones, G. S., P. A. Stott and N. Christidis (2013). 'Attribution of observed historical near–surface temperature variations to anthropogenic and natural causes using CMIP5 simulations'. In: *J. Geophys. Res. Atmos.* 118, pp. 4001–4024. ISSN: 2169-8996. DOI: 10.1002/jgrd.50239 (cit. on p. 8).

Joos, F and R Spahni (2008). 'Rates of change in natural and anthropogenic radiative forcing over the past 20,000'. In: *Proc. National Academy of Sci.* 105, pp. 1425–1430. DOI: 10.1073/pnas.0707386105 (cit. on p. 6).

Karl, T. R. et al. (1996). 'Long-Term Climate Monitoring by the Global Climate Observing System (GCOS)'. In: *Long-Term Climate Monitoring by the Global Climate Observing System*. Ed. by T. R. Karl. Springer Netherlands, pp. 5–17. ISBN: 978-94-010-4143-0. DOI: 10.1007/978-94-011-0323-7_2 (cit. on p. 10).

Keeling, C. D. (1970). 'Is carbon dioxide from fossil fuel changing man's environment?' In: *Proc. Amer. Phil. Soc.* 114, pp. 10–17 (cit. on p. 1).

Key, J. et al. (2002). 'Parameterization of shortwave ice cloud optical properties for various particle habits'. In: *J. Geophys. Res.* 107, p. 4181. DOI: 10.1029/2001JD000742 (cit. on pp. 31, 39, 74, 126, 127).

Kirchengast, G. (1996). *End-to-End GNSS Occultation Performance Simulator functionality definition*. Tech. Rep. ESA/ESTEC 1/1996. Graz, Austria: Inst. for Meteorol. and Geophys., Univ. of Graz (cit. on p. 88).

– (1998). *End-to-End GNSS Occultation Performance Simulator overview and exemplary applications*. Wiss. Ber. ESA/ESTEC 2/1998. Graz, Austria: Inst. for Meteorol. and Geophys., Univ. of Graz (cit. on p. 88).

– (2004). 'Occultations for probing atmosphere and climate: Setting the scene'. In: *Occultations for Probing Atmosphere and Climate*. Ed. by G. Kirchengast, U. Foelsche and A. K. Steiner. Berlin-Heidelberg, Germany: Springer, pp. 1–8. ISBN: 978-3540223504 (cit. on pp. 15, 45, 86).

Kirchengast, G., J. M. Fritzer and J. Ramsauer (2002). *End-to-End GNSS Occultation Performance Simulator version 4 (EGOPS4) Software User Manual*. Tech. Rep. ESA/ESTEC 2/2002. Graz, Austria: Inst. for Geophys., Astrophys., and Meteorol. (cit. on p. 88).

Kirchengast, G. and P. Hoeg (2004). 'The ACE+ mission: An atmosphere and climate explorer based on GPS, GALILEO and LEO-LEO radio occultation'. In: *Occultations for Probing Atmosphere and Climate*. Ed. by G. Kirchengast, U. Foelsche and A. K. Steiner. Berlin-Heidelberg: Springer Verlag (cit. on pp. 18, 41, 47).

Kirchengast, G. and S. Schweitzer (2007). *ACCURATE LEO-LEO infrared laser occultation initial assessment: Requirements, payload characteristics, scientific performance analysis, and breadboarding specifications*. Tech. Rep. FFG-ALR 3/2007. Graz, Austria: Wegener Center, Univ. of Graz (cit. on p. 45).

– (2011). 'Climate benchmark profiling of greenhouse gases and thermodynamic structure and wind from space'. In: *Geophys. Res. Lett.* 38, L13701. DOI: 10.1029/2011GL047617 (cit. on pp. 14, 15, 23, 27, 36, 43–45, 49–51, 57, 61, 66, 71, 74, 76, 78, 80, 84, 86–88, 90, 92, 99, 103, 107, 110, 112, 117–119, 122, 124, 130, 133, 142, 143).

Kirchengast, G. et al. (2004). *The Atmosphere and Climate Explorer mission ACE+: Scientific algorithm and performance overview*. Tech. Rep. ESA/ESTEC 2/2004. Graz, Austria: Inst. for Geophys., Astrophys., and Meteorol., Univ. of Graz (cit. on p. 90).

Kirchengast, G. et al. (2006). *Advanced retrieval processing chain for derivation of atmospheric profiles from LEO-LEO radio occultation data*. Tech. Rep. ESA/ESTEC 2/2006. Graz, Austria: Wegener Center, Univ. of Graz (cit. on p. 97).

Kirchengast, G. et al. (2007). *End-to-End Generic Occultation Performance Simulator version 5.2 (EGOPSv5.2) Software User Manual*. Tech. Rep. ESA/ESTEC 4/2007. Graz, Austria: Wegener Center, Univ. of Graz (cit. on p. 88).

Kirchengast, G. et al. (2010a). *ACCURATE—climate benchmark profiling of greeen-house gases and thermodynamic variables and wind from space (ESA Earth Explorer Opportunity Mission EE-8 proposal)*. Sci. Rep. 36-2010. Graz, Austria: Wegener Center Verlag. URL: http://www.wegcenter.at/wcv (cit. on pp. 15, 21, 24, 27, 29, 30, 36, 39, 44, 45, 49–51, 55, 61, 71, 76–78, 81, 84, 87, 88, 90, 99, 100, 105, 107, 112, 117, 119, 122, 129, 133, 143, 144).

Kirchengast, G. et al. (2010b). *ALPS – ACCURATE LIO Performance Simulator – User Guide and Documentation*. Tech. Rep. ESA-ESTEC 3/2010. Graz, Austria: Wegener Center, Univ. of Graz (cit. on pp. 110, 112).

Kursinski, E. R. et al. (1997). 'Observing Earth's atmosphere with radio occultation measurements using the global positioning system'. In: *J. Geophys. Res.* 102, pp. 23429–23465 (cit. on pp. 18, 19, 47, 84, 96, 123).

Kursinski, E. R. et al. (2000). 'The GPS radio occultation technique'. In: *Terr. Atmos. Oceanic Sci.* 11, pp. 53–114 (cit. on pp. 39, 50, 56, 123).

Kursinski, E. R. et al. (2002). 'A microwave occultation observing system optimized to characterize atmospheric water, temperature and geopotential via absorption'. In: *J. Atmos. Ocean. Tech.* 19, pp. 1897–1914. DOI: 10.1175/1520-0426(2002)019 (cit. on pp. 18, 19, 45, 47, 86, 88, 94).

Kursinski, E. R. et al. (2004). 'An active microwave limb sounder for profiling water vapor, ozone, temperature geopotential, clouds, isotopes and stratospheric winds'. In: *Occultations for Probing Atmosphere and Climate*. Ed. by G. Kirchengast, U. Foelsche and A. K. Steiner. Berlin-Heidelberg: Springer Verlag (cit. on pp. 18, 47).

Kursinski, E. R. et al. (2009). 'The Active Temperature, Ozone and Moisture Microwave Spectrometer (ATOMMS)'. In: *New Horizons in Occultation Research*. Ed. by A. K. Steiner et al. Berlin-Heidelberg: Springer Verlag. DOI: 10.1007/978-3-642-00321-9_24 (cit. on pp. 18, 47, 86).

Kyrölä, E. et al. (2004). 'GOMOS on Envisat: An overview'. In: *Adv. Space Res.* 33, pp. 1020–1028. ISSN: 0273-1177. DOI: 10.1016/S0273-1177(03)00590-8 (cit. on pp. 75, 123).

Kyrölä, E. et al. (2010). 'Retrieval of atmospheric parameters from GOMOS data'. In: *Atmos. Chem. Phys.* 10, pp. 11881–11903. DOI: 10.5194/acp-10-11881-2010. URL: http://www.atmos-chem-phys.net/10/11881/2010/ (cit. on p. 123).

Landolt-Börnstein (1984). *Geophysics of the Solid Earth, the Moon and the Planets - Numerical Data and Functional Relationships in Science and Technology*. Ed. by K. Fuchs and H. Stoffel. Vol. 2V/a. Berlin-Heidelberg: Springer Verlag (cit. on pp. 36, 51, 88).

Larsen, G. B., G. Kirchengast and P. F. Bernath (2009). *Science objectives and observational requirements of the ACCURATE mission concept*. Tech. Rep. DMI/ESA-IRDAS/ObsReq/Oct2009. Copenhagen, Denmark: Danish Meteorol. Inst. (cit. on pp. 29, 100, 105, 144).

Le Quéré, C. et al. (2013). 'Global carbon budget 2013'. In: *Earth Sys. Sci. Data Discussions* 6, pp. 689–760. DOI: 10.5194/essdd-6-689-2013. URL: http://www.earth-syst-sci-data-discuss.net/6/689/2013/ (cit. on p. 13).

Leroy, S. S., J. A. Dykema and J. G. Anderson (2006). 'Climate benchmarking using GNSS occultation'. In: *Atmosphere and Climate*. Ed. by U. Foelsche, G. Kirchengast and A. Steiner. Springer Berlin Heidelberg, pp. 287–301. ISBN: 978-3-540-34116-1. DOI: 10.1007/3-540-34121-8_24 (cit. on p. 143).

Li, F., J. Austin and J. Wilson (2008). 'The strength of the Brewer-Dobson circulation in a changing climate: Coupled chemistry-climate model simulations'. In: *J. Climate* 21, pp. 40–57. DOI: 10.1175/2007JCLI1663.1 (cit. on p. 45).

Liebe, H. J., G. Hufford and M. Cotton (1993). 'Propagation modeling of moist air and suspended water/ice particles at frequencies below 1000 GHz'. In: *AGARD Proc. Atmospheric Propagation Effects through Natural and Man-Made Obscurants for Visible to MM-Wave Radiation*. Ed. by Delfour, A., et al. Boulder, CO: NTIA, pp. 3–1–3–10. ISBN: SEE N94-30495 08-32 (cit. on pp. 39, 89).

Liou, K. N. (2002). *An Introduction to Atmospheric Radiation*. 2nd. San Diego, California, USA: Academic Press. ISBN: 0-12-451451-0 (cit. on pp. 66, 77, 78, 123).

Lockwood, M. et al. (2010). 'Are cold winters in Europe associated with low solar activity?' In: *Environ. Res. Lett.* 5, p. 024001. URL: http://stacks.iop.org/1748-9326/5/i=2/a=024001 (cit. on p. 8).

Luntama, J.-P. et al. (2008). 'Prospects of the EPS GRAS mission for operational atmospheric applications'. In: *Bull. Amer. Meteorol. Soc.* 89, pp. 1863–1875. DOI: 10.1175/2008BAMS2399.1 (cit. on pp. 18, 84).

Lusignan, B. et al. (1969). 'Sensing the Earth's atmosphere with occultation satellites'. In: *Proc. IEEE* 57, pp. 458–467 (cit. on p. 18).

MACC-II (2014). *website last visited 2014-03-29* (cit. on p. 13).

MacFarling-Meure, C. et al. (2006). 'Law Dome CO_2, CH_4 and N_2O ice core records extended to 2000 years BP'. In: *Geophys. Res. Lett.* 33. ISSN: 1944-8007. DOI: 10.1029/2006GL026152 (cit. on p. 6).

Manabe, S. and R. T. Wetherald (1967). 'Thermal equilibrium of the atmosphere with a given distribution of relative humidity'. In: *J. Atmos. Sci.* 24, pp. 241–259. DOI: 10.1175/1520-0469(1967)024<0241:TEOTAW>2.0.CO;2 (cit. on p. 10).

Mann, M. E. et al. (2008). 'Proxy-based reconstructions of hemispheric and global surface temperature variations over the past two millennia'. In: *Proc. National Academy of Sci.* 105, pp. 13252–13257. DOI: 10.1073/pnas.0805721105 (cit. on p. 6).

Masson-Delmotte, V. et al. (2013). '2013: Information from Paleoclimate Archives'. In: *Climate Change 2013: The Physical Science Basis. Contribution of Working Group I to the Fifth Assessment Report of the Intergovernmental Panel on Climate Change*. Ed. by T. F. Stocker et al. United Kingdom and New York, NY, USA: Cambridge University Press (cit. on pp. 8, 9).

McCormick, C. et al. (2007). 'Community Initiative for Continuing Earth Radio Occultation CICERO'. In: Technical Session I: Mission Metrics, SSC07-I-3. 21st Annual AIAA/USU Conference on Small Satellites. URL: http://digitalcommons.usu.edu/smallsat/2007/all2007/4/ (cit. on p. 18).

McFarquhar, G. M. and A. J. Heymsfield (1997). 'Parameterization of Tropical Cirrus Ice Crystal Size Distributions and Implications for Radiative Transfer: Results from CEPEX'. In: *J. Atmos. Sci.* 54, pp. 2187–2200. DOI: 10.1175/1520-0469(1997)054<2187:POTCIC>2.0.CO;2 (cit. on p. 126).

Melbourne, W. G. et al. (1994). *The Application of Spaceborne GPS to Atmospheric Limb Sounding and Global Change Monitoring*. 94-18. Pasadena, CA: NASA/JPL (cit. on p. 97).

MetOp (2014). *website last visited 2014-03-29*. URL: http://www.eumetsat.int/website/home/Satellites/CurrentSatellites/Metop/index.html (cit. on p. 13).

Moberg, A. et al. (2005). 'Highly variable Northern Hemisphere temperatures reconstructed from low- and high-resolution proxy data'. In: *Nature* 433, pp. 613–617. DOI: 10.1038/nature03265 (cit. on pp. 1, 6).

Monnin, E. et al. (2004). 'Evidence for substantial accumulation rate variability in Antarctica during the Holocene, through synchronization of CO_2 in the Taylor Dome, Dome C and {DML} ice cores'. In: *Earth Planet. Sci. Lett.* 224, pp. 45–54. ISSN: 0012-821X. DOI: 10.1016/j.epsl.2004.05.007. URL: http://www.sciencedirect.com/science/article/pii/S0012821X04003115 (cit. on p. 6).

Morice, C. P. et al. (2012). 'Quantifying uncertainties in global and regional temperature change using an ensemble of observational estimates: The HadCRUT4 data set'. In: *J. Geophys. Res. Atmos.* 117. ISSN: 2156-2202. DOI: 10.1029/2011JD017187 (cit. on pp. 1, 8).

OCO-2 (2014). *website last visited 2014-03-29*. URL: http://oco.jpl.nasa.gov/ (cit. on p. 13).

PAGES 2k Consortium (2013). 'Continental-scale temperature variability during the past two millennia'. In: *Nature Geosci.* 6, pp. 339–346. DOI: 10.1038/ngeo1797 (cit. on p. 8).

Pagani, M., M. A. Arthur and K. H. Freeman (1999). 'Miocene evolution of atmospheric carbon dioxide'. In: *Paleoceanography* 14, pp. 273–292. ISSN: 1944-9186. DOI: 10.1029/1999PA900006 (cit. on p. 5).

Pannekoek, A. (1903). 'Über die Erscheinungen, welche bei einer Sternbedeckung durch einen Planeten auftreten'. In: *Astronomische Nachrichten* 164, pp. 5–10. ISSN: 1521-3994. DOI: 10.1002/asna.19031640103 (cit. on p. 19).

Petit, J. R. et al. (1999). 'Climate and atmospheric history of the past 420,000 years from the Vostok ice core, Antarctica'. In: *Nature* 399, pp. 429 –436. DOI: 10.1038/20859 (cit. on p. 5).

Phinney, R. A. and D. L. Anderson (1968). 'On the radio occultation method for studying planetary atmospheres'. In: *J. Geophys. Res.* 73, pp. 1819–1827. DOI: 10.1029/JA073i005p01819 (cit. on pp. 15, 45, 86).

Plach, A., V. Proschek and G. Kirchengast (2013). *Abel transform retrieval of wind profiles from LEO-LEO IR laser occultation: End-to-end simulations and performance analysis*. Tech. Rep. ESA-ESTEC 2/2013. Graz, Austria: Wegener Center, Univ. of Graz (cit. on p. 24).

– (2014). 'Profiling wind and greenhouse gases by infrared-laser occultation: algorithm and end-to-end simulation results in windy air'. In: *Atmos. Meas. Tech.* submitted (cit. on pp. ix, 24).

Proschek, V., G. Kirchengast and S. Schweitzer (2011). 'Greenhouse gas profiling by infrared-laser and microwave occultation: retrieval algorithm and demonstration results from end-to-end simulations'. In: *Atmos. Meas. Tech.* 4, pp. 2035–2058. DOI: 10.5194/amt-4-2035-2011. URL: http://www.atmos-meas-tech.net/4/2035/2011/ (cit. on pp. ix, 16, 17, 20, 24, 26, 27, 29–31, 34, 36, 37, 41, 45, 47, 48, 50, 52, 54, 56, 58, 60, 62, 66, 70, 71, 79–81, 83, 122–124, 129, 130, 133, 135, 139–143, 148, 152).

Proschek, V., A. Plach and G. Kirchengast (2014). *Wind and greenhouse gas retrieval from LEO-LEO IR laser occultation in windy air: algorithm description and performance analysis*. Tech. Rep. EAS-ESTEC 1/2014. Graz, Austria: Wegener Center, Univ. of Graz (cit. on p. 24).

Proschek, V., S. Schweitzer and G. Kirchengast (2011). *Greenhous gas profiles retrieval from IR-laser occultation data in cloudy air*. Tech. Rep. FFG-ALR 1/2011. Graz, Austria: Wegener Center, Univ. of Graz (cit. on p. 127).

Proschek, V. et al. (2014a). 'Greenhouse gas profiling by infrared-laser and microwave occultation in cloudy air: results from end-to-end simulations'. In: *J. Geophys. Res. Atmos.* 119, pp. 12,372–12,390. DOI: 10.1002/2014JD021938 (cit. on pp. ix, 20, 23, 24, 30, 32, 33, 41, 121, 152).

Proschek, V. et al. (2014b). 'Retrieval and validation of carbon dioxide, methane and water vapor for the Canary Islands infrared-laser occultation experiment'. In: *Atmos. Meas. Tech. Discuss.* 7, pp. 11593–11652. DOI: 10.5194/amtd-7-11593-2014. URL: http://www.atmos-meas-tech-discuss.net/7/11593/2014/amtd-7-11593-2014.html (cit. on pp. ix, 20).

Rahmsdorf, S. and H. J. Schellnhuber (2007). *Der Klimawandel*. Munich, Germany: C. H. Beck (cit. on p. 5).

Ramsauer, J. and G. Kirchengast (2000). *End-to-End GNSS Occultation Performance Simulator version 3 (EGOPS3) Software User Manual*. Tech. Rep. ESA/ESTEC 1/2000. Graz, Austria: Inst. for Geophys., Astrophys., and Meteorol., Univ. of Graz (cit. on p. 88).

– (2001). *Sensitivity of atmospheric profiles retrieved from GNSS radio occultation data to instrumental errors*. Tech. Rep. ESA/ESTEC 6/2001. Graz, Austria: Inst. for Geophys., Astrophys., and Meteorol., Univ. of Graz (cit. on p. 40).

Rothman, L. S. et al. (2005). 'The HITRAN 2004 molecular spectroscopic database'. In: *J. Quantitat. Spectrosc. Radiat. Transf.* 96, pp. 139–204. DOI: 10.1016/j.jqsrt.2004.10.008 (cit. on pp. 22, 39, 52, 53, 89, 90, 103, 108–110).

Rothman, L. S. et al. (2009). 'The HITRAN 2008 molecular spectroscopic database'. In: *J. Quantitat. Spectrosc. Radiat. Transf.* 110, pp. 533–572. DOI: 10.1016/j.jqsrt.2009.02.013 (cit. on pp. 22, 39, 52, 53, 141).

Royer, D. L. et al. (2004). 'CO_2 as a primary driver of phanerozoic climate'. In: *GSA Today* 14, pp. 4–10. DOI: 10.1130/1052-5173(2004)014<4:CAAPDO>2.0.CO;2 (cit. on p. 5).

Salby, M. L. (1996). *Fundamentals of Atmospheric Physics*. Vol. 61. San Diego: Academic Press (cit. on pp. 19, 20, 23, 39, 54, 66, 105).

– (2012). *Physics of the Atmosphere and Climate*. New York: Cambridge University Press (cit. on pp. 123, 127).

Santer, B. D. et al. (2013). 'Human and natural influences on the changing thermal structure of the atmosphere'. In: *Proc. National Academy of Sci.* DOI: 10.1073/pnas.1305332110. URL: http://www.pnas.org/content/early/2013/09/10/1305332110.abstract (cit. on pp. 10, 12).

Scherllin-Pirscher, B. et al. (2011). 'Empirical analysis and modeling of errors of atmospheric profiles from GPS radio occultation'. In: *Atmos. Meas. Tech.* 9, pp. 1875–1890. DOI: 10.5194/amt-4-1875-2011. URL: http://www.atmos-meas-tech.net/4/1875/2011/ (cit. on p. 109).

Schilt, A. et al. (2010). 'Atmospheric nitrous oxide during the last 140,000 years'. In: *Earth Planet. Sci. Lett.* 300, pp. 33–43. ISSN: 0012-821X. DOI: 10.1016/j.epsl.2010.09.027. URL: http://www.sciencedirect.com/science/article/pii/S0012821X10006023 (cit. on p. 6).

Schweitzer, S. (2004). *Atmosphere and Climate Explorer mission ACE+: Humidity and temperature retrieval performance analysis (M.S. thesis)*. IGAM Wiss. Ber. 20. Graz, Austria: Inst. for Geophys., Astrophys., and Meteorol., Univ. of Graz (cit. on p. 41).

– (2010). *The ACCURATE concept and the infrared laser occultation technique: Mission design and assessment of retrieval performacne (Ph.D. thesis)*. Sci. Rep. 34-2010. Graz, Austria: Wegener Center Verlag. URL: http://www.wegcenter.at/wcv (cit. on pp. 15, 19–21, 41, 45, 49, 51, 54, 55, 58, 60–62, 66, 70, 76, 77, 80, 84, 87, 90, 92, 99, 102, 103, 107, 116, 117, 119, 122).

Schweitzer, S., G. Kirchengast and F. H. Ladstädter (2007). *Enhancement of the end-to-end occultation simulation tool EGOPS for enabling quasi-realistic simulations of LEO-LEO IR laser occultation measurments*. Tech. Rep. FFG-ALR 1/2007. Graz, Austria: Wegener Center, Univ. of Graz (cit. on p. 52).

Schweitzer, S., G. Kirchengast and V. Proschek (2011). 'Atmospheric influences on infrared-laser signals used for occultation measurements between Low Earth Orbit satellites'. In: *Atmos. Meas. Tech.* 4, pp. 2273–2292. DOI: 10.5194/amt-4-2273-2011. URL: http://www.atmos-meas-tech.net/4/2273/2011/ (cit. on pp. ix, 20–25, 39, 43, 87, 88, 96, 99, 102–104, 107, 112, 117, 122–124, 126, 127, 129, 130, 133, 138, 141–143, 152).

Schweitzer, S., V. Proschek and G. Kirchengast (2010). *Algorithms for cloud layering and greenhouse gas profiles retrieval from LIO data in cloudy air*. Tech. Rep. FFG-ALR 1/2010. Graz, Austria: Wegener Center, Univ. of Graz (cit. on pp. 50, 74).

Schweitzer, S. et al. (2008). *End-to-end Generic Occultation Performance Simulation and Processing System EGOPS: Enhancement of GPS RO data processing and IR laser occultation capabilities*. Tech. Rep. FFG-ALR 1/2008. Graz, Austria: Wegener Center, Univ. of Graz (cit. on pp. 22, 53).

Schweitzer, S. et al. (2011). 'Thermodynamic state retrieval from microwave occultation data and performance analysis based on end-to-end simulations'. In: *J. Geophys. Res.* 116, D10301. DOI: 10.1029/2010JD014850 (cit. on pp. 17–20, 23, 27, 30, 39–41, 47, 50, 54, 60, 83, 86, 88–90, 92, 94, 96, 99, 102, 104, 117, 118, 122, 124, 139, 141, 142, 146).

SciSat-1 (2014). *website last visited 2014-03-29*. URL: http://www.asc-csa.gc.ca/eng/satellites/scisat/default.asp (cit. on p. 13).

Silvestrin, P. and N. Floury (2003). *ESA/ESTEC input and recommendations for LEO-LEO observation error simulations*. Written Note to ACEPASS Study Team-IGAM/UniGraz (cit. on p. 41).

Smith, E. K. and S. Weintraub (1953). 'The constants in the equation for atmospheric refractive index at radio frequencies'. In: *Proceedings of the I.R.E.* Pp. 1035–1037 (cit. on pp. 19, 38, 89, 95).

Sofieva, V. F. (2009). *Atmospheric impacts on ILO signals: Assessment of infrared scintillations*. Tech. Rep. ESA/ESTEC TN3—Part of TR-IRPERF Report. Helsinki, Finland: Finnish Meteorol. Inst. (cit. on pp. 23, 39, 75, 76, 80, 133).

Sofieva, V. F. and E. Kyrölä (2004). 'Abel integral inversion in occultation measurements'. In: *Occultations for Probing Atmosphere and Climate*. Ed. by G. Kirchengast, U. Foelsche and A. K. Steiner. Berlin-Heidelberg: Springer Verlag (cit. on p. 104).

Sofieva, V. F. et al. (2009). 'Influence of scintillation on quality of ozone monitoring by GOMOS'. In: *Atmos. Chem. Phys.* 9, pp. 9197–9207. DOI: 10.5194/acp-9-9197-2009. URL: http://www.atmos-chem-phys.net/9/9197/2009/ (cit. on p. 133).

Solomon, S. et al., eds. (2007a). *Contribution of Working Group I to the Fourth Assessment Report of the Intergovernmental Panel on Climate Change*. Cambridge, United Kingdom and New York, NY, USA: Cambridge University Press (cit. on p. 6).

Solomon, S. et al. (2007b). 'Technical Summary'. In: *Climate Change 2007: The Physical Science Basis, Contribution of Working Group I to the Fourth Assessment Report of the Intergovernmental Panel on Climate Change*. Ed. by S. Solomon et al. Cambridge, United Kingdom and New York, NY, USA: Cambridge University Press, pp. 19–91. ISBN: 978-0521705967 (cit. on p. 45).

Steiner, A. K. and G. Kirchengast (2005). 'Error analysis for GNSS radio occultation data based on ensembles of profiles from end-to-end simulations'. In: *J. Geophys. Res.* 110, D15307. DOI: 10.1029/2004JD005251 (cit. on pp. 40, 90, 109).

Steiner, A. K., G. Kirchengast and H. P. Ladreiter (1999). 'Inversion, error analysis, and validation of GPS/MET occultation data'. In: *Ann. Geophys.* 17, pp. 122–138 (cit. on p. 97).

Steiner, A. K. et al. (2001). 'GNSS occultation sounding for climate monitoring'. In: *Phys. Chem. Earth (A)* 26, pp. 113–124 (cit. on pp. 47, 84).

Steiner, A. K. et al. (2009). 'Atmospheric temperature change detection with GPS radio occultation 1995 to 2008'. In: *Geophys. Res. Lett.* 36, L18702. DOI: 10.1029/2009GL039777 (cit. on pp. 19, 45, 47, 84).

Syndergaard, S. (1999). *Retrieval analysis and methodologies in atmospheric limb sounding using the GNSS radio occultation technique (Ph.D. thesis)*. Sci. Rep. 99-6. Copenhagen, Denmark: Danish Meteorol. Inst. (cit. on pp. 38, 51, 88, 97).

Syndergaard, S. and G. Kirchengast (2013). *Formulation and analysis of an Abel transform for deriving line-of-sight wind profiles from LEO-LEO IR laser occulation*. Tech. Rep. EAS-ESTEC 1/2013. Graz, Austria: Wegener Center, Univ. of Graz (cit. on p. 24).

Tans, P. and R. Keeling (2013). NOAA/ESRL (www.esrl.noaa.gov/gmd/ccgg/trends/) and Scripps Institution of Oceanograpyh (scrippsco2.ucsd.edu/). URL: www.esrl.noaa.gov/gmd/ccgg/trends/ (cit. on p. 6).

Thayer, G. D. (1974). 'An improved equation for the radio refractive index of air'. In: *Radio Sci.* 9, pp. 803–807 (cit. on p. 87).

Thomason, L. W. and G. Taha (2003). 'SAGE III aerosol extinction measurements: Initial results'. In: *Geophys. Res. Lett.* 30, p. 1631. DOI: 10.1029/2003GL017317 (cit. on pp. 53, 66).

Thomason, L. and T. Peter, eds. (2006). *Assessment of Stratospheric Aerosol Properties (ASAP)*. SPARC Report No. 4. Toronto, Canada: SPARC Sci. Steering Group (cit. on pp. 22, 39, 53, 66, 67).

Ware, R. et al. (1996). 'GPS sounding of the atmosphere from Low Earth Orbit: Preliminary results'. In: *Bull. Amer. Meteorol. Soc.* 77, pp. 19–40 (cit. on pp. 18, 84, 123).

Wickert, J. et al. (2001). 'Atmosphere sounding by GPS radio occultation: First results from CHAMP'. In: *Geophys. Res. Lett.* 28, pp. 3263–3266 (cit. on p. 18).

Wickert, J. et al. (2004). 'The radio occultation experiment aboard CHAMP: Operational data analysis and validation of vertical atmospheric profiles'. In: *J. Met. Soc. Japan* 82, pp. 381–395. DOI: 10.2151/jmsj.2004.381 (cit. on p. 18).

Williams, C., M. Menne and J. Lawrimore (2012). *Modification to pairwise homogeneity adjustment software to address coding errors and improve run-time efficiency*. NCDC Tech. Rep. NCDC No. GHCNM-12-02. NOAA's National Climatic Data Center, Asheville, NC: NOAA (cit. on p. 1).

Winker, D. M. et al. (2009). 'Overview of the CALIPSO mission and CALIOP data processing algorithms'. In: *J. Atmos. Oceanic Technol.* 26, pp. 2310–2323. DOI: 10.1175/2009JTECHA1281.1 (cit. on pp. 124, 130).

Wyser, K. (1998a). 'The effective radius in ice clouds'. In: *J. Climate* 11, pp. 1794–1802 (cit. on pp. 31, 39, 126).

– (1998b). 'The effective radius in large-scale models: Impact of aerosols and coalescence'. In: *Atmos. Res.* 49, pp. 213–234 (cit. on pp. 31, 39, 126).

Yunck, T. P. et al. (2000). 'AMORE: An autonomous constellation concept for atmospheric and ocean observation'. In: *Acta Astronautica* 46, pp. 35–364. ISSN: 0094-5765. DOI: 10.1016/S0094-5765(99)00231-3. URL: http://www.sciencedirect.com/science/article/pii/S0094576599002313 (cit. on p. 18).

Abstract:
The ACCURATE—Climate Benchmark Profiling of Greenhouse Gases and Thermodynamic Variables and Wind from Space satellite mission concept is a synergistic combination of the Low Earth Orbit microwave occultation (LMO) and Low Earth Orbit infrared-laser occultation (LIO) technique together termed Low Earth Orbit microwave and infrared-laser occultation (LMIO). It enables the measurement of physical and chemical profiles in the upper troposphere–lower stratosphere (UTLS) with high vertical resolution and in a long-term stable, global, consistent and self-calibrating way. This thesis contributes to the feasibility study of the LMIO mission concept. Firstly, an assessment of atmospheric influences on Infrared Laser (IRL) signals performing a limb-scan of the UTLS region was done. Thoroughly defined IRL on- absorption and off-channels are found to be ideal candidates for the LIO technique. Atmospheric broadband effects are highly correlated for channel pairs so that the differential transmission principle accurately corrects them. Secondly, an LMIO retrieval algorithm was developed to retrieve a set of greenhouse gases (GHGs) in clear-air conditions, including defocusing loss, aerosol extinction and Rayleigh scattering. A consecutive retrieval order of the forward-simulated IRL signals enables to retrieve unbiased volume mixing ratio profiles of GHGs with r.m.s. errors smaller than 1 % to 3 %. Thirdly, a LMIO retrieval was developed to cover cloudy-air conditions. IRL signals are strongly affected by cloud extinction, reducing the tropospheric penetration depth of occultation events. Intermittent cloud layers or thin cirrus, perturbing the IRL transmission profile, can be bridged and increase the penetration depth and thus the number of occultation events for climate benchmark observations. The results show promising prospects for climate benchmark contributions with unprecedented accuracy for monitoring the physical and chemical state of the UTLS.

Zum Inhalt:
Das Satellitenmissions-Konzept ACCURATE—Climate Benchmark Profiling of Greenhouse Gases and Thermodynamic Variables and Wind from Space ist eine Synergie der Mikrowellen-Okkultation (LMO) und der Infrarotlaser-Okkultation (LIO), vereinigt zu der Mikrowellen- und Infrarotlaser-Okkultation für Satelliten (LMIO). Es ermöglicht die Messung physikalischer und chemischer Profile in der oberen Tropo- und unteren Stratosphäre (UTLS) mit hoher vertikaler Auflösung, Langzeit-Stabilität, globaler Abdeckung und funktioniert selbst-kalibrierend. Diese Arbeit trägt zu Machbarkeitsstudien zum LMIO Konzept bei. Erstens: zur Erfassung der atmosphärischen Einflüsse auf das Infrarotlaser (IRL) Signal während des Limb-Scan in der UTLS. Sorgfältig gewählte IRL-absorbierende und nicht-absorbierende Kanäle sind ideale Kandidaten für die LIO Technik. Signalpaare weisen hohe Korrelation bei atmosphärischen Breitbandeffekten auf, die durch Signal-Subtraktion korrigiert werden. Zweitens: ein LMIO Retrieval Algorithmus zur Gewinnung von Treibhausgaskonzentrationen GHGs, welcher Defokusierungs-Verluste, Aerosol-Extinktion und Rayleigh-Streuung beinhaltet, wurde entwickelt. Eine Abfolge von vorwärts simulierten IRL Signalen ermöglicht eine Retrievalgenauigkeit für GHGs frei von systematischen Fehlern und Restfehlern kleiner als 1 % bis 3 %. Drittens: ein LMIO Retrieval wurde entwickelt, um auch Wolkeneffekte mit abzudecken. IRL Signale sind stark beeinflusst von Wolken und reduzieren somit die troposphärische Eindringtiefe für Okkultationen. Wolkenschichten oder dünne Zirren, welche das IRL-Transmissionsprofil stören, werden überbrückt und erhöhen somit die Eindringtiefe und daher die Anzahl der Okkultationen für Klima-Benchmark-Beobachtungen. Die Ergebnisse zeigen vielversprechende Aussichten für Klimamessungen mit noch nie dagewesener Genauigkeit zum Beobachten des physikalischen und chemischen Zustandes der Erdatmosphäre.

Wegener Center for Climate and Global Change
University of Graz
Brandhofgasse 5
A-8010 Graz, Austria
www.wegcenter.at
ISBN 978-3-9503918-0-0